UNIVERSIDAD COMPLUTENSE DE MADRID
FACULTAD DE MEDICINA

TESIS DOCTORAL

Identificación de biomarcadores predictivos de respuesta a inhibidores de la angiogénesis en tumores neuroendocrinos

Identification of predictive biomarkers of response to angiogenesis inhibitors in neuroendocrine tumours

MEMORIA PARA OPTAR AL GRADO DE DOCTOR

PRESENTADA POR

Alberto Lens Pardo

DIRIGIDA POR

Rocío García Carbonero
Beatriz Soldevilla Navarro

Madrid

UNIVERSIDAD COMPLUTENSE DE MADRID

FACULTAD DE MEDICINA

TESIS DOCTORAL

Identificación de biomarcadores predictivos de respuesta a inhibidores de la angiogénesis en tumores neuroendocrinos

Identification of predictive biomarkers of response to angiogenesis inhibitors in neuroendocrine tumours

MEMORIA PARA OPTAR AL GRADO DE DOCTOR

PRESENTADA POR

Alberto Lens Pardo

DIRECTORES

Rocío García Carbonero y Beatriz Soldevilla Navarro

Universidad Complutense de Madrid

Facultad de Medicina

Programa de doctorado en Bioquímica, Biología Molecular y Biomedicina

Identificación de biomarcadores predictivos de respuesta a inhibidores de la angiogénesis en tumores neuroendocrinos

Identification of predictive biomarkers of response to angiogenesis inhibitors in neuroendocrine tumours

Alberto Lens Pardo

Thesis directors: Dra. Rocío García Carbonero and Dra. Beatriz Soldevilla Navarro

Gastrointestinal and Neuroendocrine Tumor Group

Center of Experimental Oncology

Instituto de Investigación Sanitaria Hospital 12 de Octubre

Financial Support

This PhD project has been performed with the following funding:

- Phase II/III randomized, double-blind study of sandostatin LAR in combination with axitinib versus sandostatin LAR in combination with placebo in patients with progressive advanced G1-G2 (WHO 2010) neuroendocrine tumors of non-pancreatic origin. Pfizer and Grupo Español de Tumores Neuroendocrinos (GETNE; EUDRACT 2011-001550-29).

- Predoctoral fellowship: "Programa operativo de empleo juvenil YEI Unión Europea 2019. Comunidad de Madrid (CAM; PEJD-2019-PRE/BMD-17058).

- Predoctoral fellowship: "Contratos predoctorales de formación en investigación en salud" (PFIS). Instituto de Salud Carlos III (PFIS; FI20/00131).

- Mobility fellowship: "Ayudas para la movilidad del personal investigador" (Modalidad M-AES). Instituto de Salud Carlos III (MV23/00007).

Agradecimientos

Con el depósito de mi tesis doctoral culmina la etapa más importante de mi formación científica. En estos 5 años, he aprendido numerosas técnicas, a escribir proyectos y artículos, a pensar críticamente y a trabajar de forma independiente. También ha sido una etapa de crecimiento personal, y en este sentido, me ha enseñado las virtudes y dificultades del mundo laboral, con las que tendré que convivir a lo largo de mi carrera. Han sido años de muchísimo esfuerzo y dedicación, traducidos en incontables horas de trabajo, incluyendo fines de semanas o vacaciones, con el único objetivo de hacer mi trabajo lo mejor posible. A pesar de ello, me he equivocado infinitud de veces, pero he aprendido que estos errores son los que nos hacen mejores profesionales y personas. Todo este esfuerzo se traduce ahora en tranquilidad y satisfacción, por saber que he dado todo por aprovechar al máximo esta etapa de mi formación. A pesar de esta realización personal, soy plenamente consciente de que poco o nada de lo que presento hoy aquí hubiese sido posible sin muchas personas a las cuales estoy profundamente agradecido por haberme acompañado en este camino.

En primer lugar, me gustaría agradecer a mi directora de tesis, la Dra. Rocío García Carbonero. Muchas gracias por haberme dado la oportunidad de llevar a cabo este proyecto, siempre he sentido tu confianza y tu respaldo, y eso ha sido clave para poder crecer como investigador. Tu forma de ver la investigación, centrada en el paciente, es algo que me llevo para toda mi carrera. Gracias por todas esas horas extra que dedicas a la ciencia y a nuestra formación, y por todas las oportunidades que me has brindado en estos 5 años. Del mismo modo, también quiero agradecer a mi segunda directora, la Dra. Beatriz Soldevilla Navarro. Gracias por haber confiado en mí, y por tu supervisión y gestión del laboratorio. Gracias por todo ese trabajo, a veces oculto, que permite que el laboratorio siga en marcha.

También me gustaría dar las gracias a todos mis compañeros de grupo con los que he compartido horas y horas de trabajo y aprendizaje, pero, sobre todo, cafés, comidas y buenos ratos. En primer lugar, quiero acordarme de Jacinto. Puedo decir con total tranquilidad que, sin ti, mucho de lo que presento hoy aquí habría sido imposible. Gracias por tu ayuda diaria con los experimentos, tus ideas y sugerencias, y por todas nuestras conversaciones en la cafetería. Me has ayudado a ver el lado positivo de las cosas. Carlos, mi binomio de congresos y bioinformático de cabecera. Gracias por todo lo que me has enseñado y ayudado en estos 5 años, pero especialmente, por tu entusiasmo, ideas y propuestas, han sido un oasis en esta travesía. Creo que tienes aun mucho que darle a la ciencia. Quiero agradecer también a Bea Gil y a Patri. Vuestra ayuda con los últimos experimentos, ratones y durante mi estancia en Toronto han sido imprescindibles. Esta tesis también es vuestra. No puedo olvidarme tampoco de Bea Antón, mi compañera de sitio y oncóloga de confianza. Gracias por tu trabajo y esfuerzo y por no saber decir que no cuando necesitamos tu ayuda. A tu vuelta montamos el chiringuito. Otra persona fundamental ha sido Dani, fue un placer estrenar el COE contigo. Gracias por preocuparte por mí, y por nuestros cafés de F1, criptobros o películas. Finalmente, agradecer a todos los miembros presentes y pasados del GI NET: Arantza, Bea R, Marcos, María H, María B, Raúl, Laura, Anna, Paula, Andrea, María, Dona, Giovanni y David. Gracias por estar siempre dispuestos a enseñarme y ayudarme cuando lo necesitaba.

A su vez, quiero acordarme de otros compañeros, que, aunque no comparten grupo conmigo, siempre se han mostrado dispuestos ayudarme y enseñarme todo lo que sabían. Por ello, quiero agradecer toda la ayuda brindada por nuestro grupo hermano de cáncer de pulmón, y por otros laboratorios del Imas12 y del Sunnybrook. Más concretamente, quiero agradecer a Inés, por esta siempre dispuesta a ayudarme con los ELISA, las PCRs, los envíos o lo que hiciese falta, pero sobre todo por tomarse un café conmigo siempre que coincidíamos. También quiero agradecer a Ángel y a Javier, los predocs mayores de pulmón. Fuisteis los mejores referentes para iniciar mi camino de doctorado. No puedo olvidarme de mis compañeros del COE, Jose, Juanma, Lorena, Rocío, Nuria y Eva. Gracias por hacer que estos últimos 2 años hayan sido más agradables. Finalmente, quiero agradecer al Dr. Iacovos Michael y a todo su grupo en el que viví 6 meses de pura ciencia. Gracias por fomentar mi curiosidad, creatividad y hacerme sentir valorado. Gracias por ayudarme a reconectar con la investigación cuando más lo necesitaba. Gracias Nilakshi, Khab, William, Areeba, Rusha, Paul y Zoey.

Uno de los aprendizajes que me llevo de la tesis, es que la colaboración es imprescindible en investigación. Este trabajo es fruto de esta colaboración científica entre varias instituciones a las cuales me gustaría reconocer. En primer lugar, el Instituto de Investigación Sanitaria Hospital 12 de Octubre, hogar de nuestro grupo, el Hospital 12 de Octubre y el CNIO. Quiero agradecer también a Yolanda Rodríguez y Ana Teijo del departamento de anatomía patológica del H12O, y a Cristian Perna y Alejandra

Caminoa del departamento de anatomía patológica del Hospital Ramon y Cajal por toda su ayuda en este proyecto. También quiero mencionar a nuestros colaboradores de otras instituciones: los investigadores del ensayo AXINET y TALENT, y todos los investigadores de GETNE, al igual que todos los pacientes que han participado en estos estudios.

Asimismo, quiero agradecer a la Universidad Complutense de Madrid y al programa de doctorado de Bioquímica, Biología molecular y Biomedicina por permitirme realizar la tesis doctoral y formarme como docente. En particular a Eva de Lago, mi tutora, y a Pilar Cano y José Javier Fernández Ruiz con los que he descubierto el apasionante mundo de la enseñanza. Finalmente, quiero agradecer a todas las entidades que me han financiado estos 5 años, la Comunidad de Madrid, la Unión Europea y el Instituto de salud Carlos III. Gracias por invertir en mí formación, espero que esto me permita contribuir a servir y a mejorar la vida de las personas de este país.

Echando la vista atrás, me acuerdo en este momento de más personas, que, aunque no han formado parte de mi formación durante estos 5 años, han permitido que pueda superar con éxito esta etapa. Es el caso de María Peláez, con la que descubrí mi vocación científica durante el bachillerato, o la Dra. Mónica Marazuela y el Dr. Diego Arango, en cuyos laboratorios inicié mi andadura científica durante el grado y el máster. También quiero acordarme de las personas que me dirigieron en el día a día en estas estancias, como la Dra. Rebeca Martínez Hernández, que es para mí el ejemplo ideal de mentora, o las Dras. Estefanía Anguita y Águeda Martínez Barriocanal, con las que aprendí que el esfuerzo en ciencia vale la pena y con las que probé todo tipo de platos del mundo durante mi año en Barcelona.

Para ir terminando, quiero dar las gracias a todas las personas que, aunque no han estado conmigo en el laboratorio, han sido imprescindibles en el día a día para poder vivir mejor esta etapa. A mis amigos Urbeños: Bendito, Iñigo, Jorge, Sami y Louis. Llevamos 20 años juntos y los que nos quedan. Gracias por las cenas de los jueves de estos últimos meses, me han ayudado a desconectar y disfrutar en los momentos más duros de la tesis. A mis compañeros Bonna Fide: Gema, David, María, Josekas, Sara, Javi, Teresa, Mirabai, Inés y Henar. Me habéis inspirado siempre a ser mejor y lo seguiréis haciendo allá donde vayáis, gracias por las cenas, por los viajes y por vuestra amistad. Sé que vais a estar ahí siempre. En particular, quiero agradecer a Cristina y Manuel. Es muy bonito ver como esa amistad que se intensificó durante el año en

Barcelona ha ido creciendo hasta el día de hoy. Gracias por nuestro pádel y desayunos de todos los sábados. Gracias por escucharme, habéis sido un gran apoyo en los momentos de más sufrimiento de esta tesis. Estoy seguro de que esto es solo el principio de una amistad para toda la vida. Y a Alba, que, tras cientos de audios y bocetos, ha sabido convertir mis ideas en una portada magnifica. Gracias de verdad.

Finalmente, quiero agradecer a toda mi familia, lo más valioso que tengo. A mis abuelos Caridad y Alberto, y Mª Teresa y Matías. A mi nueva familia, Rafa, María y Lorena, cuyo cariño y generosidad he sentido a lo largo de toda la tesis doctoral. Pero, sobre todo, quiero dar las gracias por mis hermanos y por mis padres, con ellos he compartido toda mi vida y han hecho de mi quien soy. María, gracias por tu gran generosidad, siempre estas pendientes de hacer felices a los demás. Gracias por no olvidarte de Madrid e iluminar nuestras vidas. Inés, gracias por tu alegría, no hay nada como volver a casa y contagiarse con ella para superar un mal día. Después de este año, te mereces todas las cosas buenas que tienes por delante. Matías, estoy tremendamente orgulloso de cómo te has superado y madurado estos últimos años. Gracias por tu esfuerzo y dedicación, son un ejemplo a seguir en mi día a día. Ana, "nuestro bebé", siempre he sentido tu cariño. Gracias por ser la única dispuesta a jugar a cualquier juego conmigo. Lo malo es que ahora que seré doctor, se te complica más aun ganarme al Catán. Y por supuesto, a mis padres, Ana y Alberto. A ellos les debo todo. Mamá, gracias por tu entrega diaria estos 28 años. Has renunciado a infinitud de cosas por nosotros y por Papá. Todo lo que consigamos te lo debemos a ti. Gracias por quererme como lo haces. No podrías haberlo hecho mejor. Papá, gracias por inspirarme, por incitarme a ser mejor cada día y a encontrar una vocación. Gracias por enseñarme junto con Mamá, a valorar lo que realmente importa. Sois mi modelo a seguir.

Finalmente, quiero dar las gracias a mi esposa, Natalia. Me has enseñado lo que es querer de verdad, y aunque no lo merezco, tengo la fortuna de que me lo sigas demostrando día a día. Gracias por sacrificarte por mí sin esperar nada a cambio. Gracias por enfrentar tus miedos por nuestra familia. Gracias por estos maravillosos 9 años. No puedo saber qué nos depara el futuro, pero sé que quiero vivirlo contigo. Gracias por querer compartir la vida conmigo.

"El señor mismo marchará al frente de ti y estará contigo; nunca te dejará ni te abandonará. No temas ni te desanimes".

A mis padres Ana y Alberto,

mis hermanos, María, Inés, Matías y Ana,

y a mi esposa, Natalia.

INDEXES

Index

Index of figures

Index of tables

RESUMEN/ABSTRACT

Resumen

Los tumores neuroendocrinos (TNEs) constituyen un grupo heterogéneo de neoplasias que se originan a partir de células neuroendocrinas, productoras de monoaminas, péptidos y otras sustancias biológicamente activas, ampliamente distribuidas en el organismo. Los TNEs son tumores muy vascularizados y la angiogénesis juega un papel clave en su desarrollo y progresión. Esto ha llevado a la evaluación y aprobación de algunos inhibidores multiquinasa antiangiogénicos para el tratamiento de estos tumores. Aunque estos fármacos son efectivos en TNEs pancreáticos y extrapancreáticos, la magnitud global del efecto es limitada, no todos los pacientes se benefician de esta estrategia terapéutica, e incluso los que responden, eventualmente desarrollan resistencia y progresión de la enfermedad. En este contexto, el objetivo principal de este proyecto fue identificar biomarcadores predictivos de respuesta a los inhibidores de la angiogénesis en TNEs y desentrañar los mecanismos moleculares implicados. Con este propósito, analizamos muestras biológicas de pacientes incluidos en el ensayo clínico internacional de fase II/III, doble ciego, aleatorizado, controlado con placebo AXINET, que evaluó axitinib frente a placebo, ambos en combinación con análogos de somatostatina (ASS), en 256 pacientes con TNEs extrapancreáticos avanzados (Número EudraCT 2011-001550-29).

En primer lugar, hemos analizado el perfil transcriptómico de 126 pacientes con TNEs del ensayo clínico AXINET utilizando “arrays” de expresión Clariom Human S y hemos estudiado la asociación entre la expresión génica, y la supervivencia libre de progresión (SLP) y la reducción del volumen tumoral. Para ello, hemos empleado regresiones de Cox, pruebas de interacción y regresión lineal regularizada separando los pacientes tratados con axitinib y ASS, de los tratados con placebo y ASS, que se utilizaron como controles. A continuación, se generó una firma de expresión utilizando el paquete de R *singscore* y se evaluó su capacidad predictiva con regresiones de Cox y curvas de Kaplan-Meier. También se analizaron las diferencias en las características clinicopatológicas y moleculares entre pacientes con altas y bajas puntuaciones de la firma utilizando las pruebas de Chi-Cuadrado y el análisis de expresión diferencial y de enriquecimiento de vías de señalización, respectivamente. Los resultados se validaron utilizando la misma

metodología en una cohorte independiente de 29 pacientes tratados con inhibidores de la angiogénesis o ASS en el Hospital 12 de Octubre. La capacidad predictiva de los niveles plasmáticos de osteopontina (OPN), uno de los biomarcadores predictivos identificados, se evaluó en el plasma de pacientes con TNEs mediante ELISA en la cohorte de descubrimiento y en 2 cohortes de validación: una cohorte independiente de 87 pacientes del ensayo clínico AXINET, y una segunda cohorte de 99 pacientes tratados con lenvatinib, otro inhibidor de la angiogénesis, en el ensayo clínico TALENT. Finalmente, hemos sobreexpresado y reducido la expresión de OPN en líneas celulares de TNEs y hemos estudiado el papel que juega en la proliferación, migración y clonogenicidad de estos tumores. Asimismo, hemos estudiado su papel en la respuesta a los inhibidores de la angiogénesis *in vitro,* con ensayos de formación de tubos o ensayos de viabilidad celular, e *in vivo,* en modelos de embrión de pollo y de ratón.

En la primera etapa del proyecto, hemos identificado 11 genes cuya expresión se asocia de forma significativa con la SLP exclusivamente en pacientes tratados con axitinib y no en aquellos tratados con placebo. A continuación, mediante la regresión lineal regularizada, identificamos los 3 genes (*REXO1L2P, ATXN7, SPP1)* que mejor se asocian a la reducción del volumen tumoral en pacientes tratados con axitinib. Los pacientes con puntuaciones altas de la firma de estos 3 genes mostraron una SLP significativamente mayor que aquellos con puntuaciones bajas (SLP: 38.5 vs. 11.6 meses; *HR: 0.31 (0.16 – 0.59),* $p < 0.001$) cuando fueron tratados con axitinib. Sin embargo, la puntuación de la firma no se asoció con la SLP en pacientes tratados con placebo. Del mismo modo, los pacientes con altos niveles de la firma tratados con axitinib alcanzaron una mayor reducción del volumen tumoral que aquellos con bajos niveles de la firma ($p = 0.004$). Sin embargo, esta diferencia no se observó en los pacientes tratados con placebo. Estos resultados fueron validados en una cohorte independiente de pacientes tratados con inhibidores de la angiogénesis o ASS en el Hospital 12 de Octubre. El estudio de las características moleculares de estos pacientes reveló que aquellos con bajos niveles de la firma (no respondedores) tenían tumores enriquecidos en vías de señalización asociadas con resistencia a los inhibidores de la angiogénesis como la hipoxia, la vía de mTOR o la transición epitelio-mesénquima.

Para facilitar la implementación clínica, hemos evaluado la capacidad predictiva de la proteína codificada por uno de los genes de la firma, OPN (*SPP1*), en el plasma de los pacientes. En la cohorte de descubrimiento, los pacientes con altos niveles plasmáticos de OPN tuvieron una SLP significativamente menor que aquellos con niveles bajos cuando fueron tratados con axitinib (SLP: 13.2 vs. 38.5 meses, *HR: 2.04 (0.99 – 4.22), p = 0.053*), pero no cuando fueron tratados con placebo. Estos resultados se validaron en una cohorte independiente de 87 pacientes del ensayo AXINET (cohorte de validación), donde la SLP fue significativamente menor en pacientes con altos niveles plasmáticos de OPN en comparación con aquellos con niveles bajos (SLP: 14.0 vs. 71.1; *HR: 2.81 (1.18 – 6.65), p = 0.019*) cuando fueron tratados con axitinib, pero no cuando fueron tratados con placebo. La capacidad predictiva de OPN también se validó en pacientes del ensayo TALENT, que evaluó lenvatinib en TNEs pancreáticos y extrapancreáticos. En estos pacientes, aquellos con altos niveles plasmáticos de OPN tuvieron una SLP significativamente menor que aquellos con niveles bajos (SLP: 13.1 vs. 22.3 meses; *HR: 1.81 (1.09 – 3.00), p = 0.022*). Finalmente, en estudios *in vitro* hemos demostrado que OPN regula la proliferación, migración y clonogenicidad en líneas celulares de TNEs, y promueve la angiogénesis en células HUVEC. Además, OPN induce resistencia a los inhibidores multiquinasa antiangiogénicos en modelos CDX de ratón, confirmando su papel clave en la modulación de la respuesta de los TNE a estos fármacos.

En conclusión, en este trabajo hemos identificado una firma de 3 genes (*REXO1L2P*, *ATXN7* y *SPP1*) que predice la eficacia de los inhibidores multiquinasa antiangiogénicos en TNEs. Además, los niveles de OPN (*SPP1*) en plasma predicen por si solos la eficacia a estos fármacos. También hemos demostrado que OPN regula funciones oncogénicas clave como la proliferación, migración y clonogencidad en líneas celulares de TNEs, y genera resistencia a estos fármacos en células HUVEC y en modelos murinos CDX de TNE. Los niveles plasmáticos de OPN podrían utilizarse en la práctica clínica para guiar las decisiones terapéuticas sobre inhibidores de la angiogénesis, aumentando su eficacia, reduciendo costes y toxicidad innecesaria, y mejorando el balance beneficio-riesgo en pacientes con TNEs.

Abstract

Neuroendocrine tumors (NETs) are rare and heterogeneous malignancies arising from neuroendocrine cells. These tumors are hypervascular and angiogenesis plays a crucial role in their development and progression. Indeed, NETs express high levels of VEGF-VEGFR signaling pathway proteins and several omic analysis have highlighted the importance of angiogenesis in these patients. This has led to the approval of anti-angiogenic multikinase inhibitors (MKIs) as anticancer therapy for NET patients. While these drugs are active in pancreatic and extrapancreatic NETs, the global magnitude of the effect is limited, not all patients benefit from this therapeutic strategy, and even those that initially respond eventually develop resistance and experience disease progression over time. In this context, the main goal of this project was to identify predictive biomarkers of response to angiogenesis inhibitors in NETs and unravel the molecular mechanisms involved. To this aim, we analyzed biological samples of patients enrolled in the randomized, double-blind, placebo-controlled, international phase II/III AXINET clinical trial assessing axitinib versus placebo, both in combination with somatostatin analogues (SSA), in 256 patients with advanced extrapancreatic NETs (EudraCT Number 2011-001550-29)

First, we analyzed the transcriptomic profile of 126 NET patients (discovery cohort) enrolled in the AXINET trial using Clariom Human S arrays and studied the association of gene expression with progression-free survival (PFS) and tumor shrinkage. To do so, we have performed Cox regression, interaction tests, and regularized linear regression separately in axitinib/SSA- and placebo/SSA-treated patients. A gene expression signature was established using the R package *singscore* and its predictive capacity was evaluated with Kaplan-Meir curves and Cox regression models. Clinicopathological and molecular differences between high- and low-score signature patients were evaluated using Chi-square and differential expression followed by gene set enrichment analysis, respectively. These results were validated using the same methodology in an independent cohort of 29 NET patients treated with MKIs or SSA at Hospital 12 de Octubre. The predictive capacity of osteopontin (OPN) plasma levels, one of the identified predictive biomarkers, was evaluated as previously described using ELISA in the discovery cohort and in two validation cohorts: an independent cohort of 87 patients from the AXINET trial and a second cohort of 99 NET patients treated with lenvatinib, another MKI, in the

TALENT clinical trial. Finally, we overexpressed and knockdown OPN in NET cell lines to study its role in NETs proliferation, migration and clonogenicity. Similarly, we also evaluated its role in modulating response to MKIs *in vitro*, using tube formation and cell viability assays, and *in vivo* using NET cell-line derived xenografts (CDX) in the chorioallantoic membrane (CAM) of the chicken embryo and mouse models.

In the first stage of the project, we identified 11 genes that were significantly and exclusively associated with PFS in axitinib-treated and not in SSA-treated patients. Next, linear regularized regression identified the 3 genes (*REXO1L2P*, *ATXN7* and *SPP1*) that better explain tumor shrinkage in response to axitinib. Patients with high scores of this 3-gene signature had significantly better PFS than patients with low signature scores (PFS: 38.5 vs. 11.6 months; *HR: 0.31 (0.16 – 0.59), p < 0.001*) when treated with axitinib and notably, the signature score was not associated with PFS in patients treated with placebo. Similarly, high score patients treated with axitinib had significantly increased tumor shrinkage compared to those with low score (*p = 0.004*) while this difference was not observed by signature score in placebo-treated patients. These results were validated in an independent cohort of 29 NET patients treated with MKIs or SSA at Hospital 12 de Octubre. Interestingly, low-score patients (non-responders) were enriched in molecular pathways previously associated with resistance to anti-angiogenic therapy (AAT) such as hypoxia, mTORC1 signaling or EMT.

To facilitate the clinical implementation of the signature, we evaluated the predictive capacity of the protein product of one gene of the signature, OPN (*SPP1*), assessed in patient’s plasma. In the discovery cohort, patients with high OPN plasma levels had significantly worse PFS than patients with low levels when treated with axitinib (PFS: 13.2 vs. 38.5 months, *HR: 2.04 (0.99 – 4.22), p = 0.053*) but not when treated with placebo. We confirmed these findings in an independent cohort of 87 AXINET patients (validation cohort), being PFS significantly lower in patients with high plasma OPN levels as compared to those with low levels (median PFS: 14.0 vs. 71.1; *HR: 2.81 (1.18 – 6.65), p = 0.019*) when treated with axitinib and not when treated with placebo. The predictive capacity of OPN was further validated in patients enrolled in the TALENT single arm trial that assessed lenvatinib in pancreatic and extrapancreatic NETs. Among these patients, those with high OPN plasma levels had significantly worse PFS than patients with low levels (PFS: 13.1 vs. 22.3 months; *HR: 1.81 (1.09 – 3.00), p = 0.022*). Finally, *in vitro* studies demonstrated that OPN upregulation and knockdown modulates proliferation, migration and clonogenicity in NET cell lines. Moreover, OPN upregulation also promoted angiogenesis *in vitro* and resistance to MKIs in NET CDXs *in vivo,* confirming its pivotal role in modulating response to MKIs in NETs.

In conclusion, this study identified a 3-gene signature (*REXO1L2P*, *ATXN7* and *SPP1*) that predicts the efficacy of anti-angiogenic MKIs in NETs. OPN (*SPP1*) plasma levels alone, as a more readily accessible surrogate marker, can also predict efficacy of these drugs, enabling an easy implementation of this predictive biomarker in the clinical setting. Moreover, OPN promotes the acquisition of key oncogenic functions such as proliferation, migration and clonogenicity in NET cell lines and drives resistance to these drugs in NET CDX mouse models. OPN plasma levels could be used in clinical practice to guide therapeutic decisions regarding angiogenesis inhibitors, increasing efficacy and reducing cost and unnecessary toxicity of these drugs, thereby leading to an overall improvement in their benefit-risk balance in NET patients.

ABBREVIATIONS

Abbreviations

AML	Acute myeloid leukemia
AAT	Antiangiogenic therapy
AC	Atypical carcinoid
AKT	RAC-alpha serine/threonine-protein kinase
ANG	Angiopoietin
ATXN7	Ataxin 7
BMDC	Bone marrow derived cells
CAM	Chorioallantoic membrane
CAPTEM	Capecitabine and temozolomide
CDKN1B	Cyclin dependent kinase inhibitor 1B
CDX	Cell line derived xenograft
CD31	Cluster of differentiation 31
CD44	Cluster of differentiation 44
CFA	Colony formation assay
CgA	Chromogranin A
CI	Confidence interval
CN	Copy number
COX-2	Cyclooxygenase-2
CRC	Colorectal cancer
CR	Complete response
CT (scan)	Computed tomography
Ct	Cycle threshold
CTRL	Control
DAPI	4′,6-diamidino-2-phenylindole
DC	Dendritic cells

DEG	Differentially expressed genes
DFS	Disease free survival
DMEM	Dulbecco's modified Eagle medium
DMSO	Dimethyl sulfoxide
DTC	Differentiated thyroid carcinoma
EC	Endothelial cell
ECM	Extracellular matrix
ED	Embryonic development day
ELISA	Enzyme linked immunosorbent assay
EMA	European Medicines Agency
EMT	Epithelial to mesenchymal transition
EP-NET	Extrapancreatic NETs
EMEM	Eagle's minimum essential medium
eNOS	Endothelial nitric oxide synthase
ERK1/2	Mitogen-activated protein kinase 3 and 1
FBS	Fetal bovine serum
FDA	Food and drug administration
FDR	False discovery rate
FFPE	Formalin-fixed paraffin embedded
FGF	Fibroblast growth factor
F12K	Ham's F-12K (Kaighn's) medium
GI	Gastrointestinal
GSEA	Gene set enrichment analysis
G1	Grade 1
G2	Grade 2
G3	Grade 3

GEP-NET	Gastroenteropancreatic neuroendocrine tumor
GETNE	Grupo español de tumores neuroendocrinos
HCC	Hepatocellular carcinoma
HIF	Hypoxia inducible factor
H/E	Hematoxylin and eosin
HR	Hazard ratio
H12O	Hospital 12 de Octubre
IC50	Half-maximal inhibitory concentration
IHC	Immunohistochemistry
IFN	Interferon
IL	Interleukin
INSM1	Insulinoma-associated protein 1
ITGAV	Integrin αv
ITGB3	Integrin β3
JUN	JUN proto-oncogene
KD	Knockdown
KO	Knockout
KIT	Receptor protein-tyrosine kinase
LCNEC	Large cell neuroendocrine carcinoma
L-NET	Lung neuroendocrine tumor
LOH	Loss of heterozygosity
MAD	Median absolute deviation
MAPK	Mitogen-activated protein kinase
MTC	Medullary thyroid cancer
MEN1	Multiple endocrine neoplasia type 1
MEN2	Multiple endocrine neoplasia type 2

MEN4	Multiple endocrine neoplasia type 4
MKI	Multikinase inhibitor
MLP	Metastasis-like primary
MMP	Metalloproteinases
MOFA	Multi omic factor analysis
MSE	Mean-squared error
mTOR	Mechanistic target of rapamycin
MVD	Microvessel density
NEC	Neuroendocrine carcinoma
NEN	Neuroendocrine neoplasms
NES	Normalized enrichment score
NET	Neuroendocrine tumor
NF-kB	Nuclear factor kappa B
NF1	Neurofibromatosis 1
NSCLC	Non-small cell lung cancer
OPN	Osteopontin
ORR	Objective response rate
OR	Odd ratio
OS	Overall survival
OSCC	Oral squamous cell carcinoma
OE	Overexpression
O/N	Overnight
Pan-NET	Pancreatic neuroendocrine tumor
PC	Prostate cancer
PCA	Principal component analysis
PD	Progressive disease

PDGFR	Platelet derived growth factor receptor
PFS	Progression free survival
PGE2	Prostaglandin E2
PGF	Placental growth factor
PI3K	Phosphoinositide-3-kinase
PLCγ	Phospholipase Cγ
PR	Partial response
PTC	Papillary thyroid cancer
RCC	Renal cell carcinoma
RET	Proto-oncogene tyrosine-protein kinase receptor Ret
RECIST	Response evaluation criteria in solid tumor
REXO1L2P	REXO1 Like 2, pseudogene
RLT	Radioligand therapy
ROC	Receiver operating characteristic
RPMI	Roswell Park Memorial Institute
RRID	Research resource identifiers
RT	Room temperature
qRT-PCR	Quantitative real time polymerase chain reaction
RT2	RIP1-Tag2
SI-NET	Small intestine neuroendocrine tumor
SD	Stable disease
SD	Standard deviation
sgRNA	small guide RNA
shRNA	short hairpin RNA
SPP1	Secreted phosphoprotein 1
SSA	Somatostatin analogue

SST	Somatostatin receptor
STZ	Streptozocin
Syp	Synaptophysin
TAM	Tumor-associated macrophage
TEM	Temozolomide
TIE2	Angiopoietin-1 receptor
TMB	Tumor mutational burden
TSC1	Tuberous sclerosis complex 1
TSC2	Tuberous sclerosis complex 2
TC	Typical carcinoid
uPA	urokinase plasminogen activator
US	Ultrasound
VEGF	Vascular endothelial growth factor
VEGFR	Vascular endothelial growth factor receptor
VHL	Von Hippel-Lindau
WHO	World health organization
177Lu	Lutetium-177
5-FU	5-Fluorouracil
ºC	Degrees Celsius

BACKGROUND

Background

1. Neuroendocrine neoplasms

1.1 Origin and main characteristics

Neuroendocrine neoplasms (NENs) encompass a family of rare and heterogeneous malignancies originating from neuroendocrine cells, which exhibit mixed morphological and molecular features of the neural and endocrine systems (Figure 1B-C) (1). These cells are widely spread across the human body, either as dispersed cells, forming the diffuse neuroendocrine system or as organized clusters in endocrine glands such as the pancreatic islets. Seventeen types of neuroendocrine cells have been described based on their location and ability to produce, store and secrete different bioactive compounds involved in tissue homeostasis and in the regulation of diverse biological processes such as metabolism, immunity and injury response (2,3) (Figure 1A-C). Some NENs retain this ability of producing and secreting hormones and bioactive molecules, leading to a set of symptoms called functional syndromes. These symptoms may vary depending on the secreted hormone and the most frequent one is the carcinoid syndrome, primarily caused by excess serotonin secretion which causes wheezing, skin flushing, diarrhea, and fibrotic valvular heart disease (4).

Moreover, neuroendocrine cells and NENs are characterized by the presence of long, axon-like extensions (5,6) (Figure 1B), the expression of somatostatin receptors (SST) on the cell surface and the expression of neuroendocrine markers such as synaptophysin (Syp), chromogranin A (CgA) (3), insulinoma-associated protein 1 (INSM1) and neuron-specific enolase (Figure 1D).

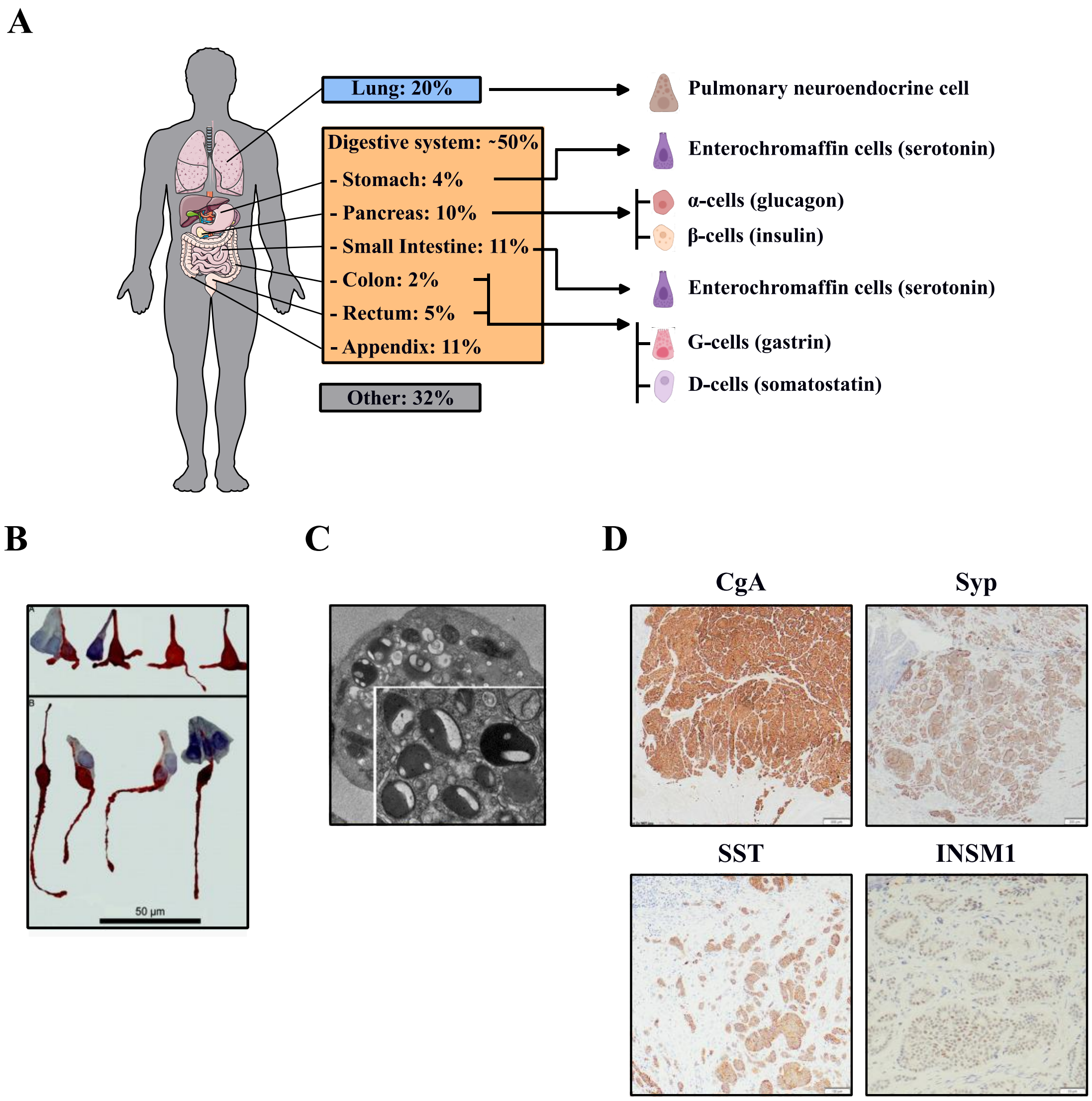

Figure 1. Origin and characteristics of NETs. A. Primary tumor site, cell of origin and hormone secreted by NETs. Figure modified from Kidd *et al.* (3) and Cuny *et al.* (7). Data from White *et al.* (8). and Dasari *et al.* (9). **B.** Long axon-like extensions of human enterochromaffin cells are shown. Images are from Gustafsson *et al.* (10). **C.** Electron micrograph of an isolated EC cell and its secretory granules. Image is from Schimmack *et al.* (11). **D.** Immunohistochemistry of SST, SYP, CgA and INSM1 in a Grade 1 SI-NET. Images kindly provided by Dr. Yolanda Rodríguez.

1.2 Classification

The World Health Organization (WHO) most recent classification (2022) categorizes NENs based on histological differentiation into well-differentiated neuroendocrine tumors (NETs) or poorly differentiated neuroendocrine carcinomas (NECs) (12). NETs are subdivided into grade 1 (G1, Ki-67 < 3%), grade 2 (G2, Ki-67 3-20%) and grade 3

(G3, Ki-67 > 20%) based on tumor proliferation which is assessed with the Ki-67 index and/or mitosis in the most proliferative area. NECs are always highly proliferative Grade 3 (Ki-67 > 20%) neoplasm and are further classified as large or small cell NECs (12). A detailed summary of the WHO classification is shown in Table 1.

Differentiation	Grade	Criteria
GEP-NENs		
Well differentiated NET	NET G1	< 2 mitosis/2 mm^2 and/or Ki-67 < 3%
	NET G2	2-20 mitosis/2 mm^2 and/or Ki-67 3-20%
	NET G3	> 20 mitosis/2 mm^2 and/or Ki-67 > 20%
Poorly differentiated NEC	LCNEC G3	> 20 mitosis/2 mm^2 and/or Ki-67 > 20% and large cell morphology
	SCLC G3	> 20 mitosis/2 mm^2 and/or Ki-67 > 20% and small cell morphology
Lung NENs		
Well differentiated NET	Typical carcinoid NET G1	< 2 mitosis/2 mm^2 and no necrosis
	Atypical Carcinoid NET G2	2-10 mitosis/2 mm^2 and/or necrosis
	Highly Proliferative NET G3	Atypical morphology > 10 mitosis/2 mm^2 and/or Ki-67 > 30%
Poorly differentiated NEC	LCNEC G3	> 10 mitosis/2 mm^2, necrosis and large cell morphology
	SCLC G3	> 10 mitosis/2 mm^2, necrosis and small cell morphology

Table 1. WHO classification of NENs. NEC, neuroendocrine carcinoma. LCNEC, large cell neuroendocrine carcinoma. SCLC, small cell lung cancer. NEN, neuroendocrine neoplasm. NET, neuroendocrine tumor. GEP-NEN, gastroenteropancreatic neuroendocrine neoplasm. G1, grade 1. G2, grade 2. G3, grade 3.

1.3 Epidemiology

NENs have been traditionally considered a rare cancer, as incidence was < 6 new cases diagnosed per 100.000 persons per year, as defined by the Surveillance of Rare Cancers in Europe (www.rarecarenet.eu). However, recent data from the National Cancer Registry and Analysis Service (NCRAS) and from the Surveillance, Epidemiology and End Results (SEER) database from the National Cancer Institute reported a 2.3- and 3.7- fold increase in the incidence in the last 2 decades up to 8.8 and 6.98 new cases per 100,000 persons per year in England (1995-2018) and in the United States of America (1989-2012), respectively (8,9) (Figure 2A).

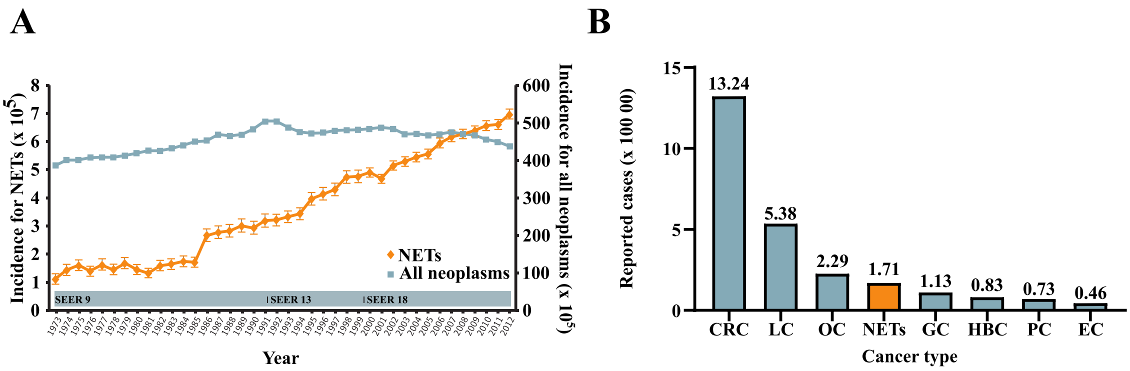

Figure 2. Incidence and prevalence of NETs. A. The incidence of NETs and all malignant neoplasms between 1973 and 2012 is shown. Data and figure are modified from Dasari *et al.* (9). **B.** Prevalence of NETs and other solid tumors in the United States. Data and figure are modified from Chauhan *et al.* (13). CRC, colorectal cancer. LC, lung cancer. OC, ovarian cancer. NET, neuroendocrine tumor. GC, gastric cancer. HBC, hepatobiliary cancer. PC, pancreatic cancer. EC, esophageal cancer.

The rising incidence might be partially explained by an increase in the use of endoscopy and improved sensitivity of imaging techniques, leading to increased detection of asymptomatic, early-stage disease (9). The most common primary sites are the lung and the small intestine, both with an incidence of 1.5 new cases per 100,000 persons per year, followed by the pancreas and the appendix, each one with an incidence of 1 new case per 100,000 persons per year (8). Despite their low incidence, NETs are the 4th more prevalent solid tumor in the U.S. and the 2nd most prevalent in the gastrointestinal (GI) tract following colorectal cancer (CRC). Moreover, the healthcare cost of each NET patient can exceed $30,000 in the U.S., which further suggest that NETs are indeed an important challenge for our healthcare systems (13) (Figure 2B).

NENs are usually considered indolent tumors compared to other solid malignancies. However, their prognosis widely depends on several prognostic factors including, among others, age, sex, primary tumor site, morphology, proliferation rate and stage (8). Indeed, elderly patients and males are associated with decreased overall survival (8). Similarly, grade and morphology are also very relevant, with an overall survival (OS) ranging from 16.2 years for G1 NETs, 8.3 years for G2 NETs, to only 10 months for G3 NECs. The primary tumor location also influences the outcome, although these differences widely vary based on stage and grade. For patients with advanced disease, G1-G2 small intestine NETs (SI-NET) show the best outcome, with a median OS of 103 months and a 5-year OS rate of 43%, followed by pancreatic NETs (Pan-NETs), with a median OS of 60 months and a 5-year OS rate of 26%. Finally, lung NETs (L-NETs) have the worst outcome with only 24 months median OS and a 5-year OS rate of 12% (8,9).

1.4 Molecular characteristics of NETs

1.4.1 Hereditary syndromes

Most NETs arise sporadically, although approximately 5% develop within hereditary syndromes. The identification of genes associated with these familial syndromes has helped to partially unravel some mechanisms involved in NET pathogenesis. Hereditary NENs are generally well differentiated tumors with low proliferation rates that can arise in multiple primary tumor locations and are associated with greater secretory activity (14,15).

The most characteristic syndromes are the multiple endocrine neoplasia type 1 (MEN1) and type 4 (MEN4), which are autosomal dominant diseases caused by loss-of-function mutations in *MEN1* (chromosome 11) and cyclin dependent kinase inhibitor 1B (*CDKN1B;* chromosome 12), respectively. These genes are involved in cell cycle progression and histone methylation and their deficiency increase the risk to develop pituitary (10-60%) and parathyroid adenomas (95%), and pancreatic (40%), gastric (10%), lung (2%) and thymic (2%) NETs (16,17). Similarly, MEN2 is an autosomal dominant disease caused by activating mutations in the proto-oncogene tyrosine-protein kinase receptor Ret (*RET;* chromosome 10). MEN2A patients, accounting for 90% of cases, can develop hyperparathyroidism (20-30%), medullary thyroid cancer (MTCs; 95%) and pheochromocytoma (30-50%). MEN2B patients, which represent 5% of cases, develop earlier MTCs and do not develop hyperparathyroidism (17).

Von Hippel-Lindau is an autosomal dominant disease caused by loss-of-function mutations in the tumor suppressor *VHL* (chromosome 3). This protein is a negative regulator of hypoxia inducible factors (HIF). In the absence of VHL, HIFs are translocated to the nucleus promoting the expression of genes involved in angiogenesis, proliferation and glycolysis leading to highly vascular retinal and central nervous system hemangiomas, as well as renal carcinomas and pancreatic NETs (18,19).

Tuberous sclerosis complex (TSC) syndrome is an autosomal dominant disease caused by mutations in *TSC1* (chromosome 9) and *TSC2* (chromosome 16) that encode for hamartin and tuberin, respectively. These proteins are involved in the mechanistic target of rapamycin (mTOR) pathway inhibition by dephosphorization of Rheb. Their loss leads to an uncontrolled activation of mTOR that enhances cell survival leading to the development of neurological and cutaneous lesions, renal angiolipomas, hamartomas and, in a small number of patients, pancreatic, pituitary and parathyroid NETs (20).

Neurofibromatosis type 1 (NF1) is an autosomal dominant disease caused by mutations in *NF1* (chromosome 17). This gene encodes for neurofibrin, a Ras inhibitor involved in cell proliferation. Its loss is associated with uncontrolled activation of mitogen-activated protein kinase (MAPK) signaling pathway leading to the development of neurofibromas, optic gliomas, pheochromocytomas and Pan-NETs (21).

1.4.2 Sporadic NETs

Sporadic cases account for 95% of NETs, and the molecular changes driving their development remain poorly understood and have mainly been studied in the most prevalent anatomical locations: the small intestine, pancreas and lungs.

NETs have a very low tumor mutational burden (TMB; 0.11–1.6 mutations/Mb) compared to their exocrine counterparts (22–25). Moreover, these mutations are concentrated in a reduced set of genes that vary by primary site (Figure 3A). In Pan-NETs, most common mutations occur in genes involved in histone methylation and chromatin remodeling such as *MEN1* (40%) or *DAXX* and *ATRX* (40%), and in genes involved the mTOR pathway (12%), including *TSC1*, *TSC2*, *PTEN* and *DEPDC5*. Indeed, activation of the mTOR pathway has been associated with a more aggressive phenotype and a worse prognosis (25,26). Conversely, insulinomas harbor recurrent mutations in *YY1* (15-30%) (25,27–29). These mutations often occur alongside copy number (CN) losses, particularly in chromosomes 9q and 11q in Pan-NETs (30). In SI-NETs, only *CDKN1B* is recurrently altered in 10% of patients (22,24). However, almost 50% of patients present chromosome 18q losses (31,32). L-NETs also harbor frequent mutations in chromatin-remodeling genes such as *MEN1* (13%), in genes involved in the SWI/SNF complex like *ARID1A or SMARCA* (15%), or in histone methyltransferases (*KMT2A*, *KMT2C*), histone demethylases (*KDM4A*, *PHF8*) and Polycomb complex genes (*CBX6*, *EZH1* and *YY1*) (45%). Sister chromatid cohesion pathway or DNA repair genes (17%) are also frequently altered in L-NETs (23,33). Finally, these tumors also present CN deletions or loss of heterozygosity (LOH) in chromosome 11q (34).

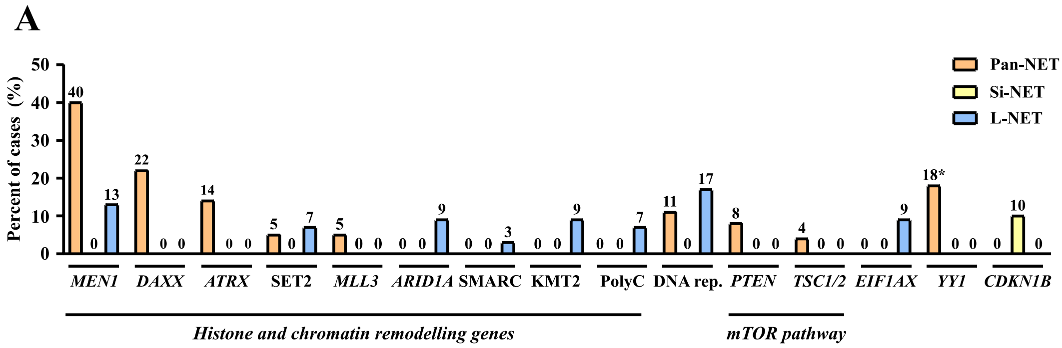

Figure 3. Common genomic alterations in NETs. A. Bar plots depict the frequency of patients harboring any genomic alteration (point mutations, CN gains or losses, amplifications or deletions) for the most frequently mutated genes in Pan-NETs, SI-NETs and L-NETs. Data from Fernandez-Cuesta (23), Laddha (33), Simbolo (34), Scarpa (25) and Banck (22) *et al*.. SET2 includes mutation in *SET2D* and *SET2C.* SMARC includes mutations in *SMARCA1*, *SMARCA2* and *SMARCA4*. KMT2 included mutations in *KMT2A*, *KMT2C, KMT2D*. PolyC, Polycomb repressive complex genes. DNA rep., DNA repair genes. **YY1* is frequently altered specifically in insulinomas.

Several groups have also characterized and classified NETs based on their epigenomic and transcriptomic features and identified several clinically relevant molecular classifications for Pan-NETs (35–37), SI-NETs (32) and L-NETs (38).

In the case of Pan-NETs, epigenomic characterization has identified 2 subtypes based on the cell of origin: α-like Pan-NETs that have activating histone methylation marks in enhancers of α-cell-specific loci such as *ARX* and *IRX2*; and β-like Pan-NETs with activation marks in enhancers of genes like *PDX1* and *SLC17A6* which are expressed in mature β-cells (35,36). Subsequent studies have subdivided the α-cell group into α-cell Pan-NETs, that are enriched in *MEN1* mutations, and α-like Pan-NETs that also harbor *ATRX* and *DAXX* mutations and are associated with a greater risk of relapse and shorter disease free survival (DFS) (37). Further transcriptomic analysis have confirmed this classification and subtypes (36,39).

Another classification derived from human Pan-NETs and from RIP1-Tag2 (RT2) mice neuroendocrine tumors showed partial overlap with the previous classification. Authors reported 3 groups: islet/insulinoma subtype, which shows overexpression of mature β-cell specific genes such as *PDX* and did not present metastasis; the MEN1-like subtype, that is enriched in non-functioning tumors and in *MEN1* and in *ATRX1*/*DAXX* mutations; and the metastasis-like primary (MLP) subtype, which is enriched in genes related to fibroblasts/stroma, stem cells and hypoxia, and is associated with non-functioning and metastatic tumors that resemble β-cell precursors or immature β-cells. Moreover, MLP tumors were also enriched in *DAXX*/*ATRX* mutations (40,41).

Less is known about SI-NETs and to date the most comprehensive molecular profiling has been performed by Karpathakis *et al*. Unsupervised clustering of CN alterations and methylation segregated patients into three groups: cluster A, which is enriched in Chr18 LOH and in *CDKN1B* mutations; cluster C, enriched in CN gains in chromosome 4, 5 and 20; and cluster B that presents very few CN alterations. Interestingly, patients from cluster C had a significant worse prognosis compared to Cluster A and B (32). However, these results could not be validated in later studies (42). RNA expression analysis has also been conducted in SI-NETs and resulted in a different 3-cluster classification. Cluster A and B have downregulation of *REST* and upregulation of *PHF21A* and *NEUROD1* and are enriched in genes related to neurosecretory function and formation of cellular protrusions. Conversely, cluster C is enriched in genes associated with angiogenesis and cytoskeleton (43).

Finally, extensive work has been performed in L-NETs. Alcala *et al.* performed a multi omic factor analysis (MOFA) integrating epigenetic and transcriptomic data. Interestingly, the top two MOFA latent factors were associated with survival and clustered patients according to their histological subtype (typical carcinoid, TC; atypical carcinoid, AC; and large cell neuroendocrine carcinoma, LCNECs). However, a subgroup of 6 ACs, namely “supracarcinoids”, clustered with LCNECs and had similar prognosis suggesting a molecular link between pulmonary carcinoids and LCNEC. Moreover, MOFA clustering integrating RNA expression, methylation and genomic data further subdivided L-NETs into three subgroups: cluster A1 which has downregulation of *HNF1A* and *HNF4A,* and high levels of *ASCL1* and *DLL3;* cluster A2 that has low levels of *ROBO1* and *SLIT1,* and is enriched in *EIF1AX* mutations; and cluster B, enriched in ACs that presented high *ANGPTL3* and *ERBB4*, absent *OTP* and *NKX2-1*, and harbored *MEN1* mutations. Finally, supracarcinoids were *DLL3*-negative and expressed high levels of *NOTCH* 1-3 (38).

Despite this heterogeneity, NETs also share some common molecular characteristics. SST expression is one of the molecular hallmarks of NETs. Indeed, around 70-80% of NETs express at least one SST, being SST2 and SST5 the most predominant ones (44). In L-NETs, SST expression is slightly lower, and is present in 55 to 64% of the cases (45,46). Their natural ligand, somatostatin, is a versatile neuropeptide that regulates neurotransmission and inhibits multiple endocrine and exocrine secretory functions, including gut and pituitary hormones, or pancreatic enzyme secretion, among others. Moreover, SST downstream signaling also inhibits proliferation of normal and tumor cells by inducing apoptosis and cell cycle arrest, and by inhibiting angiogenesis, among other mechanisms (47). This has led to the development of somatostatin analogues (SSA) for the treatment of NETs providing both functional syndrome relief and tumor growth control.

1.5 Treatment of NETs

NETs exhibit a wide range of clinical behavior depending on primary tumor site, tumor differentiation and growth rate, functionality, and extent of disease, including tumor bulk and sites of metastasis. NETs may be indolent and clinically silent and discovered incidentally, or mimic a variety of disorders due to secretory or tumor-related symptoms often leading to delayed diagnosis (48). Clinical management should take into consideration clinicopathological characteristics of the tumor, including primary site, stage, grade, and differentiation, along with patient-related factors such as age, comorbidities and overall health status. Other relevant factors to consider include the toxicity profiles of available therapies, center's expertise and patient´s perspective. Finally, it is highly recommended to treat these patients in NET expert centers within a multidisciplinary team.

1.5.1 Localized disease

Radical surgery with curative intent is the treatment of choice for most localized NETs. A more conservative approach, including endoscopic resection or watch and wait strategies may be considered in small gastroduodenal, pancreatic or rectal NETs (49–52).

1.5.2 Advanced disease

Systemic therapies represent the cornerstone of treatment for advanced unresectable NETs. Surgery may still be beneficial in selected NET cases to prevent complications like bowel obstruction or intestinal ischemia, and debulking surgery may be considered to alleviate symptoms in patients with functioning NETs (50,52). Locoregional treatments, primarily liver-directed ablative therapies such as bland embolization, chemoembolization, radioembolization, radiofrequency ablation or other, may be indicated in patients with functioning liver-dominant disease (49,50,52).

When NEN patients are ineligible for radical resection, management focuses on two main objectives: symptom control of functional syndromes and anti-proliferative treatment (49,53). We will briefly discuss the different systemic treatment options available, but a thorough discussion of their optimal use in clinical practice is beyond the scope of this thesis (Figure 4 and 5).

Symptom control

SSA are drugs that bind to SSTs inhibiting proliferation and secretion. SSA, octreotide and lanreotide, are indicated in functionally active NETs. Telotristat ethyl inhibits serotonin synthesis and is approved for the treatment of refractory carcinoid syndrome diarrhea (54). Other options that may be considered to treat refractory hormonal syndromes include SSA dose titration, the addition of IFN-α 2b, locoregional liver-directed therapies, radioligand therapy (RLT) or other systemic therapies to control tumor growth (49,51,53–55).

Anti-proliferative treatment

i. Somatostatin analogues (SSA)

SSA are also approved as antiproliferative treatments in advanced, slowly growing (up to a Ki-67 of 10%) SST-positive gastroenteropancreatic NETs (GEP-NETs) after PROMID and CLARINET phase III clinical trials demonstrated a significant improvement of progression free survival (PFS) versus placebo. They are also commonly used in non-rapidly progressive SST-positive L-NETs, although there is no a formal approval for this indication since the SPINET trial was terminated early due to slow accrual and did not meet its primary endpoint (56–58). SSA may be increasingly used in patients with higher proliferative rates based on the prospective data generated in the recently published NETTER-2 trial.

ii. Radioligand therapy (RLT)

RLT consists of a SSA (dotatate) bound to Lutetium-177 (177Lu) which is a β- and γ-emitting radionuclide with a maximum particle range of 2 mm and a half-life of 160 hours. This molecule specifically directs the radioactive isotope to SST-positive cancer cells. SST-targeted RLT is approved for the treatment of patients with unresectable or metastatic, progressive, SST-positive G1-G2 GEP-NETs based on the pivotal phase III NETTER-1 trial conducted in midgut NETs and the Rotterdam prospective patient cohort (59–61). More recently, the NETTER-2 randomized trial demonstrated RLT efficacy also in treatment-naïve G2 high and G3 low (Ki-67 10-55%) GEP-NETs. Clinical trials are ongoing to assess the efficacy of RLT in L-NETs (49). Current clinical guidelines recommend RLT as the preferred second-line treatment in midgut NETs upon progression to SSA, whereas optimal treatment sequence is a matter of debate in pancreatic or other GI primary sites (49–51,55).

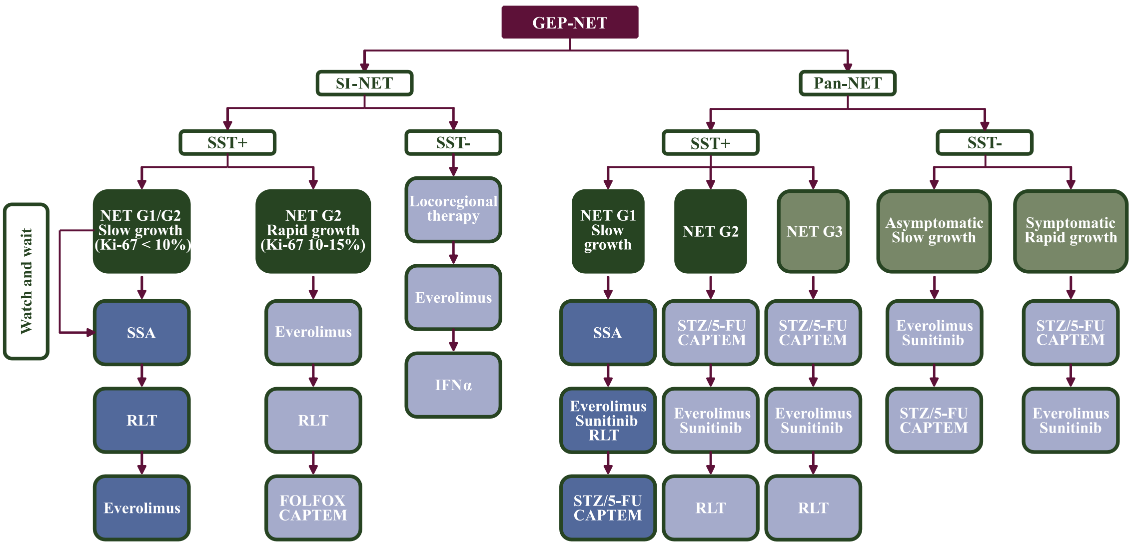

Figure 4. ESMO guidelines therapeutic algorithm for GEP-NETs. From Pavel *et al.* (55). NET, neuroendocrine tumor. G1, grade 1. G2, grade 2. G3, grade 3. SSA, somatostatin analogues. RLT, radioligand therapy. CAPTEM, capecitabine and temozolomide. IFNα, interferon α. 5-FU, 5-fluorouracil.

iii. Targeted therapies

Beyond SST-directed therapy, there are two currently available targeted therapies in Europe for advanced NETs: everolimus, approved for the treatment of pancreatic, GI and lung non-functioning NETs, and sunitinib, approved for the treatment of progressive Pan-NETs.

Everolimus is an inhibitor of mTOR, a serin-threonine kinase involved in metabolism and cell survival which signaling pathway is frequently altered in NETs. Everolimus demonstrated a significant improvement in PFS versus placebo in patients with advanced, progressive Pan-NETs (RADIANT-3 randomized trial), and in non-functioning GI- and L-NETs (RADIANT-4 phase III trial) (62,63). Everolimus is thus indicated for a broad spectrum of advanced NETs and the only one approved in L-NETs.

Sunitinib is an angiogenesis inhibitor that targets multiple receptor tyrosine kinases including the vascular endothelial growth factor receptor (VEGFR), the platelet derived growth factor receptor (PDGFR), the receptor protein-tyrosine kinase (KIT), the RET proto-oncogene (RET), CSF-1R, and FLT3. Sunitinib demonstrated improved PFS versus placebo in advanced, progressive Pan-NETs in the pivotal phase 3 randomized SUN111 trial (53,64). Several other multikinase inhibitors (MKI) have been assessed in NETs including surufatinib, cabozantinib, axitinib, pazopanib and lenvatinib, among others, but are not approved to date for this indication in Europe. Surufatinib is approved in China for pancreatic and extrapancreatic NETs. Treatment with antiangiogenic therapy (AAT) is further developed in section 2.3.1.

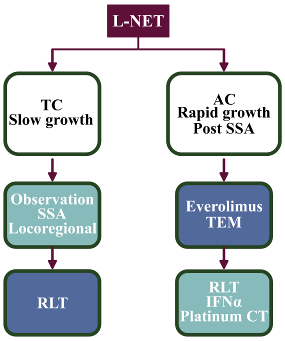

Figure 5. ESMO guidelines therapeutic algorithm for L-NETs. From Baudin *et al.* (49). NET, neuroendocrine tumor. TC, typical carcinoid. AC, atypical carcinoid. SSA, somatostatin analogues. RLT, radioligand therapy. IFNα, interferon α. ChT, chemotherapy.

iv. Chemotherapy

Streptozotocin (STZ) was the first drug to be approved (1982) by the Food and Drug Administration (FDA) for the treatment of Pan-NETs (65). It is an alkylating nitrosourea that is particularly toxic for pancreatic β-cells as it is incorporated into the cell through the glucose transporter GLUT2. STZ in combination with 5-Fluorouracil (5-FU) or doxorubicin improves response rate and survival over STZ monotherapy. However, combination with 5-FU is preferred due to a more favorable toxicity profile. More recently, temozolomide (TEM) alone or in combination with capecitabine (CAPTEM) demonstrated efficacy in Pan-NETs and is an orally administered alternative chemotherapy regimen in this setting (55). Chemotherapy efficacy in other primary sites is lower and has not been properly assessed (49).

2. Angiogenesis and NETs

2.1 Molecular basis of angiogenesis

The blood circulatory system is an organized treelike structure made of arteries, veins and capillaries that supply tissues with oxygen and nutrients and allow waste removal. Endothelial cells (ECs) constitute the inner lining of the vessel wall or endothelium, and pericytes sheathe the ECs, together constituting the basic structure of blood vessels (66–68). During development, wound healing or in certain pathological conditions such as cancer, tissues can grow beyond the diffusion limit of blood vessels and become hypoxic and/or nutrient deprived, triggering the activation of quiescent ECs to form new blood vessels from preexisting ones (67,68). This process is called angiogenesis.

Angiogenesis is initiated when VEGF-A activates ECs promoting secretion of metalloproteinases (MMPs) and basal membrane degradation. ECs at the edge of the sprout, called tip cells, show minimal proliferation and have a highly polarized morphology, emitting filopodia to guide the sprout growth towards the hypoxic or deprived areas. Conversely, stalk cells do not sprout, tend to be more proliferative and produce the basal membrane allowing the formation and elongation of the new blood vessel (67,68). When tip cells reach each other, the new vessel connects to the network and stabilization begins as proliferation is reduced, pericytes are recruited and extracellular matrix production starts enabling the onset of the blood flow. Finally, blood vessels mature and adapt to tissue specific needs in order to become functional (66,69).

2.1.1 Vascular endothelial growth factor signaling pathway

The vascular endothelial growth factor (VEGF) signaling pathway is the main regulator of angiogenesis (70). This signaling pathway includes five growth factors (VEGF-A, VEGF-B, VEGF-C, VEGF-D, and placental growth factor (PGF)) and three main receptors (VEGFR-1, VEGFR-2, and VEGFR-3). These receptors share a fundamental structure that includes seven extracellular immunoglobulin-like domain repeats, a transmembrane domain, and a split tyrosine kinase domain. The binding of VEGFs to VEGFRs triggers receptor homo- or hetero-dimerization and activation of tyrosine kinase residues in the intracellular domain, enabling cross-activation of the receptor dimers. These phosphorylated residues recruit various scaffold and signaling proteins, which in turn, regulate angiogenesis, lymphangiogenesis, and other physiological processes through distinct, specific signaling pathways (71,72).

VEGF-A and its main receptor, VEGFR-2 (also known as KDR), are the main regulators of endothelial cell function, proliferation and permeability in physiological and tumoral angiogenesis, and are common targets of angiogenesis inhibitors. VEGF-A expression is activated by HIF-1 in response to low oxygen levels. Indeed, HIFs are key regulators of cell adaptation to hypoxia, consisting of a heterodimer of an oxygen-regulated α subunit (1α and 2α) and a constitutively expressed β subunit (also known as ARNT). Under aerobic conditions, prolyl hydroxylases hydroxylate HIF-1α thereby enabling its polyubiquitination by an E3 ubiquitin ligase complex that includes the VHL protein, targeting HIFα for degradation by the proteasome. On the contrary, oxygen depletion prevents this degradation, allowing HIFα stabilization and translocation to the nucleus, where it dimerizes with HIF-1β and binds to hypoxia response elements in DNA to activate transcription of proangiogenic target genes including VEGF-A (73).

In this context, secreted VEGF-A activates VEGFR-2 in endothelial cells. Upon VEGF-A binding, homodimerized VEGFR-2 is phosphorylated at Tyr1175 (Y1175) resulting in receptor internalization into endosomes. This turns on Ca+ dependent signaling pathway, phospholipase Cγ (PLCγ) and NFAT, which together with the ERK1/2 signaling pathway regulate transcription factors involved in endothelial cell migration, proliferation and homeostasis (71,72). However, when Y949 is phosphorylated, VEGFR-2 recruits TSAd and activates Src in focal adhesions, which in turn regulates cell matrix adhesion, shape and survival, and vascular permeability by vascular endothelial cadherin phosphorylation and internalization. Moreover, it also regulates Akt mediated activation of endothelial nitric oxide synthase (eNOS) which produces NO in smooth muscle cells leading to vasodilation (71,72). Overall, all these downstream molecular pathways activate multiple mechanisms that will converge in the activation of angiogenesis (Figure 6).

The role of other members of the family has also been studied. VEGF-C and VEGF-D bind VEGFR-2 and VEGFR-3, and are involved in vasculogenesis during development and lymphangiogenesis during adulthood (66). Indeed, VEGF-C/VEGFR-3 signaling promotes lymphatic endothelial cell proliferation, migration and survival through Akt and ERK signaling pathways (71). Additionally, VEGFR-3 is also important for angiogenesis

(66), as it is involved in the modulation of VEGF-A/VEGFR-2 expression (71) and in the acquisition of the tip cell sprouting phenotype. In this regard, macrophage derived VEGF-C seems to play an important role in vessels sprouting and in the union and stabilization of sprouting tip cells (69,71).

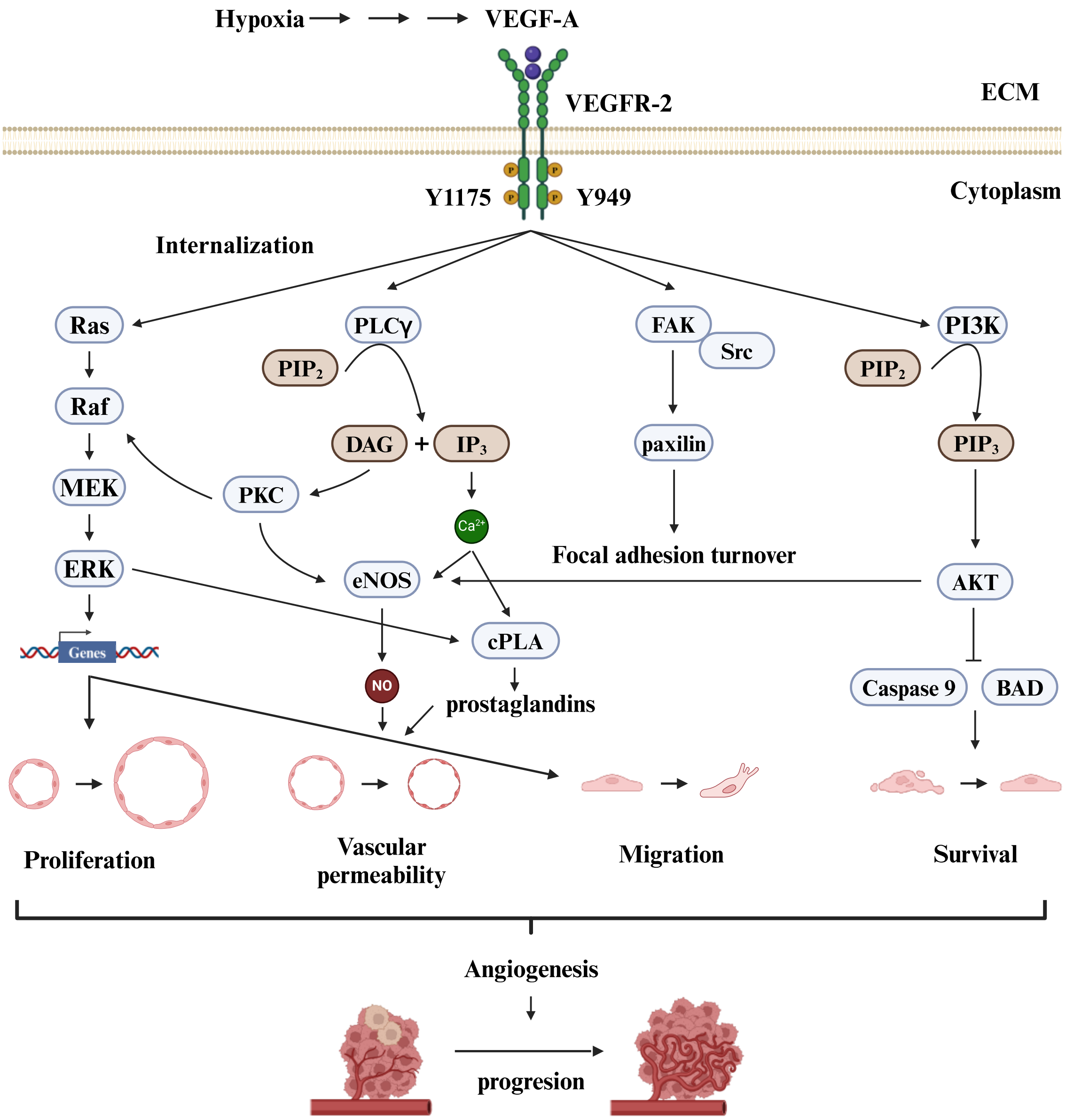

Figure 6. VEGF-A signaling pathway and angiogenesis. The main VEGF-A/VEGFR-2 downstream molecular pathways are depicted. Figure modified from Ivy *et al*. (74). ECM, extracellular matrix.

Conversely, VEGF-B seems to have limited angiogenic activity and its role is restricted to the heart, where it promotes neuronal survival and cardiovascular growth angiogenesis, probably through VEGFR-1 (73). However, the role of VEGFR-1 in angiogenesis is controversial. VEGFR-1 is expressed by endothelial cells, monocytes and macrophages, and regulates monocyte migration and endothelial progenitor cells recruitment (73). It has soluble and membrane associated forms and can bind VEGF-A, VEGF-B and PGF. It has low tyrosine kinase activity, so it seems to be a negative modulator of VEGFR-2 by forming heterodimers, and in this regard, VEGFR-1 loss increases the number of blood vessels. However, VEGFR-1 can also promote angiogenesis and tumor growth when bound to PGF and plays an important role in inflammation (71–73).

Finally, PGF has also been linked with angiogenesis and maintenance of new blood vessels. It is expressed in endothelial, inflammatory and cancer cells, and PGF/VEGFR-1 signaling activates proliferation in ECs and promotes tumor-associated macrophage (TAM) recruitment and polarization, shaping the tumor microenvironment. However, PGF is dispensable during development and has shown anti-angiogenic activity in some settings, explaining why its role in angiogenesis remains to be fully elucidated (66,73).

2.1.2 Other signaling pathways involved in angiogenesis

Other signaling pathways involved in the regulation of angiogenesis include the PDGF and fibroblast growth factor (FGF) families. PDGF family includes PDGF-A, -B, -C, and –D which form –AA, -BB, -CC and -DD homodimers or –AB heterodimers, that bind dimeric tyrosine kinase membrane receptors, PDGFR-αα, -ββ, or –αβ (75). Increased PDGF signaling is associated with increased vascularization in various cancers (76,77) as ECs secrete PDGF in a paracrine manner to recruit PDGFR positive pericytes and fibroblasts leading to tumor angiogenesis (78,79). Additionally, PDGF indirectly regulates angiogenesis by stimulating VEGF transcription and secretion (80). FGF superfamily includes 23 FGFs and four tyrosine kinase receptors, FGFR-1, -2, -3 and -4. These proteins are associated to increased angiogenesis in various tumors, and particularly, FGF-1 and FGF-2 are highly pro-angiogenic and promote endothelial cell proliferation and migration (81). Finally, angiopoietins also play an important role in vascular regulation. Ang1 binding to angiopoietin-1 receptor (TIE2) stabilizes blood vessels by increasing endothelial cell interactions, whereas EC-derived Ang2 leads to vessel remodeling in response to hypoxia and inflammation (82,83).

2.1.3 Angiogenesis in cancer

Angiogenesis is tightly regulated by a balanced interplay between pro- and anti-angiogenic factors functioning in an orderly and hierarchical manner (73,84). An imbalance between these factors can induce to the formation of new blood vessels in the tumor microenvironment (73,84) to ensure the supply of oxygen and nutrients, thereby meeting the tumor's metabolic needs (85). However, tumoral angiogenesis differs from physiological angiogenesis in multiple aspects: new cancer blood vessels are usually abnormal, heterogeneous, disorganized and leaky due to uneven thickness and lack of pericyte coverage. Enhanced vascular permeability increases interstitial pressure that impairs blood flow, oxygenation and distribution of nutrients, immune cells and drugs, inducing acidosis and hypoxia that leads to further angiogenic pathway activation (66,67,73,84). Moreover the lack of the characteristic cobblestone structure and cell–cell junctions can contributes to tumor invasion and metastasis (69).

This imbalance, which triggers tumor angiogenesis, is often induced by hypoxia but can also result from ischemia, acidosis and high interstitial pressure. These inputs activate the HIF signaling pathway and VEGF-A secretion by both cancer and stromal cells leading to VEGFR-2 activation and stimulation of mitosis, chemotaxis and morphogenesis of ECs. Tumoral angiogenesis in turn allows proliferation, migration and invasion of solid tumors (73,84,85). Similarly, VEGF-C/VEGF-D and VEGFR-3 has been shown to promote metastasis and proliferation, and are important regulators of tumor lymphangiogenesis (73).

2.2 Angiogenesis in NETs

Angiogenesis plays an essential role in the development and progression of NETs. These tumors are highly vascularized consistent with the physiological role that vascular supply plays in normal endocrine tissue to facilitate hormone secretion (86–88). Unlike other epithelial tumors, low-grade NETs are associated with a dense vascular network, which is more likely a marker of differentiation than of aggressiveness, a phenomenon known as the “neuroendocrine paradox”. This explains the association of a lower microvessel density (MVD) with increased Ki-67 index, aggressive tumor behavior and a poor prognosis (87,89–93).

Immunohistochemical analysis has confirmed that multiple proangiogenic molecules are overexpressed in NETs. VEGF-A expression has been reported in 60-90% of GEP-NETs (89,90,94–96). VEGF-C is highly expressed in metastasis of Pan-NETs (97) and expression of VEGF-C and VEGFR-2,3 has been observed in lung TCs and ACs, in contrast to lung NECs (98). Additionally, HIF-1α is expressed in 61% of L-NETs (99).

Several studies have reported that all three VEGFRs are expressed in GEP-NETs with varying intensities: VEGFR-1 in 80% of cases, VEGFR-2 in 67%, and VEGFR-3 in 53% (94,100,101). However, it remains unclear whether expression of VEGF or VEGFRs, as detected by immunohistochemistry (IHC), correlate with MVD (92,95,97).

As revised in section 1.4.2, recent omic and gene set enrichment analysis (GSEA) studies have identified certain subgroups of NETs particularly enriched in genes involved in angiogenesis and hypoxia (25,38,40,41,43,102). However, whether these subgroups may have increased benefit of angiogenesis inhibitors remains to be elucidated. Hereditary syndromes have also confirmed the role of VHL and dysregulated HIF signaling in the development of NETs, and VHL-related cancer has been shown to be particularly sensitive to drugs targeting angiogenesis (103).

Studies using the RT2 mouse model, which develops β-cell neuroendocrine tumors in the pancreatic islets of Langerhans, have confirmed the prominent role of angiogenesis in NETs. In this model, the large-T antigen from the simian virus 40 oncogene is expressed under the control of the insulin II mouse promoter. Interestingly, the hyperplastic islets in these mice are classified as non-angiogenic or angiogenic based on their morphological characteristics and their ability to induce endothelial tube formation *in vitro*. Only the angiogenic islets are able to progress to carcinomas, highlighting the critical role of angiogenesis in this Pan-NET model (104). *In vivo* studies in RT2 mice demonstrated that VEGF-A secretion drives angiogenesis and tumor progression of NETs. Both VEGF-A knockout (KO) (105,106) and inhibition of VEGFR-2 (107–109) impaired the angiogenic switch and reduced MVD and tumor burden, suggesting that targeting angiogenesis could have an antitumor effect in NETs. Conversely, overexpression of VEGF-A led to increased angiogenesis and earlier mortality (110), further confirming the crucial role of the VEGF-A/VEGFR-2 axis in the tumorigenesis and progression of NETs.

This mice model has also contributed to the study of the role of semaphorins and angiopoietins in NETs. Semaphorins, angiopoietins and their receptors, including neuropilins and plexins, are expressed in GEP-NETs (111–115). Moreover, SEMA3A is lost during tumor progression and angiogenic switch in RT2 mice and ileal NETs, and is involved in the normalization of angiogenesis following VEGFR inhibition-induced hypoxia (116–118). In contrast, other semaphorins such as SEMA4D and SEMA5A promoted tumor growth, angiogenesis, invasion and metastasis in RT2 mice (119,120). Furthermore, overexpression of Ang2 have been shown to increase MVD and enhance metastatic spread through lymphatic vessels in both xenografts models and RT2 mice (121,122).

As a result of all these studies that demonstrated the crucial role of angiogenesis in the development and progression of NETs, multiple antiangiogenic drugs have been evaluated for these tumors.

2.3 Targeting angiogenesis in NETs

2.3.1 Antiangiogenic therapies (AATs)

In this context, both preclinical and clinical research has been conducted and continues to progress to assess the efficacy of AAT, particularly for extrapancreatic NETs (EP-NETs), as no AAT is currently approved in this particular setting in western countries.

Initially, preclinical experiments using RT2 mice showed that targeting VEGF or VEGFR in NETs was effective, using either monoclonal antibodies or various antiangiogenic MKIs (107–109). Similarly, other groups evaluated MKIs that co-targeted other receptors involved in angiogenesis such as PDGFR-α, PDGBR-β and FGFR. Interestingly, co-inhibition of these receptors resulted in greater tumor regression compared to VEGFR-specific inhibitors, despite showing lower efficacy in inhibiting the angiogenic switch (123). Thus, these preclinical trials in RT2 mice have paved the way for the clinical development of AAT.

Sunitinib has been, since 2011, the only antiangiogenic MKI approved in Europe for advanced Pan-NETs. It is a potent inhibitor of several targets, including VEGFR-1, -2 and -3, PDGFR, KIT, RET, FLT3 and CSF-1R (124), and was previously approved to treat advanced renal cell carcinoma (RCC) and GI stromal tumors. The efficacy of sunitinib in Pan-NETs was confirmed in a phase III clinical trial SUN111 that included 171 patients. This multinational, double-blind, placebo-controlled trial randomly assigned patients in a 1:1 ratio to receive continuous daily administration of sunitinib at a dose of 37.5 mg/day or placebo. The objective response rate (ORR) was 9% in the sunitinib group and 0% in the placebo arm. Sunitinib also improved the median PFS by 6 months (11.4 months vs. 5.5 months; *HR (hazard ratio): 0.42, $p < 0.001$*) (64). A 5-year follow-up reported a 10-month increase in OS (38.6 months vs. 29.1 months; *HR: 0.73; $p = 0.094$*), although this difference did not achieve statistical significance likely due to the high rate of crossover (125).

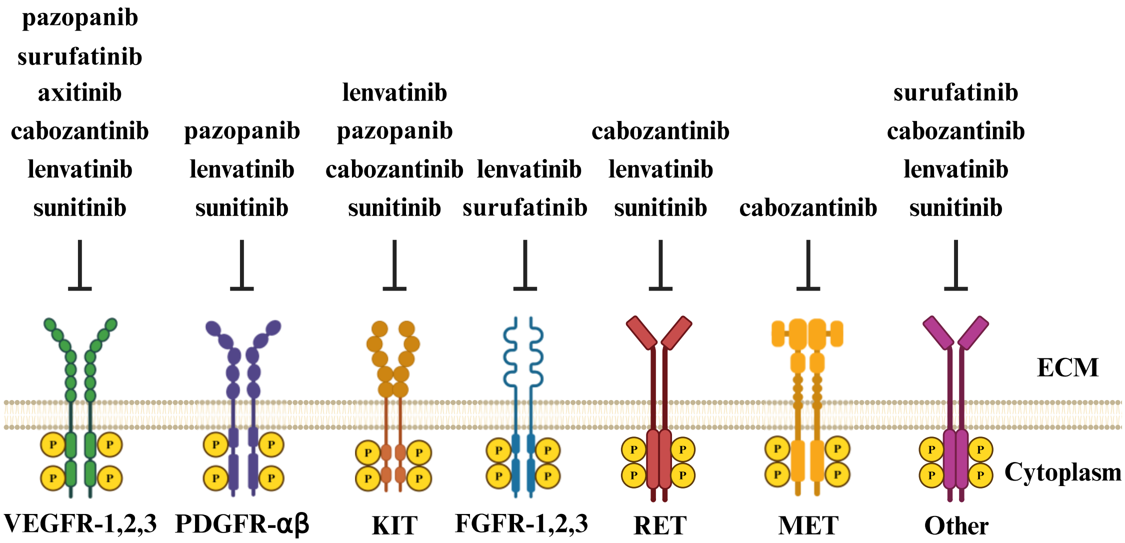

Figure 7. Antiangiogenic MKIs evaluated for the treatment of NETs. The different targets for each MKIs are shown. Modified from Grillo *et al.* (126). ECM, extracellular matrix.

Together with sunitinib, bevacizumab, a humanized monoclonal antibody that inhibits VEGF-A, was among the first AAT evaluated for NETs. Bevacizumab is approved for the treatment of a wide spectrum of solid tumors, including lung, colorectal, renal, breast, ovarian or cervix cancer. The first preliminary evidence of its efficacy in NETs derived from a small, randomized study that enrolled 44 patients with advanced NETs on stable doses of SSA that were randomized to receive bevacizumab or PEG IFN alfa-2β for 18 weeks. Among those treated with bevacizumab, 18% (4 patients) achieved a partial response (PR) and 5% experienced disease progression (PD), compared to 0% PR and 27% PD observed in patients receiving PEG IFN alfa-2β. Moreover, the PFS rate at 10 weeks was higher in the bevacizumab group compared to PEG IFN alfa-2β arm (95% vs. 68%) (127). Based on these promising results, a phase III clinical trial was launched to assess the efficacy of bevacizumab versus interferon alfa-2b, both in combination with octreotide LAR, in 427 patients with progressive advanced NETs. This trial failed to demonstrate a significant improvement in the PFS of bevacizumab (16.6 months) compared to IFN alfa-2β (15.4 months) based on centralized readings. Nevertheless, the ORR was higher in patients treated with bevacizumab compared to IFN alfa-2β (12% vs. 4%). Similarly, investigator assessment reported a 5-month improvement in PFS for bevacizumab compared to IFN alfa-2β, although the difference was not statistically significant (15.4 months vs. 10.6. months, $p = 0.33$) (128).

Surufatinib, a MKI targeting VEGFR-1, -2 and -3, FGFR and CSF-1R, is approved in China for the treatment of advanced Pan- and EP-NETs (Figure 7). Its potential advantage lies in the inhibition of FGFR and CSF-1R which are involved in resistance to VEGF/VEGFR inhibition (129,130). This drug was assessed in two chinese phase III SANET-p and SANET-ep multicenter, randomized, double-blind, placebo-controlled trials which demonstrated that surufatinib significantly improved PFS compared to placebo in 172 Pan-NETs (10.9 vs. 3.7 months, *HR: 0.49, $p = 0.001$*) (131) and 198 EP-NETs (9.2 vs. 3.8 months, *HR: 0.33, $p < 0.0001$*) (132). Expansion trials to assess pharmacology, safety and efficacy in western populations were undertaken although formal approval by FDA and European Medicines Agency (EMA) has not been seeked (133).

Cabozantinib, a MKI targeting VEGFR-1, -2 and -3, MET, RET, KIT, AXL, and FLT3, is in the late stages of clinical development for NETs (134) (Figure 7). Cabozantinib addresses one of the resistance mechanisms to VEGFR inhibition by targeting MET (109) and is currently approved for the treatment of advanced differentiated thyroid carcinoma (DTC), RCC and hepatocellular carcinoma (HCC). The phase III CABINET trial has confirmed its efficacy in Pan-NETs (N = 95) and EP-NETs (N = 203), as it significantly improved PFS per central blinded assessment in cabozantinib- versus placebo- treated patients in both cohorts: 8.4 versus 3.9 months (*HR: 0.38; $p < 0.001$*) in EP-NETs, and 13.8 versus 4.4 months (*HR: 0.23; $p < 0.001$*) in Pan-NETs. ORRs were 5% for EP-NETs and 19% for Pan-NET, compared to 0% for placebo (135). These results are currently being evaluated by regulatory authorities (FDA/EMA) to be potentially approved for the treatment of advanced NETs.

Axitinib is a very potent and selective MKI targeting VEGFR-1, -2 and -3 approved as a second-line therapy for patients with advanced RCC after failure of prior treatment with sunitinib or cytokines (136) (Figure 7). The phase II/III, double-blind, randomized, placebo-controlled AXINET clinical trial (NCT01744249), an investigator-initiated trial sponsored by the Spanish Cooperative Group of Neuroendocrine and Endocrine Tumors (GETNE), randomized 256 patients with grade 1-2 EP-NETs to be treated with axitinib or placebo, both in combination with octreotide LAR. Axitinib significantly improved ORR compared to placebo (17.5 vs. 3.8%, *$p = 0.0004$*), but the primary endpoint of this trial, PFS per investigator assessment (17.2 vs. 12.3 months, *HR: 0.816, $p = 0.169$*), was not met (137). However, an independent blinded radiological assessment showed that axitinib significantly improved PFS (16.6 vs. 9.9 months, *HR: 0.71, p = 0.017*) and had a significantly higher ORR compared to placebo (13.2% vs. 3.2%, *p = 0.0045*) (138).

Pazopanib, approved for the treatment of RCC and some subtypes of soft tissue sarcomas, targets VEGFR-1, -2 and -3, PDGFR-α and -β, and KIT (139) (Figure 7). Pazopanib has demonstrated some activity in a phase 2 randomized trial conducted in EP-NETs (N = 181), improving PFS for pazopanib-treated patients compared to those treated with placebo (11.6 vs. 8.5 months, *HR: 0.53, p = 0.0005*) (140). Lenvatinib is another MKI that targets VEGFR-1, -2 and -3, FGFR-1, -2, -3 and -4, PDGFRα, RET and KIT, and is currently approved for the treatment of advanced DTC, HCC, RCC and endometrial carcinomas (141) (Figure 7). Lenvatinib efficacy in NETs was assessed in a single arm phase II trial (TALENT, GETNE1509) that included two cohorts of pretreated patients, 55 Pan-NETs and 56 gastrointestinal NETs. This study reported an ORR per central radiological review of 29% (42.3% in Pan-NETs and 16.3% for GI-NETs) and a median PFS of 15.7 months in both Pan-NETs and GI-NETs. Interestingly, this clinical trial reported the highest response rate with targeted therapies in this setting, positioning lenvatinib as a promising agent for advanced NETs (142). However, further clinical development has not been further pursued due to company strategic reasons. Other antiangiogenic MKIs that have been tested in NETs (sorafenib, nintedanib,..) are unlikely to continue clinical development in this setting (143,144).

Overall, antiangiogenic therapy with MKIs has shown activity in pancreatic and extrapancreatic NETs. However, despite some of these drugs are approved for this indication (sunitinib by FDA/EMA, surufatinib in China) or have positive phase III clinical trial results (cabozantinib), ORR are low and PFS improvements are modest suggesting that many patients do not benefit from these therapies. On the other hand, not substantially different results have been documented with other MKIs with negative trials or in earlier stages of clinical development, such as axitinib, pazopanib or lenvatinib, highlighting the need to improve patient selection and optimize target population to improve the magnitude of clinical benefit, and avoid unnecessary toxicities and costs of treating patients that do not benefit from this therapeutic strategy.

2.3.2 Mechanisms of resistance to AAT

The intrinsic and acquired mechanisms of resistance to AAT can be summarized into 4 main molecular and cellular processes: i) upregulation of alternative proangiogenic factors; ii) recruitment of proangiogenic bone marrow derived cells (BMDCs); iii) increase of pericyte coverage; iv) and increase of the invasion and metastatic capacities (145). These mechanisms of resistance are also present in NETs and some of them have been specifically studied in the RT2 mouse model, which has helped to delineate how tumors adapt to AAT.

Indeed, several groups have reported that VEGF/VEGFR inhibition leads to treatment-induced hypoxia which increases tumor aggressiveness and promotes invasiveness by upregulating proangiogenic factors such as FGFs and Ang2 (108,146). Similarly, upregulation of the HIF1α target gene MET has been observed in NETs following VEGF/VEGFR inhibition (147,148). Allen *et al*. also observed that AAT in RT2 mice led to an upregulation of mTOR signaling in the normoxic tumor compartment. This effect was driven by increased lactate production in the hypoxic areas, where lactate was then secreted and transported, together with glutamine, into the normoxic compartment, creating a metabolic symbiosis that ultimately upregulates pS6 (mTOR target) (149).

Another resistance mechanism to VEGFR inhibition in Pan-NETs involves the recruitment of BMDCs, such as endothelial progenitor cells, pro-angiogenic monocytes, and TIE2-expressing macrophages. These cells support the formation of new blood vessels and contribute to the establishment of pre-metastatic niches (146,150). Additionally, TAMs progressively accumulate in the hyperplastic islets and invasive RT2 tumors and might also be involved in the activation of alternative proangiogenic pathways leading to resistance to VEGFR blockade (151).

In addition, in some RT2 tumors, long-term inhibition of VEGFR-2 was accompanied by vascular co-option, where the tumor hijacked preexisting adjacent “normal” vasculature (108). Vascular mimicry, in which cancer cells form vessel-like networks to meet their metabolic needs, has also been observed to be driving resistance to AAT in *MEN1* mutant Pan-NETs (152). Accordingly, epithelial-mesenchymal transition (EMT) was detected in sunitinib-treated tumors, as evidenced by increased expression of EMT markers such as snail, vimentin and neural cadherin, and decrease epithelial-cadherin expression, likely due to hypoxia induced by VEGFR inhibition (118), which has also been associated with the development of alternative blood vessels (67).

Other mechanisms of resistance to VEGFR-2 targeted AAT in Pan-NETs include an increase in pericyte coverage (153) or the degradation of hydrophobic MKIs within the acidic lysosomal compartment. Inhibition of autophagy, which permeabilizes lysosomal membranes, has been shown to enhance the antitumor activity of sunitinib in RT2 mice (154).

Overall, multiple intrinsic and acquired resistance mechanisms to AAT are present in NETs. Identifying biomarkers that predict and monitor treatment response is crucial for optimizing AAT. Moreover, improving our understanding of these mechanisms could reveal potential targets to ultimately improve outcomes in NET patients treated with AAT.

2.3.3 Predictive biomarkers of AAT

The search for predictive biomarkers of AAT has been extensively explored in multiple solid tumors (155–157). In the context of NETs, early studies investigated blood angiogenesis-related cytokines and growth factors and observed that VEGF and interleukin 8 (IL-8) levels were significantly higher in patients with progressive disease regardless of received therapy (158). Similarly, Ang2 or HIF-1α levels were associated with a shorter OS in GEP-NETs (121,159). However, since these studies were not performed in patients treated with MKIs, the predictive value of these biomarkers associated with prognosis could not be explored.

In a study by Jimenez Fonseca *et al.*, two VEGFR-3 polymorphisms (c.1480A>G (rs307826) and c.4202G>T (rs307821)) were associated to worse OS in Pan-NET patients treated with sunitinib, with *HRs* of 3.67 and 3.84, respectively (160). This study, as well as others conducted in patients with Pan-NETs and SI-NETs receiving sunitinib, also observed that higher IL-6 levels correlated with reduced OS (*HR: 1.07*), whereas elevated plasma levels of SDF-1, IL-8 and OPN were associated with reduced ORR and PFS (160,161). Additionally, IL-8 serum levels were found upregulated in sunitinib-refractory individuals, $p = 0.024$) and PGF was elevated in NET cell lines treated with sunitinib (162). Finally, Zurita *et al.* also observed that CD14+ monocyte co-expressing VEGFR-1 or CXCR4 significantly decreased during sunitinib treatment ($p = 0.04$ and $p = 0.03$, respectively) (161).

Although patients in these studies were treated with MKIs, the lack of control does not allow to discriminate predictive from prognostic makers. To this end, the optimal setting is to explore them within controlled clinical trials, though no data is available to date in the context of NETs. However, interesting studies have been conducted in other vascular-dependent solid tumors such as RCC. One example is the phase III JAVELIN renal 101 trial that assessed the efficacy of avelumab (anti-PD-L1) combined with axitinib versus sunitinib monotherapy as first-line treatment in patients with advanced RCC. Exploratory analysis identified biological features associated with differential PFS between treatment arms, including new immunomodulatory and angiogenesis gene expression signatures and mutational profiles (156). Another phase II trial conducted in treatment-naïve metastatic RCC, the IMmotion150, also explored predictive biomarkers in 305 enrolled patients that were randomized to receive atezolizumab (anti-PD-L1) alone or combined with bevacizumab versus sunitinib. Interestingly, patients treated with sunitinib with high levels of an angiogenic gene signature had improved ORR (H: 46% vs. L: 9%) and PFS (*HR 0.31; 95% CI: 0.18 – 0.55*) compared to those with a low angiogenic gene signature (155). Studies conducted in other solid tumors have identified different molecular profiles predictive of AAT efficacy, but to date none of them have been validated in clinical practice (157,163).

In summary, the identification of predictive biomarkers for antiangiogenic MKIs is possible but requires carefully designed discovery and control cohorts, as well as rigorous validation in independent cohorts to be suitable for implementation in clinical practice.

3. Osteopontin

3.1 Structure and regulation of osteopontin

Osteopontin (OPN) is a secreted phosphoprotein that belongs to the negatively charged SIBLING protein family and is encoded by *SPP1* gene (secreted phosphoprotein 1), located on chromosome 4 (4q22.1) in humans (164,165). It has 314 amino acids with a predicted molecular weight of 32 kDa. However, alternative splicing, alternative translocation and posttranslational modifications produce a wide range of molecular weights ranging from 41 to 75 kDa (164).

The *SPP1* gene undergoes alternative splicing of its 7 exons, leading to at least 5 isoforms. The main ones are OPNa, OPNb and OPNc. OPNa includes the full-length coding region (exons 2 to 7), while OPNb and OPNc lack exon 5 and 4, respectively (164,166). Two additional splicing variants, OPN-4 (lacking exons 4 and 5) and OPN-5 (which retains a portion of intron 3 from the canonical isoform) have also been identified (167). Notably, all splice variants retain key functional domains (168). Some studies suggest that alternative translation from 2 different transcription start sites may produce two different forms of OPN: a soluble OPN and an intracellular OPN lacking a signal peptide due to non-AUG alternative translation (168,169) (Figure 8).

OPN is enriched in acidic amino acids and phosphorylated serines, and undergoes post-translational modifications ,such as phosphorylation or glycosylation, and is susceptible to proteolytic cleavage or crosslinking. While the precise role of these modifications is not fully understood, they are known to alter OPN's biological functions (165,170)

OPN harbors multiple motifs and domains responsible for the interaction with multiple receptors, enabling its involvement in a wide range of biological functions (166). The RGD motif binds integrins (αvβ1, αvβ3, αvβ5, αvβ6, α5β1, and α8β1), which are involved in cell adhesion to the extracellular matrix (164). A cryptic SVVYGLR sequence located downstream of the RGD motif allows binding to α9β1, α4β1, and α4β7 integrins, and is exposed upon thrombin cleavage (164,166). Cleavage of the SVVYGLR epitope by MMP-3 or MMP-7 can disrupt α5β1 binding to RGD (164) (Figure 8). Additionally, OPN interacts with CD44, specifically the splice variants v6 and v7, but not with the standard CD44H isoform (171–173). However, the exact region responsible for CD44 binding has yet to be identified (Figure 8).

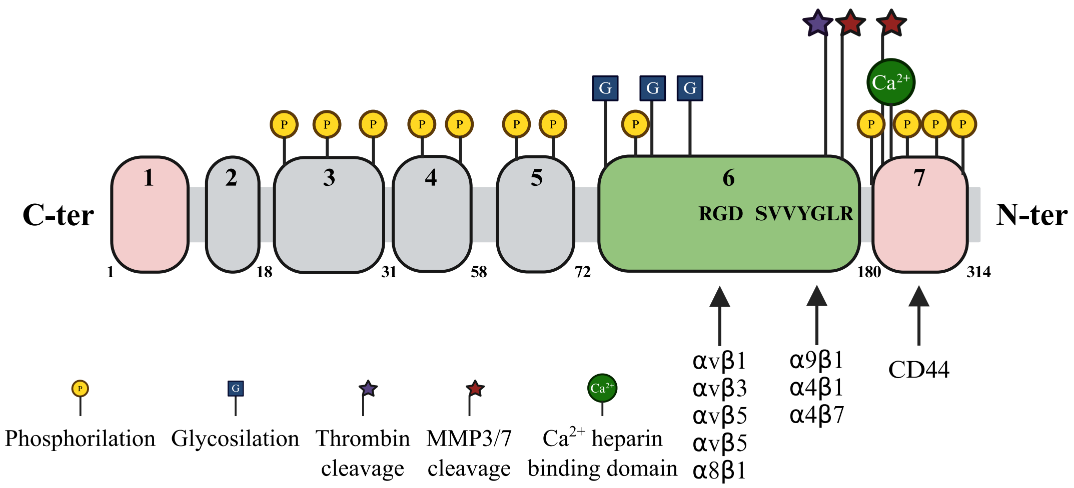

Figure 8. Schematic representation of OPN structure. The different exons, post-translational modifications, cleavage sites and receptor binding sites are shown. Modified from Abdelaziz Mohamed *et al.* (174).

3.2 Physiological role of osteopontin

OPN has several important roles in physiological conditions. In the bone, it promotes osteoclast function by facilitating attachment to the bone surface through integrin αvβ3 binding (175–177), and inhibits the formation of hydroxyapatite crystals, preventing unwanted mineralization (178). OPN also plays a key role in tissue remodeling, particularly in the bone, where it is secreted in response to mechanical stimuli under physiological conditions (179,180). In this setting, OPN stimulates the autocrine expression of CD44 and αvβ3 integrin, as well as adhesion, migration and bone resorption of osteoclasts (181).

In the immune system, OPN is highly expressed in macrophages (182) and plays a key role in their biology. OPN expression in macrophages is tightly regulated, increasing in response to several growth factors and cytokines, including endotoxin, NO, IL-1β, IFN-γ or TNF-α (183). Conversely, PPARγ signaling inhibits OPN promoter activity (184). Through different cell surface receptors, such as CD44 (185,186) and α4 and α9 integrins (via the SLAYGLR domain) (187), OPN controls the infiltration, adhesion, migration, differentiation and phagocytosis of macrophages (187–193), and inhibits IL-10 to reduce anti-inflammatory signaling, while promoting IL-12 expression (171). Dendritic cells (DCs) constitutively express high levels of both intracellular and secreted OPN (194), which is further promoted by hypoxia (195). OPN increases TNFα and IL-12 production in DCs, enhancing the stimulation of allogeneic T cells and Th1 polarization. Finally, OPN is also involved in T-cell recruitment, adhesion and proliferation (196–198), and promotes Th1 while inhibits Th2 cytokine expression (171).

3.3 Osteopontin in cancer

Cancer cells can exploit the biological activities of OPN to promote tumor progression, and OPN has been shown to play a relevant role across various cancer types. Overexpression of OPN is associated with a more aggressive phenotype, including higher grade, advanced stage, increased risk of recurrence and poor prognosis in HCC (199), breast cancer (200,201), oral squamous cell carcinoma (OSCC) (202), acute myeloid leukemia (AML) (203) and CRC (204–206). OPN serum levels also correlated with worse DFS and OS in HCC (207,208), non-small cell lung or gastric cancer (209,210), and with advanced disease stage and recurrence in bladder cancer (211).

Indeed, OPN is involved in the acquisition of several oncogenic features and promotes proliferation and migration of cancer cells in multiple malignancies such as Ret driven papillary thyroid carcinoma (PTC) (212,213), HCC (214–216), CRC (217), prostate cancer (PC) (218) or melanoma (219). This is mediated by CD44 and integrin αvβ3 binding, which activate the PI3K-Akt pathway, as well as Raf/MEK/ERK signaling, resulting in the upregulation of several effectors such as NF-κB, JUN or MMPs (214–217,219).

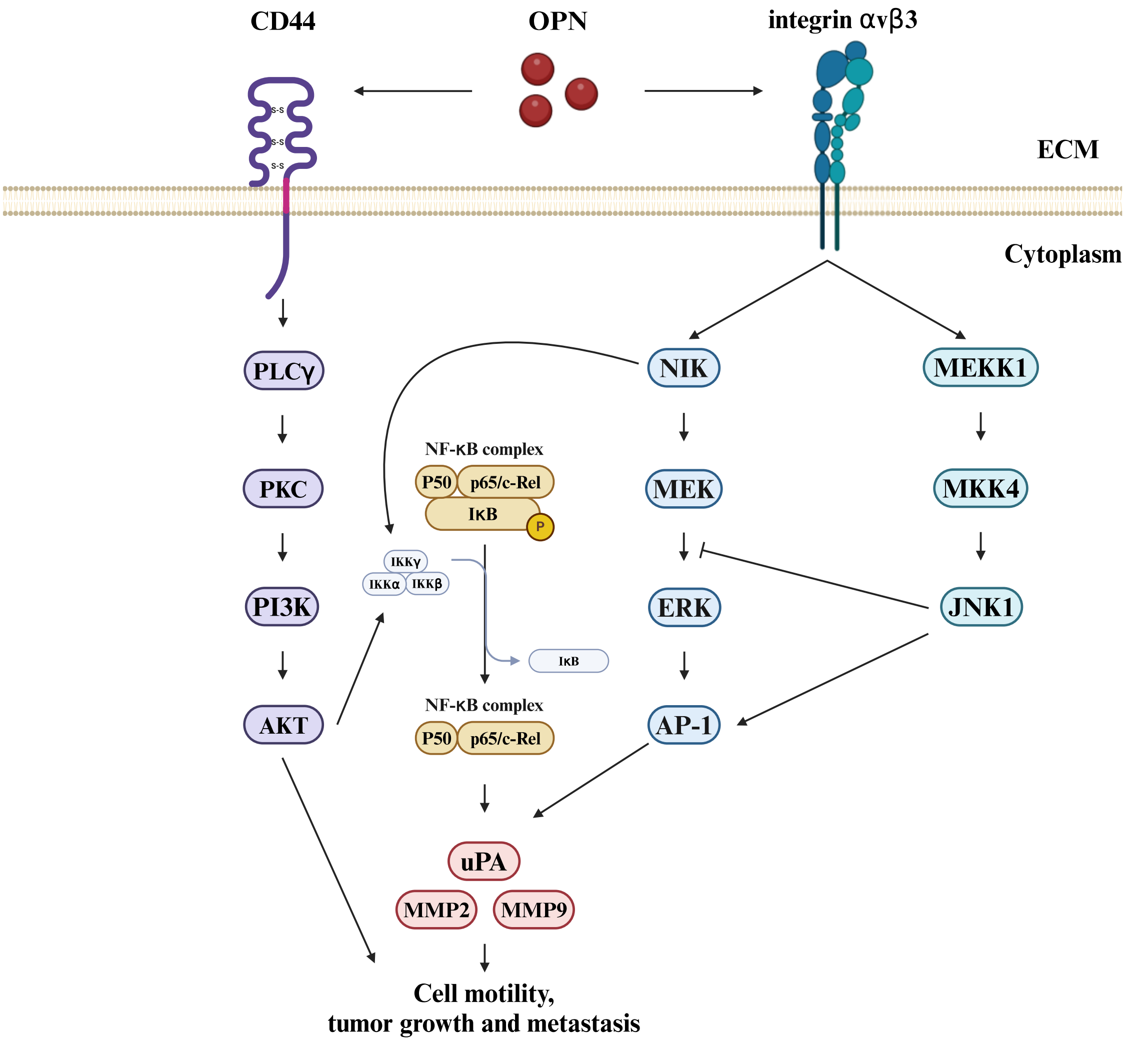

Figure 9. OPN signaling in cancer. OPN interacts with integrin αvβ3 and CD44 in cancer cells and immune cells. OPN binding to CD44 activates the PI3K-Akt pathway promoting motility and survival. Binding to integrin αvβ3 induces PI3K-Akt and NIK-mediated activation of NFkB, resulting in secretion and upregulation of uPA and MMPs. OPN binding to integrin αvβ3 also activates NIK/ERK and MEKK1/JNK1 pathways, leading to JUN (AP-1) signaling. All these pathways end up promoting motility, proliferation and metastasis. Figure modified from Rangaswami *et al*. (234).

OPN also drives EMT by increasing twist phosphorylation (220,221), invasion and metastasis through MMP-2, MMP-9, IL-8 and urokinase plasminogen activator (uPA), while inhibiting caspase 3. These effects are also mediated by activation of the MAPK and PI3K-Akt signaling pathways, which allow the translocation of NF-κB to the nucleus, upregulating HIF-1α to promote cancer cell proliferation and survival (222–224).

Finally, OPN also reshapes the immune landscape of tumors to promote cancer progression. OPN and its receptor CD44 are involved in the recruitment and polarization of TAMs to the M2 phenotype (225,226), and prevent T-cell infiltration (226) as well as cytotoxic CD8+ T lymphocyte activity *in vitro* and *in vivo* (227,228). Moreover, macrophage-specific deletion of *SPP1* increased cytotoxic T-cell infiltration (229), whereas macrophage-derived OPN fostered tumor growth, clonogenicity and further OPN expression in cancer cells (230). Interestingly, a newly proposed macrophage polarization system involving *CXCL9* and *SPP1* has shown prognostic value across various cancers. A higher ratio of *SPP1* expressing-macrophages relative to *CXCL9* is associated with poorer survival outcomes (231). Overall, OPN expression contributes to an immunosuppressive tumor microenvironment (232,233).

3.4 Osteopontin in angiogenesis

OPN plays a critical role in angiogenesis and multiple reports highlight its interaction with the VEGF-A/VEGFR-2 signaling pathway, which promotes angiogenesis in multiple human malignancies, including melanoma, lung, pancreatic or gastric cancer (219,235–237). Notably, OPN can promote the expression of VEGF in both endothelial and cancer cells (238–241), thereby enhancing angiogenesis and migration (242,243). VEGF also induces OPN and integrin αvβ3 expression in endothelial cells (244–246), further supporting the interaction between these two angiogenic molecules.

In endothelial cells, OPN´s effects are mediated by integrin αvβ3, which activates the PI3K-Akt and ERK pathways. This increases bcl-xL, activates NF-κb and promotes VEGF expression leading to increased motility, proliferation, and tube formation in endothelial cells. Accordingly, OPN knockdown diminishes proliferation, migration and tube formation ability, although these effects might be independent of VEGF in endothelial cells (247,248).

Tumor and stromal derived OPN enhance angiogenesis *in vitro* and *in vivo*, stimulating proliferation, migration, and tube formation in endothelial cells (238,240,249–251).

Accordingly, cyclooxygenase-2 (COX-2) inhibition which reduced OPN and VEGF levels, suppressed angiogenesis (252). However other authors suggest that stromal and tumor derived OPN might have different roles, and for instance, in lung adenocarcinoma, host OPN promotes macrophage recruitment and angiogenesis, while tumor-derived OPN reduces apoptosis and enhances vascular permeability without VEGF involvement. However, both contribute to pleural fluid accumulation and tumor spread (253).

OPN also appears to drive transcriptional activation of HIF1α and angiogenesis in cancer through integrin αvβ3-PI3K-NF-κB signaling (254). Accordingly, OPN knockdown (KD) resulted in reduced HIF1α and VEGF levels, along with decreased cell invasion, clonogenic survival, and increased apoptosis and senescence (241,255).

Finally, OPN can also exert its protumoral function through immune cell interactions. OPN binding to integrins leads to angiogenesis and tumor growth by promoting macrophage infiltration and COX-2 expression, resulting in increased prostaglandin E2 (PGE2) production (254,256). Thus, OPN seems to promote angiogenesis through different molecular mechanisms.

3.5 Osteopontin in resistance to cancer therapy

OPN has also been involved in resistance to different treatments, including cytotoxic chemotherapy and AAT. Elevated OPN levels have been associated with resistance to platinum-based therapies in breast cancer, non-small cell lung cancer (NSCLC) and OSCC (257–259), as well as to 5-FU based chemotherapy in OSCC, where this resistance is integrin αvβ3 dependent (260).

Moreover, several studies and systematic reviews indicate that OPN is associated with worst PFS in RCC patients receiving AAT (261) with pazopanib and sorafenib (262,263). In this regard, hypoxia induced by AAT further stimulates OPN, integrin αvβ3, HIF-1α and VEGF expression, amplifying their protumoral effects (254,264).

OPN-driven molecular mechanisms of resistance to cytotoxic chemotherapy such as epirubicin and cisplatin in HCC (265), gemcitabine in pancreatic cancer (266), mitozantrone in melanoma (249) and multiple other drugs (e.g., paclitaxel, doxorubicin, actinomycin-D, and rapamycin) in PC, may involve autophagy, which is promoted by OPN through integrin/CD44 and p38 MAPK signaling pathways (267,268). OPN-induced EMT is also a described mechanism of resistance to anticancer therapies like doxorubicin, paclitaxel, and cisplatin. Several groups have shown that OPN increases mesenchymal markers such as N-cadherin, vimentin, twist, slug, and MMP9, leading to decreased efficacy of these agents (269). Finally, OPN can promote a metabolic reprograming by increasing glucose uptake and lactate production via integrin αvβ3 and NF-kB signaling, leading to cisplatin resistance, and increased tumor growth and invasion capacity in HCC and NSCLC (259,270).

Additionally, OPN upregulates specific signaling pathways, such as p-MEK and p-ERK signaling, to induce cetuximab and gefitinib resistance in NSCLC (271,272). Finally, OPN also promotes cell survival and resistance to sorafenib in FLT3-ITD mutated AML by activating β-catenin through the PI3K-Akt-GSK3β pathway (273).

3.6 Osteopontin in NETs

The role of OPN in NETs remains largely unexplored, with only two case reports describing positive OPN staining in a gastric carcinoid and LCNEC tumors, both associated with stromal calcification (274,275). More recently, OPN isoforms were found to be expressed in MTC, where OPN correlated with smaller tumor size, PTEN nuclear expression, RAS status and non-invasive tumors (276).

Finally, two studies have specifically investigated OPN in lung and GEP-NETs. First, Jimenez-Fonseca *et al.* analyzed OPN levels in the plasma of 43 sunitinib-treated Pan-NET patients at baseline, 3 months and at the end of the study. They found that higher OPN levels were associated with shorter PFS (*HR: 1.087 (1.011-1.169),* $p = 0.023$) (160). The second study analyzed 38 NEN patients and described increased OPN levels in NET patients compared to healthy controls, with the highest levels found in grade 3 NENs. Moreover, a cutoff of 200 ng/ml predicted poorer prognosis and significantly shorter PFS in both NECs and NETs, although patients received different systemic therapies (277).

HYPOTHESIS

Hypothesis

Neuroendocrine tumors are hypervascular and angiogenesis plays a crucial role in their tumorigenesis and progression. Anti-angiogenic multikinase inhibitors have demonstrated efficacy and are approved for the treatment of advanced NETs. However, not all patients respond to these therapies, the magnitude of the benefit is limited, and all responders eventually develop resistance over time.

We hypothesize that molecular characterization of NETs can enable the development of predictive molecular biomarkers to identify the subgroup of patients most likely to respond to these treatments. This strategy will improve the overall efficacy of angiogenesis inhibitors, reduce unnecessary toxicity, lower costs, and provide a more personalized treatment approach to NET patients.

OBJECTIVES

Objectives

The primary goal of this project is to identify predictive biomarkers for antiangiogenic MKIs in NET patients. This will enable more accurate patient selection and improve the overall benefit-risk and cost-benefit balance of this therapeutic strategy.

The specific objectives of this project are the following:

Aim 1. To identify a transcriptomic signature associated with tumor response and progression-free survival in tumor samples from NET patients enrolled in the AXINET trial treated with axitinib.

Aim 2: To characterize the distinctive molecular features of NETs that benefit from axitinib.

Aim 3: To validate tumor predictive biomarkers identified in external cohorts of GEP-NET patients treated with other antiangiogenic MKIs.

Aim 4: To validate in plasma the predictive biomarkers identified to facilitate its implementation in clinical practice.

Aim 5: To study the role of osteopontin (OPN) in NET biology and angiogenesis *in vitro*.

Aim 6: To study the role of osteopontin (OPN) in NET biology and angiogenesis *in vivo*.

MATERIALS AND METHODS

Materials and Methods

1. Study design

The study design was observational, retrospective, and multicenter, and included patient diagnosed with neuroendocrine tumors from AXINET (NCT01744249) and TALENT (NCT02678780) clinical trials, as well as from Hospital 12 de Octubre. Patients enrolled in clinical trials were treated according to the study protocol and the ethical principles for medical research involving human participants established in the Declaration of Helsinki and the International Conference on Harmonization guidelines for Good Clinical Practice. Clinical data was prospectively registered and monitored. All patients provided written informed consent prior to the study entry and consented to donate samples for their use in translational studies. The handling of personal data complied with current regulations, *Ley Orgánica 3/2018, de 5 de diciembre, de Protección de Datos Personales y garantía de los derechos digitales (LOPD-GDD).* The transcriptomic profiling was conducted at the Genomic Unit of Centro de Investigación del Cáncer IBMCC-FICUS of Universidad de Salamanca - CSIC, while the determinations in plasma samples, bioinformatics analysis and *in vitro* and *in vivo* studies were performed at Instituto de Investigación Sanitaria Hospital 12 de Octubre (i+12) and Sunnybrook Institute of Research. The research project was approved by Hospital 12 de Octubre Clinical Research Ethics Committee (CEIm 18/449).

2. Study population

This study was performed in different NET patient cohorts, some were used for discovery and others for validation purposes.

<u>Discovery cohort</u>

Included patients enrolled in the AXINET clinical trial (NCT01744249) (137). AXINET is a phase II/III, international, multicenter, randomized, double-blind study that evaluated the efficacy of axitinib in combination with octreotide LAR (SSA) versus placebo with SSA, in 256 adult patients with advanced G1-G2 NETs (WHO 2010) of extrapancreatic origin between 2011 and 2021 in 26 centers from Spain, Italy and Germany. This study was an investigator-initiated trial led by Dr. Rocio Garcia-Carbonero as principal investigator and sponsored by GETNE through an unrestricted grant of Pfizer.

The main eligibility criteria included advanced G1-G2 NETs (WHO 2010) of non-pancreatic origin, with clinical or radiological disease progression within the last 12 months prior to study entry, a performance status < 2, adequate organ function and up to 2 prior lines of systemic therapy excluding angiogenesis inhibitors. Patients with pheochromocytoma, paraganglioma, adrenal, thyroid, parathyroid, or pituitary tumors were excluded. Overall, 256 patients were enrolled in the trial (Table 4). From these, 213 patients (83%) provided consent and had an adequate tumor (N = 126) and/or plasma (N = 193) sample available for translational studies, 105 patients received axitinib with SSA and 108 received placebo and SSA (Table 4). One hundred twenty-six of the 213 patients were used in the discovery phase (AXINET discovery cohort) of our project (Table 4). Among them, 106 had formalin-fixed paraffin embedded (FFPE) tumor and plasma samples, and 20 only had FFPE tumor samples.

Validation cohorts

i. AXINET validation cohort (N = 87): included 87 independent AXINET trial patients that were not part of the discovery cohort. These patients only had plasma sample available (Table 4).

ii. TALENT cohort (N = 99): included 99 out of 111 patients (88%) enrolled in the TALENT clinical trial (142), 47 of pancreatic and 52 of gastrointestinal origin (Table 7). This was a phase II open label study that evaluated the efficacy of lenvatinib in adult patients with advanced pancreatic NETs upon progression to a previous targeted agent (cohort A) or advanced GI-NETs after progression to SSA (cohort B). Other main inclusion criteria included radiological disease progression within 12 months prior to study entry, a performance status of 0 - 1, adequate organ function and measurable disease. This study was also an investigator-initiated trial led by Dr. Jaume Capdevila as principal investigator and sponsored by GETNE, that was conducted between 2015 and 2020 in 22 centers from Austria, United Kingdom, Italy and Spain. These patients only had plasma samples available.

iii. Hospital 12 de Octubre cohort (H12O; N = 29): included tumor samples from patients diagnosed with G1-G3 GEP-NETs treated according to the standard of care with antiangiogenic MKIs (N = 11) and/or SSA (N = 18) at our institution

Hospital 12 de Octubre (Table 5). These patients only had FFPE tumor samples available.

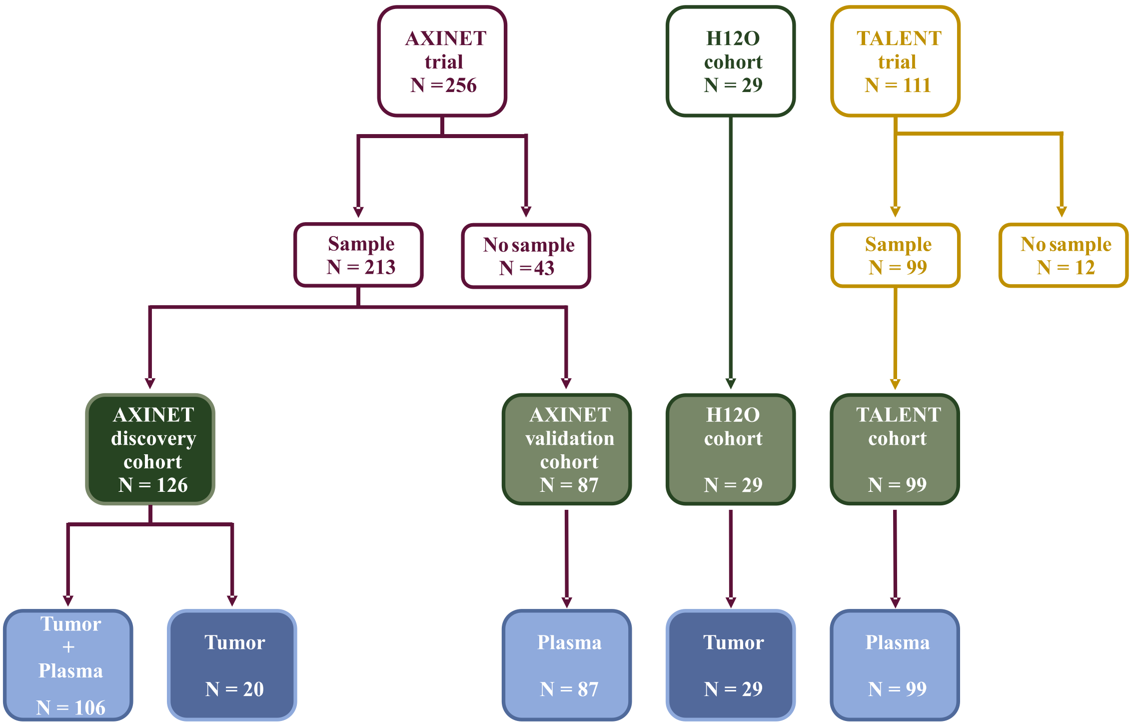

Figure 10. Flowchart of patients and samples included for discovery and validation purposes in the different cohorts of study.

Clinical characteristics

The clinical information of patients included in clinical trials was prospectively registered in the corresponding electronic case report forms following the study protocols and on-site monitored by properly trained and authorized personnel that had access to source data files. For patients of the Hospital 12 de Octubre cohort, clinical information was retrospectively collected from clinical charts by their treating physicians. For the purpose of this study, a pseudonymized database was designed and included the following variables: sex, age, tumor differentiation and proliferation index (Ki-67), functionality, primary tumor location, biopsy site, date of diagnosis, type and date of surgery, systemic therapy for advanced disease (treatment regimen, treatment period, best radiological response per RECIST v1.1 criteria, date of disease progression), and date of death or last visit in alive patients. Radiological response was assessed per investigator criteria and also per central blinded radiological reading in both trials. Patient personal information remained anonymized to basic researchers involved in translational studies. The most relevant clinical characteristics of the discovery and validation cohorts are summarized in tables 4, 5 and 7.

3. Human sample processing, collection and storage

Tumor samples were fixed in formaldehyde and embedded in paraffin for its usual processing in their hospital of origin. Hematoxylin and eosin (H/E) staining were performed, and samples were assessed by expert NEN pathologist prior to molecular analysis. The FFPE tumor samples and H/E slides were sent by each participant center to Instituto de Investigation Sanitaria Hospital 12 de Octubre where they were conserved at -20ºC.

Plasma samples were collected at the institution of origin at several time points (baseline, 1 month, 6 months and at the end of the study or upon progression). Briefly, blood samples were collected in sodium EDTA anticoagulant tubes and were centrifuged immediately at 1500 x g for 10 minutes using a refrigerated centrifuge at 4ºC. Plasma samples were sent by each participant center to Instituto de Investigation Sanitaria Hospital 12 de Octubre where they were conserved at -80ºC.

4. Nucleic acid extraction

RNA was extracted from FFPE tumor samples from 126 patients of the AXINET discovery cohort and 29 patients of the H12O cohort, providing sufficient and adequate material for gene expression analysis. Total RNA was extracted with RNeasy FFPE Kit (QIAGEN, Valencia, CA, USA) according to manufacturer's instructions. Total RNA was diluted in RNAse free water, and its integrity, purity and concentration were assessed with the Qubit® Fluorimeter (Life Technologies, Carlsbad, CA, USA) or Nanodrop 1000 (NanoDrop, Wilmington, DE, USA) instruments, respectively. RNA was stored at -80ºC until usage.

Total DNA and RNA were extracted from cell lines using standard methods with QIAamp DNA Mini Kit (QIAGEN, Valencia, CA, USA) and RNeasy Mini Kit (QIAGEN, Valencia, CA, USA), respectively. Total DNA and RNA were diluted in RNAse free water, and purity and concentration were assessed with the Nanodrop 1000 (NanoDrop, Wilmington, DE, USA) instrument using absorbance ratios at 260/280 nm. DNA and RNA were stored at -80ºC until usage.

5. Transcriptomic analysis

Gene expression analysis was performed in the Genomic Unit of Centro de Investigación del Cáncer IBMCC-FICUS of Universidad de Salamanca - CSIC using Clariom™ S Human Arrays (Affymetrix, Santa Clara, CA, USA). First, RNA signal was amplified with the GeneChip Pico Reagent kit (Applied Biosystems, Waltham, EEUU). Next, total mRNA was retrotranscribed to biotinylated double strand cDNA, covering the whole transcriptome. cDNA was then hybridized with the microarray's probes for 18 hours according to the manufacturer's protocol. Finally, the arrays were scanned and quantified using the GeneChip Scanner 3000 7G System (Affymetrix, Santa Clara, CA, USA) and the Affymetrix GeneChip Command Console 3.2 software (Affymetrix, Santa Clara, CA, USA), respectively. This protocol allowed us to determine the gene expression of 20800 individual genes.

Data normalization

The files were read and normalized using the R (v4.4.1) (278) package *affy* (279). All samples were analyzed and normalized together using *expresso* function from *affy*, applying *"RMA"* as noise correction method, *"quantiles"* as normalization method, *"pmonly"* as pm correction method and *"medianpolish"* as fusion method. Once the probes were normalized, annotation was performed at the gene level. For genes with multiple probes, those with higher variance were selected, avoiding repeated genes, and selecting probes providing more information. This normalization and filtering process resulted in a gene expression matrix with 19420 annotated genes.

Quality correction

Principal component analysis (PCA) was performed on the gene matrix to evaluate the quality of the measurements performed with the microarray. Quality values were obtained with the *Transcriptome Analysis Console* software (Affymetrix, Santa Clara, EEUU) and were correlated with the 10 principal components. The first component of the PCA significantly correlated with the RNA quality (*correlation coefficient = 0.93;* $p < 10^{-6}$) which suggests that PC1 distinguishes real biological signal from noise in the samples (Supplementary Figure 1A). Given that this variability was not strictly related to the biology of the samples, PC1 was regressed from the gene expression matrix using *removeBatchEffect* from *limma* (280) to remove the impact of sample quality on the data.

Regressing PC1 resulted in the complete loss of quality and PC1 correlation ($p = 0.948$) (Supplementary Figure 1B). Quality correction was performed first in the AXINET discovery cohort. Subsequently, data from H12O validation cohort was regressed together with data from the AXINET discovery cohort to ensure comparability.

6. Predictive signature discovery

Axitinib predictive biomarker genes were identified and selected based on their association with centrally reviewed PFS and with the best tumor shrinkage. To ensure that the identified biomarkers were specific to axitinib response, excluding those related to disease biology or response to other therapies such as SSA, patients treated with axitinib + SSA were analyzed separately from those treated with placebo + SSA as detailed below.

<u>Selection of potential predictive genes</u>

First, we assessed the association of gene expression and PFS using univariate Cox regression analysis, and the R packages *survival* and *survminer*. The 5000 genes with highest median absolute deviation (MAD) from each study arm were included in the analysis. A total of 3753 genes overlapped between both arms (75.1%). Genes with a $p\text{-}value < 0.01$ were considered significant in patients treated with axitinib + SSA, while a $p\text{-}value < 0.05$ was used for significance in patients treated with placebo + SSA. Only genes that were exclusively and significantly associated with PFS in the axitinib + SSA arm were selected as potential predictive biomarkers. The use of less stringent statistical criteria for the placebo arm allowed us to be more confident in the selection of genes exclusively associated with axitinib response. Given the high number of tests performed (N = 5000, in each cohort), multiple testing adjustment was applied using the Benjamini–Hochberg procedure in R. The *HR* and *p-value* of Cox regression analyses were visualized in a volcano plot using R and the *EnhancedVolcano* package.

Next, interaction Cox regression analysis was conducted in R to examine how the treatment arm modifies the association between gene expression of each candidate gene and PFS. All genes significantly associated with PFS in axitinib-treated patients were tested. This analysis was performed using PFS and *survival* and *survminer* packages. Genes with an interaction $p < 0.05$ were considered statistically significant and thus, were further selected and studied given its specific association to PFS in axitinib-treated patients and not in placebo treated patients.

The list of candidate genes was further reduced based on the association with tumor shrinkage in response to axitinib. To that aim, a regularized linear regression model was built using the scaled gene expression data of the candidates and maximum tumor shrinkage in response to axitinib treatment. This analysis was carried out in R using the package *glmnet* (281) and an α parameter of 0.5. Leave-one-out cross-validation (59 folds) was applied, and the square error for Gaussian models was used as performance measure. The mean-squared error (MSE) and the λ parameter were plotted, and the model with the λ parameter that minimized the MSE was selected.

Tumor shrinkage was measured as the percentage of change in tumor volume of the target lesions, comparing best response computed tomography (CT) scan to baseline CT scan. Both tumor shrinkage and PFS were centrally reviewed by an expert radiologist blinded to study treatment.

Signature definition

The expression levels of genes selected with the regularized linear regression were transformed into a unique score using the *singscore* R package (282), which utilizes rank statistics for this purpose. As a result, each patient was assigned a signature score that summarizes the expression of all selected candidate genes. Then, patients were divided into high and low score groups based on the median score of the entire AXINET study population, which was used as threshold.

Signature assessment

i. Progression Free Survival

The predictive capacity of the signature was assessed using univariate Cox regression analysis with PFS, considering the signature both as a numeric and dichotomic variable (high vs. low). Low score patients were set as the reference group. All the analysis were performed separately for patients treated with axitinib + SSA and patients treated with placebo + SSA, and a *p-value* < 0.05 was considered statistically significant. The *HR* and its 95% interval of confidence (CI) were calculated for each regression. Additionally, the median PFS for high and low score patients was calculated using the *survfit* R package. Time-dependent variables (PFS) were also estimated using the Kaplan-Meier method.

ii. Tumor shrinkage

Differences in quantitative variables (tumor shrinkage or signature score) between high and low score patients were assessed using parametric (Student's t-test) and nonparametric (Kruskal–Wallis) tests, as appropriate. Violin plots representing medians and quartiles, or scatter dot plots showing means and standard deviation (SD), were used for data visualization. Waterfall plots were employed to represent response enrichments within subgroups: complete response (CR, -100%), partial response (PR, -99% to -30%), stable disease (SD, -30% to 20%) and progressive disease (PD, > 20%) (283). Finally, Pearson and Spearman correlation tests and dispersion plots were performed to evaluate potential correlations between the signature score and tumor shrinkage. All these analyses were conducted separately for patients treated with axitinib + SSA and patients treated with placebo + SSA, and a *p-value* < 0.05 was considered statistically significant. Graphs and analysis were generated in GraphPad Prism 8.1 (GraphPad, Boston, MA, USA).

7. Differential expression and gene set enrichment analysis

Differential expression analysis was conducted in R using the *limma* package (280) to identify differentially expressed genes (DEGs) between high and low score patients. All ~ 20 000 genes were evaluated and a *p-value < 0.05* was considered statistically significant. Multiple testing adjustment was applied using the Benjamini–Hochberg procedure and a *false discovery rate (FDR) < 0.05* was considered significant. DEGs and the signature score were represented in a supervised heatmap using the *pheatmap* R package, along with key clinical characteristics including sex, functioning syndrome, grade, primary tumor location, PFS and ORR.

GSEA was performed on DEGs using the *fgsea* R package (284). Multiple cancer-related gene sets from the MsigDB database were analyzed, including 50 Hallmarks (285) and 186 KEGG gene sets (286), along with 20 additional gene sets selected for their relevance to this study. These additional sets comprised 6 Gene Ontology (287) gene sets related to adhesion and hypoxia, and 14 gene sets related to endocrine and neuroendocrine differentiation and signaling. Furthermore, a 50-gene signature specific for tumor-associated EMT from Tyler *et al.* (288) was evaluated. Multiple testing adjustment was applied using Benjamini–Hochberg method and an *FDR < 0.05* deemed significant.

Normalized enrichment scores (NES) were also reported. Significantly enriched gene sets were visualized using enrichment plots.

8. Cell type enrichment analysis

Cell type enrichment analysis was performed in R using the *xCell* package (289) and patients gene expression data. Differences between high and low score groups were evaluated using both parametric (Student's t-test) and nonparametric (Kruskal–Wallis) tests, depending on the data distribution. Multiple testing adjustment was applied using the Benjamini–Hochberg method, and an $FDR < 0.05$ was considered statistically significant. Violin plots were generated to represent the distribution, median and quartiles of each cell population across patient groups using GraphPad software (Boston, MA, USA).

9. External validation of the signature

The validation cohort was analyzed using the same pipeline as the discovery cohort (see sections 5, 7 and 8). Additionally, the association of the signature and its genes with PFS was evaluated through Cox regression analysis, using gene expression data and PFS in R. This analysis was performed separately for patients treated with MKIs (N = 11) and those treated with SSA (N = 18). A $p\text{-}value < 0.05$ was considered statistically significant and the *HR* with its 95% interval of confidence were reported.

Signature scores from the validation cohort were compared to those from the discovery cohort with the nonparametric Kruskal–Wallis test, along with appropriate post-hoc analyses. Violin plots were generated to illustrate the median and quartile scores of high and low score patients in both cohorts. Both statistical analyses and visualizations were performed using GraphPad Prism 8.1 (GraphPad, Boston, MA, USA).

10. Cell lines and culture conditions

Pancreatic neuroendocrine tumor cell lines, QGP-1 (RRID: CVCL_3143) and BON-1 (RRID: CVCL_3985), were kindly provided by Dr. Justo Castaño (Instituto Maimonides de Investigación Biomédica, Spain). Lung neuroendocrine tumor cell lines, H727 (RRID: CVCL_1584) and UMC-11 (RRID: CVCL_1784), were purchased from American Type Culture Collection (ATCC, Manassas, VA, USA). HEK293T (RRID: CVCL_0063) and HUVEC cells were kindly provided by L. Paz-Ares (Hospital 12 de Octubre and Centro

Nacional de Investigaciones Oncológicas (CNIO), Spain) and Gemma Domínguez Muñoz (Instituto de Investigaciones Biomédicas Alberto Sols, Spain), respectively.

BON-1 cell line was cultured in 1:1 DMEM/F12K medium (Sigma-Aldrich, San Luis, MO, USA and Thermo Scientific, Waltham, MA, USA). HEK293T cells were cultured in DMEM medium (Sigma-Aldrich, San Luis, MO, USA). H727, UMC-11 and QGP-1 cells were cultured in RPMI 1640 medium (Sigma-Aldrich, San Luis, MO, USA). HUVEC cells were cultured in Endothelial Cell Growth Medium (ECGM, Sigma-Aldrich, San Luis, MO, USA). HUVEC cells were also grown in 10% OPN overexpressing or control (CTRL) BON-1 conditioned ECGM medium for angiogenesis and viability assays. All mediums, except for ECGM, were supplemented with 10% fetal bovine serum (FBS, TICO Europe, Amstelveen, The Netherlands) and 1% antimycotic (penicillin-streptomycin-amphotericin; Sigma-Aldrich, San Luis, MO, USA). All cell lines were cultured at 37 °C in a humidified atmosphere of 95% O_2 and 5% CO_2 and tested monthly for mycoplasma contamination. Culture medium was changed every other day and cells were split every 2-4 days. All cell lines were authenticated by short-tandem repeat profiling in the CNIO genomic service.

11. Enzyme-Linked Immunosorbent Assay (ELISA)

OPN levels in human and mice plasma, and in culture medium were evaluated with an enzyme-linked immunosorbent assay (ELISA) kit (Human OPN DuoSet ELISA (DY1433), R&D Systems, Inc., Minneapolis, MN, USA) according to manufacturer's instructions. Briefly, 96-well microplates were coated and incubated overnight at 4ºC with 100 μl of the capture antibody. Then, microplates were blocked with 300 μl of the reagent diluent at room temperature (RT) for one hour. Next, 100 μl of undiluted or diluted samples were incubated at RT for 2 hours. Plasma samples were diluted in reagent diluent 50 times, and culture medium was diluted between 1 and 2000 times as appropriate to be measured in the working range of the assay (0.0625 ng/ml to 4 ng/ml). After sample incubation, plates were washed, and 100 μl of detection antibody were added for 2 hours at RT. Subsequently, another wash was performed, and 100 μl of working dilution HRP-streptavidin were added and incubated for 20 minutes at RT. Finally, 100 μl of substrate solution were added and incubated for 5 min at RT before stopping the reaction with 50 μl of stop solution. The absorbance at 450 nm was measured on a multimode plate reader (VICTOR Nivo, Perkin Elmer, Waltham, MA, USA).

Samples were evaluated twice, and the mean absorbance value was used to estimate OPN concentration by interpolating the absorbance from a four-parameter logistic (4PL) regression. Patients were classified into high or low OPN plasma groups based on the median population value, and the pipeline followed in section 6 was performed to evaluate the predictive capacity of OPN plasma levels to axitinib or lenvatinib.

12. DNA reagents

Several plasmids were used to modify *SPP1*/OPN expression in NET cell lines: pLentiCRISPRv2 (#52961, Addgene, Watertown, MA, USA) was kindly provided by Dr. Luis Paz-Ares (CNIO, Spain). pGIPZ-GFP-EV (#120933, Addgene, Watertown, MA, USA), pMD2.G (#12259, Addgene, Watertown, MA, USA) and pLenti-P2A-tGFP (PS100108, OriGene, Rockville, MD, USA) were available in our laboratory. pCD/NL-BH*DDD (#17531, Addgene, Watertown, MA, USA) was kindly provided by Dr. Rafael Delgado Vázquez (Instituto de Investigación Sanitaria Hospital 12 de Octubre, Spain). *SPP1* sequence (CW310176, OriGene, Rockville, MD, USA) was cloned into an untagged pLenti-P2A-Puro vector (PS100109, OriGene, Rockville, MD, USA). PiggyBac PB-37 (PB-TRE-puro-EM-7-BlastpA-CAGGs-eKr-pA), PiggyBac PB-31 (PB-TRE-puroRfA-PGKneopA-CAGGs-effLuc2AmKate2ArtTA-pA) and pBase transposase plasmids were kindly provided by Dr. Iacovos Michael (Sunnybrook Research Institute, Canada). Gateway compatible plasmids carrying *SPP1* short hairpin RNAs (shRNAs) were obtained from Thermo Scientific (Thermo Scientific, Waltham, MA, USA), and then cloned into PB-31 and PB-37 plasmids. Similarly, the *SPP1* sequence (CW310176, OriGene, Rockville, MD, USA) was cloned into the PB-37 vector using Gibson Assembly. The maps of all plasmids cloned and used in this project are shown in Supplementary Figure 2.

The five CRISPR/Cas9 guide RNA (sgRNAs) pairs with higher "On-Target Efficacy Score" and less "Combined rank" using the Broad Institute web tool (https://www.broadinstitute.org/rnai/public/analysis-tools/sgrna-design) were selected and synthesized as custom oligos (Sigma-Aldrich, St. Louis, MO, USA). Similarly, the 6 *SPP1* shRNAs with higher splash scores were obtained from Fellman *et al.* shRNA libraries (290). Finally, custom *SPP1* primers targeting exon 7 were designed using Primer 3 Plus (291), and were ordered as custom oligos (Thermo Scientific, Waltham, MA, USA). All these sequences are summarized in Table 2.

Name	Sequence (5’ to 3’)
CRISPR/Cas9 guides	
sgRNA 1F	GTAGACACATATGATGGCCG
sgRNA 1R	CGGCCATCATATGTGTCTAC
sgRNA 2F	ATAGTGTGGTTTATGGACTG
sgRNA 1R	CAGTCCATAAACCACACTAT
sgRNA 3F	GCCATCATATGTGTCTACTG
sgRNA 3R	CAGTAGACACATATGATGGC
sgRNA 4F	GTACCCTGATGCTACAGACG
sgRNA 4R	CGTCTGTAGCATCAGGGTAC
sgRNA 5F	CATCATATGTGTCTACTGTG
sgRNA 5R	CACAGTAGACACATATGATG
***SPP1* shRNAs**	
SPP1 sh293	TTCATCATCCATATCATCCATG
SPP1 sh353	TACATCATCAGAGTCGTTCGAG
SPP1 sh535	TTAGATTTTGACCTCAGTCCAT
SPP1 sh759	TATATAATCTGGACTGCTTGTG
SPP1 sh760	TTATATAATCTGGACTGCTTGT
SPP1 sh940	TCTAATTCATGAGAAATACGAA
Sequencing primers	
Exon7 F	TGGATTTGACATAGCCTTGC
Exon7 R	GCTCTCATCATTGGCTTTCC
hU6-F	GAGGGCCTATTTCCCATGATT
Puro Resistance F	GCAACCTCCCCTTCTACGAGC
PolyA R	AATATTATGCTCTCGTTAATCCATAGAGCCCACCGCATC
mCMV F	CCTCCATAGAAGACACCGGG
GA amplification primers	
SPP1 GA F	GGCGGCCATCACAAGTTTGTACAAAAAAGCAGGCTTCGCCGCGA TCGCCATGAGAATTGC
SPP1 GA R	ACCTTCTGATAGGCAGCCTGCACCTGAGGAGTGAATACGCGTATT GACCTCAGAAGATGC
SYBR primers	
SPP1 F	GAAGTTTCGCAGACCTGACAT
SPP1 R	GTATGCACCATTCAACTCCTCG
GAPDH F	TGCACCACCAACTGCTTAGC
GAPDH R	GGCATGGACTGTGGTCATGAG

Table 2. DNA reagents. The name and sequence of sgRNAs, shRNAs and primers designed and used in this study are shown. GA, Gibson assembly. R, reverse. F, forward. CMV, cytomegalovirus.

13. Stable modulation of *SPP1* in NET cell lines

Cloning

The 5 sgRNA pairs were used to generate *SPP1* knockout models. These sgRNAs were synthesized with additional nucleotides to match BsmBI sticky ends, enabling their cloning into the pLentiCRISPRv2 vector. Similarly, selected shRNAs were used to generate *SPP1* conditional knockdown (KD) models. These shRNA were synthesized with PB-37 homology regions flanking the miR-E-shRNA region, and BfuAI restriction sites in a Gateway compatible pDONR221 plasmid (Thermo Scientific, Waltham, MA, USA). The shRNAs were cloned into the PB-31 and PB-37 inducible vectors using Gateway cloning and Gibson assembly, respectively.

To generate *SPP1* conditional overexpression (OE) models, the *SPP*1 sequence (CW310176) was flanked with PB-37 homology regions by PCR amplification using Q5 High-Fidelity DNA Polymerase (New England Biolabs, Ipswich, MA, USA) according to the manufacturer´s instructions, and cloned into the PB-37 plasmid using Gibson Assembly. The specific Gibson assembly primers used are listed in Table 2.

<u>PiggyBac transfections</u>

The appropriate number of target cells were seeded 24h prior to transfection to achieve 85% confluency in a 6 well-plate. Two hours before transfection, the appropriate medium was changed to antibiotic-free medium. One microgram of pBase transposase and 3 μg of the piggyBac plasmid of interest were transfected with Lipofectamine™ 3000 (Thermo Scientific, Rockford, IL, USA) in Opti-MEM™ (Thermo Scientific, Rockford, IL, USA) according to manufacturer’s instruction. After 24 hours, fresh media was added. Selection of cells started 48 hours after transfection with the addition of the appropriate mammalian selection antibiotic, either 250-750 μg/ml of geneticin (Gibco, Waltham, MA, USA) or 1 μg/ml of blasticidin (Thermo Scientific, Rockford, IL, USA). Cells were passaged as usual until complete selection of transfected cells which was evaluated by mKate positivity using a fluorescent microscope (Zeiss, Oberkochen, Germany).

<u>Transfection and transduction for lentiviral models</u>

Two and a half million HEK293T cells were plated in a p100 dish 24 hours prior to transfection to reach a 70% confluency. The plasmids required to produce lentiviral particles, pMD2.G (2 μg) and pCD/NL-BH*DDD (8 μg), as well as the pLenti plasmid of interest (10 μg) were transfected into HEK293T cells using Lipofectamine™ 3000 (Thermo Scientific, Rockford, IL, USA) diluted in Opti-MEM™ (Thermo Scientific, Rockford, IL, USA) according to manufacturer’s instruction. pGIPz-GFP-EV was used as a control of transfection. Cells were cultured and the virus-containing medium was collected 48h post-transfection. Then, target cells were seeded to reach a 70% confluency in p100 or p60 dish the day of transduction, and virus-containing medium was added to the target plate for 4 hours together with polybrene (8µg/µl; Sigma-Aldrich, San Luis, MO, USA). To select stably transfected clones, infected cells were treated with 4 µg/ml puromycin (Sigma-Aldrich, San Luis, MO, USA) for 3 weeks post-infection. Finally, puromycin-resistant cell clones were selected for subsequent studies.

14. Western Blot

Cells were lysed at 4ºC for 30 minutes in RIPA lysis buffer (Thermo Scientific, Rockford, IL, USA) containing 10% protease (cOmplete™, Roche, Basel, Switzerland) and 10% phosphatase (PhosSTOP™, Roche, Basel, Switzerland) inhibitor cocktails. Then, lysates were pelleted for 20 min at 20000g and 4ºC. Supernatant protein extracts were aliquoted and stored at −80 °C until use. Protein quantification was performed with the standard Pierce BCA Protein Assay (Thermo Scientific, Rockford, IL, USA).

Twenty to forty µg of total protein extracts were dissolved in Laemli buffer (50 mM Tris-HCl pH 6.8, 10 % glycerol, 3 % SDS, 0.006 w/v bromophenol blue and 5 % 2-mercaptoethanol) and boiled at 95ºC for 5 minutes. Samples were separated by SDS-PAGE electrophoresis (20 min at 80V and 2h at 100 V) in 8-12% polyacrylamide gels and transferred to 0.2 µm pore size nitrocellulose membranes (Thermo Scientific, Rockford, IL, USA) using iBlot 2 Gel Transfer Device (Thermo Scientific, Rockford, IL, USA). Membranes were blocked for 1h at RT with 5% fat-free milk or 10% BSA in TBS-T (150 mM NaCl2, 0.1% TweenTM 20, 20 mM Tris buffer), as appropriate. Next, primary antibodies were probed O/N at 4ºC. After washing with TBS-T, membranes were incubated for 1h with the appropriate horseradish peroxidase conjugated secondary antibody. All antibodies were diluted in 10% BSA or 5% fat-free milk as appropriate and are listed in Table 3. Bound antibodies were detected with enhanced chemiluminescence reagent (Thermo Scientific, Rockford, IL, USA) in an ImageQuant 800 imaging system (Cytiva, Amsterdam, Netherlands). Images were analyzed using the ImageLab software 6.1.

Protein	Antibody	MW	Dilution
Western Blot			
OPN	Osteopontin [RM1018] rabbit pAb (Abcam) #ab283656	60	1:1000
CD44	CD44 (156-3C11) mouse mAb (Cell Signalling) #3570	80	1:5000
ITGAV	Integrin αV (D2N5H) rabbit mAb (Cell Signalling) #60896	135/140	1:1000
ITGB3	Integrin β3 (D7X3P) XP® rabbit mAb (Cell Signalling) #13166	100	1:1000
β-actin	β-Actin (8H10D10) mouse mAb (HRP Conjugate) (Cell Signalling) #12262	44	1:10000
VEGFR2	VEGF Receptor 2 (D5B1) rabbit mAb #9698	210/230	1:1000
Mouse IGG	Anti-mouse IgG, HRP-linked horse pAb#7076	NA	1:10000
Rabbit IGG	Anti-rabbit IgG, HRP-linked goat pAb #7074	NA	1:10000
Immunohistochemistry			
CD31	CD31 antibody [EPR17259] rabbit mAb (Abcam) #ab182981	NA	1:2000

Table 3. Antibodies. The name, molecular weight, dilution and target of the antibodies used in this study are shown. MW, molecular weight (KDa).

15. qRT-PCR

Total RNA was extracted as indicated in *Nucleic acid extraction* and cDNA was prepared from 200-1000 ng of RNA (patients and cell line samples, respectively) using the High-Capacity cDNA Reverse Transcription Kit (Thermo Scientific, Rockford, IL, USA) according to the manufacturer's instructions. cDNA was amplified using TaqMan Universal PCR mix (Thermo Scientific, Rockford, IL, USA) and *SPP1* (hs00959010_m1), *Ataxin 7 (ATXN7;* hs000165660-m1) and *REXO1 Like 2, Pseudogene (REXO1L2P;* hs05514810-gH) TaqMan assays. Endogenous *SDHA* (hs00188166_m1) was used as reference gene to normalize cycle thresholds (Cts). Relative mRNA expression levels were determined using the $2^{-\Delta\Delta Ct}$ method (292). Quantitative reverse transcription polymerase chain reaction (qRT-PCR) was performed in duplicate using a CFX Opus 96 Real-Time PCR system (BioRad, Herculed, CA, USA).

Alternatively, *SPP1* levels were also evaluated in NET cell lines by retro-transcribing 1000 ng of RNA using the SuperScript IV VILO Master Mix (Thermo Scientific, Rockford, IL, USA) according to the manufacturer's instructions. Next, cDNA was amplified using PowerTrack™ SYBR Green master mix and *SPP1* custom primers (Table 2). Endogenous *GAPDH* was evaluated using custom primers (Table 2) and was used as reference to normalize Cts. Relative mRNA expression levels were also determined using the $2^{-\Delta\Delta Ct}$ method. All reactions were performed in a QuantStudio™ 5 Real-Time PCR system (Thermo Scientific, Rockford, IL, USA). Custom primer where selected from Primer Bank (293).

16. Proliferation assay

Five to ten thousand cells per well were seeded in 96 well plates in 200 μl of the appropriate cell medium. Cell proliferation data was obtained for 24, 48, 72 and 96 hours after seeding. 8 technical replicates were performed by condition. The number of viable cells was determined by the crystal violet method. Briefly, at each time point cells were fixed for 30 minutes at RT with 0.5% glutaraldehyde in PBS (Sigma-Aldrich, San Luis, MO, USA), and then stained with crystal violet (0.5% w/v; Sigma-Aldrich, San Luis, MO, USA) for another 30 minutes at RT. Next, cells were washed with tap water and dried at RT O/N. Finally, the plates were resuspended in acetic acid (Sigma-Aldrich, San Luis, MO, USA) and absorbance was read at 595 nm on a multimode plate reader (VICTOR Nivo, Perkin Elmer, Waltham, MA, USA).

17. Colony formation assay (CFA)

Two hundred and fifty to five hundred cells per well were seeded on 6-well plates. After 9 to 14 days, colonies were fixed for 30 minutes at RT with 0.5% glutaraldehyde in PBS and stained with crystal violet (0.5% w/v), as previously described. After washing and drying, colonies were scanned, and their area and intensity were quantified using the *ColonyArea* plugin for ImageJ (version 6.1), according to the user's manual (294).

18. Migration assay

Ninety thousand cells per well were plated in the upper chamber of an 8-μm transwell plate with 300 μl of the appropriate 1% FBS medium (Corning, Somerville, MA, USA). In the bottom well, 400 μl of 2.5% FBS medium was added as a chemoattractant. Cells were incubated at 37ºC for 24 to 48 hours. Non-migrating cells were removed from the top chamber and migrating cells were quantified using CellTiter-Glo (Promega, Madison, WI, USA) according to manufacturer's instructions.

19. Cell viability assay

Four to seven thousand NET cancer cells were seeded per well in 96-well plates and incubated for 24 hours. The following day, cells were treated with increasing concentrations of axitinib (0-100 μM, Selleck Chemicals, Houston, TX, USA), cabozantinib (0-100 μM, Selleck Chemicals, Houston, TX, USA) or dimethyl sulfoxide (DMSO) for 72 hours. Five thousand HUVEC cells were seeded in 10% OPN OE or

CTRL conditioned medium and subsequently treated with increasing concentrations of axitinib (0-7.5 µM, Selleck Chemicals, Houston, TX, USA), cabozantinib (0-7.5 µM, Selleck Chemicals, Houston, TX, USA) or DMSO. All drugs were dissolved in DMSO for *in vitro* experiments. Viable cells were fixed for 30 minutes at RT with 0.5% glutaraldehyde in PBS, stained with crystal violet and absorbance was measured at 595 nm, as previously described. The half-maximal inhibitory concentration (IC50) for each drug in each cell line was estimated using GraphPad Prism 8.1 (GraphPad, Boston, MA, USA).

20. Matrigel tube formation assay

Nine thousand cells per well were seeded into 40 µl of basement membrane extract (Matrigel, BD Biosciences) in a 96-well plate. HUVEC cells grown in 10% BON-1 OPN OE or CTRL cell medium were treated with either DMSO or 0.1 µM axitinib (Selleck Chemicals, Houston, TX, USA) from the start of the experiment. After 12 to 14 hours, full-well contrast-phase images were captured using an EVOS imaging system (Thermo Scientific, Rockford, IL, USA) at 4x magnification. Images were analyzed with the *angiogenesis analyzer* plugin for Image J (295).

21. Chorioallantoic membrane (CAM) tumour xenografts

<u>Chicken embryo xenografts</u>

Fertilized white Leghorn eggs (embryonic development day 0, ED0) were placed in the hatcher (GCQ, Savannah, GA, USA) and incubated for 4 days at 37ºC with > 70% relative humidity and regular rotation. On ED4, eggs were carefully cracked using a Dremel tool fitted with a sterile cutting disc (Dremel, Mount Prospect, IL, USA). Fertilized embryos eggs were transferred into sterile weight boats (VWR, Radnor, PA, USA) and covered with square Petri dishes as lids (VWR, Radnor, PA, USA). The embryos were then placed back into the incubator set at 37ºC with >70% relative humidity until ED9.

Modified BON-1 CTRL and OPN OE and KD cells were cultured as previously described until 90% confluency. In cells modified with an inducible system, downregulation was induced with doxycycline (1 µg/ml) for 48h prior to engraftment. Cells were harvested in PBS using TryplE (Thermo Scientific, Rockford, IL, USA). Five million cells were mixed with 20 µl of matrigel (Corning, Somerville, MA, USA) and engrafted into each chicken embryo using a pipette. After 72 hours, tumors were visible and topical treatment with 10 µl of DMSO or 3 µM axitinib was applied daily for 6 to 7 days. Additionally, 10 µl of doxycycline (1 µg/ml) was applied topically every other day in models with inducible downregulation. Embryos were monitored daily to prevent contamination.

After 6 to 7 days, tumors were imaged using bright-field and/or fluorescence microscopy to detect GFP. Tumor volume and vascular flow were assessed using high-frequency ultrasound imaging (US; MS700, Fujifilm, Tokyo, Japan). To visualize the endothelium, 50 µl of diluted *lens culinaris agglutinin* (LCA) labeled with DyLight® 649 (1/10; VectorLabs, Newark, CA, USA) were injected intravenously in each embryo using an 18-gauge needle. Volume analysis was performed in VevoLab 5.8.2 software using V_F3 files and 3D reconstruction and parallel rotation analysis.

Tumour fixation

After treatment, chicken embryos were euthanized and tumors were collected and fixed O/N at 4ºC in formaldehyde (Thermo Scientific, Rockford, IL, USA) with gentle rotation. The following day, tumors were washed twice with PBS and incubated O/N at 4ºC in 30% sucrose (MP Biomedicals, Santa Ana, CA, USA). Finally, tumors were embedded in optimal cut temperature (OCT; Thermo Scientific, Rockford, IL, USA) using dry ice and serial 5 µm sections were prepared with a cryostat for hematoxylin/eosin staining and immunofluorescence analysis.

Immunofluorescence

Tumor tissue sections were fixed in methanol for 10 minutes, followed by a PBS wash. Samples were blocked with normal goat serum (NGS; Thermo Scientific, Rockford, IL, USA) and incubated O/N at 4º with primary antibodies diluted in 5% NGS. Sections were washed 5 times with PBS-T (0.02% Triton X-100) before incubation with secondary antibodies and 4′,6-diamidino-2-phenylindole (DAPI), both diluted in 5% NGS. Finally, slides were mounted using VECTASHIELD Vibrance Antifade mounting media (VectoLabs, Newark, CA, USA) and covered with a coverslip. The entire area of all slides was scanned using a ZEISS Axio Observer (Zeiss, Oberkochen, Germany) at 20x magnification. Lectin-positive area (endothelium) was evaluated in at least 8-10 regions of each tumor using QuPath.

22. Cell line-derived xenografts mouse models (CDX)

All animal procedures were approved by Comunidad de Madrid (PROEX 302.0/23) and the Animal Care and Use Committee of Hospital Universitario 12 de Octubre (CEIM19/538) and conducted according to the institutional guidelines of Hospital Universitario 12 de Octubre for biomedical research involving animals.

Cell line-derived xenograft (CDX) models were performed in 4–6-week-old athymic nude mice (Crl:NU(NC$_r$)-*Foxn1*^{nu}, Charles River Laboratories, Wilmington, MA, USA). Briefly, 1 million cells embedded in 50% matrigel (Corning, Somerville, MA, USA) and PBS, were subcutaneously injected into the flank of female athymic nude mice. Tumor volume was monitored three times a week using a digital caliper and calculated using the following formula: (smaller measure)^2 x large measure x 0.52. When tumor volume reached 150 mm^3, mice were randomized into different treatment groups: axitinib (25-40 mg/kg/day), sunitinib (20-40 mg/kg/day), cabozantinib (15-30 mg/kg/day) and vehicle. For *in vivo* studies, drugs were prepared freshly daily according to the datasheets using the following solvent: 100-200 µl of 50% H_2O, 40% PEG300, 5% Tween 80, 5% DMSO. All treatments were administered intraperitoneally five days a week for a total of 20 doses (Figure 11). Signs of toxicity were monitored (weight loss, behavior) and mice were weighed twice a week. After 20 treatment doses, mice were euthanized, and tumors, liver, spleen, kidneys and skin were collected for histological analysis. Finally, a fragment of the tumor was also cut and snap-frozen in liquid nitrogen and stored at -80ºC.

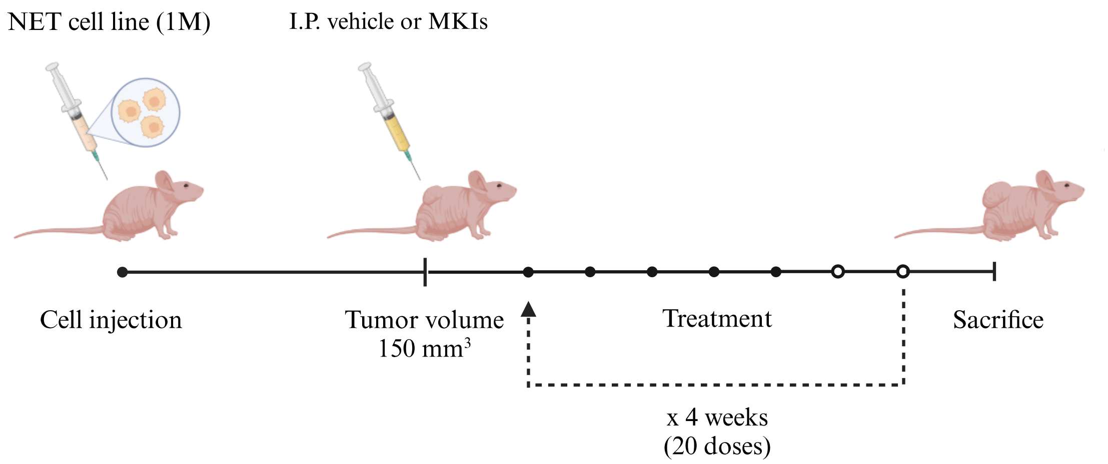

Figure 11. Scheme summarizing the CDX mouse experiments. Human NET cell lines were subcutaneously injected into the flank of athymic nude mice. When the tumor reached 150 mm^3, treatment started and consisted of 20 intraperitoneal doses of MKI or vehicle. Mice wellness and weight were tracked

to monitor toxicity, and tumor volume was measured regularly. MKIs, multi-kinase inhibitor. I.P., intraperitoneally. Filled dot, treatment day. Empty dot, rest day.

23. Histological analysis

For histological analysis, tumors were harvested and fixed in 10% buffered formalin within 30 minutes of resection. After 24h, samples were sent to the histopathology unit of CNIO, where they underwent dehydration, clearing and paraffin embedding. Next, 3 μm sections were obtained using a microtome and mounted on a superfrost plus slide, and were let to dry O/N. H/E staining and CD31 IHC were performed following standardized protocols at the CNIO histopathology Unit (Table 3).

24. Statistical analysis

Descriptive statistics were used to characterize most relevant parameters. Data was presented as mean ± SD of at least 3 independent experiments. Normality was assessed for all datasets using D'Agostino & Pearson omnibus test. The distribution of quantitative variables among study groups was evaluated using parametric (Student's t-test or ANOVA) and nonparametric (Kruskal–Wallis or Mann–Whitney) tests, along with their respective post-hoc analyses, as appropriate. Violin plots representing medians and quartiles, or scatter dot plots showing means and SD were used for data visualization. Graphs and analysis were performed in R or GraphPad Prism 8.1 (GraphPad, Boston, MA, USA). Correlation analysis was performed with parametric (Pearson) and nonparametric (Spearman) tests after logarithmic normalization. Dispersion plots were represented in GraphPad Prism 8.1 (GraphPad, Boston, MA, USA). Enrichments in categorical variables were analyzed using Fisher's exact test or Chi-square test, as appropriate, in GraphPad Prism 8.1 (GraphPad, Boston, MA, USA). Cox multivariable proportional hazards models were used to confirm the independent predictive value of the biomarkers, adjusting for other relevant and potentially confounding clinical variables. This analysis was performed using the R packages *survival* and *survminer* and forest plots were generated using *forestmodel.* Receiver operating characteristic (ROC) analysis was performed in R using the *ROCit* package. Patients with at least 12 months of PFS were classified as responders. The optimal threshold for distinguishing between responders and non-responders was determined using Youden Index. Both the sensitivity and specificity, along with the ROC curve, were represented. Unless otherwise specified a $p < 0.05$ was considered significant for all statistical analyses. *P-values* were corrected, when appropriate, for multiple testing using the Benjamini–Hochberg procedure, and an *FDR* ≤ 0.05 was considered statistically significant. The following symbols were used to denote statistical significance: *ns, non-significant*. *, $p < 0.05$. **, $p < 0.01$. ***, $p < 0.001$.

RESULTS

Results

Aim 1. To identify a transcriptomic signature associated with tumor response and PFS in tumor samples from NET patients enrolled in the AXINET trial treated with axitinib

1. A 3-gene signature (*REXO1L2P*, *ATXN7* and *SPP1*) predicts efficacy of axitinib in NETs

1.1 *SPP1*, *REXO1L2P* and *ATXN7* expression is associated with PFS and tumor shrinkage in NETs treated with axitinib

The first objective of this project was to identify axitinib predictive biomarkers in NETs. To do so, we first analyzed 126 G1-G2 EP-NET patients from the 256 patients enrolled in the AXINET trial who had FFPE tumor samples available for translational studies. Gene expression analysis was performed in tumor samples of 62 patients treated with axitinib and SSA, and of 64 patients treated with placebo and SSA (Table 4). Clinicopathological characteristics of the gene expression cohort were consistent with those of the entire AXINET study population. No significant differences were observed, except for a higher proportion of younger patients (< 65 years) in the placebo-treated group of the gene expression cohort compared to the entire AXINET cohort (*OR: 0.38, $p = 0.036$*) (Table 4).

We analyzed the association between gene expression and centrally reviewed PFS, using the latter as a surrogate marker of therapeutic benefit. To identify biomarkers specifically predictive of axitinib treatment benefit, we conducted the analysis separately in the two treatment cohorts: patients treated with axitinib + SSA in the experimental arm, and patients treated with placebo + SSA who served as controls (Figure 12A). We identified 20 genes exclusively associated with PFS in axitinib-treated patients ($p < 0.01$) (Figure 12A). Of these, 10 genes were associated with increased risk of progression ($HR > 1$), while the other 10 were linked to a decreased risk of progression ($HR < 1$) (Figure 12B). However, significance was not maintained after adjustment for multiple testing ($FDR < 0.05$) (Supplementary Table 1). A total of 261 genes were significantly associated with PFS in placebo-treated patients ($p < 0.05$) (Figure 12A; Supplementary Table 2). Notably, none of these genes overlapped with those identified in the axitinib-treated group, indicating that the 20 genes identified may be specifically associated with axitinib treatment benefit (Figure 12A).

Clinical characteristics N (%)		AXINET cohort (N = 256)		Discovery				Validation	
				Tumor sample (Gene expression)		Plasma sample (Elisa)		Plasma sample (Elisa)	
		Axitinib (N = 126)	Placebo (N = 130)	Axitinib (N = 62)	Placebo (N = 64)	Axitinib (N = 52)	Placebo (N = 54)	Axitinib (N = 43)	Placebo (N = 44)
Sex	Female	55 (43.7)	63 (48.5)	30 (48.4)	30 (46.9)	27 (51.2)	26 (48.1)	17 (39.5)	23 (52.3)
	Male	71 (56.3)	67 (51.5)	32 (51.6)	34 (53.1)	25 (48.8)	28 (51.9)	26 (60.5)	21 (47.7)
Age	≥ 65 years	33 (26.2)	28 (21.5)	17 (27.4)	6 (9.4)	13 (25.0)	5 (9.2)	16 (37.2)	14 (31.8)
	< 65 years	93 (73.8)	102 (78.5)	45 (72.6)	58 (90.6) *	39 (75.0)	49 (90.8)	27 (62.8)	30 (68.2)
Time since diagnosis	< 12 months	56 (44.4)	51 (39.2)	27 (43.6)	24 (37.5)	22 (42.3)	19 (35.2)	22 (51.2)	20 (45.5)
	≥ 12 months	70 (55.6)	79 (60.8)	35 (56.4)	40 (62.5)	30 (57.7)	35 (64.8)	21 (48.8)	24 (54.5)
Functional syndrome	Yes	41 (32.5)	31 (23.8)	22 (35.6)	13 (20.3)	18 (34.6)	10 (18.5)	15 (34.9)	12 (27.3)
	No	85 (67.4)	99 (76.1)	40 (64.5)	51 (79.7)	34 (65.4)	44 (81.5)	28 (65.1)	32 (62.7)
Location	Small intestine	61 (48.4)	61 (46.9)	30 (48.4)	31 (48.4)	27 (51.9)	27 (50.0)	22 (51.2)	21 (47.7)
	Lung	36 (28.6)	34 (26.1)	21 (33.9)	16 (25.0)	14 (27.0)	13 (24.1)	11 (25.6)	9 (20.5)
	GI other	16 (12.7)	13 (10.0)	7 (11.3)	12 (18.8)	7 (13.5)	9 (16.6)	6 (13.9)	5 (11.4)
	Unknown	9 (7.1)	15 (11.5)	3 (4.8)	4 (6.2)	3 (5.7)	4 (7.4)	4 (9.3)	8 (18.2)
	Other	4 (3.2)	7 (5.5)	1 (1.6)	1 (1.6)	1 (1.9)	1 (1.9)	0 (0.0)	1 (2.2)
Biopsy site	Primary	49 (38.9)	52 (40.0)	29 (46.8)	29 (45.3)	-	-	-	-
	Metastasis	51 (40.5)	52 (40.0)	24 (38.7)	27 (42.2)	-	-	-	-
	NA	26 (20.6)	26 (20.0)	9 (14.5)	8 (12.5)	-	-	-	-
Grade	G1	27 (21.4)	45 (34.6)	15 (24.2)	20 (31.3)	14 (27.0)	19 (35.2)	8 (18.6)	17 (38.6)
	G2	97 (77.0)	83 (63.8)	45 (72.6)	44 (68.7)	36 (69.2)	34 (62.9)	35 (81.4)	26 (59.0)
	G3	2 (1.6)	2 (1.6)	2 (3.2)	0 (0.0)	2 (3.8)	1 (1.9)	0 (0.0)	1 (2.3)
Prior lines of treatment (N)	0	55 (43.7)	62 (47.7)	22 (35.5)	30 (46.9)	22 (42.3)	26 (48.1)	18 (41.9)	18 (40.9)
	1	52 (41.3)	43 (33.1)	30 (48.4)	24 (37.5)	21 (40.4)	23 (45.6)	18 (41.9)	21 (47.7)
	2+	14 (11.1)	22 (16.9)	9 (14.5)	10 (15.6)	9(17.3)	5 (9.3)	7 (16.2)	5 (11.4)
	NA	5 (4.0)	3 82.3)	1 (1.6)	0 (0.0)	0 (0.0)	0 (0.0)	0 (0.0)	0 (0.0)
RECIST (Central)	CR	2 (1.6)	0 (0.0)	2 (3.2)	0 (0.0)	2 (3.8)	0 (0.0)	0 (0.0)	0 (0.0)
	PR	13 (10.3)	4 (3.1)	7 (11.3)	3 (4.7)	4 (7.8)	2 (3.7)	4 (9.3)	1 (2.3)
	SD	98 (77.7)	109 (83.8)	50 (80.6)	54 (84.4)	43 (82.7)	46 (85.2)	35 (81.4)	39 (88.6)
	PD	1 (0.8)	12 (9.2)	0 (0.0)	7 (10.9)	0 (0.0)	6 (11.1)	1 (2.3)	3 (6.8)
	NA	12 (9.5)	5 (3.9)	3 (4.8)	0 (0.0)	3 (5.7)	0 (0.0)	3 (7.0)	1 (2.3)
PFS (Central)	median (min - max)	16.6 (0.03 - 100)	9.9 (0.03– 96.7)	19.9 (0.03 – 94)	11.0 (0.03 – 96)	24.2 (0.03 – 94)	10.9 (0.03 – 96)	17.5 (2.0 – 86.9)	13.1 (0.03 – 81)

Table 4. Clinicopathological characteristics of patients from the AXINET trial. The clinicopathological characteristics of the AXINET discovery and validation cohorts are shown based on sample availability and technique used. Total numbers and percentages are shown. * Indicates significant enrichment.

To confirm whether the association of these 20 genes with PFS differed between axitinib-treated and placebo-treated patients, we performed an interaction test for each candidate gene and the treatment arm. Nine genes exhibited a significantly different association with PFS between the two treatments: *PLEK, B3GALT6, CUBN, REXO1L2P, RPS10-NUDT3, SLC30A9, ATXN7, PIGG* and *ANKZF1*. Additionally, *SPP1* and *MX2* showed a clear trend toward a different association, and although they did not reach statistical significance, they were retained as potential predictive biomarkers (Supplementary Table 3).

Next, we studied the role of the 11 candidate genes in tumor shrinkage to identify those with a consistent association with therapeutic benefit. To do this, we developed a regularized linear regression model, using the expression of the 11 genes candidate genes as the explanatory variable and the best tumor regression as the outcome variable (Supplementary Figure 3A). This model enabled the selection of genes that more effectively explain tumor regression in response to axitinib, minimizing redundant information and reducing the number of variables in the signature. The model with the lowest mean squared error ($\lambda\ min = 7.53$) included 3 genes: *SPP1* (*coef: 1.84*), *REXO1L2P* (*coef: 2.95*) and *ATXN7* (*coef: -1.48*), which were associated with both PFS and tumor shrinkage in response to axitinib (Supplementary Figure 3A). Moreover, gene expression of *SPP1* ($r = 0.32; p = 0.015$), *REXO1L2P* ($r = 0.26; p = 0.016$) and *ATXN7* ($r = -0.31; p = 0.044$) significantly correlated with tumor shrinkage in axitinib-treated patients, but not in placebo-treated patients (Figure 12C). Finally, pairwise Spearman correlation analysis confirmed that these genes provided independent, non-redundant information, as no significant correlation was observed (Supplementary Figure 3B).

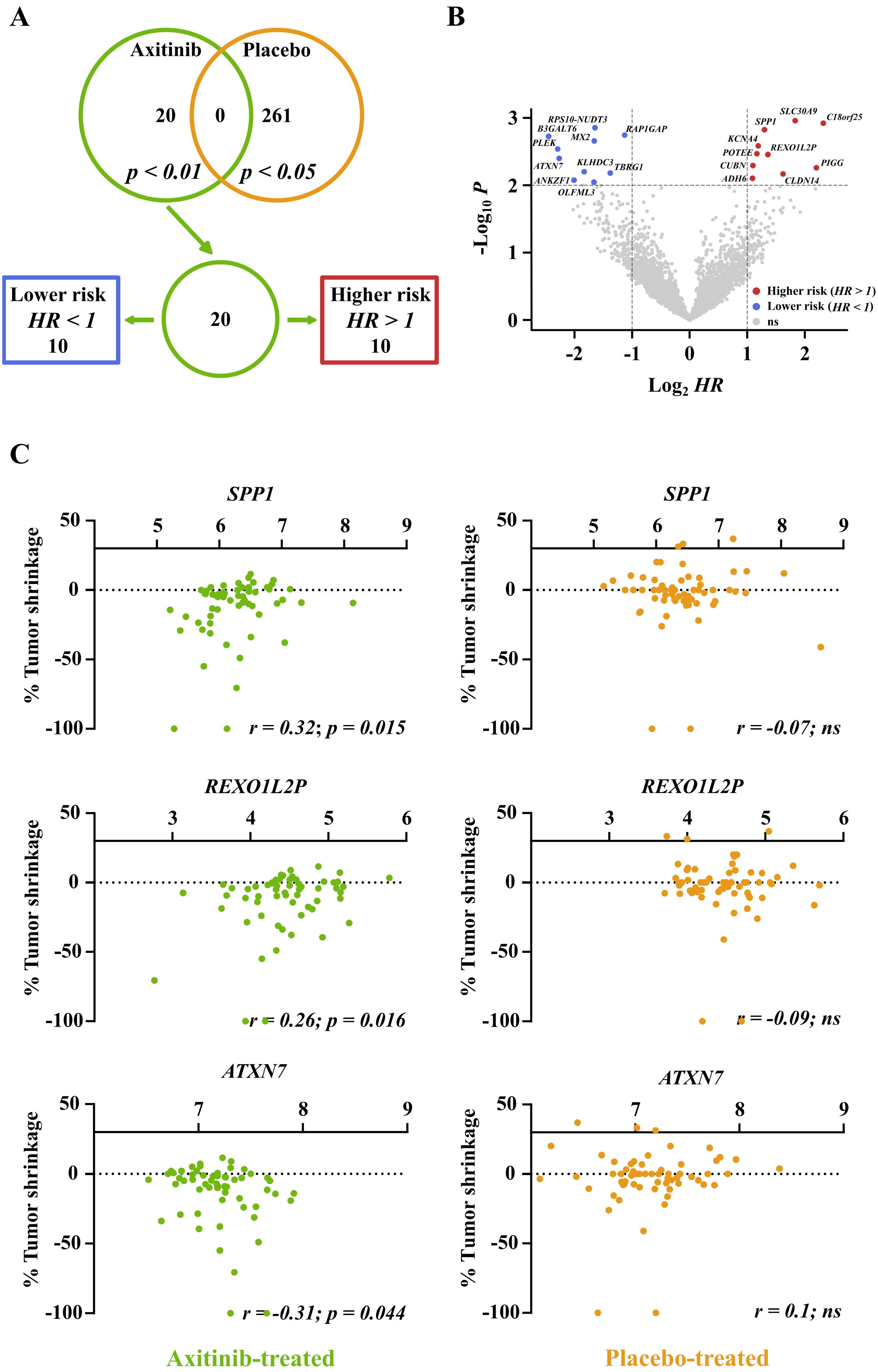
A
Axitinib
Placebo
20
0
261
p < 0.01
p < 0.05
Lower risk
HR < 1
10
20
Higher risk
HR > 1
10
B
-Log10 P
Log2 HR
RPS10-NUDT3
B3GALT6
PLEK
MX2
RAP1GAP
ATXN7
KLHDC3
TBRG1
ANKZF1
OLFML3
SLC30A9
C18orf25
SPP1
KCNA4
REXO1L2P
POTEE
CUBN
PIGG
ADH6
CLDN14
Higher risk (HR > 1)
Lower risk (HR < 1)
ns
C
SPP1
REXO1L2P
ATXN7
% Tumor shrinkage
r = 0.32; p = 0.015
r = -0.07; ns
r = 0.26; p = 0.016
r = -0.09; ns
r = -0.31; p = 0.044
r = 0.1; ns
Axitinib-treated
Placebo-treated

Figure 12. ***SPP1*, *REXO1L2P* and *ATXN7* are associated with PFS and tumor shrinkage in axitinib-treated NETs. A.** Cox regression analysis was performed to study the association between genes and PFS. The analysis was performed separately in patients treated with axitinib + SSA (green) and placebo + SSA (orange). Twenty genes were significantly associated with PFS in axitinib-treated patients ($p < 0.01$), 10 were associated with decreased ($HR < 1$, blue) and 10 with increased ($HR > 1$, red) risk of progression. Two-hundred sixty-one genes were significantly associated with PFS in placebo-treated patients ($p < 0.05$). None of the genes were associated with PFS in both study arms. **B.** Volcano plot including the 5000 genes with highest MAD is shown. The $\log_2$ (*HR*) is represented in the x-axis while the –log (*p-value*) is shown in the y-axis. The 20 genes that were significantly associated with PFS in axitinib-treated patients are highlighted. **C.** Spearman correlation analysis was performed to confirm the association between the expression of the 3 candidate genes and tumor shrinkage. The analysis was performed separately in patients treated with axitinib + SSA (green) and placebo + SSA (orange). Gene expression is shown in the x-axis whereas percentage of tumor shrinkage is shown in the y-axis. The *r* spearman coefficient is represented. *SPP1*, *REXO1L2P* and *ATXN7* were significantly correlated with tumor shrinkage in axitinib-treated patients, but not in placebo-treated patients. *Ns, non-significant*. A $p < 0.05$ was considered statistically significant. MAD, median absolute deviation. *HR, hazard ratio*.

1.2 A 3-gene signature is significantly associated with PFS and tumor shrinkage exclusively in axitinib-treated patients

Once we identified the 3 best predictive genes of response to axitinib therapy, we used the *singscore* R package to combine their individual expression levels into a single numerical score for each patient. Next, we classified patients as having a high or low signature score. To do so, ROC analysis was conducted to assess the accuracy of model predictions and determine the optimal score cutoff threshold. Patients were classified as non-responders if they progressed within 12 months of axitinib treatment, while responders were defined as those with a PFS greater than 12 months. This threshold was based on the median PFS of the placebo-arm (10 months), considering an incremental gain greater than 2 months as clinically relevant. The ROC analysis identified a cutoff of 0.466, yielding an AUC of 0.718, with a false positive rate of 87% and a true positive rate of 46% (Supplementary Figure 4A). Since the optimal cutoff value was very close to the median, the median was retained as the threshold. Thus, each patient was classified as having a high or low score, based on the median score value of the study population (median score = 0.415). The signature score and the individual expression of *SPP1*, *REXO1L2P* and *ATXN7* in the patients are represented in Figure 13A.

To evaluate the predictive capacity of the 3-gene signature in the discovery cohort, we performed Cox regression analysis separately for axitinib-treated and placebo-treated patients, using the signature score and PFS. The 3-gene signature was significantly associated with PFS in axitinib-treated patients (*HR:* $7 \cdot 10^{-4}$ *(*$3.21 \cdot 10^{-5}$ *– 3.73),* $p < 0.001$), but not in placebo-treated patients (*HR: 0.369 (0.037 – 3.73),* $p = 0.398$). Additionally, a significant interaction was observed between the signature and treatment arm of the study (*HR:* $4.83 \cdot 10^{-3}$ *(*$1.12 \cdot 10^{-4}$ *– 0.20),* $p = 0.005$), confirming that the association between the signature score and PFS is dependent on the treatment. Consistently, Cox regression analysis using the high- and low-score groups defined by the 3-gene signature levels showed that axitinib-treated patients with high scores had significantly better PFS than those with low scores (38.5 vs. 11.6 months; *HR: 0.31 (0.16 – 0.59),* $p < 0.001$) (Figure 13B). Notably, an opposite, non-significant trend was observed in placebo-treated patients with high- and low-signature scores (8.8 vs. 12 months; *HR: 1.51 (0.86 – 2.63),* $p = 0.21$) (Figure 13B).

Next, we analyzed maximum tumor shrinkage in high- and low-score patients and observed that axitinib-treated patients with high scores had significantly increased tumor shrinkage compared to those with low scores (-10.6% vs. -1.0%, respectively, $p = 0.004$) (Figure 13C). Conversely, placebo-treated patients with high scores had significantly decreased tumor shrinkage compared to those with low score (-3.5% vs. -0.0%, respectively, $p = 0.01$) (Figure 13C). Waterfall plots of axitinib- and placebo-treated patients with high- and low-signature scores have been represented in Supplementary Figure 5A. To further confirm the association between the signature score and tumor shrinkage, we performed Spearman correlation tests between tumor shrinkage and the score in axitinib- and placebo-treated patients. The score exhibited a significant negative correlation with tumor shrinkage in axitinib-treated patients ($r = -0.46$, $p < 0.001$), while no significant correlation was observed in placebo-treated patients ($r = 0.21$, $p = 0.11$) (Supplementary Figure 5B).

Moreover, patients predicted to respond to axitinib (high signature score) had significantly better PFS when treated with axitinib compared to placebo (*HR: 0.32 (0.17 – 0.60),* $p < 0.001$) (Figure 13D). In contrast, no significant PFS difference between treatment arms was observed in patients with a low signature score, confirming the predictive capacity of the 3-gene signature (*HR: 1.49 (0.84 – 2.65),* $p = 0.17$) (Figure 13D).

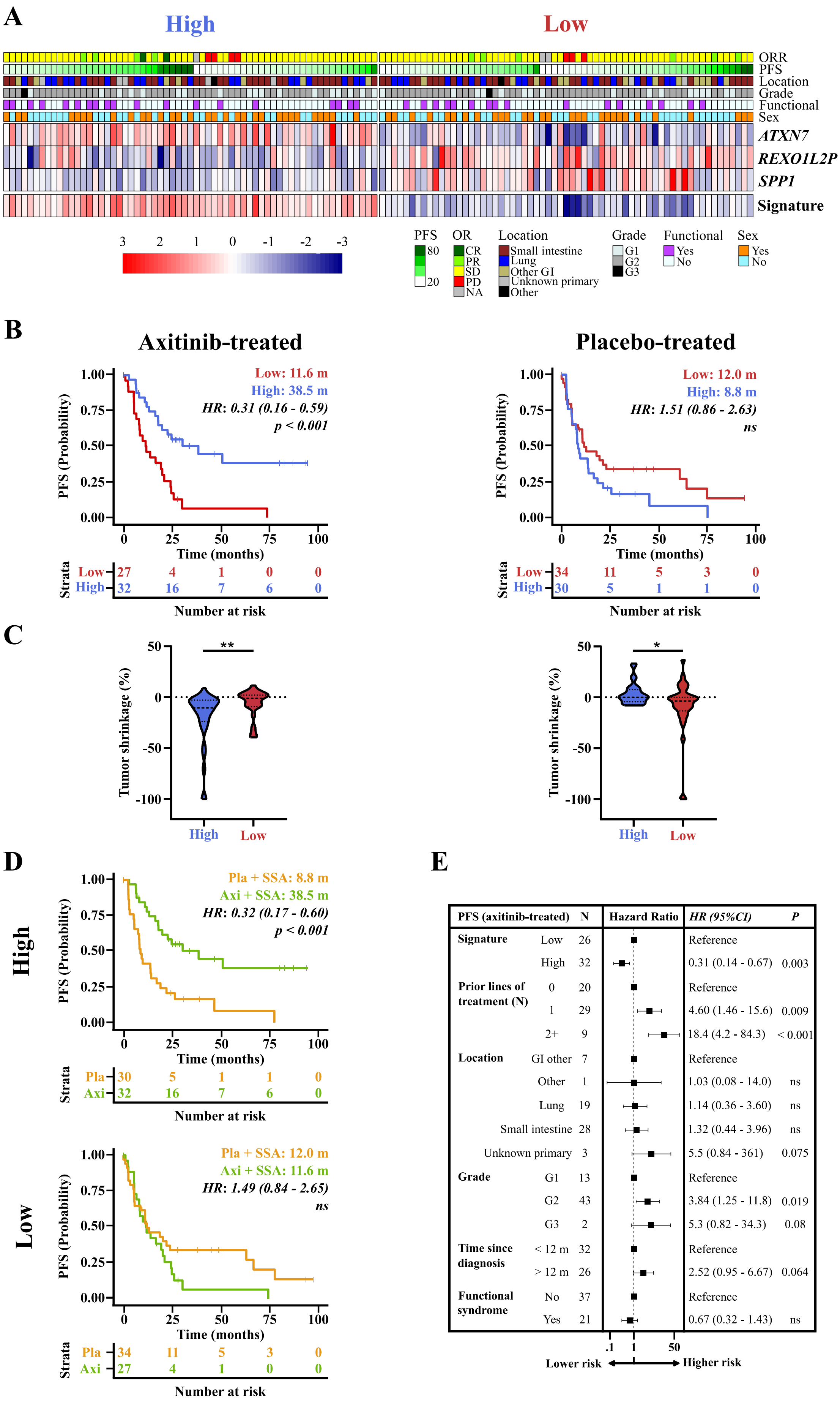
A
High
Low
ORR
PFS
Location
Grade
Functional
Sex
ATXN7
REXO1L2P
SPP1
Signature
3 2 1 0 -1 -2 -3
PFS 80 20
OR CR PR SD PD NA
Location Small intestine Lung Other GI Unknown primary Other
Grade G1 G2 G3
Functional Yes No
Sex Yes No
B
Axitinib-treated
Low: 11.6 m
High: 38.5 m
HR: 0.31 (0.16 - 0.59)
p < 0.001
Placebo-treated
Low: 12.0 m
High: 8.8 m
HR: 1.51 (0.86 - 2.63)
ns
PFS (Probability)
Time (months)
Strata
Low 27 4 1 0 0
High 32 16 7 6 0
Low 34 11 5 3 0
High 30 5 1 1 0
Number at risk
C
Tumor shrinkage (%)
**
*
High
Low
D
High
Pla + SSA: 8.8 m
Axi + SSA: 38.5 m
HR: 0.32 (0.17 - 0.60)
p < 0.001
Pla 30 5 1 1 0
Axi 32 16 7 6 0
Low
Pla + SSA: 12.0 m
Axi + SSA: 11.6 m
HR: 1.49 (0.84 - 2.65)
ns
Pla 34 11 5 3 0
Axi 27 4 1 0 0
Number at risk
E
PFS (axitinib-treated) N Hazard Ratio HR (95%CI) P
Signature Low 26 Reference
High 32 0.31 (0.14 - 0.67) 0.003
Prior lines of treatment (N) 0 20 Reference
1 29 4.60 (1.46 - 15.6) 0.009
2+ 9 18.4 (4.2 - 84.3) < 0.001
Location GI other 7 Reference
Other 1 1.03 (0.08 - 14.0) ns
Lung 19 1.14 (0.36 - 3.60) ns
Small intestine 28 1.32 (0.44 - 3.96) ns
Unknown primary 3 5.5 (0.84 - 361) 0.075
Grade G1 13 Reference
G2 43 3.84 (1.25 - 11.8) 0.019
G3 2 5.3 (0.82 - 34.3) 0.08
Time since diagnosis < 12 m 32 Reference
> 12 m 26 2.52 (0.95 - 6.67) 0.064
Functional syndrome No 37 Reference
Yes 21 0.67 (0.32 - 1.43) ns
.1 1 50
Lower risk
Higher risk

Figure 13. The 3-gene signature predicts efficacy to axitinib in NETs. A. A supervised heatmap of patients with high and low signature scores is represented. The scaled expression of the 3 genes of the signature -*SPP1*, *REXO1L2P* and *ATXN7*-, along with the signature score are shown. Red and blue represent high and low expression, respectively. Patients with high signature scores had high expression of *ATXN7* and low expression of *SPP1* and *REXO1L2P*. An opposite pattern was observed in the low signature score group. ORR, PFS, primary tumor location, grade, carcinoid syndrome and sex were annotated for each patient. No enrichment in clinical characteristics was observed in high or low score groups. **B.** Kaplan-Meier curves of patients with high- (blue) or low- (red) signature scores are shown for axitinib- and placebo-treated patients of the AXINET trial. Median PFS of each group, the HR, 95%CI and *p-value* of the Cox model are shown. The number of patients at risk per group is also represented in the table. Axitinib-treated patients with high scores had significantly better PFS than patients with low scores. No significant differences by signature score were observed in placebo-treated patients. **C.** Tumor shrinkage percentage was compared between patients with high- (blue) and low- (red) signature scores in the axitinib and placebo arms of the trial. Again, axitinib-treated patients with high scores had significantly increased tumor shrinkage compared to those with low scores, while the opposite was observed in placebo-treated patients. **D.** Kaplan-Meier curves of patients with high- or low- signature scores treated with axitinib (green) or placebo (orange) are represented. Patients predicted to respond to axitinib (high score) had significantly better PFS when treated with axitinib compared to placebo. In contrast, no significant PFS difference between treatment arms was observed in patients with a low signature score. **E.** Multivariable analysis of PFS was performed to confirm the independent predictive capacity of the signature. The *HR*, *95%CI* and *p-value* of the Cox model for the signature and other clinically relevant variables are shown. The signature, the number of previous lines of treatment and grade are independent predictors of PFS in axitinib-treated patients. *Ns, non-significant*. * $p < 0.05$, ** $p < 0.01$ and *** $p < 0.001$ were considered statistically significant.

Finally, a multivariable Cox regression model was conducted to evaluate the independent predictive value of the 3-gene signature on PFS, adjusted for tumor grade, primary tumor location, presence or not of carcinoid syndrome, time since diagnosis and the number of prior lines of therapy. The 3-gene signature remained a significant independent predictive biomarker of axitinib benefit in terms of PFS, both when the signature score was used as a continuous variable (*HR:* $4.02 \cdot 10^{-4}$ $(6.67 \cdot 10^{-6} - 0.024)$, $p < 0.001$) (Supplementary Table 4) and when used as a categorical variable classifying patients into high- and low-score groups (*HR: 0.31 (0.14 - 0.67,* $p = 0.003$) (Figure 13E). Additionally, multivariable analysis showed that tumor grade, time since diagnosis and the number of previous lines of therapy were also independent predictors of axitinib antitumor effect (Figure 13E). On the contrary, the signature was not associated with PFS in the placebo arm (Supplementary Figure 5C and Supplementary Table 4).

Aim 2: To characterize the distinctive molecular features of NETs that benefit from axitinib

2. NETs that do not respond to axitinib are enriched in pathways and cell populations involved in treatment resistance

First, we explored potential associations between high- and low-signature score patients and relevant clinical and molecular variables, including age, gender, grade, Ki-67 index, primary tumor location, carcinoid syndrome, biopsy site, time since diagnosis and number of previous lines of treatment. No significant associations were identified (data not shown).

Subsequently, we performed a differential expression analysis between patients with high- and low-signature score using *limma* R package. We identified 1204 genes that were differentially expressed ($p < 0.05$) between the groups, although only 3 genes retained statistical significance after correction for multiple testing (Supplementary Table 5). As expected, these 3 genes were *SPP1*, *REXO1L2P* and *ATXN7*, which are part of the signature used to stratify high- and low-score groups. Patients with high signature scores showed elevated *ATXN7* expression (*logFC = 0.42, FDR < 0.001*), while low-score patients exhibited higher levels of *REXO1L2P* (*logFC = -0.42, FDR = 0.002*) and *SPP1* (*logFC = -0.58, FDR = 0.006*) (Figure 13A).

We then used GSEA to investigate the potential enrichment of molecular pathways in patients with high- and low- signature scores. Thirty eight molecular pathways were significantly enriched in low-score patients (Supplementary Table 6), including cadherin binding (*NES = -1.40, FDR = 0.02*), hypoxia (*NES = -1.61, FDR = 0.003*), glycolysis (*NES = -1.67, FDR = 0.001*), angiogenesis (*NES = -2.25, FDR < 0.001*), mTORC1 signaling (*NES = -1.73, FDR < 0.001*), extracellular matrix (ECM) receptor interaction (*NES = -2.11, FDR < 0.001*) and EMT (*NES = -2.79, FDR < 0.001*) (Figure 14A). Conversely, only Notch signaling pathway was significantly enriched in high-score patients (*NES = 1.85, FDR = 0.008*) (Figure 14A).

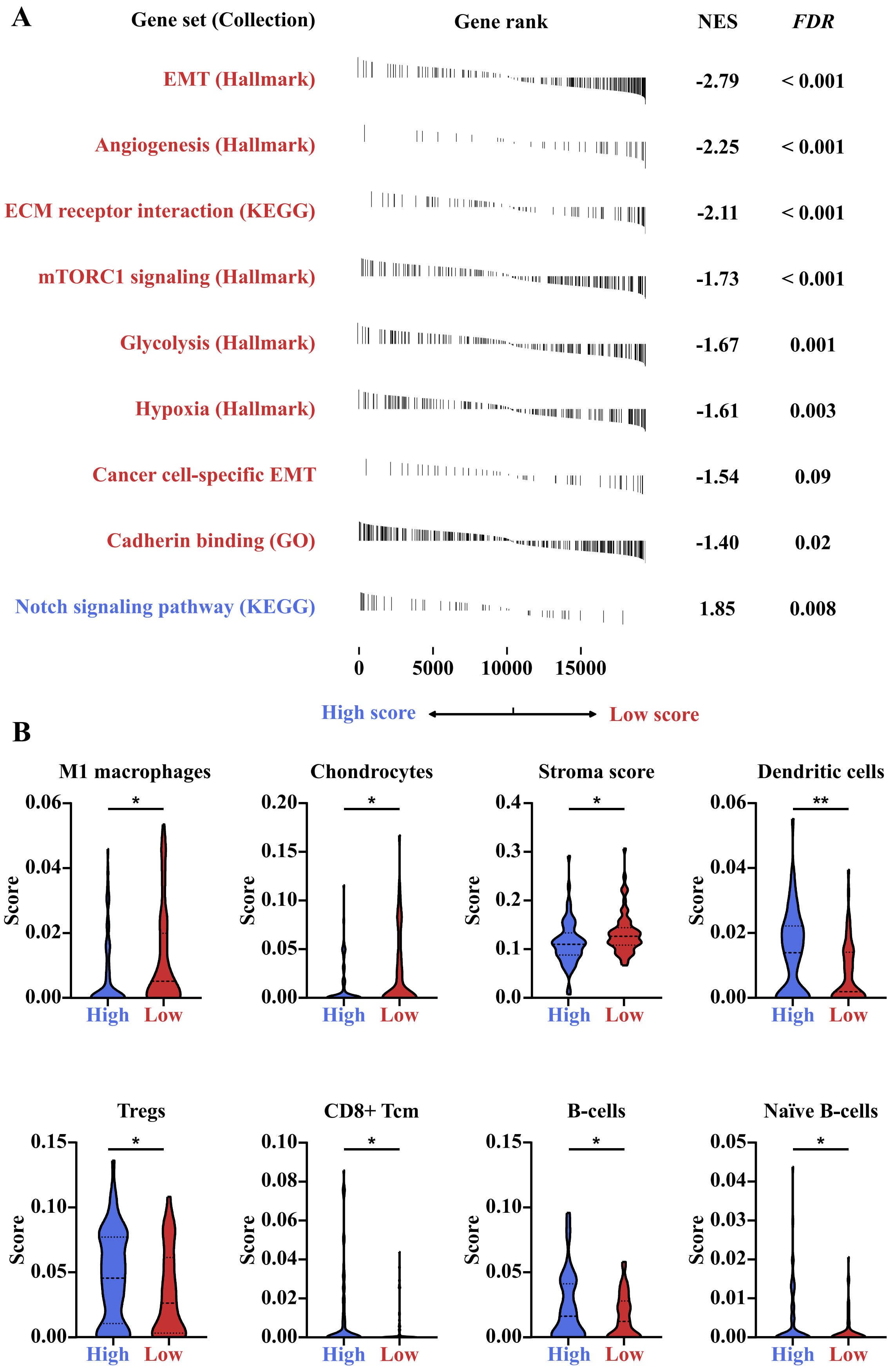

Figure 14. NETs that do not respond to axitinib are enriched in pathways and cell populations involved in treatment resistance. A. Gene set enrichment analysis was performed between patients with

high- and low- signature scores to identify the molecular pathways involved in the differential response to axitinib. Some of the most relevant significantly enriched gene sets are shown. Enrichment plots, NES and *FDR* are shown. Only the Notch signaling pathway was significantly enriched in patients with high scores (blue). Conversely, cadherin binding, hypoxia, glycolysis, angiogenesis, mTORc1 signaling, ECM receptor interaction and EMT were significantly enriched in patients with low scores of the signature (red). Accordingly, the cancer cell-specific EMT signature was also significantly enriched in patients with low signature scores. An $FDR < 0.05$ was considered statistically significant. **B.** Gene expression data was used to calculate the scores of 64 immune and stromal populations. Differential expression analysis was then performed between patients with high- and low- signature scores to identify populations involved in the response to axitinib. The score of each population is represented in the y-axis for patients with high (blue) and low (red) scores of the signature. Five immune populations were upregulated in high-score patients including dendritic cells, B and naïve B cells, T regulatory cells and central memory CD8 positive cells. Two immune populations were upregulated in low-score patients including M1 macrophages and chondrocytes. Additionally, the overall stromal score was also upregulated in low-score patients. * $p < 0.05$ and ** $p < 0.01$ were considered statistically significant. EMT, epithelial to mesenchymal transition; ECM, extracellular matrix; Treg, T regulatory cell; CD8+ Tcm, central memory CD8 positive cells.

EMT, a well-known mechanism of resistance to antiangiogenic therapy, was the most significantly enriched pathway in low-score patients. However, many genes in this pathway are also associated with fibroblasts, which are also comprised in the bulk gene expression analysis. To address this, we analyzed tumor-specific EMT genes as described by Tyler and Tirosh *et al*. (288). Interestingly, we observed a significant enrichment of this tumor-specific EMT signature in low-score patients ($NES = -1.54$, $FDR = 0.09$) (Figure 14A). Notably, *CD44* and *integrin αv (ITGAV)*, which are receptors of *SPP1*, were part of this EMT signature, further supporting the role of *SPP1* in axitinib resistance through EMT.

The mechanisms of resistance to antiangiogenic therapy also involve cell populations of the tumor microenvironment such as macrophages, endothelial cells or fibroblasts (296). To analyze their role in our study, we performed cell type enrichment analysis in xCell which showed that dendritic cells ($logFC = 0.92$, $p = 0.001$), naive B-cells ($logFC = 1.52$, $p = 0.023$), B-cells ($logFC = 0.60$, $p = 0.037$), CD8+ Tcm ($logFC = 1.42$, $p = 0.026$) and Tregs ($logFC = 0.43$, $p = 0.049$) were enriched in high-score patients, whereas chondrocytes ($logFC = -1.08$, $p = 0.018$) and M1 macrophages ($logFC = -0.76$, $p = 0.046$) were enriched in low-score patients. However, no significant differences were obtained after multiple testing correction (Figure 14B and Supplementary Table 7).

Interestingly, low-score patients also had significantly increased stroma score (*logFC = -0.23, p = 0.016*) compared to high-score patients, further supporting the role of the stroma in the response to angiogenesis inhibitors such as axitinib (Figure 14B).

Aim 3: To validate tumor predictive biomarkers identified in external cohorts of GEP-NET patients treated with other antiangiogenic MKIs

3. The 3-gene signature predicts efficacy of sunitinib in an external cohort of NET patients

To validate the external predictive value of the signature, we explored it in an independent cohort of NET patients treated with MKIs. For this purpose, we first obtained transcriptomic data from a cohort of 29 NETs patients treated at our institution Hospital 12 de Octubre according to the standard of care. This cohort included 11 patients treated with sunitinib within the approved indication (Pan-NETs), or sunitinib/axitinib given on compassionate use, and 18 patients treated with SSA. The clinical characteristics of these patients are summarized in Table 5. Compared to the AXINET cohort, the patients in the H12O cohort treated with MKIs were enriched in pancreatic primary tumors (73%; $p < 0.001$) and were more highly pretreated, with more than 50% of patients having received > 2 lines of treatment prior to the MKI ($p = 0.013$). The 18 NET patients treated with SSA served as a control group. Compared to placebo-treated AXINET patients, this group was enriched in G1 tumors (50%, $p = 0.17$) and in treatment-naïve patients, with almost 90% of them receiving SSA as their first line of therapy ($p = 0.006$) (Table 5).

Following the same pipeline applied in the AXINET discovery cohort, we calculated the signature score based on the expression of *REXO1L2P*, *ATXN7* and *SPP1* genes. Patients were then stratified into high- and low-signature score groups according to the median value of the cohort (median score = 0.359) (Figure 15A). The signature was associated with PFS in MKI-treated patients (*HR: 0.00021* $(2.99 \cdot 10^{-8} – 1.51)$, $p = 0.06$), but not in SSA-treated patients (*HR: 0.23 (0.002 – 21.40)*, $p = 0.52$) (Table 6). However, Cox regression interaction test did not reveal a statistically significant interaction between PFS and treatment (*HR:* $1.57 \cdot 10^{-3}$ $(1.99 \cdot 10^{-7} – 12.4)$; $p = 0.16$). Kaplan-Meier curves for high- and low-score patients are shown in Figure 15B.

Clinical characteristics N (%)		H12O cohort (N = 29) N (%)	
		MKIs (N = 11)	**SSA (N = 18)**
Sex	Female	5 (45.5)	8 (44.4)
	Male	6 (54.5)	10 (55.6)
Age	≥ 65 years	2 (18.2)	3 (16.6)
	< 65 years	9 (81.8)	15 (83.4)
Time since diagnosis	< 12 months	3 (27.3)	9 (50.0)
	≥ 12 months	8 (72.7)	9 (50.0)
Functional syndrome	Yes	2 (18.2)	7 (38.8)
	No	9 (81.8)	11 (61.2)
Location	Small intestine	1 (9.1)	8 (44.4)
	GI other	2 (18.2)	6 (33.3)
	Pancreas	8 (72.7)	4 (22.2)
Grade	G1	1 (9.1)	9 (50.0)
	G2	9 (81.8)	9 (50.0)
	G3	1 (9.1)	0 (0.0)
Treatment	Sunitinib	6 (54.5)	0 (0.0)
	Sunitinib + SSA	4 (36.4)	0 (0.0)
	Axitinib + SSA	1 (9.1)	0 (0.0)
	SSA	0 (0.0)	18 (100)
Prior lines of treatment (N)	0	4 (36.4)	16 (89.0)
	1	1 (9.1)	1 (5.5)
	2+	6 (54.5)	1 (5.5)
RECIST	CR	0 (0.0)	1 (5.5)
	PR	1 (9.1)	4 (22.2)
	SD	4 (36.4)	10 (55.5)
	PD	6 (54.5)	2 (11.1)
	NA	0 (0.0)	1 (5.5)
PFS	median (min - max)	7.5 months (2.39 - 41.0)	41.7 months (2.75 – 132)

Table 5. Clinicopathological characteristics of patients from the H12O validation cohort. The clinicopathological characteristics of the groups of treatment are shown. Total number and percentages are presented.

When signature genes were individually assessed in MKI-treated patients, we observed a significant association between *SPP1* expression and PFS (*HR: 2.11 (1.02 – 4.37), p = 0.044*), and a non-significant trend for *REXO1L2P* (*HR: 7.71 (0.91 – 65.4), p = 0.061*). *ATXN7* was not significantly associated with PFS in MKI-treated patients (*HR: 2.25 (0.18 – 28.3), p = 0.53*). None of these genes were associated with PFS in SSA-treated patients (Table 6).

PFS	H12O cohort (N = 29) N (%)			
	MKIs (N = 11)		SSA (N = 18)	
	HR (95%CI)	***P***	***HR (95%CI)***	***P***
Signature	0.00021 ($2.99 \cdot 10^{-8}$ – 1.51)	0.06	0.23 (0.002 – 21.40)	0.52
SPP1	2.11 (1.02 – 4.37)	0.044	1.52 (0.48 – 4.79)	0.47
REXO1L2P	7.71 (0.91 – 65.4)	0.061	2.46 (0.81 – 7.49)	0.11
ATXN7	2.25 (0.18 – 28.3)	0.53	1.12 (0.32 – 3.94)	0.85

Table 6. The 3-gene signature, *SPP1* and *REXO1L2P* predict efficacy of sunitinib in an external cohort of NET patients. The *HR* and *p-value* from the Cox regression analysis are shown for the signature and its 3 genes in MKI- and SSA-treated patients. A $p < 0.05$ was considered statistically significant. *95%CI*, 95% confidence interval.

Differential expression analysis in the H12O cohort identified 1029 genes that were differentially expressed ($p < 0.05$) between high- and low-signature score groups. However, none were significantly different after multiple testing correction (Supplementary Table 8). *SPP1* (*logFC = -0.94; p = 0.001*) and *ATXN7* (*logFC = 0.40; p = 0.004*) were differentially expressed between high- and low-score patients, whereas *REXO1L2P* did not show any significant difference (*logFC = -0.18; p = 0.26*) (Supplementary Table 8). We then attempted to validate the enrichments in molecular pathways and cell populations observed in patients with high- or low-scores from the discovery AXINET cohort using GSEA and cell type enrichment analysis. Twelve pathways were significantly enriched in high-score patients, including interferon γ (*NES = 1.51; FDR = 0.036*) and inflammatory response (*NES = 1.51; FDR = 0.024*), which were not altered in the discovery cohort. Only the neuroactive ligand-receptor interaction (*NES = -1.45; FDR = 0.045*) was significantly enriched in low-score patients. Interestingly, angiogenesis (*NES = -1.46; p = 0.043*) and cancer cell-specific EMT (*NES = -1.37; p = 0.059*) signatures were significantly enriched in low-score patients, as previously described in the discovery cohort. However, none of them remained significant after adjustment for multiple testing (Figure 15C; Supplementary Table 9). No cell population was significantly enriched in high- and low-score patients of the H12O cohort. Nevertheless, the small sample size limits the interpretation of this analysis.

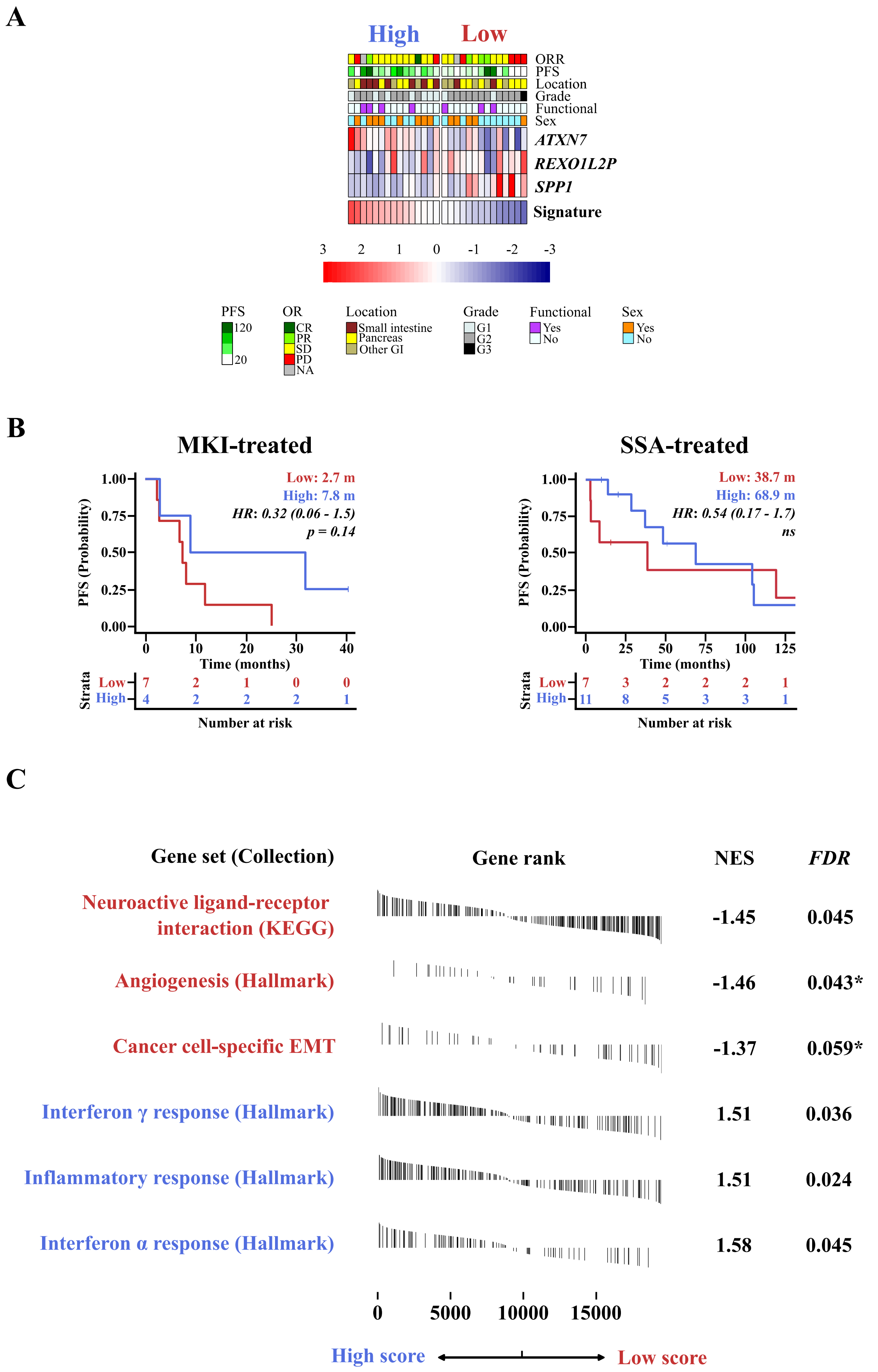
A
High
Low
ORR
PFS
Location
Grade
Functional
Sex
ATXN7
REXO1L2P
SPP1
Signature
3 2 1 0 -1 -2 -3
PFS 120 20
OR CR PR SD PD NA
Location Small intestine Pancreas Other GI
Grade G1 G2 G3
Functional Yes No
Sex Yes No
B
MKI-treated
Low: 2.7 m
High: 7.8 m
HR: 0.32 (0.06 - 1.5)
p = 0.14
PFS (Probability)
Time (months)
Strata
Low 7 2 1 0 0
High 4 2 2 2 1
Number at risk
SSA-treated
Low: 38.7 m
High: 68.9 m
HR: 0.54 (0.17 - 1.7)
ns
Low 7 3 2 2 2 1
High 11 8 5 3 3 1
C
Gene set (Collection)
Gene rank
NES
FDR
Neuroactive ligand-receptor interaction (KEGG) -1.45 0.045
Angiogenesis (Hallmark) -1.46 0.043*
Cancer cell-specific EMT -1.37 0.059*
Interferon γ response (Hallmark) 1.51 0.036
Inflammatory response (Hallmark) 1.51 0.024
Interferon α response (Hallmark) 1.58 0.045
0 5000 10000 15000
High score
Low score

Figure 15. The 3-gene signature predicts efficacy of sunitinib in an external cohort of NET patients. A. A supervised heatmap of patients with high and low signature scores is represented. The scaled expression of the 3 genes of the signature -*SPP1*, *REXO1L2P* and *ATXN7*-, along with the signature score are shown. Red and blue represent high and low expression, respectively. Patients with high signature scores had high expression of *ATXN7* and low expression of *SPP1* and *REXO1L2P*. An opposite pattern was observed in the low signature score group. ORR, PFS, primary tumor location, grade, carcinoid syndrome and sex were annotated for each patient. No enrichment in clinical characteristics was observed in high or low score groups. **B.** Kaplan-Meier curves of patients with high- (blue) or low- (red) signature scores are shown for MKI- and SSA-treated patients of the H12O validation cohort. Median PFS of each group, the HR, 95%CI and *p-value* of the Cox model are shown. The number of patients at risk per group is also represented in the table. MKI-treated patients with high scores had better PFS than patients with low scores. Almost no differences were observed in SSA-treated ones. **C.** Gene set enrichment analysis was performed between patients with high- and low- signature scores to validate the molecular pathways involved in the differential response to MKIs. Some of the most relevant significantly enriched gene sets are shown. Enrichment plots, NES, *p-value* (for cancer cell-specific and angiogenesis gene sets) and *FDR* are shown. Inflammatory, interferon α and interferon γ responses were significantly enriched in high-score patients (blue). Conversely, neuroactive ligand-receptor interaction, angiogenesis and cancer cell-specific EMT signature were significantly enriched in low score-patients (red), although the last 2 failed to remain significant after multiple testing correction. *Ns, non-significant. FDR < 0.05* were considered statistically significant. * *p-value* and not *FDR.*

Aim 4: To validate in plasma the predictive biomarkers identified to facilitate its implementation in clinical practice

4. Plasma osteopontin (OPN) levels predict efficacy of antiangiogenic MKIs in NETs

To facilitate the translation of our findings to a clinical setting, we sought to validate our signature using more accessible patient samples such as plasma, which additionally enables real-time, longitudinal monitoring. For this purpose, among the three candidate genes, we focused on *SPP1* because it was validated in the external cohort and encodes the secreted phosphoprotein OPN, that is involved in key oncogenic processes such as proliferation, angiogenesis, and invasion (234).

4.1 Plasma OPN levels predict efficacy of axitinib in NET patients

We evaluated OPN plasma levels in 106 patients from the discovery AXINET cohort using ELISA, 52 were treated with axitinib and 54 with placebo (Table 4). OPN levels ranged from 7 to 540 ng/ml. OPN plasma levels were significantly associated with PFS in axitinib-treated patients (*HR: 1.02 (1.0 – 1.04), p = 0.008)* but not in placebo-treated patients. Next, based on the population median value, patients were split into high and low OPN groups. Axitinib-treated patients with high OPN levels had significantly worse PFS compared to those with low levels (13.2 vs. 38.5 months, respectively; *HR: 2.04 (0.99 – 4.22), p = 0.053*). However, no association was observed between OPN plasma levels and PFS in patients treated with placebo (Figure 16A). Moreover, a significant interaction was observed between OPN plasma levels and treatment arm (*HR: 1.018 (1.002 – 1.035), p = 0.026*), confirming the differential association with PFS depending on the treatment.

Additionally, we validated these findings in 87 AXINET patients who were not included in the gene expression analysis (Table 4). In this AXINET validation cohort, OPN levels ranged from 6 to 193 ng/ml. Consistent with the previous results, OPN plasma levels were significantly associated with PFS in axitinib-treated patients (*HR: 1.01 (1.00 – 1.02), p = 0.03*), but not in placebo-treated patients. Axitinib-treated patients with high OPN plasma levels also had a poorer prognosis compared to those with low levels (14.5 vs. 71.7 months, respectively; *HR: 2.81 (1.18 – 6.65), p = 0.019*). No significant differences were observed in patients treated with placebo (Figure 16B).

However, no significant differences were observed in tumor shrinkage based on OPN levels, either in the discovery (*p = 0.34*) or the validation cohorts (*p = 0.58*) (Figure 16C-D). Consistently, OPN plasma levels did not correlate with tumor shrinkage in axitinib-treated patients (*r= 0.1; p = 0.48*) (Supplementary Figure 6A). Additionally, no correlation was found between OPN plasma levels and *SPP1* gene expression (*r = 0.08; p = 0.395*) or signature score (*r = -0.13; p = 0.178*) (Supplementary Figure 6B-C). We further investigated the relationship between the high- and low- classifications based on the 3-gene signature score and OPN plasma levels. Notably, only 55% of patients classified as low-signature score (non-responders) had high OPN plasma levels (non-responder), and 52% of high-signature score patients (responders) had low OPN plasma levels (responder).

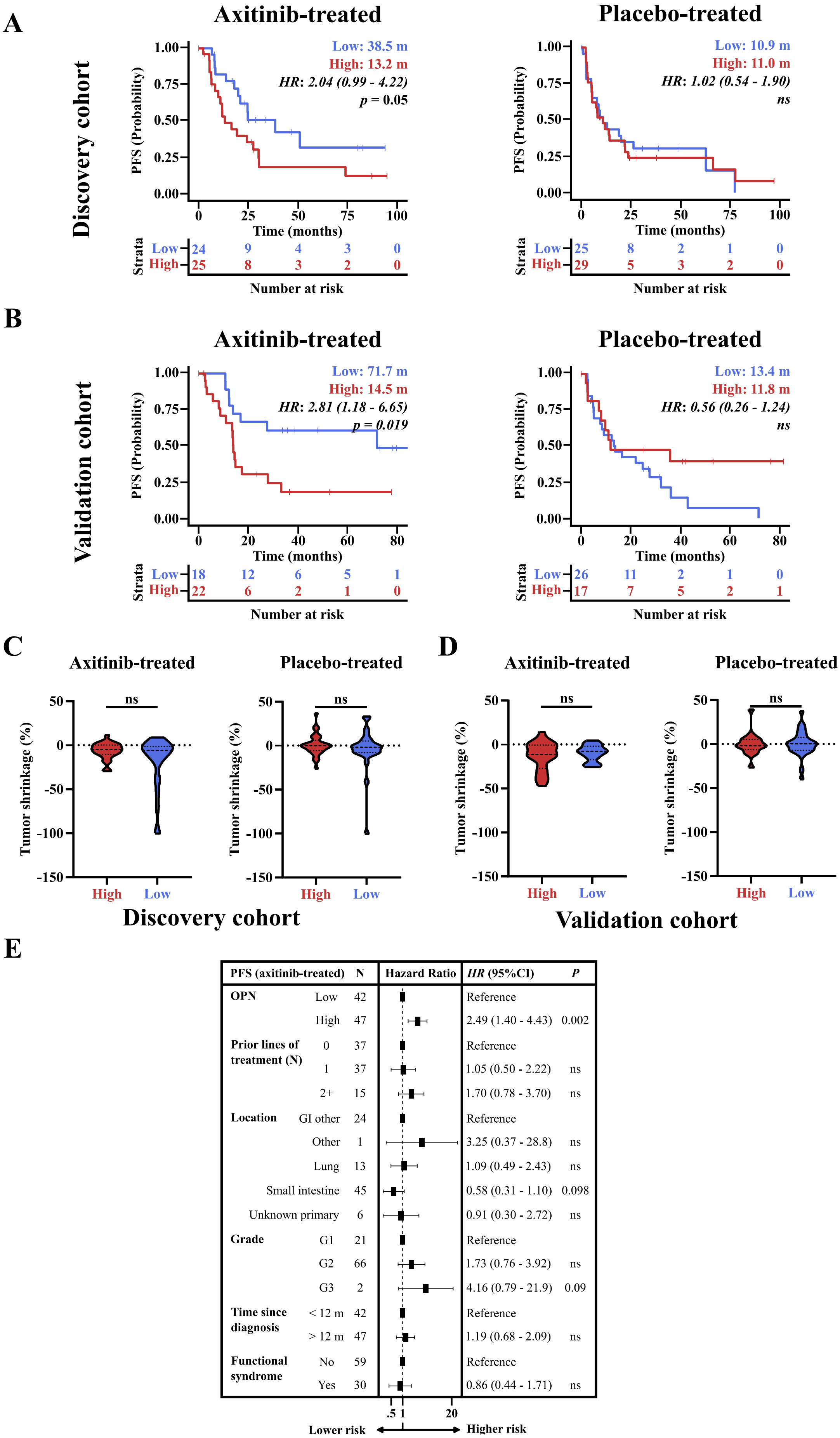
A
Discovery cohort
Axitinib-treated
Low: 38.5 m
High: 13.2 m
HR: 2.04 (0.99 - 4.22)
p = 0.05
PFS (Probability)
Time (months)
Strata
Low 24 9 4 3 0
High 25 8 3 2 0
Number at risk
Placebo-treated
Low: 10.9 m
High: 11.0 m
HR: 1.02 (0.54 - 1.90)
ns
Low 25 8 2 1 0
High 29 5 3 2 0
B
Validation cohort
Axitinib-treated
Low: 71.7 m
High: 14.5 m
HR: 2.81 (1.18 - 6.65)
p = 0.019
Low 18 12 6 5 1
High 22 6 2 1 0
Placebo-treated
Low: 13.4 m
High: 11.8 m
HR: 0.56 (0.26 - 1.24)
ns
Low 26 11 2 1 0
High 17 7 5 2 1
C
D
Tumor shrinkage (%)
ns
High
Low
Discovery cohort
Validation cohort
E
PFS (axitinib-treated)
N
Hazard Ratio
HR (95%CI)
P
OPN Low 42 Reference
High 47 2.49 (1.40 - 4.43) 0.002
Prior lines of treatment (N) 0 37 Reference
1 37 1.05 (0.50 - 2.22) ns
2+ 15 1.70 (0.78 - 3.70) ns
Location GI other 24 Reference
Other 1 3.25 (0.37 - 28.8) ns
Lung 13 1.09 (0.49 - 2.43) ns
Small intestine 45 0.58 (0.31 - 1.10) 0.098
Unknown primary 6 0.91 (0.30 - 2.72) ns
Grade G1 21 Reference
G2 66 1.73 (0.76 - 3.92) ns
G3 2 4.16 (0.79 - 21.9) 0.09
Time since diagnosis < 12 m 42 Reference
> 12 m 47 1.19 (0.68 - 2.09) ns
Functional syndrome No 59 Reference
Yes 30 0.86 (0.44 - 1.71) ns
.5 1 20
Lower risk
Higher risk

Figure 16. Plasma OPN levels predict efficacy of axitinib in NET patients. A. Kaplan-Meier curves of patients with high (red) or low (blue) OPN plasma levels are shown for axitinib- and placebo-treated patients of the AXINET discovery cohort. Median PFS of each group, the *HR*, 95%CI and *p-value* of the Cox model are shown. The number of patients at risk per group is also represented in the table. Axitinib-treated patients with high OPN plasma levels had significantly worse PFS than patients with low levels. No significant differences were observed in placebo-treated patients. **B.** Kaplan-Meier curves of patients with high (red) or low (blue) OPN plasma levels are shown for axitinib- and placebo-treated patients of the AXINET validation cohort. Axitinib-treated patients with high OPN plasma levels had significantly worse PFS than patients with low levels. No significant differences were observed in placebo-treated patients. **C-D.** Tumor shrinkage percentage was compared between patients with high (red) and low (blue) OPN plasma levels in both axitinib- and placebo-treated patients from the discovery and validation cohorts. No significant differences were observed in tumor shrinkage based on OPN levels, either in the discovery or the validation cohorts. **E.** Multivariable analysis of PFS was performed to confirm the independent predictive capacity of OPN plasma levels. The discovery and validation cohorts were combined for this analysis. The *HR, 95%CI* and *p-value* of the Cox model for OPN plasma levels and other clinically relevant variables are shown. Only OPN plasma levels remained a significant predictive biomarker of axitinib benefit in terms of PFS. *Ns, non-significant.* A $p < 0.05$ was considered statistically significant.

Multivariable Cox regression model was conducted to evaluate the independent predictive value of OPN on PFS, adjusted for tumor grade, primary tumor location, presence or not of carcinoid syndrome, time since diagnosis and the number of prior lines of therapy. OPN plasma levels remained a significant predictive biomarker of axitinib benefit in terms of PFS, both when plasma levels were used as a continuous variable (*HR*: *1.013 (1.00 – 1.022), p = 0.002*), and when used as a categorical variable classifying patients into high and low OPN plasma groups (*HR: 2.49 (1.40 – 4.43), p = 0.002*) (Figure 16E; Supplementary Table 10). Consistently, OPN plasma levels were not associated with PFS in placebo-treated patients (Supplementary Figure 6D). Multivariable models for axitinib and placebo-treated patients are summarized in Supplementary Table 10.

4.2 Plasma OPN levels predict efficacy of lenvatinib in NET patients

To further validate the predictive capacity of OPN plasma levels in patients treated with other antiangiogenic MKIs, we assessed OPN plasma levels in 99 patients with GI- and Pan-NETs from the TALENT trial who were treated with lenvatinib. This MKI targets VEGFRs, as well as other kinases, including FGFR 1-4, PDGFRα, KIT and RET (141). The clinical characteristics of these patients are summarized in Table 7.

Clinical characteristics N (%)		TALENT cohort (lenvatinib) (N = 99) N (%)	
		GI-NETs (N = 52)	Pan-NETs (N = 47)
Sex	Female	20 (38.5)	27 (57.5)
	Male	32 (61.5)	20 (42.5)
Age	≥ 65 years	20 (38.5)	14 (29.8)
	< 65 years	32 (61.5)	33 (70.2)
Functional syndrome	Yes	20 (38.5)	8 (17.0)
	No	32 (61.5)	39 (83.0)
Location	Pancreas	-	47 (100.0)
	Ileum	41 (78.8)	-
	Colon	2 (3.8)	-
	Rectum	6 (11.5)	-
	Gastric	1 (1.9)	-
	NA	2 (3.8)	-
Prior lines of treatment (N)	0	0 (0.0)	0 (0.0)
	1	52 (100.0)	3 (6.4)
	2+	0 (0.0)	44 (93.6)
RECIST (Central)	CR	0 (0.0)	0 (0.0)
	PR	9 (17.3)	18 (38.3)
	SD	38 (73.1)	24 (51.0)
	PD	1 (1.9)	2 (4.2)
	NA	4 (7.7)	3 (6.4)
PFS (Central)	median (min - max)	15.8 months (1.4 – 47.4)	11.3 months (1.4 – 45.8)

Table 7. Clinicopathological characteristics of patients from the TALENT trial. The clinicopathological characteristics for GI- and Pan-NET cohorts are shown. Total number and percentages are represented. GI, Gastrointestinal.

OPN levels ranged from 5.5 to 124 ng/ml. OPN plasma levels were significantly associated with PFS in lenvatinib-treated patients (*HR: 1.02 (1.01 – 1.03), p < 0.001)*. Patients were also split into high and low OPN groups using two different cutoffs: the median value of the TALENT cohort and the median value of the AXINET cohort. Using the TALENT cohort median value as cutoff, patients with high OPN plasma levels treated with lenvatinib showed worse PFS than those with low levels (13.1 vs. 22.4 months, respectively; *HR: 1.81 (1.09 – 3.00), p = 0.022*) (Figure 17A). Similar results were obtained when the median value of the AXINET cohort was used as cutoff (10.6 vs. 15.7 months, high vs. low; *HR: 1.94 (1.05 – 3.59), p = 0.033*) (Figure 17B). Multivariable Cox regression model was conducted to evaluate the independent predictive value of OPN plasma levels on PFS, adjusted for primary tumor location, presence or not of carcinoid syndrome, age and the number of prior lines of therapy. OPN plasma levels remained a significant predictive biomarker of lenvatinib benefit in terms of PFS, both when plasma levels were used as a continuous variable (*HR: 1.02 (1.008 – 1.032), p = 0.001*), and when used as a categorical variable classifying patients into high and low OPN plasma groups (*HR: 1.75 (1.03 – 2.96), p = 0.04)* (Figure 17C).

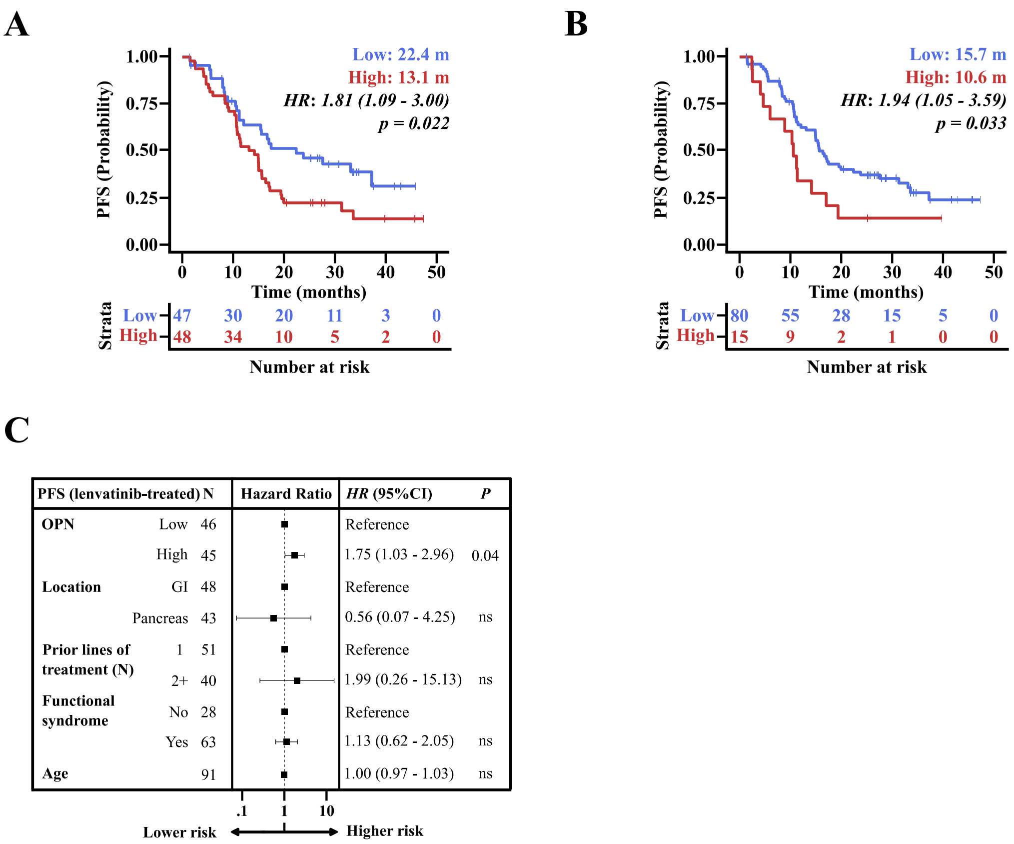

Figure 17. Plasma OPN levels predict efficacy of lenvatinib in NET patients. A. Kaplan-Meier curves of patients with high (red) or low (blue) OPN plasma levels are shown for lenvatinib-treated patients using the TALENT cohort median value as cutoff. Median PFS of each group, the *HR*, 95%CI and *p-value* of the Cox model are shown. The number of patients at risk per group is also represented in the table. Lenvatinib-treated patients with high OPN plasma levels had significantly worse PFS than patients with low levels. **B.** Kaplan-Meier curves of patients with high (red) or low (blue) OPN plasma levels are shown for lenvatinib-treated patients using the AXINET cohort median value as cutoff. Lenvatinib-treated patients with high OPN plasma levels had significantly worse PFS than patients with low levels. **C.** Multivariable analysis of PFS was performed to confirm the independent predictive capacity of OPN plasma levels in lenvatinib-treated patients. The *HR*, *95%CI* and *p-value* of the Cox model for OPN plasma levels and other clinically relevant variables are shown. Only OPN plasma levels remained a significant predictive biomarker of lenvatinib benefit in terms of PFS. *Ns, non-significant.* A $p < 0.05$ was considered statistically significant. GI, Gastrointestinal.

Aim 5: To study the role of osteopontin (OPN) in NET biology and angiogenesis *in vitro*

5. OPN promotes oncogenic functions in NETs and drives response to AAT, inducing resistance mechanisms in endothelial cells *in vitro*

5.1 OPN signaling is active in NET and HUVEC cell lines

Given the critical role of OPN in the response to antiangiogenic MKIs in NET patients, we decided to investigate the OPN-driven underlying molecular mechanisms involved the response to these drugs.

We first evaluated OPN expression in a panel of 4 neuroendocrine tumor cell lines, including the human pulmonary H727 and UMC-11, as well as the pancreatic BON-1 and QGP-1 cell lines. *SPP1* expression levels were assessed by qRT-PCR, revealing that UMC-11 exhibited the highest *SPP1* expression, while H727, BON-1 and QGP-1 showed lower expression levels (Figure 18A). This was confirmed by WB, where UMC-11 cells presented the highest OPN levels. OPN was also detected in the other cell lines, particularly in H727 cells, although with lower expression levels (Figure 18B; Supplementary Figure 7A). Similarly, analysis of OPN secretion into the cell medium revealed variable amounts of secreted OPN across NET cell lines. UMC-11 exhibited the highest OPN secretion, while BON-1 and H727 had lower levels. QGP-1 showed intermediate levels of secreted OPN (Figure 18C).

We then examined the expression of the main OPN receptors, CD44 and integrin αvβ3, in NET cell lines. Western blot analysis revealed that CD44 was not expressed, while both integrin αv and integrin β3 were expressed at similar levels across all NET cell lines (Figure 18D), except for QGP-1, which showed lower levels of integrin β3. As expected, HUVEC expressed both OPN receptors, CD44 and integrins αv and β3 (Figure 18D). These findings suggest that OPN may mediate its effects through integrin αvβ3 in cancer cells and through both receptors in endothelial cells.

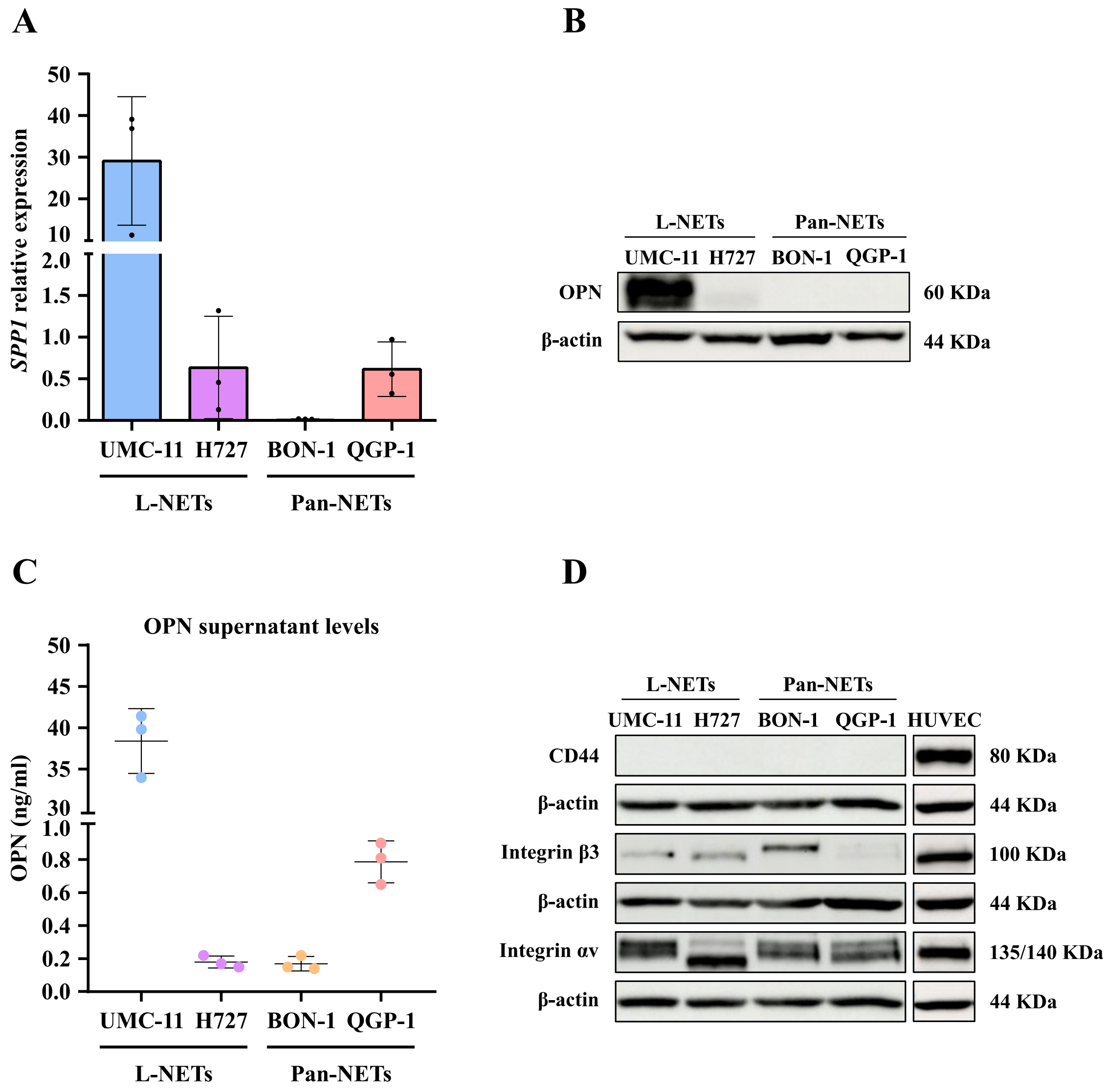

Figure 18. Characterization of *SPP1*/OPN expression in NET cell lines and HUVEC. A. qRT-PCR was performed to evaluate *SPP1* expression levels in pulmonary and pancreatic NET cell lines. The $2^{-\Delta\Delta Ct}$ is shown on the y-axis. **B.** Western blot was performed to evaluate OPN expression levels in NET cell lines. **C.** Secreted OPN levels were measured using ELISA in the cell line medium. OPN levels are shown on the y-axis. Overall, UMC-11 showed the highest *SPP1*/OPN expression. However, OPN was also expressed in the other NET cell lines. **D.** Western blot was performed to evaluate the expression of the major OPN receptors in NET and HUVEC cell lines. Representative WB are shown for each protein. β-actin was used as a loading control. Molecular weights are expressed in kilodaltons (KDa). Integrin αvβ3 was present in all HUVEC and NET cell lines. CD44 was only expressed in HUVEC. Data are expressed as the mean ± SD of 3 independent experiments.

5.2 OPN modulates several oncogenic capabilities in NET cell lines

To further investigate the role of OPN in NET cells, we modulated its expression by either overexpressing or knocking out *SPP1* in UMC-11 and BON-1 NET cell lines. The modulation of the OPN expression was confirmed through qRT-PCR (A), western blot (B) and ELISA (C) analyses (Figure 19; Supplementary Figure 8). However, complete OPN knockout was not achieved as OPN remained detectable in both the WB and ELISA assays. Nevertheless, OPN expression was significantly reduced in both cell lines, and therefore, these cell lines were treated as knockdown models in the subsequent experiments. In addition, we also established and evaluated inducible *SPP1/*OPN knockdown models. The conditional downregulation of OPN expression in BON-1 cell line was confirmed by qRT-PCR (Supplementary Figure 9). Conditional OPN KD models were also generated for the other NET cell lines using both the PB-31 and PB-37 backbones (data not shown).

Next, we analyzed the impact of OPN modulation on proliferation, migration and colony formation. OPN overexpression resulted in a significant increase in cell growth in BON-1 cell lines, while its depletion led to a significant reduction in cell proliferation (Figure 20A). Furthermore, increased OPN expression enhanced cell migration, whereas KD impaired the migratory ability (Figure 20B). Lastly, OPN overexpression induced the formation of larger and more intense colonies, whereas OPN KD had the opposite effect (Figure 20C). In UMC-11 cells, OPN overexpression did not affect cell growth or colony formation but led to increased migration (Figure 21). In contrast, OPN depletion significantly reduced cell proliferation and migration, and showed a tendency to impair clonogenicity (Figure 21).

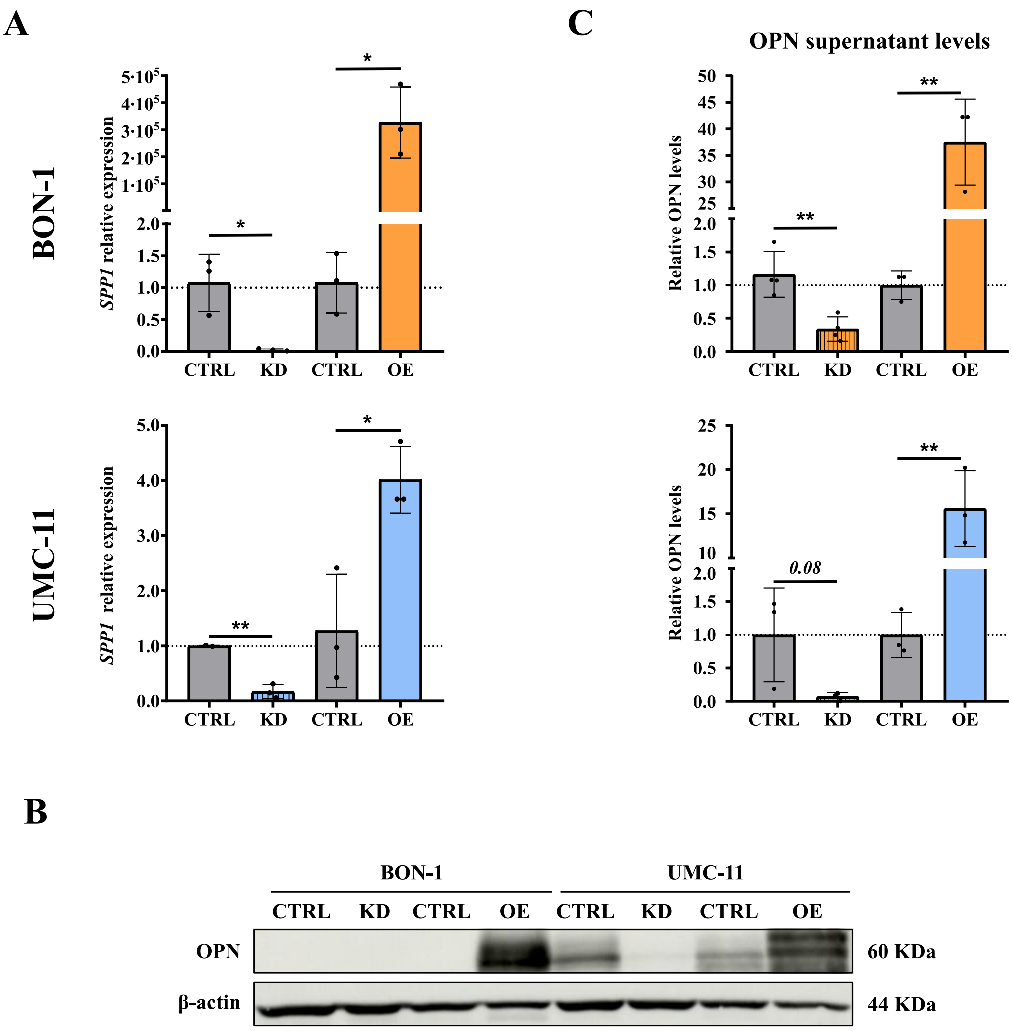

Figure 19. Validation of OPN overexpression and depletion in NET cell lines. A. qRT-PCR was performed to confirm *SPP1* overexpression and depletion in modified BON-1 and UMC-11 NET cell lines. The $2^{-\Delta\Delta Ct}$ is shown on the y-axis. **B.** Western blot was performed to confirm OPN overexpression and depletion in BON-1 and UMC-11 NET cell lines. Representative WB are shown for each protein. β-actin was used as a loading control. Molecular weights are expressed in kilodaltons (KDa). **C.** Secreted OPN levels were measured using ELISA in the culture medium of modified BON-1 and UMC-11 NET cell lines. Relative OPN levels are shown on the y-axis. OPN OE and KD effectively increased and decreased *SPP1*/OPN expression and secretion in NET cell lines, respectively. However, OPN was still detectable in OPN KD cells. CTRL, control. OE, overexpression. KD, knockdown. Data are expressed as the mean ± SD of 3-4 independent experiments. *Ns, non-significant.* * $p < 0.05$ and ** $p < 0.01$ were considered statistically significant.

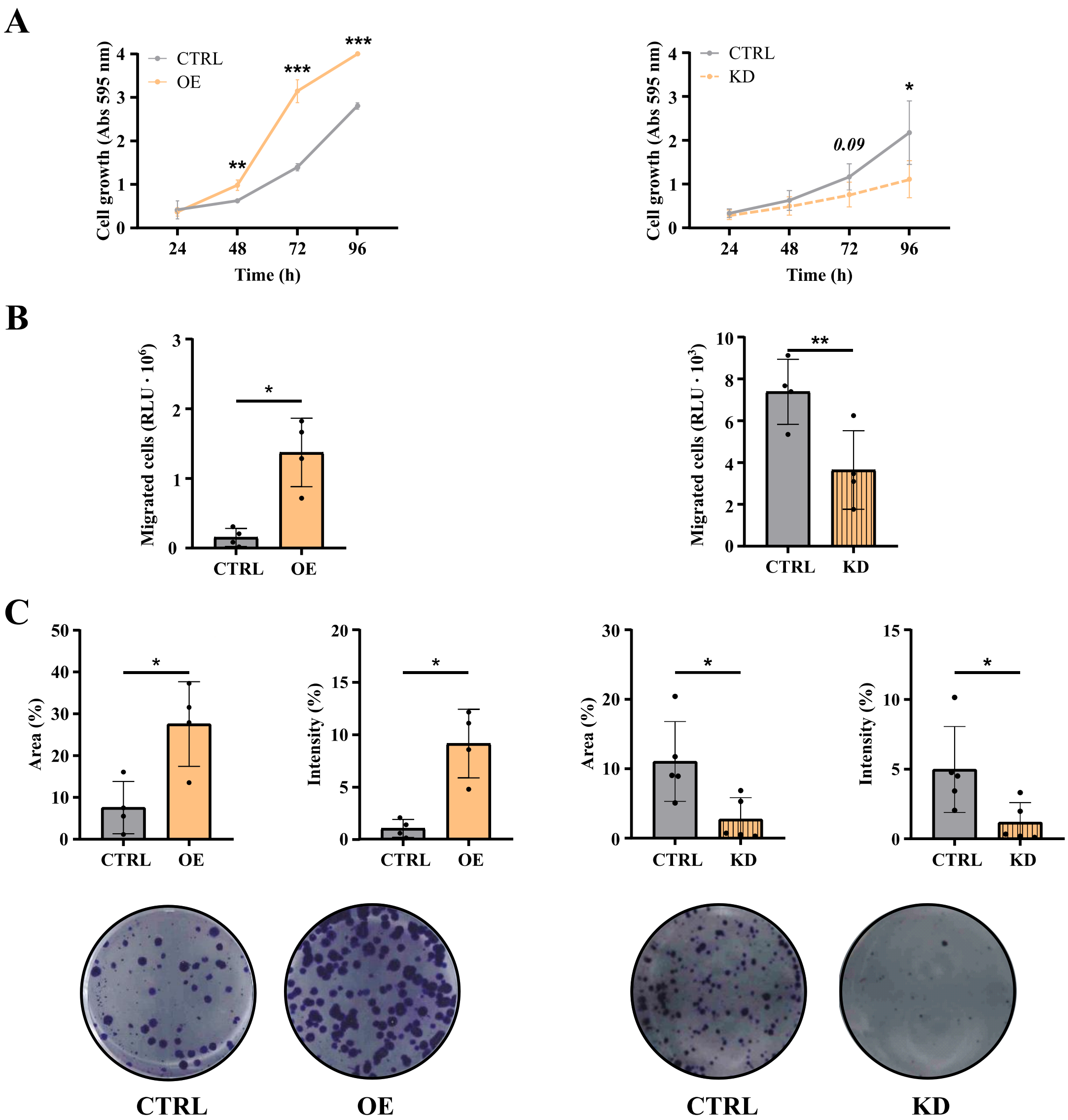

Figure 20. OPN regulates proliferation, migration and clonogenicity in pancreatic NET cell lines. A. Proliferation assays were performed using crystal violet to measure cell growth at 24, 48, 72 and 96 hours in OPN OE and KD BON-1 cells and their controls. Absorbance at 595 nm is shown on the y-axis. OPN OE (orange; n = 3) and KD (striped orange, n = 4) resulted in a significant increase and decrease in cell growth, respectively, compared to their controls. **B**. Cell migration in OPN OE and KD BON-1 cells and their controls was evaluated using transwell assays. Transmigrated cells were quantified using CellTiter-Glo after 24 hours. Relative light units are shown on the y-axis. OPN OE (orange; n = 4) and KD (striped orange, n = 4) significantly increased and decreased migration, respectively, compared to their controls **C.** Clonogenicity was evaluated using CFAs in OPN OE and KD BON-1 cell lines and their controls. Colony area and intensity percentages derived from ImageJ analysis are shown on the y-axis. OPN OE (orange, n = 4) and KD (striped orange, n = 5) significantly increased and decreased colony area and intensity, respectively, compared to controls. Representative images for each CFA condition are shown after crystal violet staining. Data are expressed as the mean ± SD of 3-5 independent experiments. CTRL, control. OE, overexpression. KD, knockdown. *Ns, non-significant.* * *p < 0.05*, ** *p < 0.01* and *** *p < 0.001* were considered statistically significant.

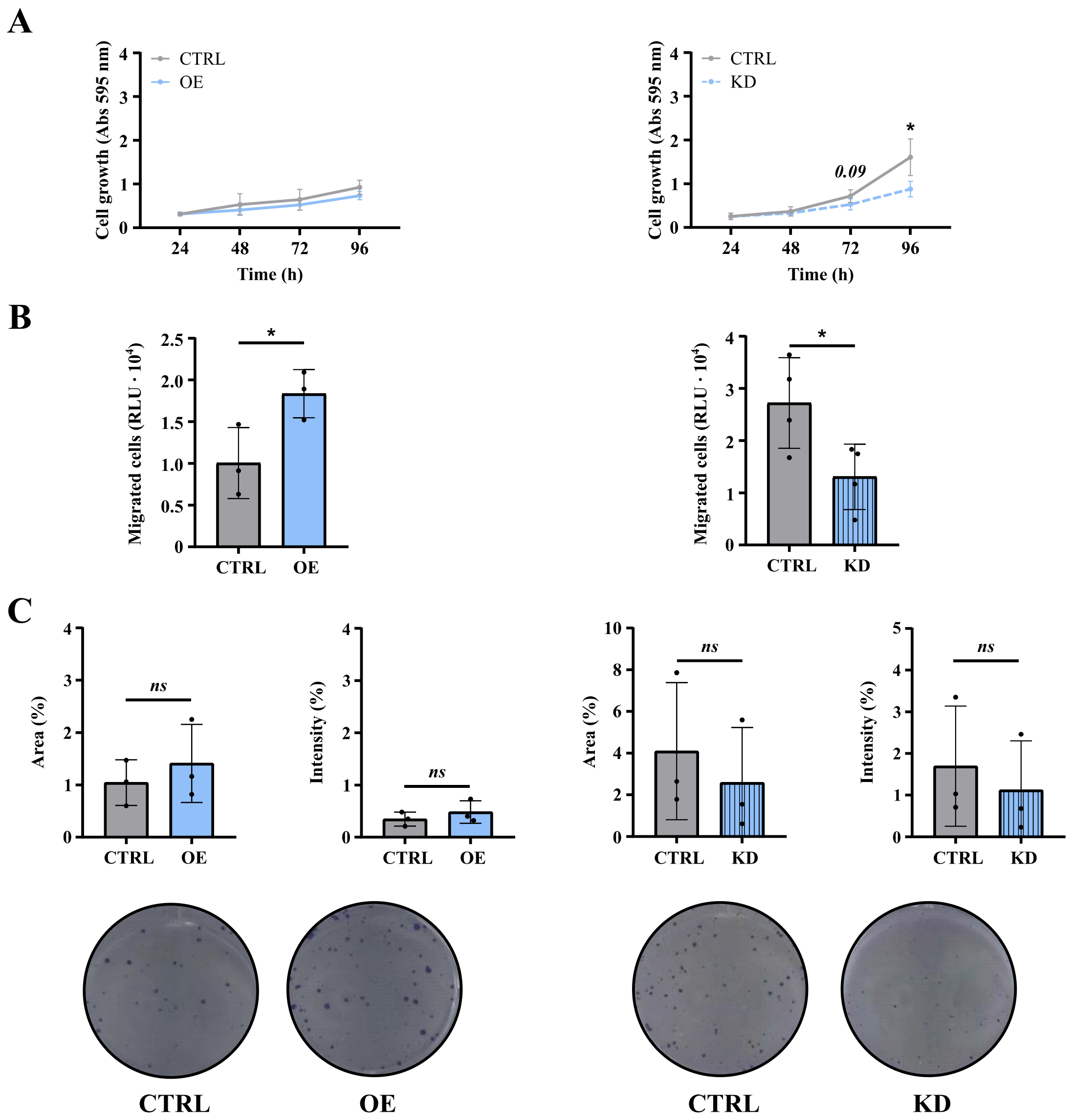

Figure 21. OPN regulates proliferation, migration and clonogenicity in lung NET cell lines. A. Proliferation assays were performed using crystal violet to measure cell growth at 24, 48, 72 and 96 hours in OPN OE and KD UMC-11 cells and their controls. Absorbance at 595 nm is shown on the y-axis. OPN OE (blue, n = 3) did not alter cell growth in UMC-11 cell lines. Conversely, OPN KD (striped blue, n = 4) resulted in a significant decrease in cell growth. **B.** Cell migration in OPN OE and KD UMC-11 cells and their controls was evaluated using transwell assays. Transmigrated cells were quantified using CellTiter-Glo after 24 hours. Relative light units are shown on the y-axis. OPN OE (blue, n = 3) and KD (striped blue, n = 4) significantly increased and decreased migration, respectively, compared to their controls. **C.** Clonogenicity was evaluated using CFAs in OPN OE and KD UMC-11 cell lines and their controls. Colony area and intensity percentages derived from ImageJ analysis are shown on the y-axis. OPN KD (n = 3) in UMC-11 cells reduced colony area and intensity compared to its control, although the differences were not statistically significant. No differences were observed in OPN OE cells (n = 3). Data are expressed as the mean ± SD of 3-4 independent experiments. CTRL, control. OE, overexpression. KD, knockdown. *Ns, non-significant.* * $p < 0.05$ was considered statistically significant.

5.3 OPN promotes resistance to MKIs in HUVEC

Next, we investigated whether NET cell lines with OPN overexpression or downregulation respond differently to antiangiogenic MKIs, such as axitinib and cabozantinib, *in vitro*. First, we evaluated the expression of VEGFR-2 in NET cell lines. BON-1 and H727 cells exhibited detectable levels of VEGFR-2 (Figure 22A). Therefore, OPN OE or KD BON-1 cell lines were treated with increasing doses of different MKIs to determine the IC50. No differences in IC50 were observed between OPN overexpressing and control BON-1 cells (Figure 22B). However, OPN downregulation appeared to slightly increase the sensitivity of BON-1 cells to axitinib compared to the control, while no differences were observed with cabozantinib (Figure 22C).

Since OPN did not modulate the response of cancer cells to the MKIs, we investigated the role of OPN in the response of endothelial cells to these drugs. To this end, we examined the response of HUVEC to axitinib and cabozantinib after culture with conditioned medium from OPN OE and CTRL BON-1 cells. HUVEC cultured with OPN OE conditioned medium exhibited a significantly higher axitinib IC50 compared to those cultured with control conditioned medium (CTRL: 0.65, OE OPN: 1.34 μM; $p = 0.045$). Similarly, HUVEC cultured with OPN OE conditioned medium also exhibited a significantly higher cabozantinib IC50 compared to those cultured with control conditioned medium (CTRL: 0.33 μM, OE OPN: 0.60 μM; $p = 0.007$). These results confirm that OPN induces resistance to antiangiogenic MKIs in HUVEC (Figure 22D).

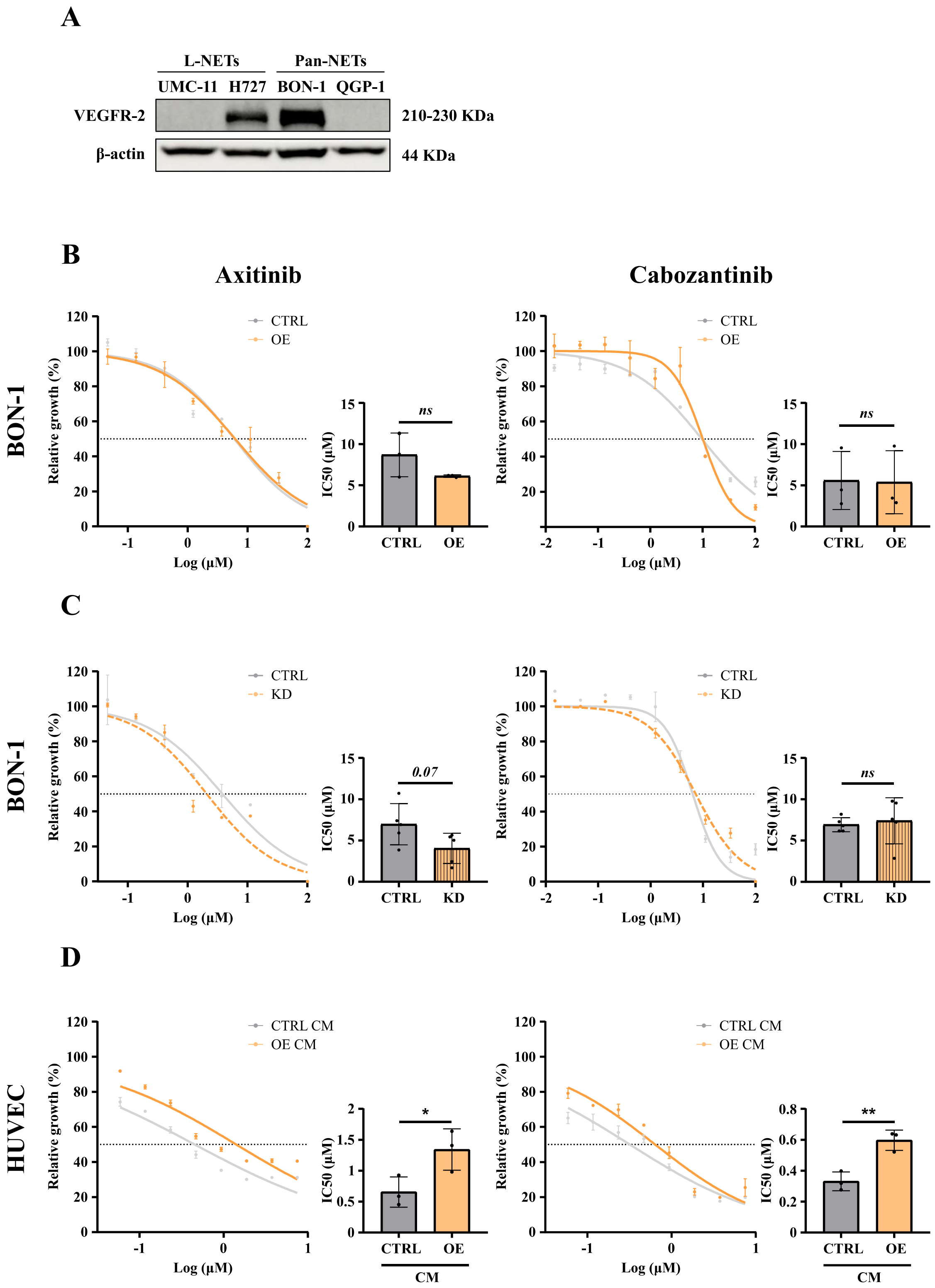

Figure 22. OPN regulates sensitivity to antiangiogenic MKIs in HUVEC. A. Western blot was performed to evaluate VEGFR-2 expression levels in NET cell lines. Representative WB are shown for each protein. β-actin was used as a loading control. Molecular weights are expressed in kilodaltons (KDa). Only BON-1 and H727 exhibited VEGFR-2 expression. **B-C.** Representative dose-response curves for BON-1 OE and KD cells (orange) and their controls (grey) are represented after treatment with axitinib and cabozantinib for 72 hours. Relative growth and log drug concentration are shown on the y- and x-axes,

respectively. The IC50s for each treatment and cell line after 72 hours are also plotted on the y-axis of the bar graph. OPN OE and KD did not alter the sensitivity to antiangiogenic MKIs in NET cell lines. **D.** Representative dose-response curves for HUVEC cells grown in BON-1 OPN OE (orange) and in BON-1 CTRL conditioned media (grey) are represented after treatment with axitinib and cabozantinib for 72 hours. Relative growth and log drug concentration are shown on the y- and x-axes, respectively. The IC50s for each treatment and cell line after 72 hours are plotted on the y-axis of the bar graph. BON-1 OPN OE conditioned media induced resistance to antiangiogenic MKIs in HUVEC. Data are expressed as the mean ± SD of 3-5 independent experiments. CTRL, control. OE, overexpression. KD, knockdown. CM, conditioned medium. *Ns, non-significant.* * $p < 0.05$ and ** $p < 0.01$ were considered statistically significant.

Next, we aimed to study the interaction between OPN and functional angiogenesis in HUVEC using matrigel tube formation assays. Therefore, HUVEC cultured with conditioned medium from BON-1 OPN OE and CTRL cells were seeded in matrigel, and angiogenesis was evaluated after 12-14 hours in the presence of DMSO or 0.1 μM axitinib. DMSO-treated HUVEC cultured in OPN OE conditioned medium showed increased total ($p = 0.06$), segment ($p = 0.037$) and master ($p = 0.034$) lengths compared to HUVEC grown in CTRL medium (Figure 23A-B). In addition, DMSO-treated HUVEC grown in the presence of OPN OE medium had increased numbers of nodes ($p = 0.025$), segments ($p = 0.033$) and meshes ($p = 0.047$), suggesting that BON-1 derived OPN can independently promote angiogenesis *in vitro* (Figure 23B). However, treatment with axitinib inhibited angiogenesis equally in HUVEC grown in BON-1 OPN OE and CTRL conditioned medium. Nevertheless, the tube-forming capacity of HUVEC *in vitro* in the presence of axitinib was still significantly increased ($p < 0.05$ for all parameters) in HUVEC grown in OPN OE medium compared to HUVEC grown in CTRL medium (Figure 23B).

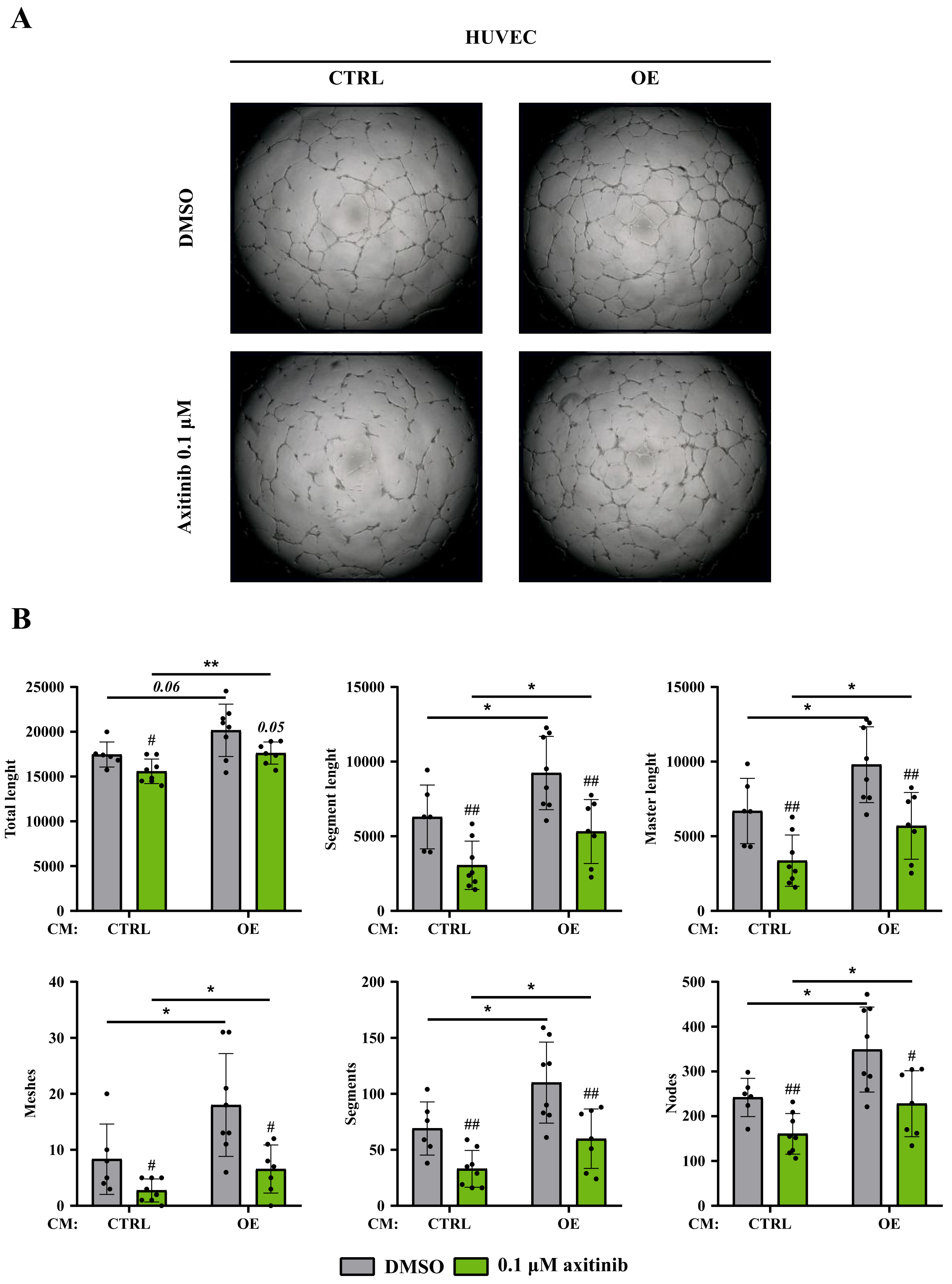

Figure 23. OPN regulates tube formation capacity in HUVEC. A. Tube formation assays were performed with HUVEC grown in BON-1 CTRL or OPN OE conditioned medium. Representative images for each condition are shown. **B.** Tubulogenic capacity was evaluated using the *angiogenesis* ImageJ plugin and the number of nodes, segments, meshes, and total, segment and master lengths were evaluated at 12-14 hours and are represented on the y-axis. Data are expressed as the mean ± SD of 6 to 8 wells from 3 independent experiments. CTRL, control. OE, overexpression. CM, conditioned medium. * $p < 0.05$ and

** $p < 0.01$ were considered statistically significant for BON-1 CTRL vs. BON-1 OE comparisons. # $p < 0.05$ and ## $p < 0.01$ were considered statistically significant for DMSO vs. 0.1 μM axitinib comparisons.

Aim 6: To study the role of osteopontin (OPN) in NET biology and angiogenesis *in vivo*

6. OPN drives resistance to antiangiogenic MKIs in *in vivo* models of NETs

6.1 The role of OPN in the response of chorioallantoic membrane (CAM) xenograft models to antiangiogenic MKIs

To explore the role of OPN in angiogenesis and response to MKIs *in vivo*, we engrafted BON-1 CTRL and BON-1 OPN OE cell lines into the chorioallantoic membrane (CAM) of chicken embryos. After 3 days, tumors became visible and were treated daily and topically with 10 μL of DMSO or 3 μM axitinib for 6 days. Overall, although the same number of cells were engrafted in both conditions, tumor size was highly variable after 3 days. Tumors were randomized into each treatment group in an attempt to balance tumor size at the start of the treatment. After treatment, tumors treated with axitinib appeared more necrotic both in the GFP channel for BON-1 CTRL xenografts, and under bright light for BON-1 OPN OE xenografts (Figure 24A). However, no significant differences in tumor volume were observed after high-frequency ultrasound imaging in either DMSO- or axitinib-treated CAM xenografts. Overall, BON-1 CTRL tumors appeared to be larger at the endpoint, regardless of the treatment received (Figure 24B). Tumor angiogenesis was evaluated by immunofluorescence using Dylight-649-labelled *lens culinaris agglutinin* (LCA, lectin). LCA was injected intravenously before the endpoint and binds to α-linked mannose residues present on the luminal surface of the endothelium (Figure 24C). DMSO-treated BON-1 OPN OE xenografts seemed to have an increased lectin area compared to DMSO-treated controls. However, only 1 CTRL xenograft was successfully injected, and no definitive conclusions can be drawn from this comparison. On the other hand, as observed *in vitro,* axitinib equally inhibited angiogenesis in BON-1 CTRL and BON-1 OPN OE xenografts, but OE tumors still had a higher percentage of lectin area compared to controls. However, differences were not statistically significant (Figure 24D).

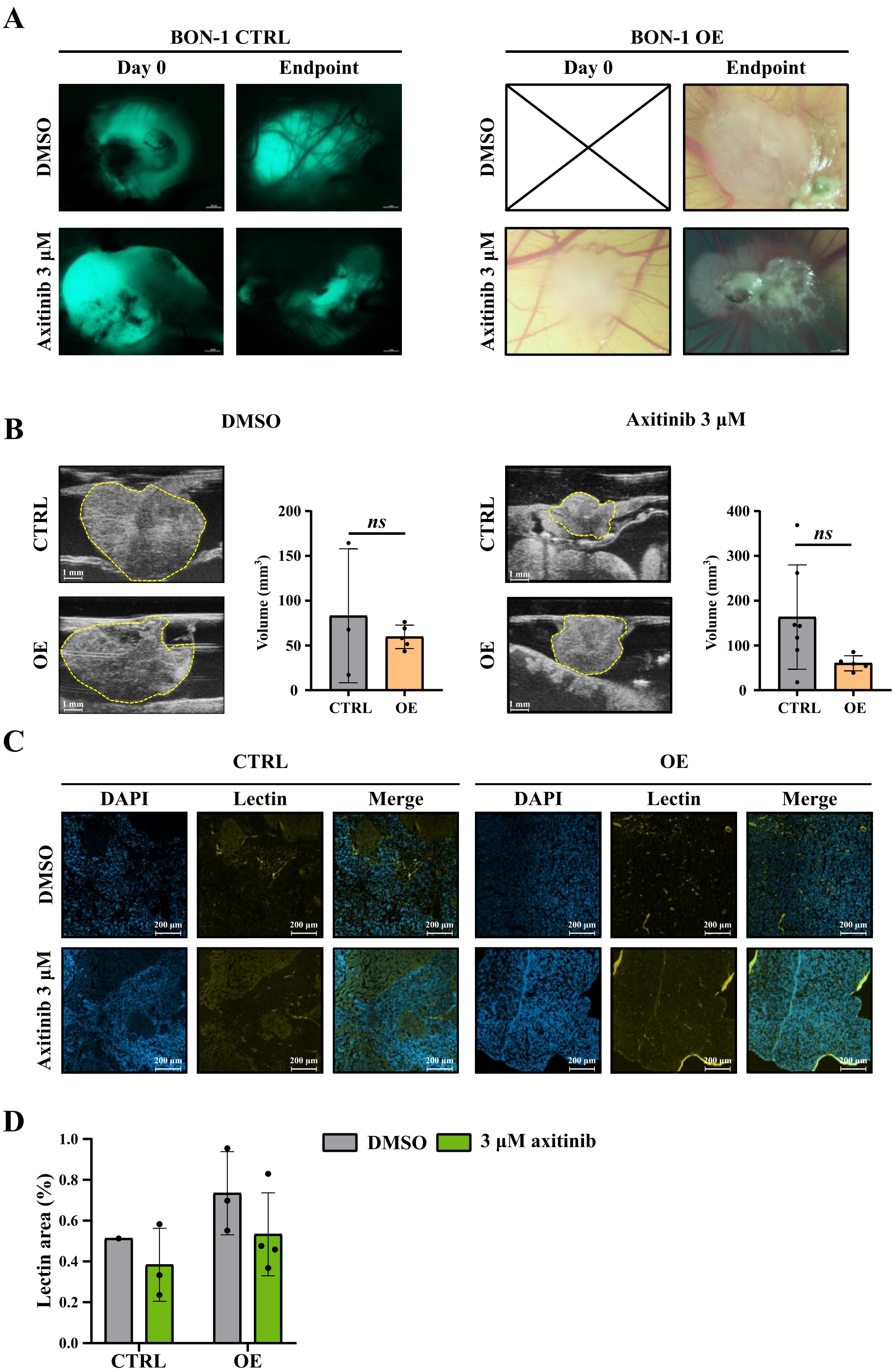

Figure 24. OPN overexpression does not affect the response to antiangiogenic MKIs in BON-1 CAM xenografts. A. Representative GFP images of BON-1 CTRL and brightfield images of BON-1 OPN OE xenografts at baseline (ED9-13) and after treatment with axitinib or DMSO (ED17-20) are shown. Axitinib-treated tumors appeared more necrotic regardless of the treatment. **B.** Representative US images of BON-

1 CTRL and OPN OE xenografts after treatment with DMSO or axitinib are shown. Volume quantification after 3D analysis is also shown on the y-axis of the bar graphs. No differences were observed between CTRL and OPN OE BON-1 xenografts in any of the treatment conditions. Data are expressed as the mean ± SD of 3-7 xenografts. **C.** Representative immunofluorescence images of BON-1 CTRL and OPN OE CAM xenograft tumors after treatment with DMSO or axitinib are shown. DAPI (blue), lectin (647 nm, yellow) and merged channels are displayed. **D.** The percentage of positive LCA area (endothelium) was evaluated in each CAM xenograft for at least 8-10 regions of each tumor using QuPath. Data are expressed as the mean ± SD of 1-4 CAM xenograft tumors. Only 1 LCA-stained xenograft was available for BON-1 CTRL xenografts treated with DMSO. OPN slightly increased LCA-positive area (endothelium) regardless of the treatment. However, the differences were not statistically significant. CTRL, control. OE, overexpression. *Ns, non-significant.* A $p < 0.05$ was considered statistically significant. CAM, chorioallantoic membrane. US, ultrasound.

Similarly, we investigated the effect of OPN downregulation on the response of NETs to axitinib. To this end, we engrafted BON-1 PB31 CTRL or BON-1 PB31 OPN-sh759 cell lines, which downregulate OPN upon doxycycline induction, into the CAM of chicken embryos. Again, tumor volume after engraftment was highly variable, and treatment groups were established based on baseline tumor size (Figure 25A-B). No obvious differences were observed in the brightfield images after treatment. Accordingly, no significant differences in volume were observed between BON-1 CTRL and OPN KD cells in either DMSO- or axitinib-treated CAMs xenografts. (Figure 25C-D). Labeled LCA could not be injected into these models.

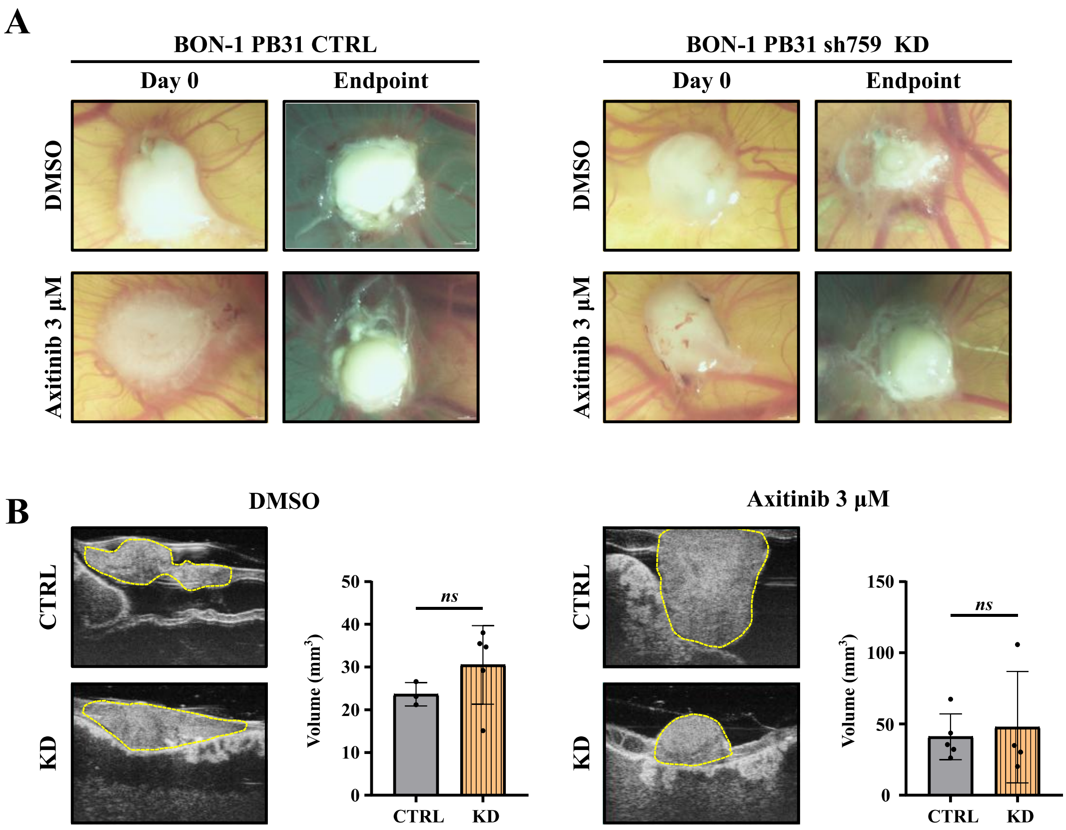

Figure 25. OPN downregulation does not affect the response to antiangiogenic MKIs in BON-1 CAM xenografts. A. Representative brightfield images of BON-1 PB31 CTRL and BON-1 PB31 OPN-sh759 xenografts at baseline (ED9-13) and after treatment with axitinib or DMSO (ED17-20) are shown. No obvious differences were observed in the brightfield images after treatment **B.** Representative US images of BON-1 PB31 CTRL and BON-1 PB31 OPN-sh759 xenografts after treatment with DMSO or axitinib are shown. Volume quantification after 3D analysis is also shown on the y-axis of the bar graphs. No differences were observed between BON-1 PB31 CTRL or BON-1 PB31 OPN-sh759 CAM xenografts in any of the treatment conditions. Data are expressed as the mean ± SD of 3-5 CAM xenografts. CTRL, control. KD, knockdown. *Ns, non-significant.* A $p < 0.05$ was considered statistically significant.

6.2 OPN overexpression induces resistance to cabozantinib in NET CDX mouse models

6.2.1 Dose response study of antiangiogenic MKIs in NET CDX mouse models

To evaluate the role of OPN in the response to MKIs *in vivo*, we studied the response to these drugs in mouse CDX models. BON-1 cells were injected subcutaneously into nude mice as described earlier in the Materials and Methods section (*Cell line-derived xenografts mouse models*). To determine the optimal treatment doses, 4 mice per group were treated with vehicle, axitinib (25 and 40 mg/kg/day), sunitinib (20 and 40 mg/kg/day) or cabozantinib (15 and 30 mg/kg/day). Reduced tumor growth was observed at all doses of antiangiogenic MKIs, although the reduction was only significant compared to the vehicle for the following drugs and concentrations: axitinib 25 mg/kg/day ($p = 0.008$), axitinib 40 mg/kg/day ($p = 0.048$), cabozantinib 30 mg/kg/day ($p = 0.018$) and sunitinib 40 mg/kg/day ($p = 0.046$) (Figure 26A). Accordingly, both doses of axitinib and cabozantinib significantly reduced tumor weight at the endpoint of the experiment. However, no differences were observed with sunitinib even at 40 mg/kg/day (Figure 26B). Unfortunately, the 25 and 40 mg/kg/day doses of axitinib were not well tolerated by the mice (see endpoint criteria in the Materials and Methods section). No apparent toxicities were observed with the remaining doses and agents.

Tumor MVD was assessed using CD31 staining after treatment with antiangiogenic MKIs (Figure 26C). Notably, the CD31-stained area was significantly reduced across all treatment groups compared to the vehicle control group (Figure 26C). This reduction occurred even in mice whose tumor growth was not significantly inhibited compared to vehicles.

6.2.2 OPN promotes resistance to cabozantinib in NET CDX mouse models

After optimizing the protocol for NET mouse CDXs, we evaluated the effect of OPN OE on the response to antiangiogenic MKIs *in vivo*. BON-1 CTRL and OPN OE cells were injected subcutaneously into nude mice as described earlier in the Materials and Methods section (*Cell line-derived xenografts mouse models*). BON-1 CTRL and OPN OE CDXs were treated with either vehicle or cabozantinib (30 mg/kg/day). A significant reduction in tumor growth was observed in BON-1 CTRL CDXs (Figure 27A-B) treated with cabozantinib 30 mg/kg/day compared to vehicle ($p = 0.04$). However, no significant reduction in tumor growth was observed in BON-1 OPN OE CDXs treated with cabozantinib 30 mg/kg/day compared to vehicle ($p = ns$), indicating that OPN induces resistance to MKIs *in vivo.* Importantly, BON-1 OPN OE CDXs had significantly higher OPN plasma levels than BON-1 CTRL CDXs, confirming the *in vivo* upregulation of OPN in our model (Supplementary Figure 10). Finally, cabozantinib significantly reduced tumor weight at the endpoint in BON-1 CTRL CDXs ($p = 0.02$), but not in BON-1 OPN OE CDXs (Figure 27B).

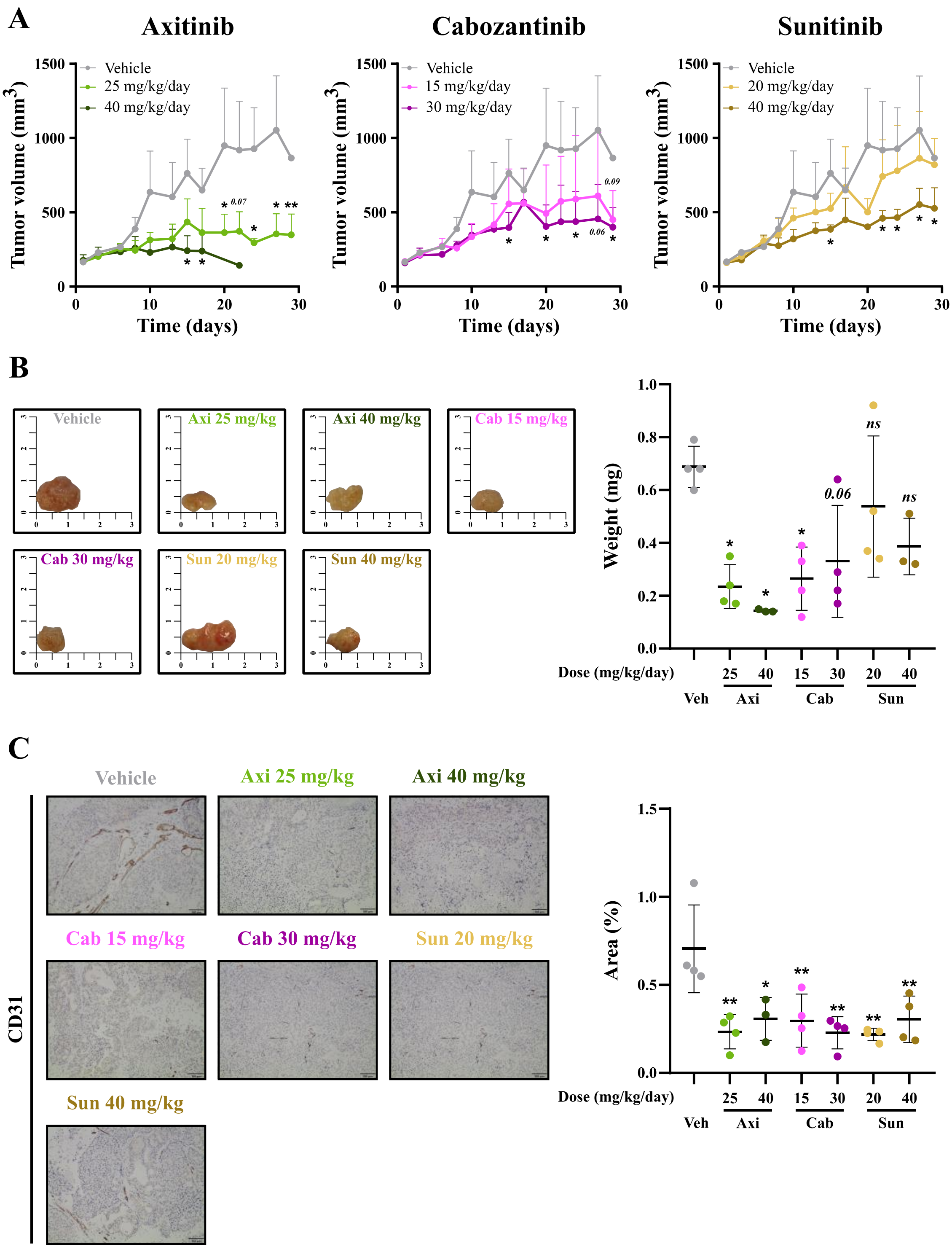

Figure 26. Dose-response study of antiangiogenic MKIs in NET mouse CDX models. A. Tumor volume in BON-1 CDX models was measured at indicated time points after treatment with axitinib at 25 and 40 mg/day, cabozantinib at 15 and 30 mg/kg/day, sunitinib at 20 and 40 mg/kg/day, and vehicle. Tumor volume in mm^3 and time in days are shown on the y- and x-axes respectively. All treatments except low-dose sunitinib elicited tumor responses. **B.** Representative tumor images for each treatment condition are shown. Endpoint tumor weights in mg are also shown on the y-axis for each condition. Axitinib and cabozantinib, but not sunitinib, significantly reduced tumor weight at the endpoint **C.** CD31 staining was

performed on CDX tumors after treatment. Representative IHC images are shown for each condition. The percentage of CD31-stained area is shown on the y-axis and was evaluated in at least 5 bright fields per tumor. All treatments significantly reduced the CD31-positive (endothelium) area compared to the vehicle. Data are expressed as the mean ± SD of 3-4 mice. *Ns, non-significant*. * $p < 0.05$ and ** $p < 0.01$ were considered statistically significant. *P-values* were calculated between the MKI- and vehicle-treated mice at each time point. Veh, vehicle. Axi, axitinib, Cab, cabozantinib. Sun, sunitinib

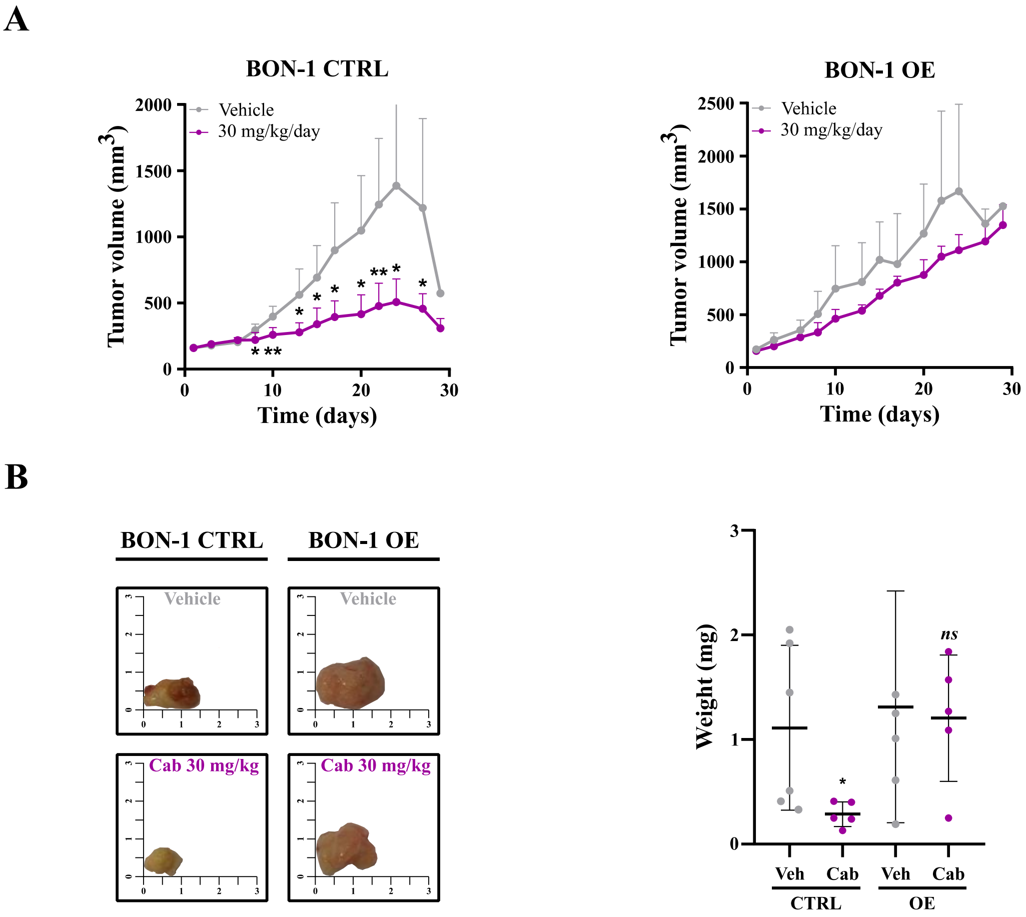

Figure 27. OPN promotes resistance to cabozantinib in NET CDX mouse models. A. Tumor volume in BON-1 CTRL and OPN OE CDX models was measured at indicated time points following treatment with cabozantinib at 30 mg/kg/day or vehicle. Cabozantinib significantly reduced tumor growth in BON-1 CTRL CDXs, but not in OPN OE CDXs**. B.** Representative tumor images for each treatment condition are shown. Endpoint tumor weights are also shown on the y-axis for each condition. Cabozantinib significantly reduced tumor weight in BON-1 CTRL CDXs, but not in OPN OE CDXs. Data are expressed as the mean ± SD of 5 or 6 mice. *Ns, non-significant.* * $p < 0.05$ and ** $p < 0.01$ were considered statistically significant. *P-values* were calculated between the MKI- and vehicle-treated mice at each time point. Veh, vehicle. Cab, cabozantinib.

DISCUSSION

Discussion

Neuroendocrine tumors are highly vascularized neoplasms, consistent with the physiological role of vasculature in endocrine tissues, and angiogenesis plays a critical role in their tumorigenesis and progression. These tumors often overexpress proangiogenic factors including VEGF ligands and their receptors, among others (89,90,94–96,98), and certain NET subtypes exhibit particularly enhanced proangiogenic activity (25,38,40,41,43,251,297). This has led to the approval of antiangiogenic MKIs as an anticancer therapy for NET patients (64,131,132). While these drugs are active in Pan- and EP-NETs (135,137,142), the overall magnitude of the effect is limited, not all patients benefit from this therapeutic strategy, and even those who initially respond eventually develop resistance and experience disease progression over time. In this context, the main objective of this project was to identify predictive biomarkers of response to angiogenesis inhibitors in NETs and to elucidate the molecular mechanisms involved. To this end, we analyzed biological samples from patients enrolled in a randomized, placebo-controlled, international, phase 3 clinical trial assessing axitinib versus placebo, both in combination with SSA, in patients with advanced EP-NETs (AXINET trial, EudraCT number 2011-001550-29). Moreover, selected candidates were validated in independent patient cohorts and preclinical models.

1. A 3-gene signature (*REXO1L2P, ATXN7* and *SPP1*) predicts efficacy of axitinib in NETs

The AXINET trial enrolled 256 patients with advanced EP-NETs who were randomly assigned (1:1) to receive octreotide LAR with either axitinib or placebo. Enrolled patients could optionally consent to donate plasma and/or tumor samples for translational research studies. The primary endpoint was PFS per investigator assessment. In addition, a central blinded radiologic review was also performed in 239 patients (93%). By central blinded review, axitinib demonstrated a significant improvement in ORR (13.2 vs. 3.2%, *OR: 4.59,* $p = 0.007$) and PFS (16.6 vs. 9.9 months, *HR: 0.71,* $p = 0.017$) compared to placebo (138). PFS is the preferred primary efficacy endpoint universally accepted by regulatory authorities and clinical researchers in diseases with prolonged overall survival, such as NETs, and in the context of primarily cytostatic rather than cytotoxic drugs such as angiogenesis inhibitors. For the development of our signature, we chose the best tumor shrinkage and PFS per central blinded reading rather than per investigator assessment to minimize assessment bias.

First, we evaluated the transcriptomic profile of 126 NETs from patients enrolled in the AXINET trial who provided informed consent and had exceeding tumor tissue available for translational studies. We identified that the expression of 20 genes was significantly associated with PFS exclusively in axitinib-treated patients ($p < 0.01$), although none remained significant after adjustment for multiple testing ($FDR < 0.05$). Of these, interaction tests showed that 9 genes had a significantly different association with PFS by treatment arm (axitinib vs. placebo), and 2 were of borderline significance, further supporting their potential predictive role of axitinib efficacy. Regularized linear regression reduced and optimized the model to 3 genes (*SPP1*, *REXO1L2P* and *ATXN7)*, which were associated with both PFS and tumor shrinkage in response to axitinib, but not to placebo. Moreover, pairwise correlation analysis confirmed that these genes provided independent, non-redundant information. These candidates were therefore selected to develop our predictive signature, which allows classification of patients' risk of progression based on their individual expression of *SPP1*, *REXO1L2P* and *ATXN7*.

The three genes of the signature have different biological functions. *REXO1L2P* is a pseudogene with no known coding protein. Its homolog, REXO1, is a nuclear exonuclease involved in the hydrolysis of phosphodiester bonds in nucleic acids. A recent paper suggests that Circ-CCDC66 may increase REXO1 levels and promote cervical cancer progression (298). However, the role of *REXO1L2P* or REXO1 in angiogenesis, treatment resistance or NETs remains unknown.

ATXN7 encodes for ataxin-7, a protein best known for its involvement in spinocerebellar ataxia type 7 and reticular degeneration. These diseases result from CAG repeat expansions in the coding region, resulting in polyglutamine tails that disrupt normal protein function (299). Beyond neurodegenerative diseases, *ATXN7* has also been implicated in cancer. Several studies suggest that circulating ATXN7 promotes breast cancer progression and increases resistance to doxorubicin (300), and accelerates malignancy in NSCLC (301). In addition, *ATXN7* fusions and mutations have been observed in CRC and thyroid cancer, respectively (302,303), and ATXN7 expression levels have been associated with worse survival in HCC (304). ATXN7 is also a component of the STAGA co-activator complex, which regulates transcription and chromatin modification. It mediates interactions with the CRX transcription factor involved in photoreceptor cell differentiation. While the role of ATXN7 in chromatin modification and cancer may be of interest in the context of NETs (299,305), its role in angiogenesis and response to AAT with MKIs remains to be elucidated.

Finally, *SPP1* encodes for osteopontin (OPN), a secreted phosphoprotein involved in bone and tissue remodeling (179,180), as well as in the immune system, where it plays a key role in macrophages (187–193), dendritic cells (194,306) and lymphocytes (196–198). OPN has been extensively studied in cancer, where it is typically associated with higher grade, more advanced disease, an increased risk of recurrence and poor prognosis (200,201,204,206). OPN can also promote cell proliferation, migration and adhesion in cancer cells (214,216,218). Notably, OPN levels correlate with VEGF, and are crucial for tumor angiogenesis in several human cancers, including melanoma, lung, pancreatic and gastric cancer (219,235–237). Interestingly, OPN plays an important role in drug resistance, particularly to MKIs in several cancer types. Some authors have reported that OPN levels are associated with PFS in patients with metastatic RCC treated with sorafenib alone or in combination with IFN-α (263). Moreover, a systematic review suggested that OPN is a prognostic biomarker for PFS in response to VEGF-targeted therapy in RCC (261), and preliminary data also suggest that OPN may be relevant in the response of Pan-NETs to MKIs. In this regard, Jimenez Fonseca *et al.* reported that higher OPN levels were associated with shorter PFS in patients treated with sunitinib (160). In addition, baseline OPN plasma levels were predictive of poorer outcomes in 38 NEN patients, correlating with significantly shorter PFS in NET patients (277). However, these studies lacked adequate controls, which made it difficult to differentiate between prognostic and predictive biomarkers.

Unlike previous studies (155,157), we combined the expression levels of our candidate genes into a single numeric score to assess their combined predictive value for axitinib benefit. We then classified patients as high or low risk based on the population median signature score, supported by the optimal cutoff value from ROC analysis, which was very close to the median. In our discovery cohort (N = 126), axitinib-treated patients with high signature scores showed significantly better PFS than patients with low scores (38.5 vs. 11.6 months, *HR: 0.31 (0.16 – 0.59), $p < 0.001$*). Notably, an opposite, non-significant trend was observed in placebo-treated patients with high and low scores (8.8 vs. 12.0 months, *HR: 1.51 (0.86 – 2.63), $p = 0.21$*). Accordingly, a significant interaction was observed between the signature and the treatment arm (*HR: $4.83 \cdot 10^{-3}$ ($1.12 \cdot 10^{-4}$ – 0.20),* *p = 0.005*). These data suggest that axitinib responders (high-score patients) have a more aggressive phenotype and may respond poorly to other therapies, such as SSA, compared to low-score patients. This is consistent with previous transcriptomic analyses in NETs, where patients of the MLP subtype, characterized by enrichment in genes related to fibroblasts/stroma, stem cells, and hypoxia, were associated with a more metastatic and clinically aggressive subtype (40,102). Importantly, the 3-gene signature score was also associated with tumor shrinkage in axitinib-treated but not in placebo-treated patients, further supporting its predictive ability of axitinib benefit. Finally, multivariable analysis confirmed the independent predictive value of the 3-gene signature for PFS, adjusted for tumor grade, primary tumor location, presence or absence of carcinoid syndrome, time since diagnosis, and the number of prior lines of therapy.

2. NETs that do not respond to axitinib are enriched in pathways and cell populations involved in treatment resistance

The second aim of this project was to identify distinctive molecular features involved in the response or resistance to axitinib in NET patients. GSEA revealed that low-score tumors (axitinib non-responders) were enriched in gene sets related to hypoxia, glycolysis, angiogenesis, mTOR signaling and EMT pathways, which may reflect some of the intrinsic mechanisms of resistance to angiogenesis inhibitors in NETs. Indeed, hypoxia, typically induced by VEGFR inhibition, increases tumor invasiveness and metastasis, and promotes treatment resistance through the activation of the HIF1α signaling pathway (66). Similarly, EMT often leads to vascular mimicry, in which both cancer and endothelial cells acquire EMT and stem-like properties. This enables cancer cells to adapt, form tube-like structures and establish connections with the surrounding microcirculation (67). In addition, EMT also promotes vascular co-option, allowing cancer cells to migrate and hijack preexisting blood vessels, thereby incorporating them into the tumor (67,69). These two mechanisms render VEGF-targeted therapy ineffective and may lead to disease progression, metastasis and resistance. Accordingly, we have also observed an enrichment in a gene set of cancer cell-specific EMT genes. Interestingly. this gene set included *CD44* and *ITGAV*, receptors of OPN, further supporting the role of OPN and EMT in the response to MKIs in NETs (288). The acquisition of alternative proangiogenic molecular pathways is also a well-known mechanism of resistance to AAT (108). For instance, the enrichment of mTOR pathway genes in low score patients may represent an alternative proangiogenic signaling pathway, as studies in the RT2 mouse model suggest that mTOR could be implicated in a metabolic symbiosis involved in the resistance to AAT (149).

In terms of response mechanisms, only the Notch pathway was significantly enriched in high-score patients (axitinib responders). Notch signaling inhibits neuroendocrine differentiation, a process typically associated with an aggressive behavior (307). However, the genes at the edge of this gene set included both repressors of the Notch signaling pathway, such as *NUMB* and *CIR1*, and coactivators, such as *EP300* (308), making it difficult to draw a clear conclusion about the role of Notch signaling in this context.

Cell populations from the tumor microenvironment are also implicated in the response to angiogenesis inhibitors. This is the case for proangiogenic monocytes and tumor-associated macrophages, which can promote revascularization by expressing a variety of cytokines, growth factors and proteases (66,67). VEGFR inhibition in Pan-NETs has been shown to recruit BMDCs, including endothelial progenitor cells, pro-angiogenic monocytic cells and TIE2-expressing macrophages. These cells contribute to the formation of new blood vessels and the establishment of the premetastatic niche (146,150,151). Consistent with these findings, we identified an enrichment of M1 macrophages in low-score patients, although the M1 subtype is usually associated with pro-inflammatory and cytotoxic antitumor activity (296,309). These findings are consistent with the fact that OPN (*SPP1*), which is highly expressed in low-score patients, plays a key role in macrophage infiltration, adhesion, migration, differentiation, and phagocytosis (187–193). They also support the growing evidence of macrophages' role in NET tumorigenesis, progression, and response to therapy(310–312). Finally, low-score patients were also enriched in stroma score. In line with this observation, several reports have suggested that stromal populations, such as fibroblasts or pericytes, play a critical role in resistance to AATs. Indeed, pericytes can be recruited by endothelial cells in response to VEGFR inhibition, providing protection against VEGF depletion and promoting endothelial cell survival (145). Increased pericyte coverage has also been observed in Pan-NETs, where it shields endothelial cells from the effects of VEGFR-2 targeted AAT (153). Fibroblasts can further support tumor angiogenesis by expressing various alternative proangiogenic genes and recruiting additional BMDCs to the tumor (296). Thus, this stromal enrichment is also consistent with OPN role in the tumor microenvironment (232,233).

3. The 3-gene signature predicts efficacy of sunitinib in an external cohort of NET patients

A key aspect of this work was the validation of our findings using different techniques, across different samples, and in independent patient cohorts. First, we confirmed the association of *SPP1*, *REXO1L2P* and the signature with PFS in tumor samples from an independent cohort of NET patients treated with MKIs or SSA in routine clinical practice. As in the discovery cohort, we confirmed the predictive specificity of our biomarkers for MKI-treated patients, but not for SSA-treated patients. Remarkably, we were able to validate our data despite the small sample size of this independent cohort (N = 29), which consisted of NET patients with relatively different clinical characteristics from those in the discovery cohort. MKI-treated patients were highly pretreated and enriched in pancreatic primary tumor origin, while SSA-treated patients were predominantly G1 and treatment-naïve. Our validation also suggests that our signature may be useful for other antiangiogenic MKIs beyond axitinib. This is consistent with the reported predictive ability of OPN for other MKIs such as sorafenib in RCC (263) and sunitinib in Pan-NETs (160). Exploratory GSEA and cell population's analysis in this cohort showed a significant enrichment in tumor-specific EMT and angiogenesis in low-score patients. Nevertheless, the small sample size and heterogeneity of this cohort limited the statistical power to draw firm conclusions regarding the molecular features involved in the response and resistance to sunitinib.

4. Plasma osteopontin (OPN) levels predict efficacy of antiangiogenic MKIs in NETs

A key challenge in translational science is finding simple and feasible ways to translate findings into clinical practice. Although gene expression analysis has become more affordable and accessible to researchers, it still requires specialized, often expensive equipment and complex data analysis. Therefore, we sought to validate the predictive value of OPN in patients' plasma using ELISA, which could be easily implemented in the clinical setting, offering a less invasive approach and allowing for real-time longitudinal monitoring.

OPN is a secreted protein and its plasma levels have previously been associated with advanced disease and worse clinical outcomes in other cancers (207,208,211). Additionally, OPN plasma levels have been associated with poorer prognosis in small retrospective cohorts of NENs, including patients treated with sunitinib (160,277). As opposed to previous studies, the randomized, double-blind, placebo-controlled AXINET trial allowed us to differentiate the predictive and prognostic value of OPN in a large cohort of prospectively monitored patients. We first assessed OPN levels in plasma samples from patients in our discovery cohort (N = 106) and confirmed that OPN plasma levels were significantly associated with PFS in axitinib-treated patients (13.2 vs. 38.5 months in patients with high vs. low OPN levels, respectively, *HR: 2.04 (0.99 – 4.22), p = 0.053*), but not in placebo-treated patients. Moreover, a significant interaction between OPN plasma levels and treatment arm (*HR: 1.018 (1.002 – 1.035), p = 0.026*) confirmed the treatment-dependent association of OPN levels with PFS. Multivariable analysis validated the independent predictive value of this surrogate biomarker of axitinib efficacy, adjusting for grade, primary tumor location, carcinoid syndrome, time since diagnosis and the number of prior lines of therapy.

However, no significant correlation was observed between plasma OPN levels and *SPP1* gene expression or signature score. Notably, only 55% of patients classified as low-signature score had high OPN plasma levels (non-responders), and 52% of patients with high signature scores had low OPN plasma levels (responders). While this is not entirely unexpected, since it is well known that mRNA-protein correlations are often imperfect (313–315), it suggests that OPN may originate from multiple sources, including cell populations in the tumor microenvironment. In addition, because the signature included three genes, results may differ compared to OPN alone. The complexity is further compounded by the fact that plasma OPN levels reflect secretion, which could be influenced by other secretion-related mechanisms or host-derived OPN levels. In fact, some studies have shown that both host- and tumor-derived OPN may cooperate or play different roles in cancer. For instance, host-derived OPN promoted macrophage recruitment and angiogenesis, whereas tumor-derived OPN impaired apoptosis and promoted vascular permeability independently of VEGF in lung cancer (253). Similarly, in melanoma, host-derived stromal OPN promoted tumor progression, angiogenesis and metastasis *in vivo* and vascular mimicry *in vitro* (249). In addition, some authors have reported that tumorless mice can upregulate OPN production in response to MKIs, suggesting a role for host-derived OPN in the response to these drugs (316).

To identify the source of OPN in NET patients, we examined the expression of *SPP1* and the OPN receptor genes, *CD44*, integrin β3 (*ITGB3)* and *ITGAV* in NETs of pancreatic, lung, intestinal and gastric origin using publicly available single-cell RNA-seq data.

Interestingly, *SPP1* was predominantly expressed in macrophages and dendritic cells and not in cancer cells. *CD44* was also highly expressed in macrophages and dendritic cells, as well as in monocytes and NK cells. *ITGB3* and *ITGAV* expression levels were low in these tumors (data not shown). These findings are consistent with the well-established role of OPN in macrophages (187–193) and DCs (194,306) in physiological conditions and in cancer, where OPN induces angiogenesis in melanoma by increasing macrophage infiltration and COX-2-dependent PGE2 production (317); and where OPN expression in DCs enhances tumor migration (195). Therefore, these data suggest that OPN may be derived from immune cells and that these populations may have an important role in the response of NETs to AAT with MKIs. However, further experiments and a larger single-cell RNA-seq cohort are needed to confirm these preliminary findings.

The predictive capacity of OPN plasma levels was then validated in two independent cohorts: AXINET trial patients who had only plasma samples available and were thus not included in the discovery cohort (N = 87), and TALENT trial patients treated with lenvatinib (N = 99). Analysis of OPN plasma levels using ELISA in the AXINET validation cohort confirmed the predictive value of OPN in the response of EP-NETs to axitinib. Moreover, the analysis of OPN plasma levels in the TALENT cohort confirmed the predictive capacity of OPN in the response of Pan- and EP-NETs to other MKIs such as lenvatinib. Taken together, the validation in these two external cohorts further supports the critical role of OPN in the response of NETs to antiangiogenic MKIs.

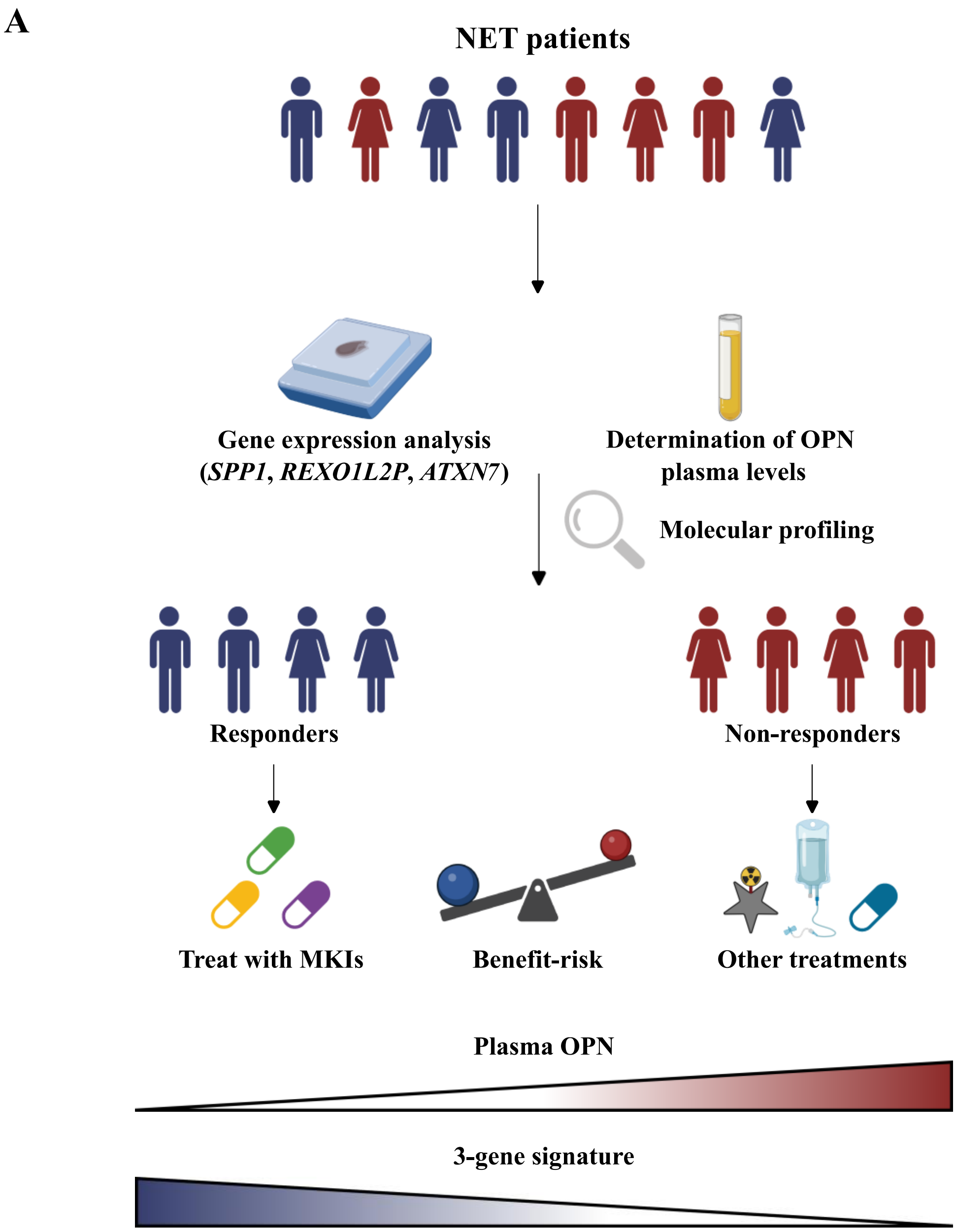

Figure 28. Schematic representation of the discovered biomarkers and their clinical implications. A. The signature and OPN plasma levels could be used in clinical practice to guide therapeutic decisions regarding angiogenesis inhibitors, increasing efficacy and reducing the cost and unnecessary toxicity of these drugs, ultimately improving the benefit-risk ratio in NET patients.

5. OPN promotes oncogenic functions in NETs and drives response to AAT, inducing resistance mechanisms in endothelial cells *in vitro*

Given the critical role of OPN in the response to antiangiogenic MKIs in NET patients, we also explored the role of OPN in neuroendocrine tumor cells and in the underlying molecular mechanisms driving the response to these drugs. A number of reports have demonstrated that OPN plays a relevant role in cancer (212,213,222,224), angiogenesis (238,239,241,248) and tumor resistance (259,265,266,268,270) through tumor-intrinsic mechanisms, but specific information in NETs is scarce. To date, only two case reports of a gastric carcinoid tumor and a LCNEC have described positive OPN staining (274,275). More recently, OPN isoforms have also been shown to be expressed in medullary thyroid carcinoma (276). In line with this, we show that both OPN and its receptor, integrin αvβ3, are expressed in NET cell lines. However, it remains to be confirmed whether integrin αv and integrin β3 form a functional heterodimer in NET cell lines. As reported in other studies, both CD44 and integrin αvβ3 were highly expressed in HUVEC (318,319). However, CD44 expression was not observed in NET cell lines, suggesting that OPN may signal through different receptors in cancer and stromal cell populations.

As described for other cancers (212,213,222,224), upregulation of OPN expression in NET cell lines promoted proliferation, migration and colony formation, whereas downregulation of OPN had the opposite effect. The only exception was UMC-11 OPN OE cells, which exhibit no significant change in proliferation and clonogenicity, likely because these cells already express high levels of OPN.

A growing body of evidence has shown that OPN promotes drug resistance in cancer (249,265,266,268,269), particularly to VEGF-targeted therapies (261), including MKIs such as sorafenib (263) or pazopanib (262). We therefore investigated the role of OPN in the response to MKIs in NET cell lines. However, viability assays performed in OPN OE and KD cell lines did not show significantly different IC50 for any of the MKIs in any of the cell lines studied. This may be due to the relatively low expression of VEGFR-2, the major target of these MKIs, in cancer cells. Moreover, AAT with MKIs also targets endothelial cells and is primarily an angiogenesis inhibitor which cannot be properly assessed in this *in vitro* model. Similarly, OPN is also involved in the regulation of immune cells, particularly macrophages (187–193) and dendritic cells (306), which are absent in this model but may contribute to the acquisition of resistance.

Next, we evaluated how OPN may promote resistance to MKIs *in vitro* in endothelial cells using viability and tube formation assays. Interestingly, HUVEC cultured in 10% of BON-1 OPN OE conditioned medium had a significantly higher IC50 to antiangiogenic MKIs such as axitinib and cabozantinib compared to HUVEC grown in CTRL media, suggesting that OPN promotes resistance to these MKIs *in vitro*. However, the effect was modest, with only a 1.8-fold increase for cabozantinib and a 2.1-fold increase for axitinib. This is likely due to the oversimplified model used, which does not capture the full range of physiological roles that OPN plays in immune and stromal cells. To better study the role of OPN in angiogenesis and response to MKIs *in vitro*, we performed tube formation assays. In this setting, conditioned medium from BON-1 OPN overexpressing cells enhanced HUVEC tube formation assays compared to BON-1 CTRL conditioned medium. This is consistent with previous studies showing that OPN promotes motility, proliferation, and tube formation in endothelial cells (247,248). Moreover, HUVEC cultured with OPN overexpressing conditioned medium showed higher tube formation capacity compared to those cultured in control medium when treated with axitinib. Nevertheless, a similar reduction in angiogenesis was observed between conditions upon axitinib treatment. This suggests that OPN alone may not be able to induce complete resistance to axitinib, and that this model may not fully recapitulate the role OPN plays in NET patients. Again, immune cells or other factors may contribute to the acquisition of resistance.

6. OPN drives resistance to antiangiogenic MKIs in *in vivo* models of NETs

Finally, we analyzed the role of OPN in modulating the response to AAT MKIs *in vivo.* These models are a better setting to evaluate sensitivity to these drugs because their mechanisms of action and resistance, including OPN-driven mechanisms, involve cells from the tumor microenvironment (145).

We first studied the role of OPN in the response to axitinib in the chorioallantoic membrane (CAM) xenograft model. This model is widely used in the field to study angiogenesis as it offers a rapid assay that can be easily adapted to study angiogenesis-dependent processes such as tumor growth under different conditions, including AAT (320). We engrafted BON-1 cell lines with OPN OE and their controls into CAMs of chicken embryos and treated them with either DMSO or axitinib. OPN overexpression did not increase tumor growth in DMSO-treated xenografts, and axitinib did not elicit a tumor response in either CTRL or OPN OE BON-1 CAM xenografts. This result may be attributed to certain limitations of the model. The first one was the high variability in tumor growth between xenografts. Despite engrafting the same number of cells, the tumors reached very different sizes at the onset of treatment. To try to minimize this size variability, we attempted to balance the treatment groups based on tumor size, although tumor volume was difficult to assess by eye at this stage. In addition, many chicken embryos died during the treatment window, some due to excessive tumor growth and others due to infections, which were frequent in this model. Again, this may have biased the xenografts that reached the endpoint and the ultrasound volume analysis. Additionally, this model provided a very narrow treatment window of opportunity of 6 days, which may not have been sufficient to detect differences between slow-growing tumors like NETs, treated with primarily cytostatic drugs such as angiogenesis inhibitors. Finally, the topical treatment also posed limitations, as we cannot really know the actual dose reaching the tumor. Similar challenges were faced for the OPN knockdown experiment, where no differences in tumor volume were seen in response to either DMSO or axitinib. Despite this, we evaluated tumor angiogenesis by immunofluorescence of DyLight™ 649-labelled LCA that was injected intravenously into the CAM xenografts. LCA binds to α-linked mannose residues present on the luminal surface of the endothelium (321). Interestingly, BON-1 OPN OE xenografts had increased lectin-positive area compared to controls, both when treated with DMSO or axitinib. However, the differences were not statistically significant. In this regard, dye injections limited the statistical power of the experiment, as only a few CAM xenografts could be effectively injected, and for instance, only one DMSO-treated BON-1 CTRL xenograft could be analyzed. Another limitation was that CAMs xenografts could not be perfused, and thus blood cells, which emit a lot of autofluorescence, interfered with the immunofluorescence analysis. We are currently working to confirm these results using immunohistochemistry for CD31.

Finally, we decided to study the role of OPN in mouse models that do not have most of these limitations. In fact, treatment started with the same tumor volume for all mice, and the window of opportunity provided more than enough time to assess the tumor growth and response to the AAT. Moreover, the treatment was administered intraperitoneally, which ensured better drug delivery to the tumor. Importantly, a significant reduction in tumor growth and weight was observed in cabozantinib-treated CTRL BON-1 CDXs, but not in OPN OE CDXs, supporting our hypothesis that OPN overexpression induces resistance to MKIs *in vivo.* This aligns with several studies highlighting the critical role of OPN in angiogenesis (249,252) and treatment resistance to VEGFR-targeted therapies (261) such as sorafenib (263), pazopanib (262) or sunitinib (160). Tumors are currently being analyzed for CD31 (endothelium) or CD68 (macrophages) staining by immunohistochemistry to see what role they play in the acquisition of the resistance to AAT.

7. Limitations of the study

An important limitation of this study is that tumor samples for gene expression were not collected at the time of study entry, as archival tissue samples were accepted for pragmatic reasons. All patients enrolled in the AXINET trial had metastatic disease at study entry, but some of them were diagnosed with stage IV disease, while others had early-stage disease at diagnosis and eventually developed metastases over the course of the disease. As a result, many of the analyzed tumor samples were obtained prior to the development of metastatic disease. Additionally, over 50% of the patients received prior systemic therapies, which could have altered the molecular profile of the tumor upon selective pressure, potentially affecting gene expression at the time of axitinib treatment. Nevertheless, prior AAT was not permitted. Fortunately, 52 patients (41%) in our discovery cohort received axitinib or placebo as their first systemic therapy, ensuring that their tumors were not exposed to prior treatment pressure. Importantly, exploratory subgroup analysis suggests that prior treatments did not affect the predictive capacity of the signature (data not shown).

However, the most evident challenge to potentially implement our findings into the clinical setting is determining an optimal threshold for the signature and for plasma OPN levels that are valid across multiple cohorts. In this regard, no differences were observed between the AXINET cohort and the H12O validation cohort in scores between patients with either high or low scores (Supplementary Figure 11). Moreover, when we analyzed the predictive capacity of plasma OPN levels in lenvatinib-treated patients using the discovery cohort cutoff, we found that subgroups based on OPN levels were still significantly associated with PFS. This may help establish an objective threshold for clinical implementation, independent of clinical characteristics or the MKI used.

Another limitation of this study is the scarce number of *in vitro* and *in vivo* models available to study NETs. For instance, no small intestinal NET cell line such as P-STS or GOT-1 was available in our laboratory (322). Moreover, these 2D cultures usually do not recapitulate the whole tumor architecture and microenvironment, which are crucial for studying drugs such as antiangiogenic MKIs. In this regard, NEN organoid cell lines have been recently established, but almost all of them account for high grade lung NECs (323,324). Similarly, no successful well-differentiated NET patient-derived xenograft has been established. Thus, we have dissected the role of OPN in NET response to MKIs by studying separately the different components *in vitro*, including cancer and endothelial cells. Additionally, to overcome some of these limitations, we studied the role of OPN in the response to MKIs *in vivo* using two different models: CAM xenografts and mouse CDXs. These models allowed us to evaluate the role of OPN in the response to these drugs, not only in cancer cells, but also in the tumor microenvironment. However, the chicken embryo does not have a fully functional immune system between ED9 and ED20 (325). Similarly, athymic mice lack some of the key immune cell populations, including T cells. Importantly, these mouse models do have macrophages, and we are currently trying to assess their role in this context. However, the role of OPN in other immune cells, such as dendritic cells or lymphocytes, remains to be elucidated. In this regard, it would be interesting to study OPN in immunocompetent mouse models such as RT2 mice (104), but again, these models are rare and limited to Pan-NETs.

CONCLUSIONS

Conclusions

1. A 3-gene signature based on tumor expression levels of *REXO1L2P*, *ATXN7* and *SPP1* predicts the efficacy of axitinib, an anti-angiogenic MKI, in extrapancreatic NETs.
2. NETs with low signature scores, and thus resistant to antiangiogenic therapy, are enriched in EMT, hypoxia and mTOR signaling pathway genes, as well as in immune and stromal populations, such as macrophages, that have been previously implicated in treatment resistance.
3. The predictive value of the 3-gene signature, and more specifically, *SPP1* and *REXO1L2P*, was validated in an external cohort of patients with pancreatic and extrapancreatic NETs treated with antiangiogenic MKIs.
4. Detection of plasma levels of osteopontin (OPN), the protein product of *SPP1*, is sufficient to predict the efficacy of axitinib in extrapancreatic NETs, and its predictive value has been externally validated for other anti-angiogenic MKIs such as lenvatinib, in pancreatic and extrapancreatic NETs.
5. OPN plays a key role in promoting oncogenic functions such as tumor cell proliferation, migration and clonogenicity in pancreatic and extrapancreatic NET cell lines *in vitro*, and induces tube formation and resistance to AAT in endothelial cells.
6. OPN drives resistance to anti-angiogenic MKIs in CDX mouse models of NETs.

REFERENCES

References

1. Andersson-Rolf A, Clevers H, Dayton TL. Diffuse Hormonal Systems. In: Feingold KR, Anawalt B, Blackman MR, Boyce A, Chrousos G, Corpas E, et al., editors. Endotext [Internet]. South Dartmouth (MA): MDText.com, Inc.; 2021.

2. Garg A, Sui P, Verheyden JM, Young LR, Sun X. Consider the lung as a sensory organ: A tip from pulmonary neuroendocrine cells. Curr Top Dev Biol. 2019;132:67–89.

3. Kidd M, Modlin IM, Bodei L, Drozdov I. Decoding the Molecular and Mutational Ambiguities of Gastroenteropancreatic Neuroendocrine Neoplasm Pathobiology. Cell Mol Gastroenterol Hepatol. 2015 Jan 12;1(2):131–53.

4. Halperin DM, Shen C, Dasari A, Xu Y, Chu Y, Zhou S, et al. Frequency of carcinoid syndrome at neuroendocrine tumour diagnosis: a population-based study. The Lancet Oncology. 2017 Apr 1;18(4):525–34.

5. Hauso Ø, Gustafsson BI, Waldum HL. Long slender cytoplasmic extensions: a common feature of neuroendocrine cells? J Neuroendocrinol. 2007 Sep;19(9):739–42.

6. Saghafinia S, Homicsko K, Di Domenico A, Wullschleger S, Perren A, Marinoni I, et al. Cancer cells retrace a stepwise differentiation program during malignant progression. Cancer Discov. 2021 Apr 28;candisc.1637.2020.

7. Cuny T, Herder W de, Barlier A, Hofland LJ. Role of the tumor microenvironment in digestive neuroendocrine tumors. Endocrine-Related Cancer. 2018 Nov 1;25(11):R519–44.

8. White BE, Rous B, Chandrakumaran K, Wong K, Bouvier C, Van Hemelrijck M, et al. Incidence and survival of neuroendocrine neoplasia in England 1995–2018: A retrospective, population-based study. Lancet Reg Health Eur. 2022 Sep 23;23:100510.

9. Dasari A, Shen C, Halperin D, Zhao B, Zhou S, Xu Y, et al. Trends in the Incidence, Prevalence, and Survival Outcomes in Patients With Neuroendocrine Tumors in the United States. JAMA Oncol. 2017 Oct;3(10):1335–42.

10. Gustafsson BI, Bakke I, Tømmerås K, Waldum HL. A new method for visualization of gut mucosal cells, describing the enterochromaffin cell in the rat gastrointestinal tract. Scandinavian Journal of Gastroenterology. 2006 Jan;41(4):390–5.

11. Schimmack S, Svejda B, Lawrence B, Kidd M, Modlin IM. The diversity and commonalities of gastroenteropancreatic neuroendocrine tumors. Langenbecks Arch Surg. 2011 Mar;396(3):273–98.

12. Couvelard A, Cazes A, Cros J. Updates in histopathological classification and tissue biomarkers of digestive neuroendocrine neoplasms: What the clinician should know. Best Practice & Research Clinical Endocrinology & Metabolism. 2023 Sep 1;37(5):101795.

13. Chauhan A, Kohn E, Del Rivero J. Neuroendocrine Tumors: Less known, often misunderstood and rapidly growing. JAMA Oncol. 2020 Jan 1;6(1):21–2.

14. Faggiano A, Ferolla P, Grimaldi F, Campana D, Manzoni M, Davì MV, et al. Natural history of gastro-entero-pancreatic and thoracic neuroendocrine tumors. Data from a large prospective and retrospective Italian epidemiological study: the NET management study. J Endocrinol Invest. 2012 Oct;35(9):817–23.

15. Ramundo V, Milone F, Severino R, Savastano S, Di Somma C, Vuolo L, et al. Clinical and prognostic implications of the genetic diagnosis of hereditary NET syndromes in asymptomatic patients. Horm Metab Res. 2011 Oct;43(11):794–800.

16. Busygina V, Bale AE. Multiple Endocrine Neoplasia Type 1 (MEN1) as a Cancer Predisposition Syndrome: Clues into the Mechanisms of MEN1-related Carcinogenesis. The Yale Journal of Biology and Medicine. 2007 Oct;79(3–4):105.

17. McDonnell JE, Gild ML, Clifton-Bligh RJ, Robinson BG. Multiple endocrine neoplasia: an update. Intern Med J. 2019 Aug;49(8):954–61.

18. Sims KB. Von Hippel-Lindau disease: gene to bedside. Current Opinion in Neurology. 2001 Dec;14(6):695.

19. Zhuang Z, Frerich JM, Huntoon K, Yang C, Merrill MJ, Abdullaev Z, et al. Tumor derived vasculogenesis in von Hippel-Lindau disease-associated tumors. Sci Rep. 2014 Feb 17;4(1):4102.

20. Dworakowska D, Grossman AB. Are neuroendocrine tumours a feature of tuberous sclerosis? A systematic review. 2009 Mar 1.

21. Relles D, Baek J, Witkiewicz A, Yeo CJ. Periampullary and Duodenal Neoplasms in Neurofibromatosis Type 1: Two Cases and an Updated 20-Year Review of the Literature Yielding 76 Cases. Journal of Gastrointestinal Surgery. 2010 Jun 1;14(6):1052–61.

22. Banck MS, Kanwar R, Kulkarni AA, Boora GK, Metge F, Kipp BR, et al. The genomic landscape of small intestine neuroendocrine tumors. J Clin Invest. 2013 Jun;123(6):2502–8.

23. Fernandez-Cuesta L, Peifer M, Lu X, Sun R, Ozretić L, Seidal D, et al. Frequent mutations in chromatin-remodelling genes in pulmonary carcinoids. Nat Commun. 2014 Mar 27;5:3518.

24. Francis JM, Kiezun A, Ramos AH, Serra S, Pedamallu CS, Qian ZR, et al. Somatic mutation of CDKN1B in small intestine neuroendocrine tumors. Nat Genet. 2013 Dec;45(12):1483–6.

25. Scarpa A, Chang DK, Nones K, Corbo V, Patch AM, Bailey P, et al. Whole-genome landscape of pancreatic neuroendocrine tumours. Nature. 2017 02;543(7643):65–71.

26. Missiaglia E, Dalai I, Barbi S, Beghelli S, Falconi M, della Peruta M, et al. Pancreatic Endocrine Tumors: Expression Profiling Evidences a Role for AKT-mTOR Pathway. J Clin Oncol. 2010 Jan 10;28(2):245–55.

27. Cao Y, Gao Z, Li L, Jiang X, Shan A, Cai J, et al. Whole exome sequencing of insulinoma reveals recurrent T372R mutations in YY1. Nature Communications. 2013 Dec 10;4(1):2810.

28. Jiao Y, Shi C, Edil BH, de Wilde RF, Klimstra DS, Maitra A, et al. DAXX/ATRX, MEN1, and mTOR pathway genes are frequently altered in pancreatic neuroendocrine tumors. Science. 2011 Mar 4;331(6021):1199–203.

29. Kawasaki K, Toshimitsu K, Matano M, Fujita M, Fujii M, Togasaki K, et al. An Organoid Biobank of Neuroendocrine Neoplasms Enables Genotype-Phenotype Mapping. Cell. 2020 Oct 30.

30. Hong X, Qiao S, Li F, Wang W, Jiang R, Wu H, et al. Whole-genome sequencing reveals distinct genetic bases for insulinomas and non-functional pancreatic neuroendocrine tumours: leading to a new classification system. Gut. 2020 May;69(5):877–87.

31. Elias E, Ardalan A, Lindberg M, Reinsbach SE, Muth A, Nilsson O, et al. Independent somatic evolution underlies clustered neuroendocrine tumors in the human small intestine. Nat Commun. 2021 Nov 4;12(1):6367.

32. Karpathakis A, Dibra H, Pipinikas C, Feber A, Morris T, Francis J, et al. Prognostic Impact of Novel Molecular Subtypes of Small Intestinal Neuroendocrine Tumor. Clin Cancer Res. 2016 Jan 1;22(1):250–8.

33. Laddha SV, da Silva EM, Robzyk K, Untch BR, Ke H, Rekhtman N, et al. Integrative Genomic Characterization Identifies Molecular Subtypes of Lung Carcinoids. Cancer Res. 2019 01;79(17):4339–47.

34. Simbolo M, Mafficini A, Sikora KO, Fassan M, Barbi S, Corbo V, et al. Lung neuroendocrine tumours: deep sequencing of the four World Health Organization histotypes reveals chromatin-remodelling genes as major players and a prognostic role for TERT, RB1, MEN1 and KMT2D. The Journal of Pathology. 2017;241(4):488–500.

35. Cejas P, Drier Y, Dreijerink KMA, Brosens LAA, Deshpande V, Epstein CB, et al. Enhancer signatures stratify and predict outcomes of non-functional pancreatic neuroendocrine tumors. Nat Med. 2019;25(8):1260–5.

36. Chan CS, Laddha SV, Lewis PW, Koletsky MS, Robzyk K, Da Silva E, et al. ATRX, DAXX or MEN1 mutant pancreatic neuroendocrine tumors are a distinct alpha-cell signature subgroup. Nat Commun. 2018 12;9(1):4158.

37. Di Domenico A, Pipinikas CP, Maire RS, Bräutigam K, Simillion C, Dettmer MS, et al. Epigenetic landscape of pancreatic neuroendocrine tumours reveals distinct cells of origin and means of tumour progression. Communications Biology. 2020 Dec 7;3(1):1–11.

38. Alcala N, Leblay N, Gabriel A a. G, Mangiante L, Hervas D, Giffon T, et al. Integrative and comparative genomic analyses identify clinically relevant pulmonary carcinoid groups and unveil the supra-carcinoids. Nat Commun. 2019 20;10(1):3407.

39. Diedisheim M, Dermine S, Jouinot A, Septier A, Gaujoux S, Dousset B, et al. Prognostic transcriptome classes of duodenopancreatic neuroendocrine tumors. Endocr Relat Cancer. 2021 Jun 1.

40. Sadanandam A, Wullschleger S, Lyssiotis CA, Grötzinger C, Barbi S, Bersani S, et al. A Cross-Species Analysis in Pancreatic Neuroendocrine Tumors Reveals Molecular Subtypes with Distinctive Clinical, Metastatic, Developmental, and Metabolic Characteristics. Cancer Discov. 2015 Dec;5(12):1296–313.

41. Young K, Lawlor RT, Ragulan C, Patil Y, Mafficini A, Bersani S, et al. Immune landscape, evolution, hypoxia-mediated viral mimicry pathways and therapeutic potential in molecular subtypes of pancreatic neuroendocrine tumours. Gut. 2020 Sep 3.

42. Simbolo M, Vicentini C, Mafficini A, Fassan M, Pedron S, Corbo V, et al. Mutational and copy number asset of primary sporadic neuroendocrine tumors of the small intestine. Virchows Arch. 2018 Dec;473(6):709–17.

43. Andersson E, Arvidsson Y, Swärd C, Hofving T, Wängberg B, Kristiansson E, et al. Expression profiling of small intestinal neuroendocrine tumors identifies subgroups with clinical relevance, prognostic markers and therapeutic targets. Mod Pathol. 2016;29(6):616–29.

44. Rogoza O, Megnis K, Kudrjavceva M, Gerina-Berzina A, Rovite V. Role of Somatostatin Signalling in Neuroendocrine Tumours. Int J Mol Sci. 2022 Jan 27;23(3):1447.

45. Kiesewetter B, Mazal P, Kretschmer-Chott E, Mayerhoefer ME, Raderer M. Pulmonary neuroendocrine tumours and somatostatin receptor status: an assessment of unlicensed use of somatostatin analogues in the clinical practice. ESMO Open. 2022 May 4;7(3):100478.

46. Righi L, Volante M, Tavaglione V, Billè A, Daniele L, Angusti T, et al. Somatostatin receptor tissue distribution in lung neuroendocrine tumours: a clinicopathologic and immunohistochemical study of 218 'clinically aggressive' cases. Annals of Oncology. 2010 Mar 1;21(3):548–55.

47. Theodoropoulou M, Stalla GK. Somatostatin receptors: from signaling to clinical practice. Front Neuroendocrinol. 2013 Aug;34(3):228–52.

48. Basuroy R, Bouvier C, Ramage JK, Sissons M, Srirajaskanthan R. Delays and routes to diagnosis of neuroendocrine tumours. BMC Cancer. 2018 Nov 16;18(1):1122.

49. Baudin E, Caplin M, Garcia-Carbonero R, Fazio N, Ferolla P, Filosso PL, et al. Lung and thymic carcinoids: ESMO Clinical Practice Guidelines for diagnosis, treatment and follow-up☆. Annals of Oncology. 2021 Apr 1;32(4):439–51.

50. Kos-Kudła B, Castaño JP, Denecke T, Grande E, Kjaer A, Koumarianou A, et al. European Neuroendocrine Tumour Society (ENETS) 2023 guidance paper for nonfunctioning pancreatic neuroendocrine tumours. Journal of Neuroendocrinology. 2023;35(12):e13343.

51. Lamarca A, Bartsch DK, Caplin M, Kos-Kudla B, Kjaer A, Partelli S, et al. European Neuroendocrine Tumor Society (ENETS) 2024 guidance paper for the management of well-differentiated small intestine neuroendocrine tumours. J Neuroendocrinol. 2024 Sep;36(9):e13423.

52. Partelli S, Bartsch DK, Capdevila J, Chen J, Knigge U, Niederle B, et al. ENETS Consensus Guidelines for Standard of Care in Neuroendocrine Tumours: Surgery for Small Intestinal and Pancreatic Neuroendocrine Tumours. Neuroendocrinology. 2017;105(3):255–65.

53. Pavel M, O'Toole D, Costa F, Capdevila J, Gross D, Kianmanesh R, et al. ENETS Consensus Guidelines Update for the Management of Distant Metastatic Disease of Intestinal, Pancreatic, Bronchial Neuroendocrine Neoplasms (NEN) and NEN of Unknown Primary Site. Neuroendocrinology. 2016 Jan 5;103(2):172–85.

54. Kulke MH, Hörsch D, Caplin ME, Anthony LB, Bergsland E, Öberg K, et al. Telotristat Ethyl, a Tryptophan Hydroxylase Inhibitor for the Treatment of Carcinoid Syndrome. JCO. 2017 Jan;35(1):14–23.

55. Pavel M, Öberg K, Falconi M, Krenning EP, Sundin A, Perren A, et al. Gastroenteropancreatic neuroendocrine neoplasms: ESMO Clinical Practice Guidelines for diagnosis, treatment and follow-up. Ann Oncol. 2020 Jul;31(7):844–60.

56. Baudin E, Capdevila J, Hörsch D, Singh S, Caplin ME, Wolin EM, et al. Treatment of advanced BP-NETS with lanreotide autogel/depot vs placebo: the phase III SPINET study. Endocr Relat Cancer. 2024 Sep 1;31(9):e230337.

57. Caplin ME, Pavel M, Ćwikła JB, Phan AT, Raderer M, Sedláčková E, et al. Lanreotide in Metastatic Enteropancreatic Neuroendocrine Tumors. New England Journal of Medicine. 2014 Jul 17;371(3):224–33.

58. Rinke A, Müller HH, Schade-Brittinger C, Klose KJ, Barth P, Wied M, et al. Placebo-Controlled, Double-Blind, Prospective, Randomized Study on the Effect of Octreotide LAR in the Control of Tumor Growth in Patients With Metastatic Neuroendocrine Midgut Tumors: A Report From the PROMID Study Group. JCO. 2009 Oct;27(28):4656–63.

59. Brabander T, van der Zwan WA, Teunissen JJM, Kam BLR, Feelders RA, de Herder WW, et al. Long-Term Efficacy, Survival, and Safety of [177Lu-DOTA0,Tyr3]octreotate in Patients with Gastroenteropancreatic and Bronchial Neuroendocrine Tumors. Clin Cancer Res. 2017 Aug 15;23(16):4617–24.

60. Strosberg J, El-Haddad G, Wolin E, Hendifar A, Yao J, Chasen B, et al. Phase 3 Trial of 177Lu-Dotatate for Midgut Neuroendocrine Tumors. New England Journal of Medicine. 2017 Jan 12;376(2):125–35.

61. Strosberg JR, Caplin ME, Kunz PL, Ruszniewski PB, Bodei L, Hendifar A, et al. 177Lu-Dotatate plus long-acting octreotide versus high-dose long-acting octreotide in patients with midgut neuroendocrine tumours (NETTER-1): final overall survival and long-term safety results from an open-label, randomised, controlled, phase 3 trial. The Lancet Oncology [Internet]. 2021 Nov 15.

62. Yao JC, Shah MH, Ito T, Bohas CL, Wolin EM, Van Cutsem E, et al. Everolimus for advanced pancreatic neuroendocrine tumors. N Engl J Med. 2011 Feb 10;364(6):514–23.

63. Yao JC, Fazio N, Singh S, Buzzoni R, Carnaghi C, Wolin E, et al. Everolimus for the treatment of advanced, non-functional neuroendocrine tumours of the lung or gastrointestinal tract (RADIANT-4): a randomised, placebo-controlled, phase 3 study. The Lancet. 2016 Mar 5;387(10022):968–77.

64. Raymond E, Dahan L, Raoul JL, Bang YJ, Borbath I, Lombard-Bohas C, et al. Sunitinib malate for the treatment of pancreatic neuroendocrine tumors. N Engl J Med. 2011 Feb 10;364(6):501–13.

65. Capdevila J, Ducreux M, García Carbonero R, Grande E, Halfdanarson T, Pavel M, et al. Streptozotocin, 1982-2022: Forty Years from the FDA's Approval to Treat Pancreatic Neuroendocrine Tumors. Neuroendocrinology. 2022;112(12):1155–67.

66. Carmeliet P, Jain RK. Molecular mechanisms and clinical applications of angiogenesis. Nature. 2011 May;473(7347):298–307.

67. Eelen G, Treps L, Li X, Carmeliet P. Basic and Therapeutic Aspects of Angiogenesis Updated. Circ Res. 2020 Jul 3;127(2):310–29.

68. Mühleder S, Fernández-Chacón M, Garcia-Gonzalez I, Benedito R. Endothelial sprouting, proliferation, or senescence: tipping the balance from physiology to pathology. Cell Mol Life Sci. 2021 Feb;78(4):1329–54.

69. Potente M, Gerhardt H, Carmeliet P. Basic and therapeutic aspects of angiogenesis. Cell. 2011 Sep 16;146(6):873–87.

70. Weis SM, Cheresh DA. Pathophysiological consequences of VEGF-induced vascular permeability. Nature. 2005 Sep 22;437(7058):497–504.

71. Karaman S, Leppänen VM, Alitalo K. Vascular endothelial growth factor signaling in development and disease. Development. 2018 Jul 20;145(14):dev151019.

72. Simons M, Gordon E, Claesson-Welsh L. Mechanisms and regulation of endothelial VEGF receptor signalling. Nat Rev Mol Cell Biol. 2016 Oct;17(10):611–25.

73. Liu ZL, Chen HH, Zheng LL, Sun LP, Shi L. Angiogenic signaling pathways and anti-angiogenic therapy for cancer. Signal Transduct Target Ther. 2023 May 11;8:198.

74. Ivy SP, Wick JY, Kaufman BM. An overview of small-molecule inhibitors of VEGFR signaling. Nat Rev Clin Oncol. 2009 Oct;6(10):569–79.

75. Heldin CH. Targeting the PDGF signaling pathway in tumor treatment. Cell Communication and Signaling. 2013 Dec 20;11(1):97.

76. Cao Y. Multifarious functions of PDGFs and PDGFRs in tumor growth and metastasis. Trends Mol Med. 2013 Aug;19(8):460–73.

77. Tejada ML, Yu L, Dong J, Jung K, Meng G, Peale FV, et al. Tumor-driven paracrine platelet-derived growth factor receptor alpha signaling is a key determinant of stromal cell recruitment in a model of human lung carcinoma. Clin Cancer Res. 2006 May 1;12(9):2676–88.

78. Cao R, Björndahl MA, Religa P, Clasper S, Garvin S, Galter D, et al. PDGF-BB induces intratumoral lymphangiogenesis and promotes lymphatic metastasis. Cancer Cell. 2004 Oct;6(4):333–45.

79. Xue Y, Lim S, Yang Y, Wang Z, Jensen LDE, Hedlund EM, et al. PDGF-BB modulates hematopoiesis and tumor angiogenesis by inducing erythropoietin production in stromal cells. Nat Med. 2011 Dec 4;18(1):100–10.

80. Lu C, Shahzad MMK, Moreno-Smith M, Lin Y, Jennings NB, Allen JK, et al. Targeting pericytes with a PDGF-B aptamer in human ovarian carcinoma models. Cancer Biology & Therapy. 2010 Feb;9(3):176–82.

81. Beenken A, Mohammadi M. The FGF family: biology, pathophysiology and therapy. Nat Rev Drug Discov. 2009 Mar;8(3):235–53.

82. Cascone T, Heymach JV. Targeting the Angiopoietin/Tie2 Pathway: Cutting Tumor Vessels With a Double-Edged Sword? JCO. 2012 Feb;30(4):441–4.

83. Huang D, Ding Y, Zhou M, Rini BI, Petillo D, Qian CN, et al. Interleukin-8 mediates resistance to antiangiogenic agent sunitinib in renal cell carcinoma. Cancer Res. 2010 Feb 1;70(3):1063–71.

84. Ramjiawan RR, Griffioen AW, Duda DG. Anti-angiogenesis for cancer revisited: Is there a role for combinations with immunotherapy? Angiogenesis. 2017 May;20(2):185–204.

85. De Palma M, Biziato D, Petrova TV. Microenvironmental regulation of tumour angiogenesis. Nat Rev Cancer. 2017 Aug;17(8):457–74.

86. Lauricella E, Mandriani B, Cavallo F, Pezzicoli G, Chaoul N, Porta C, et al. Angiogenesis in NENs, with a focus on gastroenteropancreatic NENs: from biology to current and future therapeutic implications. Front Oncol. 2022;12:957068.

87. Rodallec M, Vilgrain V, Couvelard A, Rufat P, O'Toole D, Barrau V, et al. Endocrine pancreatic tumours and helical CT: contrast enhancement is correlated with microvascular density, histoprognostic factors and survival. Pancreatology. 2006;6(1–2):77–85.

88. Wallace S, Ajani JA, Charnsangavej C, DuBrow R, Yang DJ, Chuang VP, et al. Carcinoid tumors: imaging procedures and interventional radiology. World J Surg. 1996 Feb;20(2):147–56.

89. Couvelard A, O'Toole D, Turley H, Leek R, Sauvanet A, Degott C, et al. Microvascular density and hypoxia-inducible factor pathway in pancreatic endocrine tumours: negative correlation of microvascular density and VEGF expression with tumour progression. Br J Cancer. 2005 Jan 17;92(1):94–101.

90. Marion-Audibert AM, Barel C, Gouysse G, Dumortier J, Pilleul F, Pourreyron C, et al. Low microvessel density is an unfavorable histoprognostic factor in pancreatic endocrine tumors. Gastroenterology. 2003 Oct 1;125(4):1094–104.

91. Poncet G, Villaume K, Walter T, Pourreyron C, Theillaumas A, Lépinasse F, et al. Angiogenesis and tumor progression in neuroendocrine digestive tumors. J Surg Res. 2009 Jun 1;154(1):68–77.

92. Takahashi Y, Akishima-Fukasawa Y, Kobayashi N, Sano T, Kosuge T, Nimura Y, et al. Prognostic value of tumor architecture, tumor-associated vascular characteristics, and expression of angiogenic molecules in pancreatic endocrine tumors. Clin Cancer Res. 2007 Jan 1;13(1):187–96.

93. Uccella S, La Rosa S, Scaldaferri D, Monti L, Maragliano R, Sorrenti E, et al. New insights into hypoxia-related mechanisms involved in different microvascular patterns of bronchopulmonary carcinoids and poorly differentiated neuroendocrine carcinomas. Role of ribonuclease T2 (RNASET2) and HIF-1α. Hum Pathol. 2018 Sep;79:66–76.

94. La Rosa S, Uccella S, Finzi G, Albarello L, Sessa F, Capella C. Localization of vascular endothelial growth factor and its receptors in digestive endocrine tumors: correlation with microvessel density and clinicopathologic features. Hum Pathol. 2003 Jan;34(1):18–27.

95. Terris B, Scoazec JY, Rubbia L, Bregeaud L, Pepper MS, Ruszniewski P, et al. Expression of vascular endothelial growth factor in digestive neuroendocrine tumours. Histopathology. 1998 Feb;32(2):133–8.

96. Zhang J, Jia Z, Li Q, Wang L, Rashid A, Zhu Z, et al. Elevated expression of vascular endothelial growth factor correlates with increased angiogenesis and decreased progression-free survival among patients with low-grade neuroendocrine tumors. Cancer. 2007 Apr 15;109(8):1478–86.

97. Hansel DE, Rahman A, Hermans J, Krijger RR de, Ashfaq R, Yeo CJ, et al. Liver Metastases Arising from Well-Differentiated Pancreatic Endocrine Neoplasms Demonstrate Increased VEGF-C Expression. Modern Pathology. 2003 Jul 1;16(7):652–9.

98. Mairinger FD, Walter RFH, Werner R, Christoph DC, Ting S, Vollbrecht C, et al. Activation of Angiogenesis Differs Strongly Between Pulmonary Carcinoids and Neuroendocrine Carinomas and Is Crucial for Carcinoid Tumourgenesis. J Cancer. 2014 May 15;5(6):465–71.

99. La Salvia A, Carletti R, Verrico M, Feola T, Puliani G, Bassi M, et al. Angioside: The role of Angiogenesis and Hypoxia in Lung Neuroendocrine Tumours According to Primary Tumour Location in Left or Right Parenchyma. J Clin Med. 2022 Oct 9;11(19):5958.

100. Bösch F, Altendorf-Hofmann A, Jacob S, Auernhammer CJ, Spitzweg C, Boeck S, et al. Distinct Expression Patterns of VEGFR 1-3 in Gastroenteropancreatic Neuroendocrine Neoplasms: Supporting Clinical Relevance, but not a Prognostic Factor. J Clin Med. 2020 Oct 21;9(10):3368.

101. Gilbert JA, Adhikari LJ, Lloyd RV, Halfdanarson TR, Muders MH, Ames MM. Molecular markers for novel therapeutic strategies in pancreatic endocrine tumors. Pancreas. 2013 Apr;42(3):411–21.

102. Tanaka A, Ogawa M, Zhou Y, Otani Y, Hendrickson RC, Miele MM, et al. Proteogenomic characterization of pancreatic neuroendocrine tumors uncovers hypoxia and immune signatures in clinically aggressive subtypes. iScience [Internet]. 2024 Aug 16.

103. Else T, Jonasch E, Iliopoulos O, Beckermann KE, Narayan V, Maughan BL, et al. Belzutifan for von Hippel-Lindau Disease: Pancreatic Lesion Population of the Phase 2 LITESPARK-004 Study. Clin Cancer Res. 2024 May 1;30(9):1750–7.

104. Hanahan D. Heritable formation of pancreatic beta-cell tumours in transgenic mice expressing recombinant insulin/simian virus 40 oncogenes. Nature. 1985 May 9;315(6015):115–22.

105. Christofori G, Naik P, Hanahan D. Vascular endothelial growth factor and its receptors, flt-1 and flk-1, are expressed in normal pancreatic islets and throughout islet cell tumorigenesis. Mol Endocrinol. 1995 Dec;9(12):1760–70.

106. Inoue M, Hager JH, Ferrara N, Gerber HP, Hanahan D. VEGF-A has a critical, nonredundant role in angiogenic switching and pancreatic beta cell carcinogenesis. Cancer Cell. 2002 Mar;1(2):193–202.

107. Bergers G, Brekken R, McMahon G, Vu TH, Itoh T, Tamaki K, et al. Matrix metalloproteinase-9 triggers the angiogenic switch during carcinogenesis. Nat Cell Biol. 2000 Oct;2(10):737–44.

108. Casanovas O, Hicklin DJ, Bergers G, Hanahan D. Drug resistance by evasion of antiangiogenic targeting of VEGF signaling in late-stage pancreatic islet tumors. Cancer Cell. 2005 Oct 1;8(4):299–309.

109. Sennino B, Ishiguro-Oonuma T, Wei Y, Naylor RM, Williamson CW, Bhagwandin V, et al. Suppression of tumor invasion and metastasis by concurrent inhibition of c-Met and VEGF signaling in pancreatic neuroendocrine tumors. Cancer Discov. 2012 Mar;2(3):270–87.

110. Gannon G, Mandriota SJ, Cui L, Baetens D, Pepper MS, Christofori G. Overexpression of vascular endothelial growth factor-A165 enhances tumor angiogenesis but not metastasis during beta-cell carcinogenesis. Cancer Res. 2002 Jan 15;62(2):603–8.

111. Bollard J, Patte C, Radkova K, Massoma P, Chardon L, Valantin J, et al. Neuropilin-2 contributes to tumor progression in preclinical models of small intestinal neuroendocrine tumors. J Pathol. 2019 Nov;249(3):343–55.

112. Cohen T, Herzog Y, Brodzky A, Greenson J, Eldar S, Gluzman-Poltorak Z, et al. Neuropilin-2 is a novel marker expressed in pancreatic islet cells and endocrine pancreatic tumours. The Journal of pathology [Internet]. 2002 Sep.

113. Figueroa-Vega N, Díaz A, Adrados M, Alvarez-Escolá C, Paniagua A, Aragonés J, et al. The association of the angiopoietin/Tie-2 system with the development of metastasis and leukocyte migration in neuroendocrine tumors. Endocrine-related cancer [Internet]. 2010 May 10.

114. Lantuéjoul S, Constantin B, Drabkin H, Brambilla C, Roche J, Brambilla E. Expression of VEGF, semaphorin SEMA3F, and their common receptors neuropilins NP1 and NP2 in preinvasive bronchial lesions, lung tumours, and cell lines. J Pathol. 2003 Jul;200(3):336–47.

115. Puliani G, Sesti F, Anastasi E, Verrico M, Tarsitano MG, Feola T, et al. Angiogenic factors as prognostic markers in neuroendocrine neoplasms. Endocrine. 2022 Apr;76(1):208–17.

116. Bollard J, Massoma P, Vercherat C, Blanc M, Lepinasse F, Gadot N, et al. The axon guidance molecule semaphorin 3F is a negative regulator of tumor progression and proliferation in ileal neuroendocrine tumors. Oncotarget. 2015 Oct 2;6(34):36731–45.

117. Maione F, Molla F, Meda C, Latini R, Zentilin L, Giacca M, et al. Semaphorin 3A is an endogenous angiogenesis inhibitor that blocks tumor growth and normalizes tumor vasculature in transgenic mouse models. J Clin Invest. 2009 Nov;119(11):3356–72.

118. Maione F, Capano S, Regano D, Zentilin L, Giacca M, Casanovas O, et al. Semaphorin 3A overcomes cancer hypoxia and metastatic dissemination induced by antiangiogenic treatment in mice. J Clin Invest. 2012 May;122(5):1832–48.

119. Saxena S, Hayashi Y, Wu L, Awaji M, Atri P, Varney ML, et al. Pathological and functional significance of Semaphorin-5A in pancreatic cancer progression and metastasis. Oncotarget. 2017 Dec 23;9(5):5931–43.

120. Zuazo-Gaztelu I, Pàez-Ribes M, Carrasco P, Martín L, Soler A, Martínez-Lozano M, et al. Antitumor Effects of Anti-Semaphorin 4D Antibody Unravel a Novel Proinvasive Mechanism of Vascular-Targeting Agents. Cancer Res. 2019 Oct 15;79(20):5328–41.

121. Detjen KM, Rieke S, Deters A, Schulz P, Rexin A, Vollmer S, et al. Angiopoietin-2 Promotes Disease Progression of Neuroendocrine Tumors. Clinical Cancer Research. 2010 Jan 14;16(2):420–9.

122. Mazzieri R, Pucci F, Moi D, Zonari E, Ranghetti A, Berti A, et al. Targeting the ANG2/TIE2 axis inhibits tumor growth and metastasis by impairing angiogenesis and disabling rebounds of proangiogenic myeloid cells. Cancer Cell. 2011 Apr 12;19(4):512–26.

123. Bergers G, Song S, Meyer-Morse N, Bergsland E, Hanahan D. Benefits of targeting both pericytes and endothelial cells in the tumor vasculature with kinase inhibitors. J Clin Invest. 2003 May 1;111(9):1287–95.

124. Christensen JG. A preclinical review of sunitinib, a multitargeted receptor tyrosine kinase inhibitor with anti-angiogenic and antitumour activities. Ann Oncol. 2007 Sep;18 Suppl 10:x3-10.

125. Faivre S, Niccoli N, Castellano C, Valle J, Hammel P, Raoul J, et al. Sunitinib in pancreatic neuroendocrine tumors: updated progression-free survival and final overall survival from a phase III randomized study. Annals of oncology : official journal of the European Society for Medical Oncology [Internet]. 2017 Jan 2.

126. Grillo F, Florio T, Ferraù F, Kara E, Fanciulli G, Faggiano A, et al. Emerging multitarget tyrosine kinase inhibitors in the treatment of neuroendocrine neoplasms. Endocr Relat Cancer. 2018 Sep;25(9):R453–66.

127. Yao JC, Phan A, Hoff PM, Chen HX, Charnsangavej C, Yeung SCJ, et al. Targeting Vascular Endothelial Growth Factor in Advanced Carcinoid Tumor: A Random Assignment Phase II Study of

Depot Octreotide With Bevacizumab and Pegylated Interferon Alfa-2b. JCO. 2008 Mar 10;26(8):1316–23.

128. Yao JC, Guthrie KA, Moran C, Strosberg JR, Kulke MH, Chan JA, et al. Phase III Prospective Randomized Comparison Trial of Depot Octreotide Plus Interferon Alfa-2b Versus Depot Octreotide Plus Bevacizumab in Patients With Advanced Carcinoid Tumors: SWOG S0518. J Clin Oncol. 2017 May 20;35(15):1695–703.

129. Ellis LM, Hicklin DJ. Pathways mediating resistance to vascular endothelial growth factor-targeted therapy. Clin Cancer Res. 2008 Oct 15;14(20):6371–5.

130. Sitohy B, Nagy JA, Dvorak HF. Anti-VEGF/VEGFR therapy for cancer: Reassessing the target. Cancer Res. 2012 Apr 15;72(8):1909–14.

131. Xu J, Shen L, Bai C, Wang W, Li J, Yu X, et al. Surufatinib in advanced pancreatic neuroendocrine tumours (SANET-p): a randomised, double-blind, placebo-controlled, phase 3 study. The Lancet Oncology. 2020 Nov 1;21(11):1489–99.

132. Xu J, Shen L, Zhou Z, Li J, Bai C, Chi Y, et al. Surufatinib in advanced extrapancreatic neuroendocrine tumours (SANET-ep): a randomised, double-blind, placebo-controlled, phase 3 study. The Lancet Oncology. 2020 Nov 1;21(11):1500–12.

133. Dasari A, Li D, Sung MW, Tucci C, Kauh JS, Kania MK, et al. Efficacy and safety of surufatinib in United States (US) patients (pts) with neuroendocrine tumors (NETs). JCO. 2020 May 20;38(15_suppl):4610–4610.

134. Yakes FM, Chen J, Tan J, Yamaguchi K, Shi Y, Yu P, et al. Cabozantinib (XL184), a novel MET and VEGFR2 inhibitor, simultaneously suppresses metastasis, angiogenesis, and tumor growth. Mol Cancer Ther. 2011 Dec;10(12):2298–308.

135. Chan JA, Geyer S, Zemla T, Knopp MV, Behr S, Pulsipher S, et al. Phase 3 Trial of Cabozantinib to Treat Advanced Neuroendocrine Tumors. New England Journal of Medicine [Internet]. 2024.

136. Hu-Lowe DD, Zou HY, Grazzini ML, Hallin ME, Wickman GR, Amundson K, et al. Nonclinical antiangiogenesis and antitumor activities of axitinib (AG-013736), an oral, potent, and selective inhibitor of vascular endothelial growth factor receptor tyrosine kinases 1, 2, 3. Clin Cancer Res. 2008 Nov 15;14(22):7272–83.

137. Garcia-Carbonero R, Benavent M, Jiménez Fonseca P, Castellano D, Alonso T, Teule A, et al. A phase II/III randomized double-blind study of octreotide acetate LAR with axitinib versus octreotide acetate LAR with placebo in patients with advanced G1-G2 NETs of non-pancreatic origin (AXINET trial-GETNE-1107). JCO. 2021 Jan 20;39(3_suppl):360–360.

138. Garcia-Carbonero, Benavent M, Jimenez-Fonseca, Castellano D, Grande E, Teule A, et al. The AXINET trial (GETNE1107): Axitinib plus octreotide LAR improves PFS by blinded central radiological assessment vs placebo plus octreotide LAR in G1-2 extrapancreatic NETs. ESMO 2021. 2021 Oct 1.

139. Hurwitz H, Dowlati A, Savage S, Fernando N, Lasalvia S, Whitehead B, et al. Safety, tolerability and pharmacokinetics of oral administration of GW786034 in pts with solid tumors. JCO. 2005 Jun;23(16_suppl):3012–3012.

140. Bergsland EK, Mahoney MR, Asmis TR, Hall N, Kumthekar P, Maitland ML, et al. Prospective randomized phase II trial of pazopanib versus placebo in patients with progressive carcinoid tumors (CARC) (Alliance A021202). JCO. 2019 May 20;37(15_suppl):4005–4005.

141. Hussein Z, Mizuo H, Hayato S, Namiki M, Shumaker R. Clinical Pharmacokinetic and Pharmacodynamic Profile of Lenvatinib, an Orally Active, Small-Molecule, Multitargeted Tyrosine Kinase Inhibitor. Eur J Drug Metab Pharmacokinet. 2017 Dec;42(6):903–14.

142. Capdevila J, Fazio N, Lopez C, Telué A, Valle J, Tatufo S, et al. Lenvatinib in Patients With Advanced Grade 1/2 Pancreatic and Gastrointestinal Neuroendocrine Tumors: Results of the Phase II TALENT Trial (GETNE1509). Journal of clinical oncology : official journal of the American Society of Clinical Oncology [Internet]. 2021 Oct 7.

143. Hobday TJ, Rubin J, Holen K, Picus J, Donehower R, Marschke R, et al. MC044h, a phase II trial of sorafenib in patients (pts) with metastatic neuroendocrine tumors (NET): A Phase II Consortium (P2C) study. JCO. 2007 Jun 20;25(18_suppl):4504–4504.

144. Iyer RV, Konda B, Fountzilas C, Mukherjee S, Owen D, Attwood K, et al. Multicenter phase 2 trial of nintedanib in advanced nonpancreatic neuroendocrine tumors. Cancer. 2020 Aug 15;126(16):3689–97.

145. Bergers G, Hanahan D. Modes of resistance to anti-angiogenic therapy. Nat Rev Cancer. 2008 Aug;8(8):592–603.

146. Pàez-Ribes M, Allen E, Hudock J, Takeda T, Okuyama H, Viñals F, et al. Antiangiogenic Therapy Elicits Malignant Progression of Tumors to Increased Local Invasion and Distant Metastasis. Cancer Cell. 2009 Mar 3;15(3):220–31.

147. You WK, Sennino B, Williamson CW, Falcón B, Hashizume H, Yao LC, et al. VEGF and c-Met Blockade Amplify Angiogenesis Inhibition in Pancreatic Islet Cancer. Cancer Res. 2011 Jul 15;71(14):4758–68.

148. Fjällskog MLH, Lejonklou MH, Oberg KE, Eriksson BK, Janson ET. Expression of molecular targets for tyrosine kinase receptor antagonists in malignant endocrine pancreatic tumors. Clin Cancer Res. 2003 Apr;9(4):1469–73.

149. Allen E, Miéville P, Warren CM, Saghafinia S, Li L, Peng MW, et al. Metabolic Symbiosis Enables Adaptive Resistance to Anti-angiogenic Therapy that Is Dependent on mTOR Signaling. Cell Rep. 2016 May 10;15(6):1144–60.

150. Rigamonti N, Kadioglu E, Keklikoglou I, Wyser Rmili C, Leow CC, De Palma M. Role of Angiopoietin-2 in Adaptive Tumor Resistance to VEGF Signaling Blockade. Cell Reports. 2014 Aug 7;8(3):696–706.

151. Krug S, Abbassi R, Griesmann H, Sipos B, Wiese D, Rexin P, et al. Therapeutic targeting of tumor-associated macrophages in pancreatic neuroendocrine tumors. International Journal of Cancer. 2018;143(7):1806–16.

152. Chu X, Gao X, Jansson L, Quach M, Skogseid B, Barbu A. Multiple Microvascular Alterations in Pancreatic Islets and Neuroendocrine Tumors of a Men1 Mouse Model. The American Journal of Pathology. 2013 Jun 1;182(6):2355–67.

153. Franco M, Pàez-Ribes M, Cortez E, Casanovas O, Pietras K. Use of a mouse model of pancreatic neuroendocrine tumors to find pericyte biomarkers of resistance to anti-angiogenic therapy. Hormone and metabolic research [Internet]. 2011 Nov.

154. Wiedmer T, Blank A, Pantasis S, Normand L, Bill R, Krebs P, et al. Autophagy Inhibition Improves Sunitinib Efficacy in Pancreatic Neuroendocrine Tumors via a Lysosome-dependent Mechanism. Mol Cancer Ther. 2017 Nov;16(11):2502–15.

155. McDermott DF, Huseni MA, Atkins MB, Motzer RJ, Rini BI, Escudier B, et al. Clinical activity and molecular correlates of response to atezolizumab alone or in combination with bevacizumab versus sunitinib in renal cell carcinoma. Nat Med. 2018 Jun;24(6):749–57.

156. Motzer RJ, Robbins PB, Powles T, Albiges L, Haanen JB, Larkin J, et al. Avelumab plus axitinib versus sunitinib in advanced renal cell carcinoma: biomarker analysis of the phase 3 JAVELIN Renal 101 trial. Nat Med. 2020 Nov;26(11):1733–41.

157. Pommier AJC, Farren M, Patel B, Wappett M, Michopoulos F, Smith NR, et al. Leptin, BMI, and a Metabolic Gene Expression Signature Associated with Clinical Outcome to VEGF Inhibition in Colorectal Cancer. Cell Metab. 2016 Jan 12;23(1):77–93.

158. Pavel ME, Hassler G, Baum U, Hahn EG, Lohmann T, Schuppan D. Circulating levels of angiogenic cytokines can predict tumour progression and prognosis in neuroendocrine carcinomas. Clinical Endocrinology. 2005;62(4):434–43.

159. Pinato D, Tan T, Toussi S, Ramachandran R, Martin N, Meeran K, et al. An expression signature of the angiogenic response in gastrointestinal neuroendocrine tumours: correlation with tumour phenotype and survival outcomes. British journal of cancer [Internet]. 2014 Jul 1.

160. Jiménez-Fonseca P, Martín MN, Carmona-Bayonas A, Calvo A, Fernández-Mateos J, Redrado M, et al. Biomarkers and polymorphisms in pancreatic neuroendocrine tumors treated with sunitinib. Oncotarget. 2018 Dec 11;9(97):36894–905.

161. Zurita AJ, Khajavi M, Wu HK, Tye L, Huang X, Kulke MH, et al. Circulating cytokines and monocyte subpopulations as biomarkers of outcome and biological activity in sunitinib-treated patients with advanced neuroendocrine tumours. Br J Cancer. 2015 Mar 31;112(7):1199–205.

162. Hilfenhaus G, Göhrig A, Pape UF, Neumann T, Jann H, Zdunek D, et al. Placental growth factor supports neuroendocrine tumor growth and predicts disease prognosis in patients. 2013 Jun 1.

163. de Haas S, Delmar P, Bansal AT, Moisse M, Miles DW, Leighl N, et al. Genetic variability of VEGF pathway genes in six randomized phase III trials assessing the addition of bevacizumab to standard therapy. Angiogenesis. 2014 Oct;17(4):909–20.

164. Kahles F, Findeisen HM, Bruemmer D. Osteopontin: A novel regulator at the cross roads of inflammation, obesity and diabetes. Mol Metab. 2014 Jul;3(4):384–93.

165. Lin EYH, Xi W, Aggarwal N, Shinohara ML. Osteopontin (OPN)/SPP1: from its biochemistry to biological functions in the innate immune system and the central nervous system (CNS). Int Immunol. 2022 Dec 16;35(4):171–80.

166. Gimba ER, Tilli TM. Human osteopontin splicing isoforms: known roles, potential clinical applications and activated signaling pathways. Cancer Lett. 2013 Apr 30;331(1):11–7.

167. Silva GR, Mattos DS, Bastos ACF, Viana BPPB, Brum MCM, Ferreira LB, et al. Osteopontin-4 and Osteopontin-5 splice variants are expressed in several tumor cell lines. Mol Biol Rep. 2020 Oct;47(10):8339–45.

168. Bastos ACS da F, Gomes AVP, Silva GR, Emerenciano M, Ferreira LB, Gimba ERP. The Intracellular and Secreted Sides of Osteopontin and Their Putative Physiopathological Roles. International Journal of Molecular Sciences. 2023 Jan;24(3):2942.

169. Shinohara ML, Kim HJ, Kim JH, Garcia VA, Cantor H. Alternative translation of osteopontin generates intracellular and secreted isoforms that mediate distinct biological activities in dendritic cells. Proceedings of the National Academy of Sciences. 2008 May 20;105(20):7235–9.

170. Anborgh PH, Mutrie JC, Tuck AB, Chambers AF. Pre- and post-translational regulation of osteopontin in cancer. J Cell Commun Signal. 2011 Jun;5(2):111–22.

171. Ashkar S, Weber GF, Panoutsakopoulou V, Sanchirico ME, Jansson M, Zawaideh S, et al. Eta-1 (Osteopontin): An Early Component of Type-1 (Cell-Mediated) Immunity. Science. 2000 Feb 4;287(5454):860–4.

172. Katagiri YU, Sleeman J, Fujii H, Herrlich P, Hotta H, Tanaka K, et al. CD44 variants but not CD44s cooperate with beta1-containing integrins to permit cells to bind to osteopontin independently of arginine-glycine-aspartic acid, thereby stimulating cell motility and chemotaxis. Cancer Res. 1999 Jan 1;59(1):219–26.

173. Weber GF, Ashkar S, Glimcher MJ, Cantor H. Receptor-ligand interaction between CD44 and osteopontin (Eta-1). Science. 1996 Jan 26;271(5248):509–12.

174. Abdelaziz Mohamed I, Gadeau AP, Hasan A, Abdulrahman N, Mraiche F. Osteopontin: A Promising Therapeutic Target in Cardiac Fibrosis. Cells. 2019 Dec;8(12):1558.

175. Chellaiah M, Soga N, Swanson S, McAllister S, Alvarez U, Wang D, et al. Rho-A is critical for osteoclast podosome organization, motility, and bone resorption. The Journal of biological chemistry [Internet]. 2000 Apr 21.

176. Reinholt FP, Hultenby K, Oldberg A, Heinegård D. Osteopontin--a possible anchor of osteoclasts to bone. Proc Natl Acad Sci U S A. 1990 Jun;87(12):4473–5.

177. Ross FP, Chappel J, Alvarez JI, Sander D, Butler WT, Farach-Carson MC, et al. Interactions between the bone matrix proteins osteopontin and bone sialoprotein and the osteoclast integrin alpha v beta 3 potentiate bone resorption. J Biol Chem. 1993 May 5;268(13):9901–7.

178. Hunter GK, Hauschka PV, Poole AR, Rosenberg LC, Goldberg HA. Nucleation and inhibition of hydroxyapatite formation by mineralized tissue proteins. Biochem J. 1996 Jul 1;317(Pt 1):59–64.

179. Choi ST, Kim JH, Kang EJ, Lee SW, Park MC, Park YB, et al. Osteopontin might be involved in bone remodelling rather than in inflammation in ankylosing spondylitis. Rheumatology (Oxford). 2008 Dec;47(12):1775–9.

180. Klein-Nulend J, Roelofsen J, Semeins CM, Bronckers AL, Burger EH. Mechanical stimulation of osteopontin mRNA expression and synthesis in bone cell cultures. J Cell Physiol. 1997 Feb;170(2):174–81.

181. Chellaiah MA, Kizer N, Biswas R, Alvarez U, Strauss-Schoenberger J, Rifas L, et al. Osteopontin Deficiency Produces Osteoclast Dysfunction Due to Reduced CD44 Surface Expression. Mol Biol Cell. 2003 Jan;14(1):173–89.

182. Shinohara ML, Jansson M, Hwang ES, Werneck MBF, Glimcher LH, Cantor H. T-bet-dependent expression of osteopontin contributes to T cell polarization. Proc Natl Acad Sci U S A. 2005 Nov 22;102(47):17101–6.

183. Ogawa D, Stone JF, Takata Y, Blaschke F, Chu VH, Towler DA, et al. Liver X Receptor Agonists Inhibit Cytokine-Induced Osteopontin Expression in Macrophages Through Interference With Activator Protein-1 Signaling Pathways. Circulation Research. 2005 Apr 15;96(7):e59–67.

184. Oyama Y, Akuzawa N, Nagai R, Kurabayashi M. PPARgamma ligand inhibits osteopontin gene expression through interference with binding of nuclear factors to A/T-rich sequence in THP-1 cells. Circ Res. 2002 Feb 22;90(3):348–55.

185. Suzuki K, Zhu B, Rittling SR, Denhardt DT, Goldberg HA, Mcculloch CAG, et al. Colocalization of Intracellular Osteopontin With CD44 Is Associated With Migration, Cell Fusion, and Resorption in Osteoclasts*. Journal of Bone and Mineral Research. 2002 Aug 1;17(8):1486–97.

186. Zhu B, Suzuki K, Goldberg HA, Rittling SR, Denhardt DT, McCulloch CAG, et al. Osteopontin modulates CD44-dependent chemotaxis of peritoneal macrophages through G-protein-coupled receptors: evidence of a role for an intracellular form of osteopontin. J Cell Physiol. 2004 Jan;198(1):155–67.

187. Lund SA, Wilson CL, Raines EW, Tang J, Giachelli CM, Scatena M. Osteopontin mediates macrophage chemotaxis via α4 and α9 integrins and survival via the α4 integrin. J Cell Biochem. 2013 May;114(5):1194–202.

188. Crawford HC, Matrisian LM, Liaw L. Distinct roles of osteopontin in host defense activity and tumor survival during squamous cell carcinoma progression in vivo. Cancer Res. 1998 Nov 15;58(22):5206–15.

189. Giachelli CM, Lombardi D, Johnson RJ, Murry CE, Almeida M. Evidence for a role of osteopontin in macrophage infiltration in response to pathological stimuli in vivo. Am J Pathol. 1998 Feb;152(2):353–8.

190. Heilmann K, Hoffmann U, Witte E, Loddenkemper C, Sina C, Schreiber S, et al. Osteopontin as two-sided mediator of intestinal inflammation. J Cell Mol Med. 2009 Jun;13(6):1162–74.

191. McKee MD, Nanci A. Secretion of Osteopontin by macrophages and its accumulation at tissue surfaces during wound healing in mineralized tissues: a potential requirement for macrophage adhesion and phagocytosis. Anat Rec. 1996 Jun;245(2):394–409.

192. Weber GF, Zawaideh S, Hikita S, Kumar VA, Cantor H, Ashkar S. Phosphorylation-dependent interaction of osteopontin with its receptors regulates macrophage migration and activation. Journal of Leukocyte Biology. 2002;72(4):752–61.

193. Yamamoto N, Sakai F, Kon S, Morimoto J, Kimura C, Yamazaki H, et al. Essential role of the cryptic epitope SLAYGLR within osteopontin in a murine model of rheumatoid arthritis. J Clin Invest. 2003 Jul 15;112(2):181–8.

194. Shinohara ML, Lu L, Bu J, Werneck MBF, Kobayashi KS, Glimcher LH, et al. Osteopontin expression is essential for interferon-alpha production by plasmacytoid dendritic cells. Nat Immunol. 2006 May;7(5):498–506.

195. Yang M, Ma C, Liu S, Sun J, Shao Q, Gao W, et al. Hypoxia skews dendritic cells to a T helper type 2-stimulating phenotype and promotes tumour cell migration by dendritic cell-derived osteopontin. Immunology. 2009 Sep;128(1 Pt 2):e237–49.

196. Bruemmer D, Collins AR, Noh G, Wang W, Territo M, Arias-Magallona S, et al. Angiotensin II-accelerated atherosclerosis and aneurysm formation is attenuated in osteopontin-deficient mice. J Clin Invest. 2003 Nov;112(9):1318–31.

197. Matsui Y, Rittling SR, Okamoto H, Inobe M, Jia N, Shimizu T, et al. Osteopontin Deficiency Attenuates Atherosclerosis in Female Apolipoprotein E–Deficient Mice. Arteriosclerosis, Thrombosis, and Vascular Biology. 2003 Jun;23(6):1029–34.

198. O'Regan AW, Chupp GL, Lowry JA, Goetschkes M, Mulligan N, Berman JS. Osteopontin is associated with T cells in sarcoid granulomas and has T cell adhesive and cytokine-like properties in vitro. J Immunol. 1999 Jan 15;162(2):1024–31.

199. Pan H, Ou Y, Peng S, Liu S, Pl P, Lee P, et al. Overexpression of osteopontin is associated with intrahepatic metastasis, early recurrence, and poorer prognosis of surgically resected hepatocellular carcinoma. Cancer [Internet]. 2003 Jan 7.

200. Psyrri A, Kalogeras KT, Wirtz RM, Kouvatseas G, Karayannopoulou G, Goussia A, et al. Association of osteopontin with specific prognostic factors and survival in adjuvant breast cancer trials of the Hellenic Cooperative Oncology Group. J Transl Med. 2017 Feb 13;15(1):30.

201. Rudland PS, Platt-Higgins A, El-Tanani M, De Silva Rudland S, Barraclough R, Winstanley JHR, et al. Prognostic significance of the metastasis-associated protein osteopontin in human breast cancer. Cancer Res. 2002 Jun 15;62(12):3417–27.

202. Ito T, Hashimoto Y, Tanaka E, Kan T, Tsunoda S, Sato F, et al. An inducible short-hairpin RNA vector against osteopontin reduces metastatic potential of human esophageal squamous cell carcinoma in vitro and in vivo. Clin Cancer Res. 2006 Feb 15;12(4):1308–16.

203. Liersch R, Gerss J, Schliemann C, Bayer M, Schwöppe C, Biermann C, et al. Osteopontin is a prognostic factor for survival of acute myeloid leukemia patients. Blood [Internet]. 2012 May 31.

204. Likui W, Hong W, Shuwen Z. Clinical significance of the upregulated osteopontin mRNA expression in human colorectal cancer. J Gastrointest Surg. 2010 Jan;14(1):74–81.

205. Weber GF, Lett GS, Haubein NC. Categorical meta-analysis of Osteopontin as a clinical cancer marker. Oncol Rep. 2011 Feb;25(2):433–41.

206. Zhao M, Liang F, Zhang B, Yan W, Zhang J. The impact of osteopontin on prognosis and clinicopathology of colorectal cancer patients: a systematic meta-analysis. Sci Rep. 2015 Aug 3;5(1):12713.

207. Kim J, Ki SS, Lee SD, Han CJ, Kim YC, Park SH, et al. Elevated plasma osteopontin levels in patients with hepatocellular carcinoma. Am J Gastroenterol. 2006 Sep;101(9):2051–9.

208. Zhang H, Ye QH, Ren N, Zhao L, Wang YF, Wu X, et al. The prognostic significance of preoperative plasma levels of osteopontin in patients with hepatocellular carcinoma. J Cancer Res Clin Oncol. 2006 Nov 1;132(11):709–17.

209. Mack PC, Redman MW, Chansky K, Williamson SK, Farneth NC, Lara PN, et al. Lower osteopontin plasma levels are associated with superior outcomes in advanced non-small-cell lung cancer patients receiving platinum-based chemotherapy: SWOG Study S0003. J Clin Oncol. 2008 Oct 10;26(29):4771–6.

210. Yazici O, Dogan M, Ozal G, Aktas SH, Demirkazik A, Utkan G, et al. Osteopontin is a Prognostic Factor in Patients with Advanced Gastric Cancer. Comb Chem High Throughput Screen. 2021;24(8):1229–35.

211. Park MG, Oh MM, Yoon JH, Park JY, Park HS, Moon DG, et al. The value of plasma osteopontin levels as a predictive factor of disease stage and recurrence in patients with bladder urothelial carcinoma: a prospective study. Kaohsiung J Med Sci. 2012 Oct;28(10):526–30.

212. Castellone MD, Celetti A, Guarino V, Cirafici AM, Basolo F, Giannini R, et al. Autocrine stimulation by osteopontin plays a pivotal role in the expression of the mitogenic and invasive phenotype of RET/PTC-transformed thyroid cells. Oncogene. 2004 Mar;23(12):2188–96.

213. Teramoto H, Castellone MD, Malek RL, Letwin N, Frank B, Gutkind JS, et al. Autocrine activation of an osteopontin-CD44-Rac pathway enhances invasion and transformation by H-RasV12. Oncogene. 2005 Jan 13;24(3):489–501.

214. Chen X, Xia Y, Xue T, Zhang H, Ye S. Down-regulation of osteopontin inhibits metastasis of hepatocellular carcinoma cells via a mechanism involving MMP-2 and uPA. Oncology reports [Internet]. 2011 Mar.

215. Sun S, Dong Q, Ye Q, Sun H, Hl J, Zhu X, et al. Lentiviral-mediated miRNA against osteopontin suppresses tumor growth and metastasis of human hepatocellular carcinoma. Hepatology (Baltimore, Md) [Internet]. 2008 Dec.

216. Zhang R, Pan X, Huang Z, Weber GF, Zhang G. Osteopontin enhances the expression and activity of MMP-2 via the SDF-1/CXCR4 axis in hepatocellular carcinoma cell lines. PLoS One. 2011;6(8):e23831.

217. Cheng Y, Wen G, Sun Y, Shen Y, Zeng Y, Du M, et al. Osteopontin Promotes Colorectal Cancer Cell Invasion and the Stem Cell-Like Properties through the PI3K-AKT-GSK/3β-β/Catenin Pathway. Med Sci Monit. 2019 Apr 23;25:3014–25.

218. Robertson BW, Bonsal L, Chellaiah MA. Regulation of Erk1/2 activation by osteopontin in PC3 human prostate cancer cells. Molecular Cancer. 2010 Sep 26;9(1):260.

219. Rangaswami H, Kundu GC. Osteopontin stimulates melanoma growth and lung metastasis through NIK/MEKK1-dependent MMP-9 activation pathways. Oncol Rep. 2007 Oct;18(4):909–15.

220. Li NY, Weber CE, Mi Z, Wai PY, Cuevas BD, Kuo PC. Osteopontin up-regulates critical epithelial-mesenchymal transition transcription factors to induce an aggressive breast cancer phenotype. J Am Coll Surg. 2013 Jul;217(1):17–26; discussion 26.

221. Yu X, Zheng Y, Zhu X, Gao X, Wang C, Sheng Y, et al. Osteopontin promotes hepatocellular carcinoma progression via the PI3K/AKT/Twist signaling pathway. Oncol Lett. 2018 Oct;16(4):5299–308.

222. Liu J, Liu Q, Wan Y, Zhao Z, Yu H, Luo H, et al. Osteopontin promotes the progression of gastric cancer through the NF-κB pathway regulated by the MAPK and PI3K. International journal of oncology [Internet]. 2014 Jul.

223. Ng L, Wan TMH, Lam CSC, Chow AKM, Wong SKM, Man JHW, et al. Post-operative plasma osteopontin predicts distant metastasis in human colorectal cancer. PLoS One. 2015;10(5):e0126219.

224. Song G, Ouyang G, Mao Y, Ming Y, Bao S, Hu T. Osteopontin promotes gastric cancer metastasis by augmenting cell survival and invasion through Akt-mediated HIF-1alpha up-regulation and MMP9 activation. Journal of cellular and molecular medicine [Internet]. 2009 Aug.

225. Liu L, Zhang R, Deng J, Dai X, Zhu X, Fu Q, et al. Construction of TME and Identification of crosstalk between malignant cells and macrophages by SPP1 in hepatocellular carcinoma. Cancer Immunol Immunother. 2022 Jan;71(1):121–36.

226. Zheng SS, Wu YF, Zhang BH, Huang C, Xue TC. A novel myeloid cell marker genes related signature can indicate immune infiltration and predict prognosis of hepatocellular carcinoma: Integrated analysis of bulk and single-cell RNA sequencing. Front Mol Biosci. 2023;10:1118377.

227. Klement JD, Poschel DB, Lu C, Merting AD, Yang D, Redd PS, et al. Osteopontin Blockade Immunotherapy Increases Cytotoxic T Lymphocyte Lytic Activity and Suppresses Colon Tumor Progression. Cancers. 2021 Jan;13(5):1006.

228. Klement JD, Paschall AV, Redd PS, Ibrahim ML, Lu C, Yang D, et al. An osteopontin/CD44 immune checkpoint controls CD8+ T cell activation and tumor immune evasion. J Clin Invest. 2018 Dec 3;128(12):5549–60.

229. Liu Y, Xun Z, Ma K, Liang S, Li X, Zhou S, et al. Identification of a tumour immune barrier in the HCC microenvironment that determines the efficacy of immunotherapy. Journal of Hepatology. 2023 Apr 1;78(4):770–82.

230. Rao G, Wang H, Li B, Huang L, Xue D, Wang X, et al. Reciprocal interactions between tumor-associated macrophages and CD44-positive cancer cells via osteopontin/CD44 promote tumorigenicity in colorectal cancer. Clin Cancer Res. 2013 Feb 15;19(4):785–97.

231. Bill R, Wirapati P, Messemaker M, Roh W, Zitti B, Duval F, et al. CXCL9:SPP1 macrophage polarity identifies a network of cellular programs that control human cancers. Science. 2023 Aug 4;381(6657):515–24.

232. Qi J, Sun H, Zhang Y, Wang Z, Xun Z, Li Z, et al. Single-cell and spatial analysis reveal interaction of FAP+ fibroblasts and SPP1+ macrophages in colorectal cancer. Nat Commun. 2022 Apr 1;13(1):1742.

233. Sangaletti S, Tripodo C, Sandri S, Torselli I, Vitali C, Ratti C, et al. Osteopontin shapes immunosuppression in the metastatic niche. Cancer Res. 2014 Sep 1;74(17):4706–19.

234. Rangaswami H, Bulbule A, Kundu GC. Osteopontin: role in cell signaling and cancer progression. Trends Cell Biol. 2006 Feb;16(2):79–87.

235. Lazar M, Sullivan J, Chipitsyna G, Gong Q, Ng CY, Salem AF, et al. Involvement of osteopontin in the matrix-degrading and proangiogenic changes mediated by nicotine in pancreatic cancer cells. J Gastrointest Surg. 2010 Oct;14(10):1566–77.

236. Lin Q, Guo L, Lin G, Chen Z, Chen T, Lin J, et al. Clinical and prognostic significance of OPN and VEGF expression in patients with non-small-cell lung cancer. Cancer Epidemiol. 2015 Aug;39(4):539–44.

237. Tang H, Wang J, Bai F, Zhai H, Gao J, Hong L, et al. Positive correlation of osteopontin, cyclooxygenase-2 and vascular endothelial growth factor in gastric cancer. Cancer Invest. 2008 Feb;26(1):60–7.

238. Chakraborty G, Jain S, Kundu GC. Osteopontin promotes vascular endothelial growth factor-dependent breast tumor growth and angiogenesis via autocrine and paracrine mechanisms. Cancer Res. 2008 Jan 1;68(1):152–61.

239. Cui R, Takahashi F, Ohashi R, Yoshioka M, Gu T, Tajima K, et al. Osteopontin is involved in the formation of malignant pleural effusion in lung cancer. Lung Cancer. 2009 Mar;63(3):368–74.

240. Wang ZM, Cui YH, Li W, Chen SY, Liu TS. Lentiviral-mediated siRNA targeted against osteopontin suppresses the growth and metastasis of gastric cancer cells. Oncol Rep. 2011 Apr;25(4):997–1003.

241. Yang L, Zhao W, Zuo WS, Wei L, Song XR, Wang XW, et al. Silencing of osteopontin promotes the radiosensitivity of breast cancer cells by reducing the expression of hypoxia inducible factor 1 and vascular endothelial growth factor. Chin Med J (Engl). 2012 Jan;125(2):293–9.

242. Wang C, Ying J, Nie X, Zhou T, Xiao D, Swarnkar G, et al. Targeting angiogenesis for fracture nonunion treatment in inflammatory disease. Bone Res. 2021 Jun 7;9:29.

243. Wein M, Huelter-Hassler D, Nelson K, Fretwurst T, Nahles S, Finkenzeller G, et al. Differential osteopontin expression in human osteoblasts derived from iliac crest and alveolar bone and its role in early stages of angiogenesis. Journal of bone and mineral metabolism [Internet]. 2019 Jan.

244. Infanger M, Kossmehl P, Shakibaei M, Baatout S, Witzing A, Grosse J, et al. Induction of three-dimensional assembly and increase in apoptosis of human endothelial cells by simulated microgravity: impact of vascular endothelial growth factor. Apoptosis. 2006 May;11(5):749–64.

245. Infanger M, Grosse J, Westphal K, Leder A, Ulbrich C, Paul M, et al. Vascular endothelial growth factor induces extracellular matrix proteins and osteopontin in the umbilical artery. Ann Vasc Surg. 2008 Mar;22(2):273–84.

246. Senger DR, Ledbetter SR, Claffey KP, Papadopoulos-Sergiou A, Peruzzi CA, Detmar M. Stimulation of endothelial cell migration by vascular permeability factor/vascular endothelial growth factor through cooperative mechanisms involving the alphavbeta3 integrin, osteopontin, and thrombin. Am J Pathol. 1996 Jul;149(1):293–305.

247. Tang H, Wang J, Bai F, Hong L, Liang J, Gao J, et al. Inhibition of osteopontin would suppress angiogenesis in gastric cancer. Biochem Cell Biol. 2007 Feb;85(1):103–10.

248. Wang Y, Yan W, Lu X, Qian C, Zhang J, Li P, et al. Overexpression of osteopontin induces angiogenesis of endothelial progenitor cells via the avβ3/PI3K/AKT/eNOS/NO signaling pathway in glioma cells. Eur J Cell Biol. 2011 Aug;90(8):642–8.

249. Kumar S, Sharma P, Kumar D, Chakraborty G, Gorain M, Kundu GC. Functional Characterization of Stromal Osteopontin in Melanoma Progression and Metastasis. PLOS ONE. 2013 Jul 23;8(7):e69116.

250. Matsumoto T, Abe M. Bone destruction in multiple myeloma. Ann N Y Acad Sci. 2006 Apr;1068:319–26.

251. Tanaka Y, Abe M, Hiasa M, Oda A, Amou H, Nakano A, et al. Myeloma cell-osteoclast interaction enhances angiogenesis together with bone resorption: a role for vascular endothelial cell growth factor and osteopontin. Clin Cancer Res. 2007 Feb 1;13(3):816–23.

252. Yao L, Liu F, Hong L, Sun L, Liang S, Wu K, et al. The function and mechanism of COX-2 in angiogenesis of gastric cancer cells. Journal of Experimental & Clinical Cancer Research. 2011 Jan 25;30(1):13.

253. Psallidas I, Stathopoulos GT, Maniatis NA, Magkouta S, Moschos C, Karabela SP, et al. Secreted phosphoprotein-1 directly provokes vascular leakage to foster malignant pleural effusion. Oncogene. 2013 Jan;32(4):528–35.

254. Raja R, Kale S, Thorat D, Soundararajan G, Lohite K, Mane A, et al. Hypoxia-driven osteopontin contributes to breast tumor growth through modulation of HIF1α-mediated VEGF-dependent angiogenesis. Oncogene. 2014 Apr 17;33(16):2053–64.

255. Mi Z, Guo H, Kuo PC. Identification of osteopontin-dependent signaling pathways in a mouse model of human breast cancer. BMC Res Notes. 2009 Jul 1;2:119.

256. Jain S, Chakraborty G, Kundu G. The crucial role of cyclooxygenase-2 in osteopontin-induced protein kinase C alpha/c-Src/IkappaB kinase alpha/beta-dependent prostate tumor progression and angiogenesis. Cancer research [Internet]. 2006 Jan 7.

257. Luo SD, Chen YJ, Liu CT, Rau KM, Chen YC, Tsai HT, et al. Osteopontin Involves Cisplatin Resistance and Poor Prognosis in Oral Squamous Cell Carcinoma. Biomed Res Int. 2015;2015:508587.

258. Elbaiomy MA, Akl T, Elhelaly R, El-Beshbishi W, El Ghonemy MS, Elzehery R. Osteopontin level and promoter polymorphism in patients with metastatic breast cancer. Curr Oncol. 2020 Oct;27(5):e444–50.

259. Ouyang X, Huang Y, Jin X, Zhao W, Hu T, Wu F, et al. Osteopontin promotes cancer cell drug resistance, invasion, and lactate production and is associated with poor outcome of patients with advanced non-small-cell lung cancer. Onco Targets Ther. 2018;11:5933–41.

260. Nakamura T, Shinriki S, Jono H, Ueda M, Nagata M, Guo J, et al. Osteopontin-integrin α(v)β(3) axis is crucial for 5-fluorouracil resistance in oral squamous cell carcinoma. FEBS Lett. 2015 Jan 16;589(2):231–9.

261. Funakoshi T, Lee C, Hsieh J. A systematic review of predictive and prognostic biomarkers for VEGF-targeted therapy in renal cell carcinoma. Cancer treatment reviews [Internet]. 2014 May.

262. Tran H, Liu Y, Zurita A, Lin Y, Baker-Neblett K, Martin A, et al. Prognostic or predictive plasma cytokines and angiogenic factors for patients treated with pazopanib for metastatic renal-cell cancer: a retrospective analysis of phase 2 and phase 3 trials. The Lancet Oncology [Internet]. 2012 Aug.

263. Zurita AJ, Jonasch E, Wang X, Khajavi M, Yan S, Du DZ, et al. A cytokine and angiogenic factor (CAF) analysis in plasma for selection of sorafenib therapy in patients with metastatic renal cell carcinoma. Ann Oncol. 2012 Jan;23(1):46–52.

264. Takagi H, Suzuma K, Otani A, Oh H, Koyama S, Ohashi H, et al. Role of Vitronectin Receptor-Type Integrins and Osteopontin in Ischemia-Induced Retinal Neovascularization. Japanese Journal of Ophthalmology. 2002 May 1;46(3):270–8.

265. Liu G, Fan X, Tang M, Chen R, Wang H, Jia R, et al. Osteopontin induces autophagy to promote chemo-resistance in human hepatocellular carcinoma cells. Cancer Lett. 2016 Dec 28;383(2):171–82.

266. Yang MC, Wang HC, Hou YC, Tung HL, Chiu TJ, Shan YS. Blockade of autophagy reduces pancreatic cancer stem cell activity and potentiates the tumoricidal effect of gemcitabine. Mol Cancer. 2015 Oct 12;14:179.

267. Hsieh IS, Huang WH, Liou HC, Chuang WJ, Yang RS, Fu WM. Upregulation of drug transporter expression by osteopontin in prostate cancer cells. Mol Pharmacol. 2013 May;83(5):968–77.

268. Zheng YH, Tian C, Meng Y, Qin YW, Du YH, Du J, et al. Osteopontin stimulates autophagy via integrin/CD44 and p38 MAPK signaling pathways in vascular smooth muscle cells. Journal of Cellular Physiology. 2012;227(1):127–35.

269. Das S, Samant RS, Shevde LA. Nonclassical activation of Hedgehog signaling enhances multidrug resistance and makes cancer cells refractory to Smoothened-targeting Hedgehog inhibition. J Biol Chem. 2013 Apr 26;288(17):11824–33.

270. Lu C, Fang S, Weng Q, Lv X, Meng M, Zhu J, et al. Integrated analysis reveals critical glycolytic regulators in hepatocellular carcinoma. Cell Communication and Signaling. 2020 Jun 23;18(1):97.

271. Cui J, Wang J, Lin C, Liu J, Zuo W. Osteopontin Mediates Cetuximab Resistance via the MAPK Pathway in NSCLC Cells. Onco Targets Ther. 2019 Nov 26;12:10177–85.

272. Fu Y, Zhang Y, Lei Z, Liu T, Cai T, Wang A, et al. Abnormally activated OPN/integrin αVβ3/FAK signalling is responsible for EGFR-TKI resistance in EGFR mutant non-small-cell lung cancer. Journal of Hematology & Oncology. 2020 Dec 7;13(1):169.

273. Yi H, Zeng D, Shen Z, Liao J, Wang X, Liu Y, et al. Integrin alphavbeta3 enhances β-catenin signaling in acute myeloid leukemia harboring Fms-like tyrosine kinase-3 internal tandem duplication mutations: implications for microenvironment influence on sorafenib sensitivity. Oncotarget. 2016 May 26;7(26):40387–97.

274. Kuroda N, Hamaguchi N, Ohara M, Hirouchi T, Mizuno K, Lee GH. Large cell neuroendocrine carcinoma of the lung with calcification and expression of osteopontin. Med Mol Morphol. 2007 Dec;40(4):218–20.

275. Yamagishi S, Suzuki T, Ohkuro H, Yagihashi S. Ossifying gastric carcinoid tumor containing bone morphogenetic protein, osteopontin and osteonectin. Journal of endocrinological investigation [Internet]. 2004 Oct.

276. Ferreira LB, Eloy C, Pestana A, Lyra J, Moura M, Prazeres H, et al. Osteopontin expression is correlated with differentiation and good prognosis in medullary thyroid carcinoma. Eur J Endocrinol. 2016 Apr;174(4):551–61.

277. Kidess E, Giesecke Y, Eichhorn I, Mohr R, Jann H, Fischer C, et al. Osteopontin is a prognostic circulating biomarker in patients with neuroendocrine neoplasms. J Cancer Res Clin Oncol. 2023 Sep;149(12):10925–33.

278. R Core Team. R: A language and environment for statistical computing. R Foundation for Statistical Computing. R Foundation for Statistical Computing, Vienna, Austria URL https://wwwR-project.org/. 2021.

279. Gautier L, Cope L, Bolstad BM, Irizarry RA. affy—analysis of Affymetrix GeneChip data at the probe level. Bioinformatics. 2004 Feb 12;20(3):307–15.

280. Ritchie ME, Phipson B, Wu D, Hu Y, Law CW, Shi W, et al. limma powers differential expression analyses for RNA-sequencing and microarray studies. Nucleic Acids Research. 2015 Apr 20;43(7):e47.

281. Friedman JH, Hastie T, Tibshirani R. Regularization Paths for Generalized Linear Models via Coordinate Descent. Journal of Statistical Software. 2010 Feb 2;33:1–22.

282. Foroutan M, Bhuva DD, Lyu R, Horan K, Cursons J, Davis MJ. Single sample scoring of molecular phenotypes. BMC Bioinformatics. 2018 Nov 6;19(1):404.

283. Eisenhauer EA, Therasse P, Bogaerts J, Schwartz LH, Sargent D, Ford R, et al. New response evaluation criteria in solid tumours: revised RECIST guideline (version 1.1). Eur J Cancer. 2009 Jan;45(2):228–47.

284. Korotkevich G, Sukhov V, Budin N, Shpak B, Artyomov MN, Sergushichev A. Fast gene set enrichment analysis [Internet]. bioRxiv; 2021.

285. Liberzon A, Birger C, Thorvaldsdóttir H, Ghandi M, Mesirov JP, Tamayo P. The Molecular Signatures Database (MSigDB) hallmark gene set collection. Cell Syst. 2015 Dec 23;1(6):417–25.

286. Kanehisa M, Furumichi M, Sato Y, Kawashima M, Ishiguro-Watanabe M. KEGG for taxonomy-based analysis of pathways and genomes. Nucleic Acids Res. 2023 Jan 6;51(D1):D587–92.

287. Thomas PD, Ebert D, Muruganujan A, Mushayahama T, Albou LP, Mi H. PANTHER: Making genome-scale phylogenetics accessible to all. Protein Science. 2022;31(1):8–22.

288. Tyler M, Tirosh I. Decoupling epithelial-mesenchymal transitions from stromal profiles by integrative expression analysis. Nat Commun. 2021 May 10;12(1):2592.

289. Aran D, Hu Z, Butte AJ. xCell: digitally portraying the tissue cellular heterogeneity landscape. Genome Biology. 2017 Nov 15;18(1):220.

290. Pelossof R, Fairchild L, Huang CH, Widmer C, Sreedharan VT, Sinha N, et al. Prediction of ultra-potent shRNAs with a sequential classification algorithm. Nat Biotechnol. 2017 Apr;35(4):350–3.

291. Untergasser A, Cutcutache I, Koressaar T, Ye J, Faircloth BC, Remm M, et al. Primer3--new capabilities and interfaces. Nucleic Acids Res. 2012 Aug;40(15):e115.

292. Livak KJ, Schmittgen TD. Analysis of relative gene expression data using real-time quantitative PCR and the 2(-Delta Delta C(T)) Method. Methods. 2001 Dec;25(4):402–8.

293. Wang X, Spandidos A, Wang H, Seed B. PrimerBank: a PCR primer database for quantitative gene expression analysis, 2012 update. Nucleic Acids Research. 2012 Jan 1;40(D1):D1144–9.

294. Guzmán C, Bagga M, Kaur A, Westermarck J, Abankwa D. ColonyArea: An ImageJ Plugin to Automatically Quantify Colony Formation in Clonogenic Assays. PLOS ONE. 2014 Mar 19;9(3):e92444.

295. Carpentier G, Berndt S, Ferratge S, Rasband W, Cuendet M, Uzan G, et al. Angiogenesis Analyzer for ImageJ — A comparative morphometric analysis of "Endothelial Tube Formation Assay" and "Fibrin Bead Assay." Scientific Reports. 2020 Jul 14;10:11568.

296. van Beijnum JR, Nowak-Sliwinska P, Huijbers EJM, Thijssen VL, Griffioen AW. The great escape; the hallmarks of resistance to antiangiogenic therapy. Pharmacol Rev. 2015;67(2):441–61.

297. Yang KC, Kalloger SE, Aird JJ, Lee MKC, Rushton C, Mungall KL, et al. Proteotranscriptomic classification and characterization of pancreatic neuroendocrine neoplasms. Cell Reports. 2021 Oct 12;37(2):109817.

298. Zhang Y, Li X, Zhang J, Mao L. Circ-CCDC66 upregulates REXO1 expression to aggravate cervical cancer progression via restraining miR-452-5p. Cancer Cell International. 2021 Jan 6;21(1):20.

299. Palhan VB, Chen S, Peng GH, Tjernberg A, Gamper AM, Fan Y, et al. Polyglutamine-expanded ataxin-7 inhibits STAGA histone acetyltransferase activity to produce retinal degeneration. Proc Natl Acad Sci U S A. 2005 Jun 14;102(24):8472–7.

300. Wang H, Shan S, Wang H, Wang X. CircATXN7 contributes to the progression and doxorubicin resistance of breast cancer via modulating miR-149-5p/HOXA11 pathway. Anticancer Drugs. 2022 Jan 1;33(1):e700–10.

301. Li D, Fu Z, Dong C, Song Y. Downregulation of circATXN7 represses non-small cell lung cancer growth by releasing miR-7-5p. Thorac Cancer. 2022 Jun;13(11):1597–610.

302. Kalvala A, Gao L, Aguila B, Dotts K, Rahman M, Nana-Sinkam SP, et al. Rad51C-ATXN7 fusion gene expression in colorectal tumors. Mol Cancer. 2016 Jun 13;15(1):47.

303. Montero-Conde C, Leandro-Garcia LJ, Chen X, Oler G, Ruiz-Llorente S, Ryder M, et al. Transposon mutagenesis identifies chromatin modifiers cooperating with Ras in thyroid tumorigenesis and detects ATXN7 as a cancer gene. Proc Natl Acad Sci U S A. 2017 Jun 20;114(25):E4951–60.

304. Han C, Yu L, Liu X, Yu T, Qin W, Liao X, et al. ATXN7 Gene Variants and Expression Predict Post-Operative Clinical Outcomes in Hepatitis B Virus-Related Hepatocellular Carcinoma. Cell Physiol Biochem. 2016;39(6):2427–38.

305. Martinez E, Palhan VB, Tjernberg A, Lymar ES, Gamper AM, Kundu TK, et al. Human STAGA Complex Is a Chromatin-Acetylating Transcription Coactivator That Interacts with Pre-mRNA Splicing and DNA Damage-Binding Factors In Vivo. Mol Cell Biol. 2001 Oct;21(20):6782–95.

306. Renkl AC, Wussler J, Ahrens T, Thoma K, Kon S, Uede T, et al. Osteopontin functionally activates dendritic cells and induces their differentiation toward a Th1-polarizing phenotype. Blood. 2005 Aug 1;106(3):946–55.

307. Crabtree JS, Singleton CS, Miele L. Notch Signaling in Neuroendocrine Tumors. Frontiers in Oncology. 2016 Apr 14;6:94.

308. Weinsheimer S, Lenk GM, van der Voet M, Land S, Ronkainen A, Alafuzoff I, et al. Integration of expression profiles and genetic mapping data to identify candidate genes in intracranial aneurysm. Physiological Genomics. 2007 Dec;32(1):45–57.

309. Ostuni R, Kratochvill F, Murray PJ, Natoli G. Macrophages and cancer: from mechanisms to therapeutic implications. Trends in Immunology. 2015 Apr 1;36(4):229–39.

310. Lu F, Ye M, Shen Y, Xu Y, Hu C, Chen J, et al. Hypoxic tumor-derived exosomal miR-4488 induces macrophage M2 polarization to promote liver metastasis of pancreatic neuroendocrine neoplasm through RTN3/FABP5 mediated fatty acid oxidation. International Journal of Biological Sciences. 2024 Jun 3;20(8):3201–18.

311. Ye M, Lu F, Gu D, Xue B, Xu L, Hu C, et al. Hypoxia exosome derived CEACAM5 promotes tumor-associated macrophages M2 polarization to accelerate pancreatic neuroendocrine tumors metastasis via MMP9. FASEB J. 2024 Jul 15;38(13):e23762.

312. Zhong Y, Tian Y, Wang Y, Bai J, Long Q, Yan L, et al. Small Extracellular Vesicle piR-hsa-30937 Derived from Pancreatic Neuroendocrine Neoplasms Upregulates CD276 in Macrophages to Promote Immune Evasion. Cancer Immunol Res. 2024 Jul 2;12(7):840–53.

313. Edfors F, Danielsson F, Hallström BM, Käll L, Lundberg E, Pontén F, et al. Gene-specific correlation of RNA and protein levels in human cells and tissues. Molecular Systems Biology. 2016 Oct 26;12(10):883.

314. Kosti I, Jain N, Aran D, Butte AJ, Sirota M. Cross-tissue Analysis of Gene and Protein Expression in Normal and Cancer Tissues. Sci Rep. 2016 May 4;6(1):24799.

315. Pascal LE, True LD, Campbell DS, Deutsch EW, Risk M, Coleman IM, et al. Correlation of mRNA and protein levels: Cell type-specific gene expression of cluster designation antigens in the prostate. BMC Genomics. 2008 May 23;9(1):246.

316. Ebos JML, Lee CR, Christensen JG, Mutsaers AJ, Kerbel RS. Multiple circulating proangiogenic factors induced by sunitinib malate are tumor-independent and correlate with antitumor efficacy. Proceedings of the National Academy of Sciences. 2007 Oct 23;104(43):17069–74.

317. Kale S, Raja R, Thorat D, Soundararajan G, Patil TV, Kundu GC. Osteopontin signaling upregulates cyclooxygenase-2 expression in tumor-associated macrophages leading to enhanced angiogenesis and melanoma growth via α9β1 integrin. Oncogene. 2014 May;33(18):2295–306.

318. Casali BC, Baptista MP, Pachane BC, Cortez AA, Altei WF, Selistre-de-Araújo HS. Blockage of αvβ3 integrin in 3D culture of triple-negative breast cancer and endothelial cells inhibits migration

and discourages endothelial-to-mesenchymal plasticity. Biochemistry and Biophysics Reports. 2024 Jul 1;38:101686.

319. Fuchs K, Hippe A, Schmaus A, Homey B, Sleeman JP, Orian-Rousseau V. Opposing effects of high- and low-molecular weight hyaluronan on CXCL12-induced CXCR4 signaling depend on CD44. Cell Death Dis. 2013 Oct;4(10):e819–e819.

320. Storgard C, Mikolon D, Stupack DG. Angiogenesis assays in the chick CAM. Methods Mol Biol. 2005;294:123–36.

321. Jilani SM, Murphy TJ, Thai SNM, Eichmann A, Alva JA, Iruela-Arispe ML. Selective Binding of Lectins to Embryonic Chicken Vasculature. J Histochem Cytochem. 2003 May 1;51(5):597–604.

322. Hofving T, Arvidsson Y, Almobarak B, Inge L, Pfragner R, Persson M, et al. The neuroendocrine phenotype, genomic profile and therapeutic sensitivity of GEPNET cell lines. Endocr Relat Cancer. 2018 Jan 15;25(3):367–80.

323. Dayton TL, Alcala N, Moonen L, den Hartigh L, Geurts V, Mangiante L, et al. Druggable growth dependencies and tumor evolution analysis in patient-derived organoids of neuroendocrine neoplasms from multiple body sites. Cancer Cell. 2023 Dec 11;41(12):2083-2099.e9.

324. Ear PH, Marinoni I, Dayton T, Guenter R, Quelle DE, Battistella A, et al. NET Models Meeting 2024 white paper: the current state of neuroendocrine tumour research models and our future aspirations. Endocr Oncol. 2024 Jan 1;4(1):e240055.

325. Garcia P, Wang Y, Viallet J, Macek Jilkova Z. The Chicken Embryo Model: A Novel and Relevant Model for Immune-Based Studies. Front Immunol. 2021;12:791081.

Annex I

Annex I

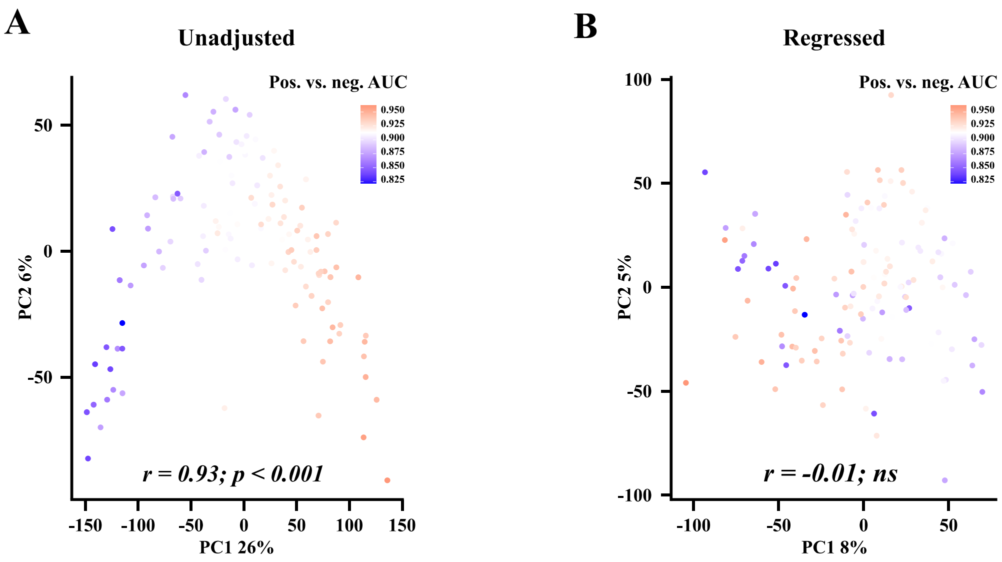

Supplementary Figure 1. Quality correction of transcriptomic data. A. PCA was performed on the gene matrix to evaluate the quality of the samples. PC1 and PC2, along with their percentage of explained variance are shown on the x and y- axes, respectively. The 126 samples are plotted, and the RNA quality score (Pos. vs. Neg. AUC) is shown. Red and blue colors represent high and low quality, respectively. The correlation coefficient and its *p-value* are shown. PC1 was significantly correlated with the RNA quality (*correlation coefficient = 0.93; p-value* $< 10^{-6}$), suggesting that the variance in the data is associated with noise. **B.** Given that this variance was not strictly related to the biology of the samples, PC1 was regressed using *removeBatchEffect* from *limma*. The PC1 from the resulting gene matrix no longer correlated with RNA quality (*p = 0.948*). *Ns, non-significant*. *** $p < 0.001$ was considered statistically significant. PC, principal component. AUC, area under the curve.

A

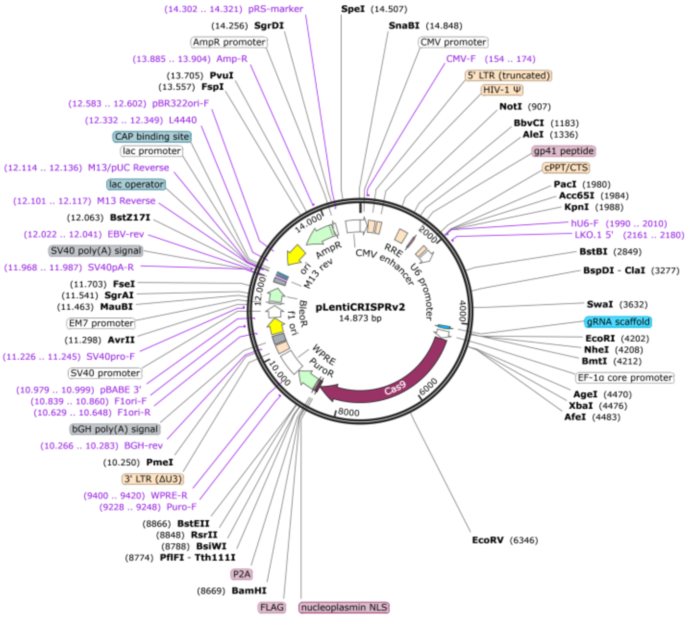
pLentiCRISPRv2
14.873 bp
(14.302 .. 14.321) pRS-marker
(14.256) SgrDI
AmpR promoter
(13.885 .. 13.904) Amp-R
(13.705) PvuI
(13.557) FspI
(12.583 .. 12.602) pBR322ori-F
(12.332 .. 12.349) L4440
CAP binding site
lac promoter
(12.114 .. 12.136) M13/pUC Reverse
lac operator
(12.101 .. 12.117) M13 Reverse
(12.063) BstZ17I
(12.022 .. 12.041) EBV-rev
SV40 poly(A) signal
(11.968 .. 11.987) SV40pA-R
(11.703) FseI
(11.541) SgrAI
(11.463) MauBI
EM7 promoter
(11.298) AvrII
(11.226 .. 11.245) SV40pro-F
SV40 promoter
(10.979 .. 10.999) pBABE 3'
(10.839 .. 10.860) F1ori-F
(10.629 .. 10.648) F1ori-R
bGH poly(A) signal
(10.266 .. 10.283) BGH-rev
(10.250) PmeI
3' LTR (ΔU3)
(9400 .. 9420) WPRE-R
(9228 .. 9248) Puro-F
(8866) BstEII
(8848) RsrII
(8788) BsiWI
(8774) PflFI - Tth111I
P2A
(8669) BamHI
FLAG
nucleoplasmin NLS
SpeI (14.507)
SnaBI (14.848)
CMV promoter
CMV-F (154 .. 174)
5' LTR (truncated)
HIV-1 Ψ
NotI (907)
BbvCI (1183)
AleI (1336)
gp41 peptide
cPPT/CTS
PacI (1980)
Acc65I (1984)
KpnI (1988)
hU6-F (1990 .. 2010)
LKO.1 5' (2161 .. 2180)
BstBI (2849)
BspDI - ClaI (3277)
SwaI (3632)
gRNA scaffold
EcoRI (4202)
NheI (4208)
BmtI (4212)
EF-1α core promoter
AgeI (4470)
XbaI (4476)
AfeI (4483)
EcoRV (6346)
AmpR
ori
M13 rev
CMV enhancer
RRE
U6 promoter
BleoR
f1 ori
WPRE
PuroR
Cas9
2000
4000
6000
8000
10.000
12.000
14.000

B

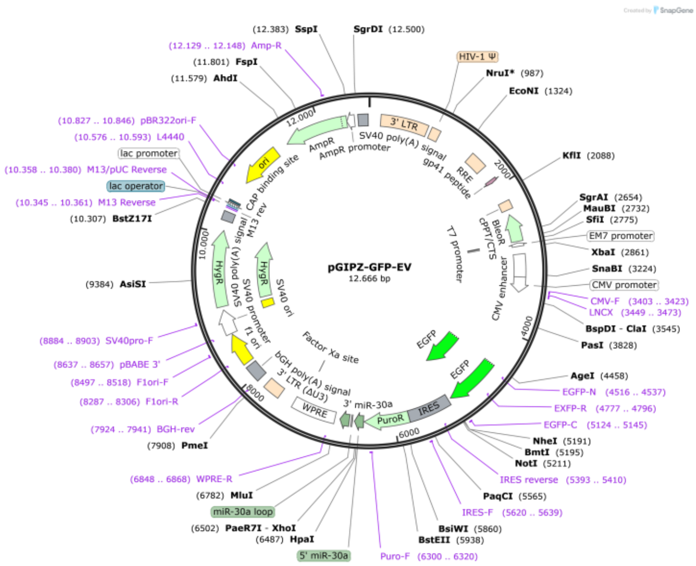
pGIPZ-GFP-EV
12.666 bp
(12.383) SspI
SgrDI (12.500)
(12.129 .. 12.148) Amp-R
(11.801) FspI
(11.579) AhdI
(10.827 .. 10.846) pBR322ori-F
(10.576 .. 10.593) L4440
lac promoter
(10.358 .. 10.380) M13/pUC Reverse
lac operator
(10.345 .. 10.361) M13 Reverse
(10.307) BstZ17I
(9384) AsiSI
(8884 .. 8903) SV40pro-F
(8637 .. 8657) pBABE 3'
(8497 .. 8518) F1ori-F
(8287 .. 8306) F1ori-R
(7924 .. 7941) BGH-rev
(7908) PmeI
(6848 .. 6868) WPRE-R
(6782) MluI
miR-30a loop
(6502) PaeR7I - XhoI
(6487) HpaI
5' miR-30a
Puro-F (6300 .. 6320)
BstEII (5938)
BsiWI (5860)
IRES-F (5620 .. 5639)
PaqCI (5565)
IRES reverse (5393 .. 5410)
NotI (5211)
BmtI (5195)
NheI (5191)
EGFP-C (5124 .. 5145)
EXFP-R (4777 .. 4796)
EGFP-N (4516 .. 4537)
AgeI (4458)
PasI (3828)
BspDI - ClaI (3545)
LNCX (3449 .. 3473)
CMV-F (3403 .. 3423)
CMV promoter
SnaBI (3224)
XbaI (2861)
EM7 promoter
SfiI (2775)
MauBI (2732)
SgrAI (2654)
KflI (2088)
EcoNI (1324)
NruI* (987)
HIV-1 Ψ
3' LTR
SV40 poly(A) signal
AmpR
AmpR promoter
ori
CAP binding site
M13 rev
SV40 poly(A) signal
HygR
SV40 ori
SV40 promoter
f1 ori
Factor Xa site
bGH poly(A) signal
3' LTR (ΔU3)
WPRE
3' miR-30a
PuroR
IRES
EGFP
T7 promoter
RRE
gp41 peptide
BleoR
cPPT/CTS
CMV enhancer
2000
4000
6000
8000
10.000
12.000

C

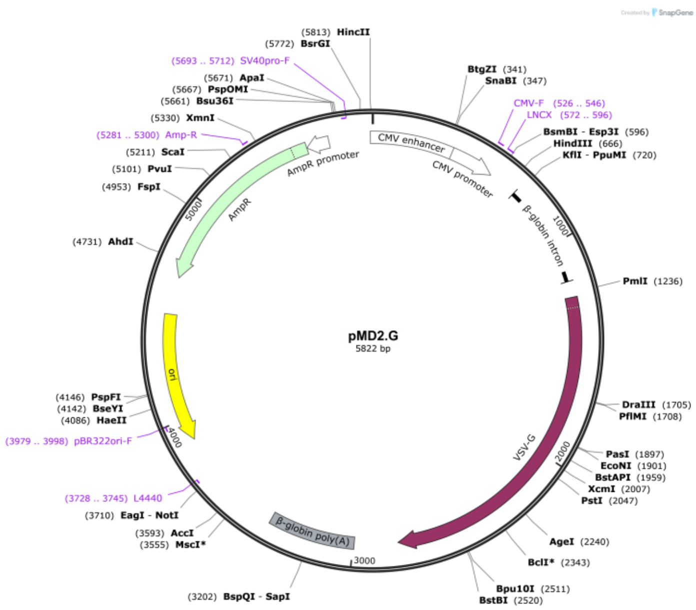
pMD2.G
5822 bp
(5813) HincII
(5772) BsrGI
(5693 .. 5712) SV40pro-F
(5671) ApaI
(5667) PspOMI
(5661) Bsu36I
(5330) XmnI
(5281 .. 5300) Amp-R
(5211) ScaI
(5101) PvuI
(4953) FspI
(4731) AhdI
(4146) PspFI
(4142) BseYI
(4086) HaeII
(3979 .. 3998) pBR322ori-F
(3728 .. 3745) L4440
(3710) EagI - NotI
(3593) AccI
(3555) MscI*
(3202) BspQI - SapI
BtgZI (341)
SnaBI (347)
CMV-F (526 .. 546)
LNCX (572 .. 596)
BsmBI - Esp3I (596)
HindIII (666)
KflI - PpuMI (720)
PmlI (1236)
DraIII (1705)
PflMI (1708)
PasI (1897)
EcoNI (1901)
BstAPI (1959)
XcmI (2007)
PstI (2047)
AgeI (2240)
BclI* (2343)
Bpu10I (2511)
BstBI (2520)
CMV enhancer
CMV promoter
β-globin intron
VSV-G
β-globin poly(A)
ori
AmpR
AmpR promoter
1000
2000
3000
4000
5000

D

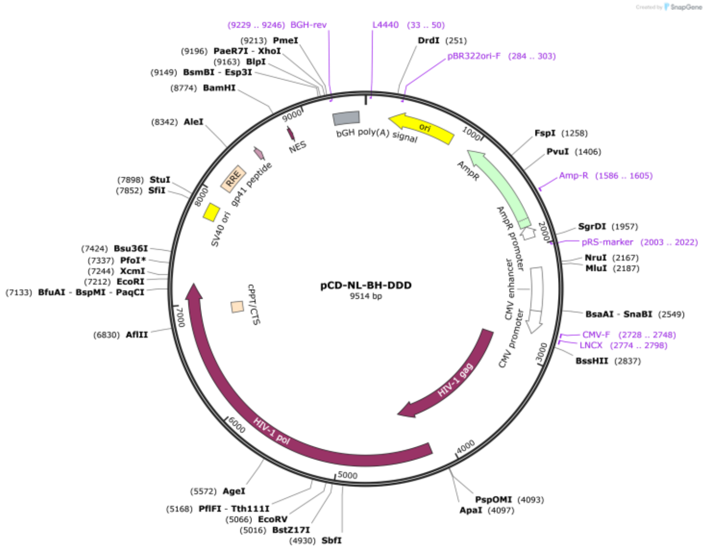
pCD-NL-BH-DDD
9514 bp
(9229 .. 9246) BGH-rev
L4440 (33 .. 50)
DrdI (251)
pBR322ori-F (284 .. 303)
(9213) PmeI
(9196) PaeR7I - XhoI
(9163) BlpI
(9149) BsmBI - Esp3I
(8774) BamHI
(8342) AleI
FspI (1258)
PvuI (1406)
Amp-R (1586 .. 1605)
(7898) StuI
(7852) SfiI
SgrDI (1957)
pRS-marker (2003 .. 2022)
NruI (2167)
MluI (2187)
(7424) Bsu36I
(7337) PflFI*
(7244) XcmI
(7212) EcoRI
(7133) BfuAI - BspMI - PaqCI
BsaAI - SnaBI (2549)
(6830) AflII
CMV-F (2728 .. 2748)
LNCX (2774 .. 2798)
BssHII (2837)
(5572) AgeI
(5168) PflFI - Tth111I
(5066) EcoRV
(5016) BstZ17I
(4930) SbfI
PspOMI (4093)
ApaI (4097)
bGH poly(A) signal
ori
AmpR
AmpR promoter
CMV enhancer
CMV promoter
HIV-1 gag
HIV-1 pol
cPPT/CTS
SV40 ori
RRE
gp41 peptide
NES

E

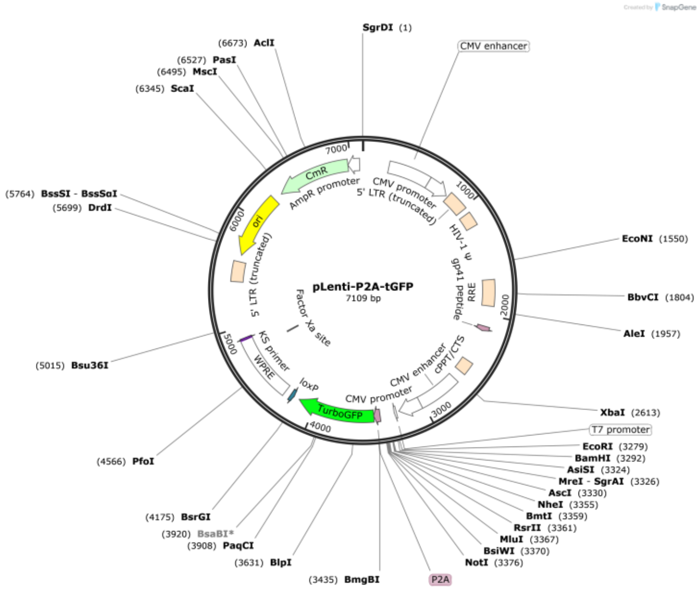
pLenti-P2A-tGFP
7109 bp
SgrDI (1)
CMV enhancer
(6673) AclI
(6527) PasI
(6495) MscI
(6345) ScaI
(5764) BssSI - BssSαI
(5699) DrdI
EcoNI (1550)
BbvCI (1804)
AleI (1957)
(5015) Bsu36I
XbaI (2613)
T7 promoter
EcoRI (3279)
BamHI (3292)
AsiSI (3324)
MreI - SgrAI (3326)
AscI (3330)
NheI (3355)
BmtI (3359)
RsrII (3361)
MluI (3367)
BsiWI (3370)
NotI (3376)
(4566) PfoI
(4175) BsrGI
(3920) BsaBI*
(3908) PaqCI
(3631) BlpI
(3435) BmgBI
P2A
CmR
AmpR promoter
CMV promoter
5' LTR (truncated)
ori
HIV-1 ψ
RRE
gp41 peptide
cPPT/CTS
CMV enhancer
CMV promoter
TurboGFP
loxP
WPRE
KS primer
5' LTR (truncated)
Factor Xa site

F

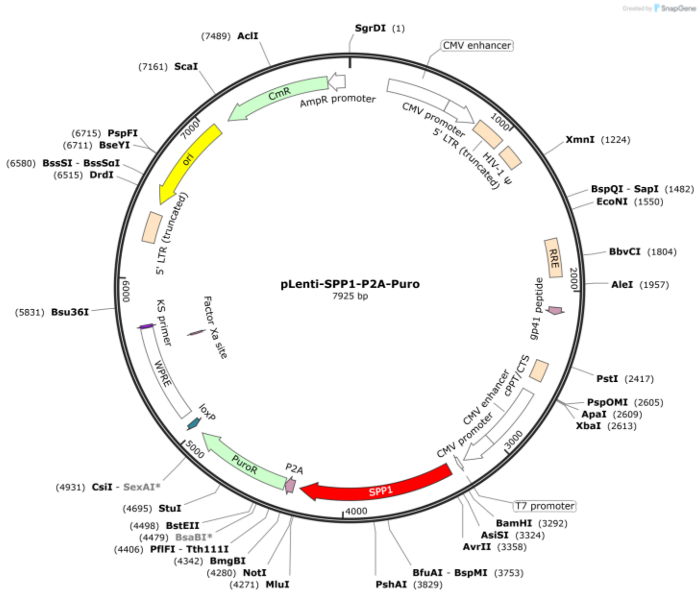
pLenti-SPP1-P2A-Puro
7925 bp
SgrDI (1)
CMV enhancer
(7489) AclI
(7161) ScaI
(6715) PspFI
(6711) BseYI
(6580) BssSI - BssSαI
(6515) DrdI
XmnI (1224)
BspQI - SapI (1482)
EcoNI (1550)
BbvCI (1804)
AleI (1957)
(5831) Bsu36I
PstI (2417)
PspOMI (2605)
ApaI (2609)
XbaI (2613)
(4931) CsiI - SexAI*
(4695) StuI
(4498) BstEII
(4479) BsaBI*
(4406) PflFI - Tth111I
(4342) BmgBI
(4280) NotI
(4271) MluI
T7 promoter
BamHI (3292)
AsiSI (3324)
AvrII (3358)
BfuAI - BspMI (3753)
PshAI (3829)
CmR
AmpR promoter
CMV promoter
5' LTR (truncated)
HIV-1 ψ
ori
RRE
gp41 peptide
cPPT/CTS
CMV enhancer
CMV promoter
SPP1
P2A
PuroR
loxP
WPRE
KS primer
Factor Xa site

G

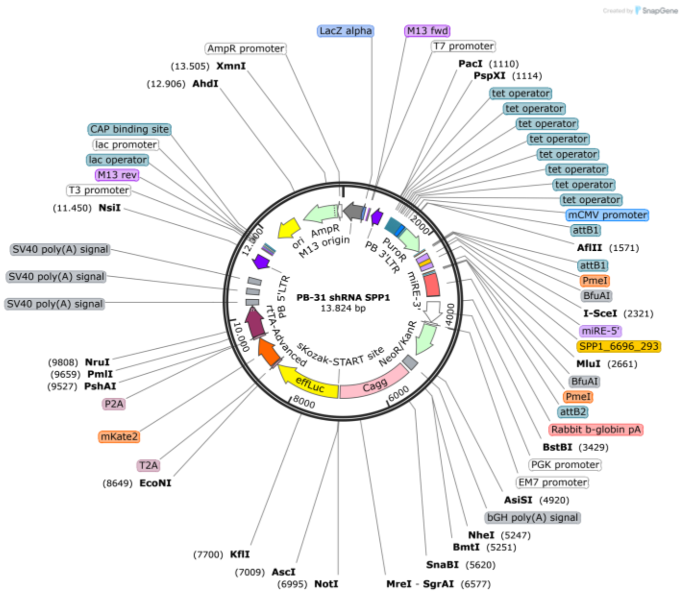
PB-31 shRNA SPP1
13.824 bp
LacZ alpha
M13 fwd
AmpR promoter
T7 promoter
(13.505) XmnI
PacI (1110)
(12.906) AhdI
PspXI (1114)
tet operator
tet operator
tet operator
tet operator
tet operator
tet operator
tet operator
tet operator
CAP binding site
lac promoter
lac operator
M13 rev
T3 promoter
(11.450) NsiI
mCMV promoter
attB1
AflII (1571)
attB1
PmeI
BfuAI
I-SceI (2321)
miRE-5'
SPP1_6696_293
MluI (2661)
BfuAI
PmeI
attB2
Rabbit b-globin pA
BstBI (3429)
PGK promoter
EM7 promoter
AsiSI (4920)
bGH poly(A) signal
NheI (5247)
BmtI (5251)
SnaBI (5620)
MreI - SgrAI (6577)
(6995) NotI
(7009) AscI
(7700) KflI
SV40 poly(A) signal
SV40 poly(A) signal
SV40 poly(A) signal
(9808) NruI
(9659) PmlI
(9527) PshAI
P2A
mKate2
T2A
(8649) EcoNI
ori
AmpR
M13 origin
PB 3'LTR
PuroR
miRE-3'
NeoR/KanR
Cagg
effLuc
sKozak-START site
rtTA-Advanced
PB 5'LTR
2000
4000
6000
8000
10.000
12.000

H

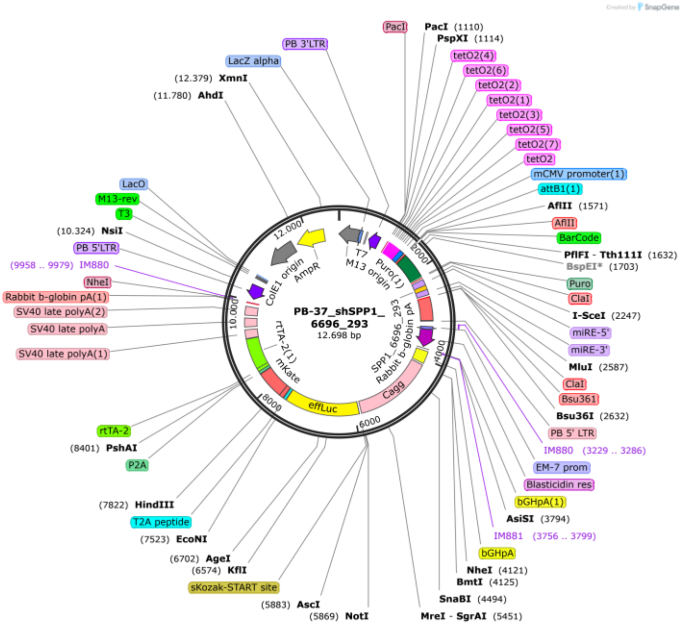
PB-37_shSPP1_
6696_293
12.698 bp
PacI
PacI (1110)
PspXI (1114)
PB 3'LTR
LacZ alpha
(12.379) XmnI
(11.780) AhdI
tetO2(4)
tetO2(6)
tetO2(2)
tetO2(1)
tetO2(3)
tetO2(5)
tetO2(7)
tetO2
mCMV promoter(1)
attB1(1)
AflII (1571)
AflII
BarCode
PflFI - Tth111I (1632)
BspEI* (1703)
Puro
ClaI
I-SceI (2247)
miRE-5'
miRE-3'
MluI (2587)
ClaI
Bsu36I
Bsu36I (2632)
PB 5' LTR
IM880 (3229 .. 3286)
EM-7 prom
Blasticidin res
bGHpA(1)
AsiSI (3794)
IM881 (3756 .. 3799)
bGHpA
NheI (4121)
BmtI (4125)
SnaBI (4494)
MreI - SgrAI (5451)
(5869) NotI
(5883) AscI
sKozak-START site
(6574) KflI
(6702) AgeI
(7523) EcoNI
T2A peptide
(7822) HindIII
P2A
(8401) PshAI
rtTA-2
LacO
M13-rev
T3
(10.324) NsiI
PB 5'LTR
(9958 .. 9979) IM880
NheI
Rabbit b-globin pA(1)
SV40 late polyA(2)
SV40 late polyA
SV40 late polyA(1)
ColE1 origin
AmpR
M13 origin
Puro(1)
SPP1_6696_293
Rabbit b-globin pA
Cagg
effLuc
mKate
rtTA-2(1)
2000
4000
6000
8000
10.000
12.000

I

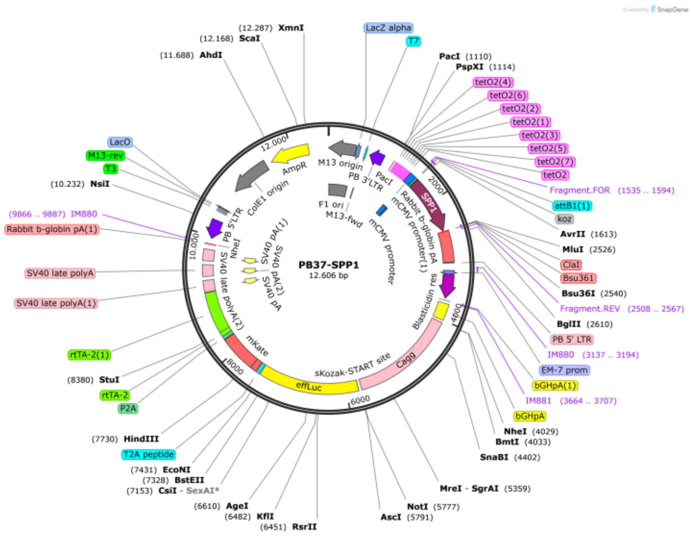
PB37-SPP1
12.606 bp
(12.287) XmnI
(12.168) ScaI
(11.688) AhdI
LacZ alpha
T7
PacI (1110)
PspXI (1114)
tetO2(4)
tetO2(6)
tetO2(2)
tetO2(1)
tetO2(3)
tetO2(5)
tetO2(7)
tetO2
Fragment.FOR (1535 .. 1594)
attB1(1)
koz
AvrII (1613)
MluI (2526)
ClaI
Bsu36I
Bsu36I (2540)
Fragment.REV (2508 .. 2567)
BglII (2610)
PB 5' LTR
IM880 (3137 .. 3194)
EM-7 prom
bGHpA(1)
IM881 (3664 .. 3707)
bGHpA
NheI (4029)
BmtI (4033)
SnaBI (4402)
MreI - SgrAI (5359)
NotI (5777)
AscI (5791)
(6451) RsrII
(6482) KflI
(6610) AgeI
(7153) CsiI - SexAI*
(7328) BstEII
(7431) EcoNI
T2A peptide
(7730) HindIII
P2A
rtTA-2
(8380) StuI
rtTA-2(1)
LacO
M13-rev
T3
(10.232) NsiI
(9866 .. 9887) IM880
Rabbit b-globin pA(1)
SV40 late polyA
SV40 late polyA(1)
AmpR
ColE1 origin
M13 origin
PB 3'LTR
PacI
F1 ori
M13-fwd
mCMV promoter
Rabbit b-globin pA
mCMV promoter(1)
SPP1
Blasticidin res
Cagg
effLuc
sKozak-START site
mKate
PB 5'LTR
NheI
SV40 late polyA(2)
SV40 pA(1)
SV40 pA(2)
SV40 pA
2000
4000
6000
8000
10.000
12.000

J

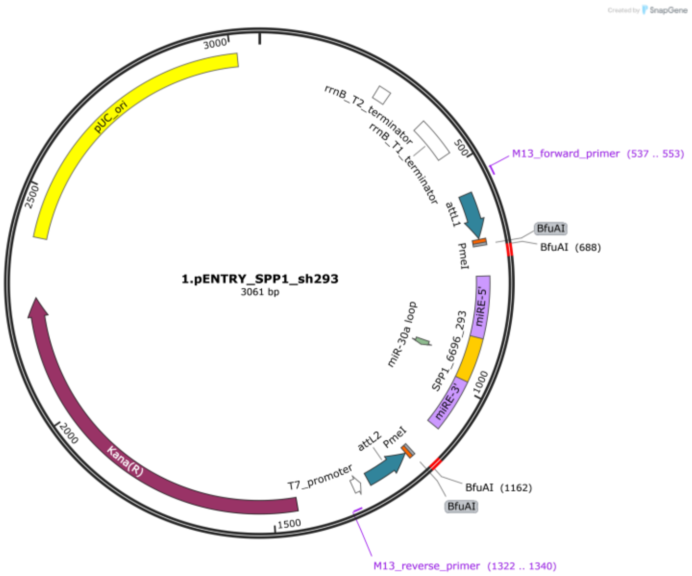

Supplementary Figure 2. Vector maps. The maps of all plasmids cloned and used in this project are shown. Genes, ORFs, tags and promoters, restriction enzymes and primers are shown among other relevant functional features. Maps were generated in SnapGene. **A.** pLentiCRISPR v2 (#52961, Addgene). **B.** pGIPZ-GFP-EV (#120933, Addgene). **C.** pMD2.G (#12259, Addgene). **D.** pCD/NL-BH*DDD (#17531, Addgene). **E.** pLenti-P2A-tGFP. **F.** pLenti-SPP1-P2A-Puro. **G.** PB-31 shRNA-SPP1. **H.** PB-37BC-shRNA-SPP1. **I.** PB-37-SPP1. **J.** pENTRY-shRNA-SPP1.

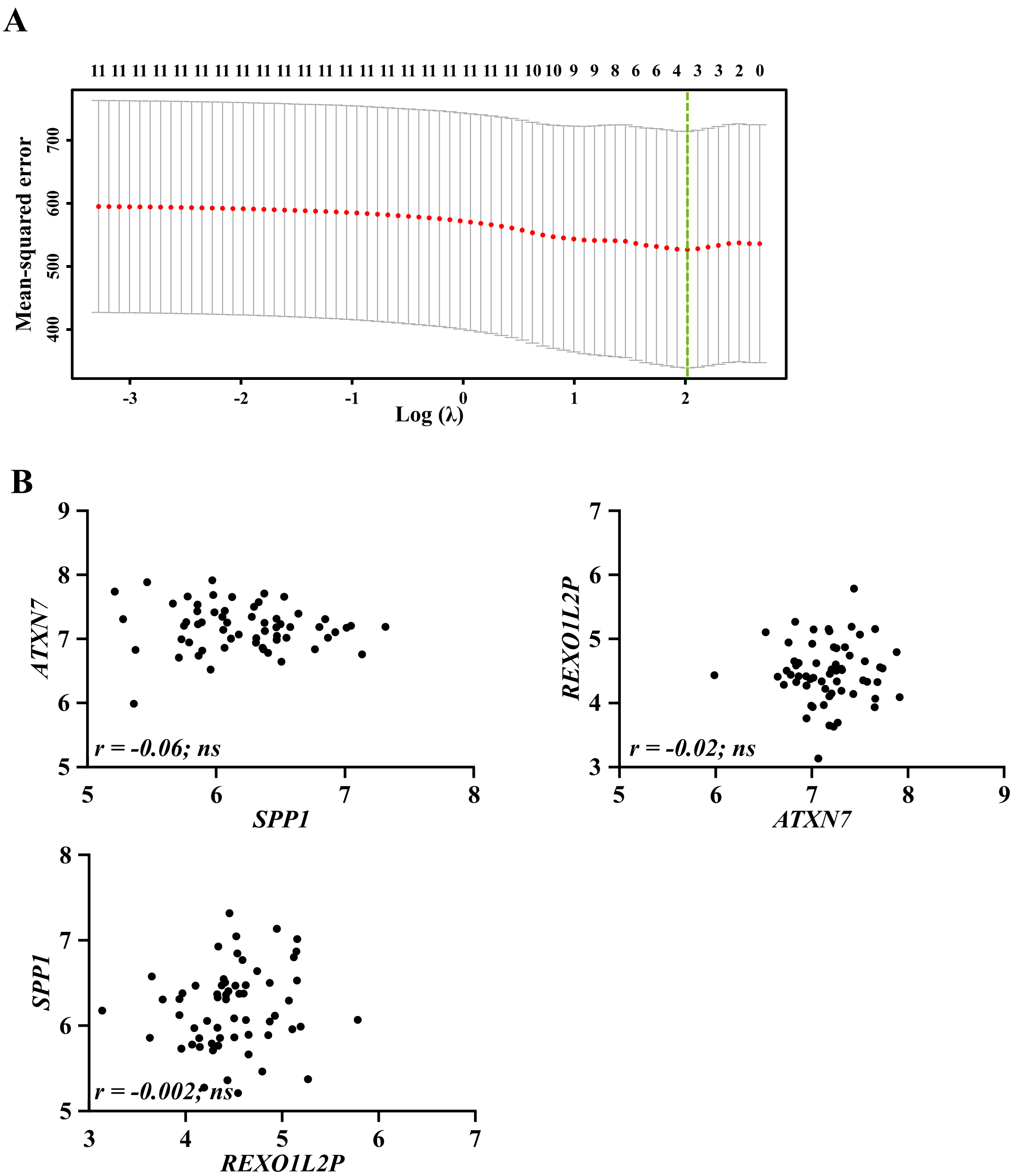

Supplementary Figure 3. Regularized linear regression. A. We studied the association of the 11 candidates with tumor shrinkage using regularized linear regression. A model was built using the gene expression of the 11 candidates as independent variables and tumor shrinkage as the outcome variable. The graph summarizes all the candidate models. The upper x-axis shows the number of genes included in each model. The lower x-axis represents the log value of λ. Finally, the y-axis represents the mean-squared error of the model. The vertical green line highlights the model with the minimum mean-squared error. This model included 3 genes: *SPP1*, *REXO1L2P* and *ATXN7*, and a λ of 7.53. **B.** Pairwise Pearson correlation analysis was performed to confirm that these 3 genes provided independent, non-redundant information. The Pearson correlation coefficient (*r*) is shown. No significant correlation was observed, confirming the independence of these 3 genes. *Ns, non-significant*. A $p < 0.05$ was considered statistically significant.

A

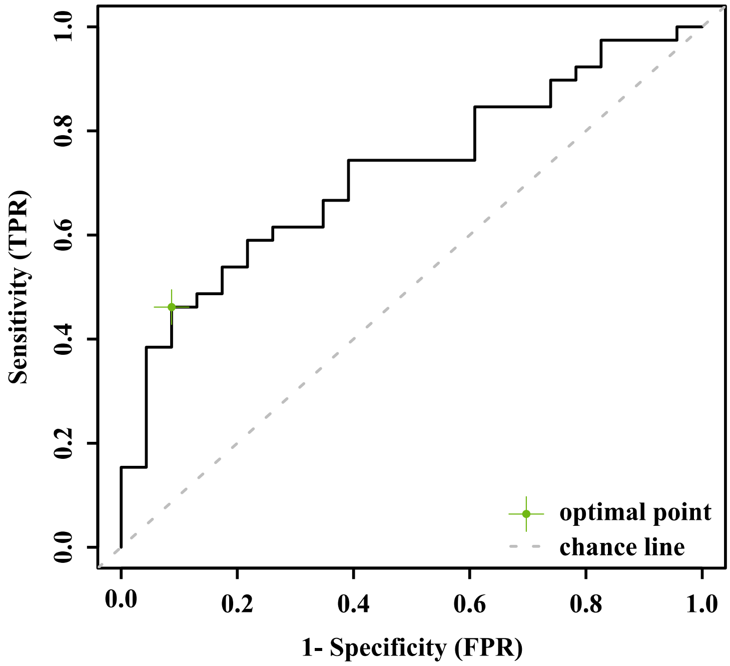

Supplementary Figure 4. Median signature score is an effective threshold to evaluate axitinib efficacy. A. ROC analysis was conducted to determine the optimal score cutoff to predict axitinib efficacy. Based on the placebo median PFS (10 months), 12 months was set as the cutoff value to distinguish axitinib responders from non-responders. The true positive rate and the false positive rate are represented on the y- and x-axes, respectively. The ROC analysis identified a cutoff value of 0.466, yielding an AUC of 0.718, with a false positive rate of 87% and a true positive rate of 46%. The median signature score for our population was 0.415, which is relatively close to the identified cutoff, and was used to differentiate responders from non-responders. TPR, true positive rate. FPR, false positive rate.

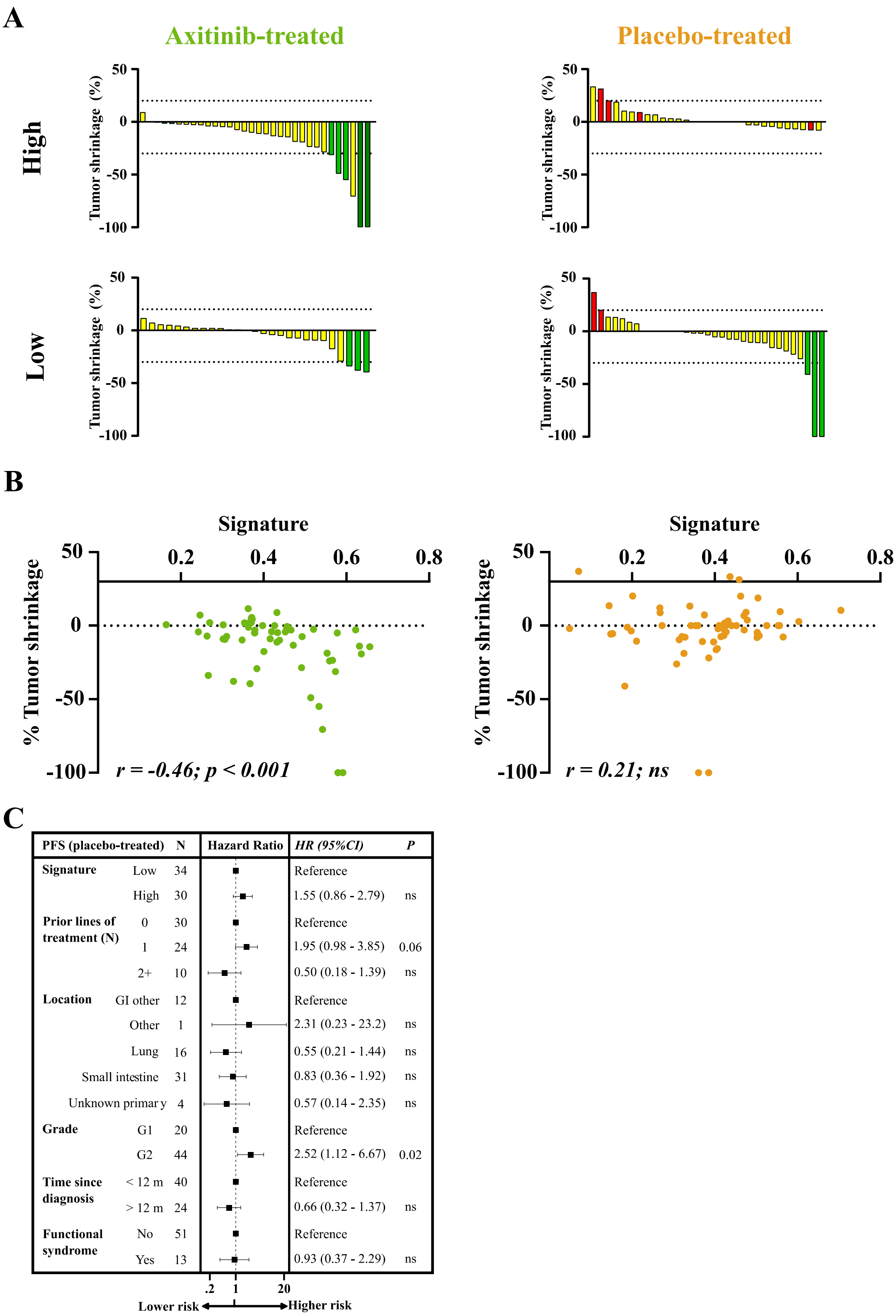

Supplementary Figure 5. The 3-gene signature predicts efficacy to axitinib in NETs. A. Waterfall plots of patients with high and low signature scores treated with axitinib and placebo, respectively, are shown. Tumor shrinkage is represented on the y-axis. Each bar represents one patient, and the color indicates the best OR: CR, dark green; PR, green; SD, yellow; and PD, red. Axitinib-treated patients with high scores are enriched in CR and PR compared to patients with low scores. Accordingly, patients with high signature scores are also enriched for SD with higher tumor shrinkage compared to patients with low scores. No differences were observed in placebo treated patients. **B.** Spearman correlation analysis was performed to confirm the association of the signature with tumor shrinkage. The analysis was conducted separately in axitinib and placebo-treated patients. Tumor shrinkage and signature score are represented on the y- and x-axes, respectively. The Spearman correlation coefficient (*r*) is represented. The signature significantly correlated with tumor shrinkage in axitinib-treated patients (green). No correlation was observed in placebo-treated patients (orange). **C.** Multivariable analysis was performed to identify potential baseline prognostic factors for PFS in placebo-treated patients. The *HR*, *95%CI* and *p-value* of the Cox model for the signature and for other clinically relevant variables are shown. Grade was an independent prognostic factor in the placebo arm. Moreover, the number of prior lines of treatment was also almost significantly associated with PFS in the model. *Ns, non-significant.* A $p < 0.05$ was considered statistically significant.

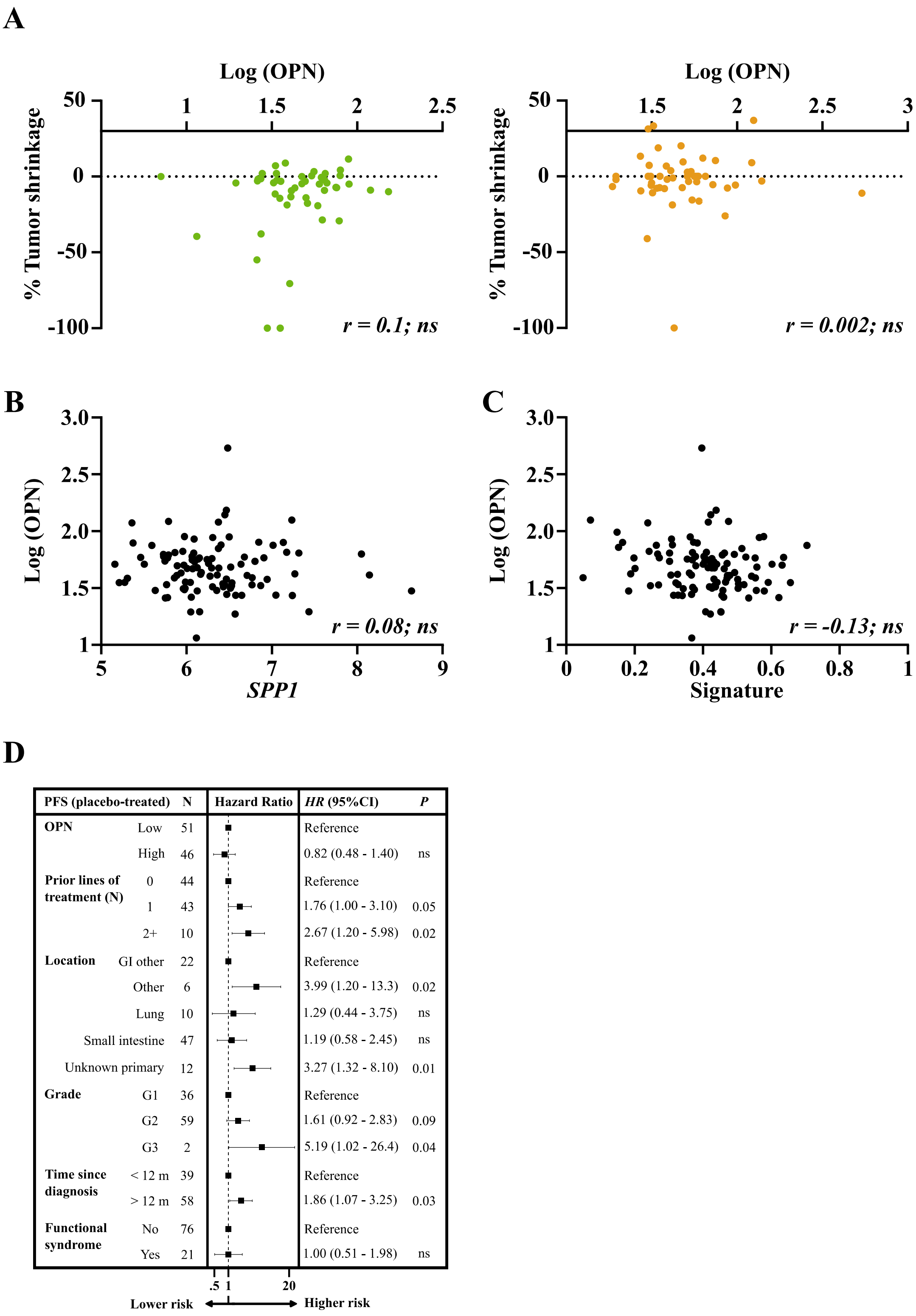

Supplementary Figure 6. Plasma OPN levels are not associated with tumor shrinkage and *SPP1* expression. A. Spearman correlation analysis was performed to study the association between plasma OPN levels with tumor shrinkage. The analysis was performed separately in axitinib- (green) and placebo-treated patients (orange). The Spearman correlation coefficient (*r*) is represented. Tumor shrinkage percentage and the log OPN plasma concentration are shown on the y- and x-axes, respectively. OPN plasma levels did not correlate with tumor shrinkage in either axitinib- or placebo-treated patients. **B.** Similarly, Spearman correlation analysis was performed to study the association between plasma OPN levels, and *SPP1* expression or the signature score. *SPP1* expression levels and log OPN plasma concentration are plot on the x- and y-axes, respectively. No correlation was observed between OPN plasma levels and *SPP1* tumoral gene expression. **C.** Moreover, OPN plasma levels did not correlate with the signature score. In this case, the signature score is shown on the x-axis, while the log OPN plasma concentrations on the y-axis. **D.** Multivariable analysis was performed to identify potential baseline prognostic factors for PFS in placebo-treated patients. The *HR*, *95%CI* and *p-value* of the Cox model for the signature and for other clinically relevant variables are shown. OPN plasma levels were not associated with PFS. However, the number of prior lines of treatment, the primary tumor location, grade and time since diagnosis were independent prognostic factors in the placebo arm. *Ns, non-significant*. A $p < 0.05$ was considered statistically significant.

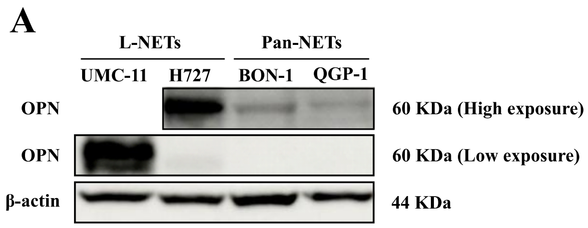

Supplementary Figure 7. Characterization of OPN expression in NET cell lines. A. Western blot was performed to evaluate OPN expression levels in NET cell lines. OPN membrane was revealed using 2 different exposure times to detect OPN in cell lines with lower expression. Representative WB are shown for each one of the proteins. β-actin was used as a loading control. Molecular weights are expressed in kilodaltons (KDa). OPN was expressed at high levels in UMC-11 cells. High exposure led to OPN detection in H727, BON-1 and QGP-1 cells.

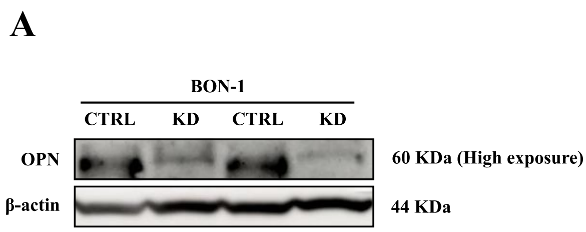

Supplementary Figure 8. Validation of OPN depletion in BON-1 cell line. A. Western blot was performed to confirm OPN depletion in BON-1 NET cell line. OPN membrane was revealed using higher exposure time to detect OPN in cell lines with lower expression. Representative WB are shown for each one of the proteins. β-actin was used as a loading control. Molecular weights are expressed in kilodaltons (KDa). CTRL, control. KD, knockdown.

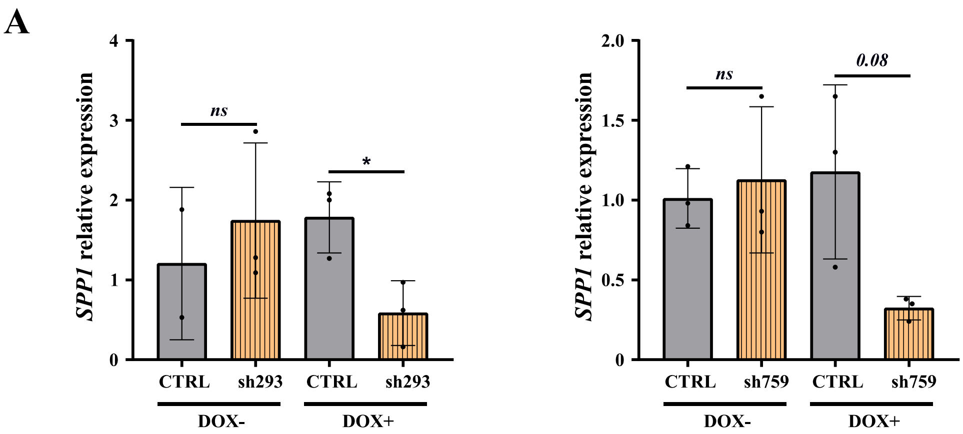

Supplementary Figure 9. Validation of conditional OPN downregulation in BON-1 cells. A. qRT-PCR was performed to confirm *SPP1* downregulation in BON-1 NET cell lines. The $2^{-\Delta\Delta Ct}$ is represented on the y-axis. Conditional downregulation was induced with doxycycline treatment. Data are expressed as the mean ± SD of 3 independent experiments. CTRL, control. KD, knockdown. DOX, doxycycline. *Ns, non-significant.* * *p < 0.05* was considered statistically significant.

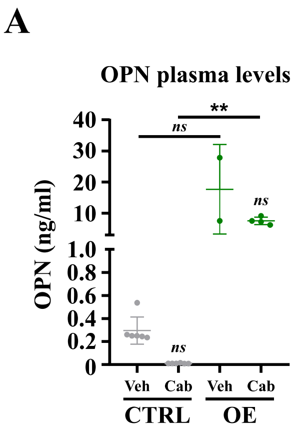

Supplementary Figure 10. OPN is upregulated in the plasma of BON-1 OPN OE CDXs. A. Secreted OPN levels were measured using ELISA in the plasma of BON-1 CTRL and OPN OE CDXs treated with vehicle and cabozantinib. OPN concentration is represented on the y-axis. BON-1 OPN OE CDXs showed significantly higher OPN expression compared to BON-1 CTRL CDXs. Data are expressed as the mean ± SD of 2-6 mice. *Ns, non-significant.* ** *p < 0.01* was considered statistically significant.

A

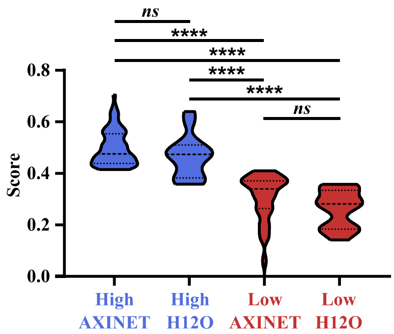

Supplementary Figure 11. Signature score is comparable in the AXINET and H12O validation cohorts. A. Violin plots of the signature score were represented in patients with high and low signature scores from the AXINET and H12O cohorts. Signature score is plotted on the y-axis. No statistically significant differences were observed between patients from the AXINET and H12O cohorts with either high or low signature scores. Moreover, high- and low-signature score patients from the H12O cohort had significantly different scores from low- and high-signature score patients from the AXINET cohort, respectively. *Ns, non-significant. **** $p < 0.0001$* was considered statistically significant.

Gene symbol	*Hazard ratio*	*Standard error*	*z*	*P-value*	*FDR*
SLC30A9	3.562	0.390	3.260	0.001	1.000
KCNA4	2.283	0.274	3.016	0.003	1.000
PIGG	4.596	0.549	2.779	0.006	1.000
RAP1GAP	0.457	0.250	-3.126	0.002	1.000
OLFML3	0.316	0.441	-2.612	0.009	1.000
TBRG1	0.385	0.352	-2.718	0.007	1.000
POTEE	2.246	0.276	2.927	0.003	1.000
PLEK	0.204	0.533	-2.979	0.003	1.000
B3GALT6	0.168	0.578	-3.090	0.002	1.000
ANKZF1	0.249	0.528	-2.637	0.008	1.000
CUBN	2.141	0.272	2.798	0.005	1.000
RPS10-NUDT3	0.320	0.357	-3.189	0.001	1.000
C18orf25	4.997	0.495	3.251	0.001	1.000
MX2	0.317	0.374	-3.068	0.002	1.000
KLHDC3	0.281	0.465	-2.732	0.006	1.000
ATXN7	0.208	0.545	-2.881	0.004	1.000
SPP1	2.459	0.283	3.178	0.002	1.000
REXO1L2P	2.565	0.323	2.917	0.004	1.000
ADH6	2.131	0.285	2.657	0.008	1.000
CLDN14	3.078	0.415	2.707	0.007	1.000
INTS3	0.276	0.500	-2.575	0.010	1.000
MVB12B	0.344	0.416	-2.570	0.010	1.000
RALBP1	2.971	0.425	2.562	0.010	1.000
PTPN3	0.328	0.437	-2.552	0.011	1.000
ALCAM	1.615	0.188	2.549	0.011	1.000
HBA2	0.711	0.134	-2.544	0.011	1.000
CCDC68	2.627	0.380	2.539	0.011	1.000
DDHD1	4.547	0.598	2.531	0.011	1.000
TBC1D19	2.493	0.364	2.509	0.012	1.000
CT45A3	1.713	0.215	2.503	0.012	1.000
PRKG2	0.347	0.426	-2.484	0.013	1.000
HECTD4	0.395	0.376	-2.471	0.014	1.000
COPZ1	0.417	0.356	-2.454	0.014	1.000
PCSK1	0.645	0.179	-2.448	0.014	1.000
ATP8A2	0.355	0.424	-2.448	0.014	1.000
TMEM261	2.929	0.443	2.424	0.015	1.000
UBE2B	2.748	0.418	2.421	0.016	1.000
CDK9	0.351	0.433	-2.416	0.016	1.000
KIRREL	3.373	0.508	2.393	0.017	1.000
REPS2	0.426	0.359	-2.376	0.018	1.000
FBXW11	2.262	0.344	2.376	0.018	1.000
ZNF266	0.334	0.462	-2.374	0.018	1.000
FGFR2	2.464	0.380	2.372	0.018	1.000
CNTN3	0.575	0.234	-2.367	0.018	1.000
KCNH7	0.475	0.317	-2.350	0.019	1.000
LSAMP	0.279	0.544	-2.348	0.019	1.000

MCU	0.390	0.401	-2.347	0.019	1.000
TMEM65	0.344	0.455	-2.346	0.019	1.000
NYAP2	0.318	0.489	-2.345	0.019	1.000
GBA	0.446	0.344	-2.343	0.019	1.000
MBD4	0.334	0.469	-2.340	0.019	1.000
SORBS3	0.433	0.359	-2.332	0.020	1.000
CBX3	1.756	0.243	2.319	0.020	1.000
CLTC	0.261	0.580	-2.317	0.021	1.000
SARAF	2.209	0.343	2.313	0.021	1.000
CABYR	2.044	0.310	2.308	0.021	1.000
ZNF763	0.348	0.458	-2.305	0.021	1.000
TNFAIP1	3.508	0.546	2.301	0.021	1.000
HIST1H2AK	3.077	0.489	2.297	0.022	1.000
MPC2	0.417	0.382	-2.291	0.022	1.000
GXYLT2	2.193	0.344	2.285	0.022	1.000
HECW2	0.344	0.470	-2.274	0.023	1.000
DNAJC9	0.246	0.616	-2.274	0.023	1.000
DHRS11	2.985	0.482	2.267	0.023	1.000
TNKS2	2.740	0.446	2.261	0.024	1.000
GRIN1	2.995	0.486	2.258	0.024	1.000
DHRS12	0.339	0.481	-2.252	0.024	1.000
FAM91A1	2.007	0.309	2.251	0.024	1.000
KCNJ6	0.599	0.228	-2.251	0.024	1.000
ZBTB44	0.327	0.498	-2.248	0.025	1.000
PLPPR1	0.490	0.318	-2.246	0.025	1.000
SDAD1	3.783	0.594	2.240	0.025	1.000
CPSF2	3.047	0.499	2.232	0.026	1.000
ITM2C	0.509	0.303	-2.229	0.026	1.000
C16orf62	2.497	0.412	2.220	0.026	1.000
PREPL	0.368	0.456	-2.189	0.029	1.000
SPIN1	0.266	0.607	-2.182	0.029	1.000
FN1	1.715	0.248	2.175	0.030	1.000
SGK1	1.372	0.146	2.168	0.030	1.000
ATAD2	2.623	0.446	2.161	0.031	1.000
GDF10	0.337	0.504	-2.159	0.031	1.000
SENP1	0.291	0.572	-2.158	0.031	1.000
TBC1D8B	0.467	0.353	-2.153	0.031	1.000
CCDC42	0.320	0.530	-2.151	0.032	1.000
RGS4	0.642	0.206	-2.150	0.032	1.000
TPT1	1.673	0.239	2.149	0.032	1.000
UBE2T	2.121	0.350	2.148	0.032	1.000
CAMLG	1.322	0.130	2.139	0.032	1.000
SCML1	0.338	0.508	-2.138	0.033	1.000
TMOD1	0.369	0.467	-2.136	0.033	1.000
HIST1H4D	2.225	0.376	2.129	0.033	1.000
SOX6	0.567	0.267	-2.128	0.033	1.000
MON2	0.448	0.380	-2.112	0.035	1.000

PAG1	1.658	0.240	2.111	0.035	1.000
SERP2	0.501	0.328	-2.110	0.035	1.000
C6orf183	0.305	0.565	-2.104	0.035	1.000
ZNF717	0.375	0.468	-2.098	0.036	1.000
DIP2B	0.363	0.484	-2.096	0.036	1.000
SLC7A5	2.160	0.367	2.096	0.036	1.000
G3BP1	2.071	0.348	2.096	0.036	1.000
YPEL2	0.502	0.330	-2.091	0.037	1.000
CRKL	0.281	0.607	-2.091	0.037	1.000
REXO1L10P	0.353	0.499	-2.088	0.037	1.000
POLR2B	0.484	0.348	-2.085	0.037	1.000
CKS2	2.366	0.413	2.084	0.037	1.000
TMEM126A	2.729	0.482	2.084	0.037	1.000
CEP70	1.530	0.205	2.081	0.037	1.000
ZNF711	0.378	0.468	-2.077	0.038	1.000
SCN2A	0.526	0.309	-2.077	0.038	1.000
ZNF433	0.334	0.529	-2.076	0.038	1.000
VSIG4	2.047	0.346	2.072	0.038	1.000
GPR158	0.468	0.370	-2.055	0.040	1.000
HERPUD1	0.454	0.386	-2.048	0.041	1.000
RHPN2	0.397	0.451	-2.047	0.041	1.000
SCAI	2.063	0.354	2.045	0.041	1.000
POLR3E	0.429	0.414	-2.042	0.041	1.000
TRMT11	2.577	0.464	2.040	0.041	1.000
UNC5C	1.950	0.328	2.039	0.042	1.000
C11orf73	0.586	0.262	-2.038	0.042	1.000
TMEM62	0.436	0.408	-2.036	0.042	1.000
VRK1	0.615	0.240	-2.032	0.042	1.000
ARL14EP	1.811	0.293	2.030	0.042	1.000
SCRG1	1.831	0.298	2.030	0.042	1.000
RBPJ	1.996	0.341	2.025	0.043	1.000
NAV1	0.432	0.415	-2.024	0.043	1.000
ST6GAL2	2.479	0.449	2.022	0.043	1.000
TMEM163	0.376	0.484	-2.020	0.043	1.000
C1orf116	0.577	0.273	-2.013	0.044	1.000
MAP6	0.501	0.344	-2.011	0.044	1.000
COA7	0.353	0.519	-2.007	0.045	1.000
SLC12A2	1.545	0.217	2.005	0.045	1.000
PHLDB2	0.546	0.302	-2.003	0.045	1.000
C9orf129	0.489	0.358	-2.001	0.045	1.000
ZBTB7C	0.454	0.395	-1.998	0.046	1.000
SLC2A14	1.611	0.239	1.996	0.046	1.000
RB1	2.091	0.370	1.991	0.047	1.000
TSPYL4	0.489	0.360	-1.991	0.047	1.000
ADCK2	2.339	0.428	1.986	0.047	1.000
NTNG1	0.371	0.500	-1.984	0.047	1.000
RPA3	2.116	0.378	1.982	0.048	1.000

TRIM68	0.361	0.515	-1.980	0.048	1.000
STAT1	0.481	0.370	-1.977	0.048	1.000
POTEF	2.241	0.408	1.976	0.048	1.000
FABP1	1.149	0.071	1.974	0.048	1.000
CBLL1	0.409	0.455	-1.967	0.049	1.000
NOSIP	0.361	0.518	-1.967	0.049	1.000
SMARCC1	2.575	0.481	1.967	0.049	1.000
PRRG4	1.773	0.292	1.962	0.050	1.000
CDK13	0.441	0.417	-1.962	0.050	1.000

Supplementary Table 1. Genes significantly associated with PFS in axitinib-treated patients. Cox regression analysis was performed for the 5000 genes with higher MAD in axitinib-treated patients using PFS (N = 62). A total of 149 genes were significantly associated with PFS. Of these, 20 had a $p < 0.01$. 10 were associated with increased risk of progression ($HR > 1$) and 10 with decreased risk of progression ($HR < 1$). Only genes significantly associated with PFS are shown. The *HR*, its *standard error*, the *z-statistic*, the *p-value* and *FDR* are shown for each gene. A *p-value* < 0.05 was considered statistically significant.

Gene symbol	*Hazard ratio*	*Standard error*	*z*	*P-value*	*FDR*
SEPSECS	5.097	0.434	3.755	0.001	0.662
GALNT10	0.276	0.375	-3.437	0.001	0.662
GPR119	2.926	0.313	3.435	0.001	0.662
SLC1A2	2.145	0.224	3.414	0.001	0.662
FAM69A	0.210	0.458	-3.405	0.001	0.662
DHODH	2.892	0.319	3.325	0.001	0.738
COQ2	3.894	0.420	3.237	0.001	0.863
CYB5A	1.968	0.215	3.147	0.002	0.876
AMD1	0.224	0.486	-3.077	0.002	0.876
CYP3A43	1.797	0.191	3.076	0.002	0.876
GNPNAT1	4.174	0.466	3.067	0.002	0.876
WNT11	4.460	0.490	3.053	0.002	0.876
BTAF1	4.696	0.516	2.997	0.003	0.876
DHRS12	0.284	0.424	-2.972	0.003	0.876
NEFM	1.354	0.103	2.941	0.003	0.876
CYBRD1	0.443	0.277	-2.937	0.003	0.876
FAM171B	0.173	0.600	-2.923	0.004	0.876
GALNT5	0.568	0.195	-2.897	0.004	0.876
HSD17B6	1.740	0.193	2.866	0.004	0.876
ZSWIM6	0.308	0.413	-2.858	0.004	0.876
AGMO	1.665	0.179	2.857	0.004	0.876
GYS2	1.920	0.229	2.852	0.004	0.876
PLGLB2	2.517	0.324	2.850	0.004	0.876
SBNO2	0.315	0.408	-2.833	0.005	0.876
EYS	1.773	0.202	2.828	0.005	0.876
RWDD3	3.521	0.446	2.821	0.005	0.876

TMEM27	1.674	0.184	2.805	0.005	0.876
DSTN	0.607	0.178	-2.802	0.005	0.876
RUNX1T1	0.451	0.284	-2.800	0.005	0.876
MAP2K6	3.370	0.435	2.791	0.005	0.876
MFAP4	0.440	0.296	-2.775	0.006	0.890
FGFR1	0.407	0.327	-2.747	0.006	0.919
IFNAR2	2.208	0.291	2.724	0.006	0.919
ABCA1	2.530	0.343	2.703	0.007	0.919
GPHN	2.815	0.383	2.700	0.007	0.919
PPIAP30	3.062	0.415	2.699	0.007	0.919
CYP2A6	1.389	0.122	2.690	0.007	0.919
AP2M1	0.286	0.466	-2.687	0.007	0.919
TBX15	2.071	0.272	2.680	0.007	0.919
ANXA13	1.734	0.208	2.650	0.008	0.919
KCTD5	2.234	0.304	2.648	0.008	0.919
TRIP10	0.414	0.334	-2.640	0.008	0.919
TRMT10B	3.052	0.424	2.630	0.009	0.919
ULBP2	2.073	0.278	2.622	0.009	0.919
XRCC4	3.119	0.435	2.617	0.009	0.919
JMJD1C	0.478	0.282	-2.617	0.009	0.919
PPFIA2	2.415	0.340	2.595	0.009	0.919
CTSZ	0.310	0.451	-2.595	0.009	0.919
LECT2	3.308	0.461	2.595	0.010	0.919
SMAD2	2.093	0.285	2.591	0.010	0.919
CHGA	0.696	0.141	-2.576	0.010	0.919
SAMD8	0.286	0.486	-2.575	0.010	0.919
G6PC	1.497	0.159	2.541	0.011	0.919
CREM	0.429	0.333	-2.537	0.011	0.919
CRYM	1.756	0.224	2.512	0.012	0.919
AMY1C	0.581	0.219	-2.477	0.013	0.919
MLIP	1.741	0.225	2.463	0.014	0.919
C1QTNF3-AMACR	2.713	0.405	2.462	0.014	0.919
EMP2	0.497	0.285	-2.455	0.014	0.919
TMEM55A	0.311	0.479	-2.443	0.015	0.919
SLC37A4	2.868	0.432	2.439	0.015	0.919
HPR	1.350	0.123	2.437	0.015	0.919
BUD31	0.434	0.343	-2.434	0.015	0.919
SLC2A13	0.402	0.375	-2.431	0.015	0.919
EMP3	0.457	0.323	-2.426	0.015	0.919
C1orf116	0.475	0.307	-2.425	0.015	0.919
DYM	0.378	0.402	-2.421	0.016	0.919
ECHS1	1.877	0.260	2.418	0.016	0.919
IFNA8	2.728	0.415	2.418	0.016	0.919
TCFL5	2.213	0.330	2.408	0.016	0.919
MRLN	0.335	0.456	-2.405	0.016	0.919
SRP14	0.450	0.333	-2.397	0.017	0.919

WNT2B	0.477	0.310	-2.395	0.017	0.919
GPRC5A	0.678	0.163	-2.395	0.017	0.919
FXYD7	3.697	0.547	2.392	0.017	0.919
FXYD4	2.776	0.427	2.391	0.017	0.919
C6	1.799	0.247	2.376	0.018	0.919
NKTR	0.534	0.264	-2.375	0.018	0.919
ITGB8	0.523	0.273	-2.375	0.018	0.919
P4HTM	0.370	0.419	-2.372	0.018	0.919
GABARAPL1	0.676	0.165	-2.366	0.018	0.919
GPC5	1.667	0.216	2.364	0.018	0.919
SEC11C	1.678	0.219	2.364	0.018	0.919
LPP	0.432	0.356	-2.364	0.018	0.919
METTL17	2.244	0.343	2.359	0.018	0.919
C4BPB	1.763	0.241	2.350	0.019	0.919
PPIAL4C	2.379	0.369	2.348	0.019	0.919
NGDN	0.546	0.258	-2.347	0.019	0.919
CRNKL1	0.447	0.344	-2.338	0.019	0.919
ROR1-AS1	0.399	0.394	-2.331	0.020	0.919
FAT4	0.431	0.362	-2.325	0.020	0.919
ADH4	1.564	0.193	2.321	0.020	0.919
NDUFC2-KCTD14	0.514	0.288	-2.318	0.021	0.919
SCRG1	0.685	0.163	-2.317	0.021	0.919
TMEM165	0.462	0.334	-2.311	0.021	0.919
CNTLN	2.744	0.437	2.311	0.021	0.919
ADAMTS6	0.506	0.295	-2.311	0.021	0.919
INTS4P2	1.953	0.290	2.311	0.021	0.919
CNN1	0.753	0.123	-2.304	0.021	0.919
GLI3	0.469	0.329	-2.302	0.021	0.919
PRY	1.864	0.271	2.301	0.021	0.919
DCBLD2	0.545	0.264	-2.300	0.022	0.919
RDH16	1.418	0.152	2.294	0.022	0.919
NAAA	1.978	0.297	2.293	0.022	0.919
EI24	2.927	0.470	2.287	0.022	0.919
TSPY3	2.674	0.431	2.283	0.022	0.919
SLC22A18AS	2.511	0.404	2.278	0.023	0.919
RNF2	1.946	0.294	2.264	0.024	0.919
GNMT	2.082	0.325	2.258	0.024	0.919
KIAA0895	2.654	0.434	2.251	0.024	0.919
DDX19B	2.771	0.453	2.251	0.024	0.919
H1FX	0.355	0.460	-2.250	0.024	0.919
A1CF	1.511	0.184	2.247	0.025	0.919
CD59	0.504	0.305	-2.247	0.025	0.919
HPX	1.418	0.156	2.246	0.025	0.919
ALKBH5	0.471	0.336	-2.242	0.025	0.919
PPP1CC	0.600	0.228	-2.241	0.025	0.919
DEFB130	0.365	0.451	-2.235	0.025	0.919

PCDHGC3	0.357	0.461	-2.232	0.026	0.919
PIK3C2B	0.330	0.497	-2.230	0.026	0.919
ATP6V0A2	0.433	0.376	-2.228	0.026	0.919
BCL2L11	1.626	0.218	2.227	0.026	0.919
RNF43	3.388	0.548	2.227	0.026	0.919
STEAP4	0.672	0.179	-2.226	0.026	0.919
TSPAN15	0.444	0.365	-2.224	0.026	0.919
PHLDA2	0.306	0.532	-2.224	0.026	0.919
CELF2	0.365	0.455	-2.218	0.027	0.919
SORBS2	2.508	0.415	2.217	0.027	0.919
CNTNAP5	0.520	0.295	-2.217	0.027	0.919
ZNF518A	2.103	0.336	2.210	0.027	0.919
WBSCR28	2.138	0.344	2.208	0.027	0.919
SOCS6	2.569	0.428	2.206	0.027	0.919
DES	0.591	0.239	-2.205	0.028	0.919
SERPINC1	1.520	0.190	2.201	0.028	0.919
ITIH2	1.335	0.132	2.200	0.028	0.919
ADAMTS1	0.736	0.140	-2.197	0.028	0.919
ZFP62	2.130	0.344	2.196	0.028	0.919
CDK10	2.523	0.422	2.194	0.028	0.919
HEXDC	2.595	0.436	2.189	0.029	0.919
DPT	0.653	0.195	-2.185	0.029	0.919
TNIK	0.604	0.231	-2.183	0.029	0.919
PLEKHA2	0.421	0.397	-2.182	0.029	0.919
ORM1	1.236	0.097	2.179	0.029	0.919
PSMG3-AS1	2.548	0.430	2.176	0.030	0.919
TAT	1.352	0.139	2.176	0.030	0.919
H3F3B	0.506	0.314	-2.172	0.030	0.919
PPAT	2.644	0.448	2.172	0.030	0.919
SLC25A36	0.444	0.374	-2.170	0.030	0.919
PPP1R18	0.502	0.318	-2.169	0.030	0.919
PGLS	0.458	0.361	-2.169	0.030	0.919
CDC42EP3	0.540	0.285	-2.168	0.030	0.919
RNF19A	0.358	0.474	-2.168	0.030	0.919
TCEAL1	0.427	0.394	-2.162	0.031	0.919
FERMT2	0.338	0.503	-2.157	0.031	0.919
TMEM243	0.544	0.283	-2.155	0.031	0.919
MAF	0.498	0.324	-2.155	0.031	0.919
ENOPH1	2.495	0.425	2.151	0.032	0.919
ARHGAP6	0.477	0.345	-2.146	0.032	0.919
OXSR1	0.396	0.432	-2.143	0.032	0.919
SOCS5	0.398	0.430	-2.141	0.032	0.919
SMAP2	2.091	0.345	2.137	0.033	0.919
FLJ33360	2.528	0.434	2.137	0.033	0.919
HNRNPR	2.172	0.363	2.136	0.033	0.919
C11orf54	1.742	0.261	2.128	0.033	0.919
FN3KRP	2.401	0.412	2.126	0.034	0.919

MMP2	0.533	0.296	-2.124	0.034	0.919
CYP2C9	1.580	0.215	2.124	0.034	0.919
DDX39B	2.481	0.429	2.121	0.034	0.919
NBPF26	2.966	0.513	2.118	0.034	0.919
TPM2	0.609	0.234	-2.115	0.034	0.919
TPH1	0.871	0.065	-2.114	0.035	0.919
SULT2A1	1.389	0.155	2.114	0.035	0.919
TSPAN12	2.682	0.468	2.110	0.035	0.919
ZMAT1	1.778	0.273	2.110	0.035	0.919
ACSS3	2.213	0.377	2.107	0.035	0.919
ITPR3	0.418	0.414	-2.106	0.035	0.919
SHISA5	0.433	0.398	-2.102	0.036	0.919
C1orf145	0.350	0.500	-2.100	0.036	0.919
MBNL1	0.576	0.263	-2.097	0.036	0.919
GOLGA8A	1.530	0.203	2.095	0.036	0.919
ZNF337	0.344	0.509	-2.095	0.036	0.919
SLC7A11	1.983	0.327	2.094	0.036	0.919
MPC1	3.088	0.539	2.091	0.037	0.919
SNAP29	2.082	0.351	2.089	0.037	0.919
TCEAL2	0.653	0.204	-2.088	0.037	0.919
FBXO32	0.599	0.245	-2.088	0.037	0.919
PICALM	0.615	0.233	-2.085	0.037	0.919
SLIT3	0.576	0.265	-2.084	0.037	0.919
VIM	2.616	0.462	2.081	0.037	0.919
LPAL2	1.692	0.253	2.081	0.037	0.919
PPP1R12B	0.698	0.173	-2.079	0.038	0.919
MYB	1.727	0.263	2.078	0.038	0.919
NAPA	0.453	0.381	-2.077	0.038	0.919
IL7R	0.790	0.114	-2.076	0.038	0.919
UBL3	0.415	0.423	-2.076	0.038	0.919
TGFBR2	0.565	0.275	-2.075	0.038	0.919
CBFA2T2	2.502	0.442	2.073	0.038	0.919
NSRP1	0.553	0.286	-2.073	0.038	0.919
GLDC	2.527	0.448	2.069	0.039	0.919
NQO1	0.384	0.464	-2.067	0.039	0.919
RAD23B	2.106	0.360	2.067	0.039	0.919
MEST	2.000	0.335	2.066	0.039	0.919
SH3GLB2	2.284	0.400	2.066	0.039	0.919
ECM1	0.452	0.384	-2.066	0.039	0.919
APOF	1.893	0.309	2.065	0.039	0.919
HOXC9	0.671	0.193	-2.065	0.039	0.919
RSPH3	2.205	0.383	2.063	0.039	0.919
NBEAL1	2.216	0.386	2.061	0.039	0.919
GP1BB	2.639	0.471	2.060	0.039	0.919
TRIM8	2.920	0.520	2.060	0.039	0.919
FGA	1.219	0.096	2.059	0.040	0.919
DST	0.604	0.246	-2.051	0.040	0.919

MSLN	0.430	0.411	-2.050	0.040	0.919
BAIAP2L1	1.657	0.247	2.047	0.041	0.919
ZDHHC20	0.495	0.344	-2.044	0.041	0.919
GLYAT	1.377	0.157	2.043	0.041	0.919
FAXC	0.485	0.355	-2.040	0.041	0.919
RBMS2	0.482	0.358	-2.039	0.041	0.919
CAP2	0.519	0.322	-2.039	0.042	0.919
CAV1	0.586	0.262	-2.038	0.042	0.919
CYP2A7	1.328	0.139	2.037	0.042	0.919
CDC42	0.475	0.366	-2.034	0.042	0.919
AQP1	0.551	0.294	-2.031	0.042	0.919
HEATR1	1.998	0.341	2.029	0.042	0.919
ATP2B4	0.664	0.202	-2.029	0.043	0.919
MYH11	0.705	0.173	-2.025	0.043	0.919
ENPP5	0.439	0.406	-2.024	0.043	0.919
JAM2	0.757	0.138	-2.024	0.043	0.919
PALLD	0.687	0.185	-2.023	0.043	0.919
IQCF3	2.209	0.392	2.021	0.043	0.919
RORA	0.494	0.349	-2.018	0.044	0.919
PCDH7	0.665	0.202	-2.016	0.044	0.919
CXXC4	1.473	0.192	2.014	0.044	0.919
CCDC169-SOHLH2	0.511	0.335	-2.009	0.045	0.919
SAMHD1	0.612	0.245	-2.007	0.045	0.919
CNTN3	0.677	0.195	-2.003	0.045	0.919
GOLGA6L10	2.071	0.364	2.000	0.046	0.919
ACSM5	2.104	0.372	1.999	0.046	0.919
ITIH3	1.401	0.169	1.997	0.046	0.919
AADAT	1.535	0.215	1.993	0.046	0.919
RGS1	0.684	0.191	-1.992	0.046	0.919
DHFR	3.158	0.578	1.990	0.047	0.919
PARVA	0.556	0.295	-1.990	0.047	0.919
PPP2R3B	0.313	0.584	-1.989	0.047	0.919
DUSP6	0.518	0.332	-1.982	0.048	0.919
PDE8B	1.641	0.250	1.982	0.048	0.919
TEAD1	0.477	0.373	-1.981	0.048	0.919
BEX2	0.411	0.449	-1.979	0.048	0.919
POU6F2	1.352	0.153	1.979	0.048	0.919
UBE2T	1.752	0.284	1.978	0.048	0.919
SECTM1	0.526	0.325	-1.978	0.048	0.919
TXNL4A	1.884	0.321	1.976	0.048	0.919
SRSF2	0.429	0.430	-1.971	0.049	0.919
ZBTB4	0.469	0.386	-1.965	0.049	0.919
ITGA3	0.543	0.311	-1.965	0.050	0.919
GIPC2	0.767	0.135	-1.963	0.050	0.919
HAO2	1.513	0.211	1.963	0.050	0.919
SLC38A4	1.483	0.201	1.963	0.050	0.919

NPTN	0.466	0.389	-1.963	0.050	0.919
MOB3B	0.532	0.322	-1.963	0.050	0.919
GNA14	0.530	0.324	-1.962	0.050	0.919

Supplementary Table 2. Genes significantly associated with PFS in placebo-treated patients. Cox regression analysis was performed for the 5000 genes with higher MAD in placebo-treated patients using PFS (N = 64). A total of 261 genes were significantly associated with PFS. Only genes significantly associated with PFS are shown. The *HR*, its *standard error*, the *z-statistic*, the *p-value* and *FDR* are shown for each gene. A *p-value < 0.05* was considered statistically significant.

Gene symbol	*Hazard ratio*	*95%CI*	*Standard error*	*z*	*P-value*
PLEK	0.13	2.35 - 26.98	0.622	-3.336	0.001
B3GALT6	0.12	2.02 - 36.67	0.738	-2.918	0.004
CUBN	2.68	0.18 - 0.73	0.346	2.852	0.004
REXO1L2P	3.68	0.10 - 0.69	0.482	2.703	0.007
RPS10-NUDT3	0.34	1.29 - 6.56	0.414	-2.580	0.010
SLC30A9	3.21	0.11 - 0.83	0.503	2.321	0.020
ATXN7	0.23	1.22 - 15.94	0.654	-2.274	0.023
PIGG	4.93	0.05 - 0.81	0.711	2.245	0.025
ANKZF1	0.26	1.13 - 13.24	0.626	-2.167	0.030
SPP1	1.83	0.29 - 1.00	0.312	1.942	0.052
MX2	0.38	0.91 - 7.74	0.546	-1.791	0.073

Supplementary Table 3. Genes with significant interaction with treatment arm. Interaction tests were performed for the 20 candidates to assess the potential interaction between PFS and treatment arm (N = 126). The interaction *HR* and 95%*CI* are shown, as well as the *standard error*, *z-statistic* and *p-value*. 9 genes had a significantly different association with PFS in both arms of the trial. *SPP*1 and *MX2* were retained as potential biomarkers as they showed an almost significant interaction. Only genes with significant interaction are shown. A *p-value < 0.05* was considered statistically significant.

PFS		*HR (95%CI)*		Multivariable (*P-value*)	
		Axitinib (N = 62)	Placebo (N = 64)	Axitinib (N = 62)	Placebo (N = 64)
Signature		$4.02 \cdot 10^{-4}$ ($6.67 \cdot 10^{-6}$ – 0.024)	0.81 (0.07 – 9.212)	*$1.83 \cdot 10^{-4}$*	0.867
Prior lines of treatment (N)	0 (Ref.)	*Ref.*	*Ref.*	*Ref.*	*Ref.*
	1	2.61 (0.80 – 8.52)	1.94 (0.96 – 3.93)	*0.109*	*0.064*
	2+	16.21 (3.66 – 71.87)	0.52 (0.19 – 1.45)	*0.00025*	*0.210*
Location	GI other (Ref.)	*Ref.*	*Ref.*	*Ref.*	*Ref.*
	Other	0.69 (0.05 – 9.91)	3.03 (0.29 – 31.36)	*0.785*	*0.352*
	Lung	0.77 (0.25 – 2.40)	0.58 (0.21 – 1.57)	*0.662*	*0.281*
	Small intestine	1.18(0.39 – 3.58)	0.85 (0.36 – 1.99)	*0.766*	*0.707*
	Unknown	2.66 (0.43 – 16.68)	0.58 (0.14 – 2.42)	*0.295*	*0.457*
Grade	G1 (Ref.)	*Ref.*	*Ref.*	*Ref.*	*Ref.*
	G2	4.13 (1.35 – 12.70)	2.28 (0.99 – 5.26)	*0.013*	*0.052*
	G3	4.38 (0.72 – 27.09)	NA	*0.111*	NA
Time since diagnosis	High	2.42 (0.94 – 6.23)	1.62 (0.78 – 3.38)	*0.066*	*0.199*
Carcinoid syndrome	Yes	0.80 (0.38 – 1.67)	0.94 (0.38 – 2.36)	*0.557*	*0.902*

Supplementary Table 4. Multivariable analysis of the signature in axitinib- and placebo-treated patients. Cox multivariable proportional hazards models using PFS and the signature as a numeric score, along with other possible confounding variables in axitinib- (N = 62) and placebo-treated (N = 64) patients are shown. *HR* and *p-values* are shown. The signature is independently associated with PFS in axitinib-treated patients, but not in placebo-treated patients. Grade and the number of prior lines of treatment were independent predictors of PFS in both arms of the trial. A *p-value* < 0.05 was considered statistically significant. *95%CI, 95% confidence interval. Ref, reference*.

Gene symbol	*Log (FC)*	*t*	*P-value*	*FDR*
ATXN7	0.418	7.053	$9.51 \cdot 10^{-11}$	0.001
REXO1L2P	-0.422	-5.506	$1.91 \cdot 10^{-7}$	0.002
SPP1	-0.578	-5.169	$8.74 \cdot 10^{-7}$	0.006
EBLN2	0.187	4.173	$5.49 \cdot 10^{-5}$	0.268
ATXN2	0.196	4.025	$9.65 \cdot 10^{-5}$	0.376
ANKRD36B	0.422	3.951	$1.27 \cdot 10^{-4}$	0.381
MYL12B	-0.302	-3.932	$1.37 \cdot 10^{-4}$	0.381
TRMT10A	-0.151	-3.814	$2.11 \cdot 10^{-4}$	0.514
POLR3B	0.152	3.749	$2.67 \cdot 10^{-4}$	0.548
SKA1	-0.132	-3.704	$3.14 \cdot 10^{-4}$	0.548
PDE4C	-0.167	-3.690	$3.30 \cdot 10^{-4}$	0.548
LMAN2	-0.283	-3.683	$3.38 \cdot 10^{-4}$	0.548
LDHA	-0.673	-3.657	$3.71 \cdot 10^{-4}$	0.550
GALNT1	-0.278	-3.633	$4.03 \cdot 10^{-4}$	0.550
TGFBI	-0.335	-3.597	$4.57 \cdot 10^{-4}$	0.550
ANGPTL2	-0.336	-3.574	$4.96 \cdot 10^{-4}$	0.550
CERCAM	-0.180	-3.568	0.001	0.550
ASPRV1	0.227	3.537	0.001	0.550
PPP4R2	0.247	3.533	0.001	0.550
DALRD3	0.200	3.527	0.001	0.550
CBX3	-0.359	-3.512	0.001	0.550
LOC101927844	0.160	3.480	0.001	0.550
PPIE	0.171	3.472	0.001	0.550
MRC2	-0.164	-3.469	0.001	0.550
PATE2	0.150	3.459	0.001	0.550
CCPG1	-0.183	-3.455	0.001	0.550
PLEKHF2	0.236	3.449	0.001	0.550
FOXD4L5	0.211	3.407	0.001	0.601
HIST1H2BE	-0.164	-3.397	0.001	0.601
FZD7	-0.218	-3.381	0.001	0.601
ALDH1A1	0.151	3.375	0.001	0.601
IL17RD	-0.174	-3.372	0.001	0.601
PRR5-ARHGAP8	-0.147	-3.362	0.001	0.602
CTC1	0.150	3.350	0.001	0.608
ABLIM3	0.241	3.337	0.001	0.615
KIAA0895L	0.152	3.317	0.001	0.624
ASPN	-0.378	-3.317	0.001	0.624
FBN1	-0.352	-3.305	0.001	0.631
CAMKK2	-0.185	-3.295	0.001	0.634
CD99L2	-0.156	-3.286	0.001	0.638
DAZ3	0.153	3.269	0.001	0.639
FZR1	0.145	3.267	0.001	0.639
RAB4A	-0.219	-3.259	0.001	0.639
TPM1	-0.481	-3.250	0.001	0.639
SIMC1	-0.172	-3.249	0.001	0.639
ARHGDIA	-0.166	-3.234	0.002	0.642

LHX9	0.127	3.227	0.002	0.642
PDXK	-0.291	-3.208	0.002	0.642
LPCAT3	0.323	3.182	0.002	0.642
DDOST	-0.204	-3.176	0.002	0.642
THUMPD3-AS1	0.166	3.173	0.002	0.642
MAGEA1	0.167	3.169	0.002	0.642
DYTN	0.115	3.164	0.002	0.642
MXRA5	-0.207	-3.156	0.002	0.642
SERINC3	0.185	3.151	0.002	0.642
FLYWCH1	0.164	3.147	0.002	0.642
SCML1	0.219	3.146	0.002	0.642
GZF1	-0.188	-3.142	0.002	0.642
C5orf60	0.140	3.136	0.002	0.642
TCEA1	-0.275	-3.126	0.002	0.642
LINC01547	0.125	3.126	0.002	0.642
ABHD12	-0.124	-3.124	0.002	0.642
MZT1	-0.148	-3.120	0.002	0.642
KIAA1210	0.112	3.108	0.002	0.642
TVP23B	-0.263	-3.105	0.002	0.642
MADD	0.176	3.105	0.002	0.642
ILF2	0.214	3.095	0.002	0.642
DSE	-0.169	-3.094	0.002	0.642
NIPAL1	0.097	3.092	0.002	0.642
GIGYF1	-0.129	-3.090	0.002	0.642
PLPPR1	0.328	3.083	0.003	0.642
MRPL21	0.149	3.083	0.003	0.642
MRPS36	-0.271	-3.077	0.003	0.642
PCF11	0.283	3.071	0.003	0.642
IGFBP3	-0.420	-3.068	0.003	0.642
F2R	-0.115	-3.066	0.003	0.642
FAM156B	-0.156	-3.061	0.003	0.642
CYP2S1	-0.169	-3.056	0.003	0.642
AKT3	-0.191	-3.054	0.003	0.642
CCDC43	-0.143	-3.052	0.003	0.642
PTGES3L-AARSD1	-0.152	-3.048	0.003	0.642
RGPD2	0.268	3.041	0.003	0.642
MPP6	-0.170	-3.034	0.003	0.642
GABARAPL1	-0.518	-3.031	0.003	0.642
ABCA5	0.229	3.029	0.003	0.642
AIM1	0.169	3.027	0.003	0.642
CLLU1OS	0.127	3.026	0.003	0.642
ASIC2	0.140	3.021	0.003	0.642
NPIPA8	0.289	3.018	0.003	0.642
KDSR	-0.183	-3.015	0.003	0.642
RP11-281A20.2	0.160	3.012	0.003	0.642
TWSG1	-0.104	-3.009	0.003	0.642
MMP1	0.142	3.006	0.003	0.642

BCOR	0.151	3.000	0.003	0.642
LGALS1	-0.359	-3.000	0.003	0.642
MYL9	-0.475	-2.999	0.003	0.642
ANKRD17	0.161	2.996	0.003	0.642
PDIA3	-0.188	-2.989	0.003	0.642
CHN2	-0.195	-2.986	0.003	0.642
SNRPF	-0.184	-2.982	0.003	0.642
OR6C1	0.092	2.980	0.003	0.642
LZTFL1	-0.261	-2.979	0.003	0.642
GNAO1	0.271	2.972	0.004	0.642
SETD5	0.159	2.971	0.004	0.642
CLIP2	0.162	2.971	0.004	0.642
NRTN	-0.128	-2.966	0.004	0.642
FAM117B	0.244	2.964	0.004	0.642
FAM153B	-0.110	-2.964	0.004	0.642
RPL36AL	-0.236	-2.963	0.004	0.642
MRPL51	-0.224	-2.962	0.004	0.642
DBH	0.150	2.960	0.004	0.642
ADGRA2	-0.152	-2.954	0.004	0.642
TAS2R7	0.137	2.952	0.004	0.642
LINC01270	0.112	2.952	0.004	0.642
FOXL2NB	-0.109	-2.949	0.004	0.643
LONP2	0.156	2.945	0.004	0.643
PROSER2	0.120	2.937	0.004	0.649
OR1S2	0.168	2.937	0.004	0.649
RNASE1	-0.370	-2.934	0.004	0.649
CD248	-0.147	-2.927	0.004	0.651
CLDN14	-0.195	-2.922	0.004	0.651
ZBTB9	0.147	2.921	0.004	0.651
GRAMD4	-0.204	-2.918	0.004	0.651
NDUFS4	-0.137	-2.916	0.004	0.651
ZNF396	-0.106	-2.916	0.004	0.651
HIST1H2AG	-0.219	-2.909	0.004	0.651
INSRR	0.135	2.907	0.004	0.651
ART4	0.142	2.894	0.004	0.651
MTUS1	-0.451	-2.894	0.004	0.651
GBP4	0.126	2.887	0.005	0.651
CDK5RAP3	-0.175	-2.881	0.005	0.651
GSTA1	-0.580	-2.881	0.005	0.651
NID1	-0.271	-2.879	0.005	0.651
TMEM179	-0.144	-2.877	0.005	0.651
SPECC1L	0.155	2.877	0.005	0.651
TIMP3	-0.172	-2.874	0.005	0.651
MAVS	0.111	2.874	0.005	0.651
HS3ST3B1	0.176	2.868	0.005	0.651
TULP3	-0.172	-2.867	0.005	0.651
CBY1	-0.148	-2.867	0.005	0.651

UGCG	-0.198	-2.865	0.005	0.651
MAGT1	-0.182	-2.863	0.005	0.651
MPHOSPH9	0.167	2.861	0.005	0.651
FOSL2	-0.154	-2.856	0.005	0.651
ANTXR1	-0.391	-2.854	0.005	0.651
FAM98A	-0.163	-2.852	0.005	0.651
SURF1	0.110	2.852	0.005	0.651
SP2	0.129	2.849	0.005	0.651
OR10G2	0.122	2.845	0.005	0.651
APAF1	0.247	2.840	0.005	0.651
MGAM2	-0.229	-2.839	0.005	0.651
SPATA2	0.127	2.838	0.005	0.651
DDN	0.113	2.838	0.005	0.651
ZNF646	0.136	2.838	0.005	0.651
SSR2	-0.220	-2.830	0.005	0.651
HSBP1L1	0.175	2.826	0.005	0.651
RPS6KA2	-0.243	-2.824	0.006	0.651
PROB1	-0.099	-2.819	0.006	0.651
ZC3H18	0.107	2.819	0.006	0.651
COX5A	-0.288	-2.818	0.006	0.651
MLXIP	0.103	2.817	0.006	0.651
EEF1A2	-0.232	-2.811	0.006	0.651
CREB5	0.131	2.805	0.006	0.651
OFD1	0.365	2.802	0.006	0.651
ATP6V1G2	0.165	2.802	0.006	0.651
EPPIN-WFDC6	0.158	2.802	0.006	0.651
ATP5G2	-0.158	-2.801	0.006	0.651
DSTN	-0.413	-2.800	0.006	0.651
OR4S1	-0.104	-2.797	0.006	0.651
NPC2	-0.283	-2.796	0.006	0.651
TTI1	0.182	2.794	0.006	0.651
COL6A1	-0.283	-2.794	0.006	0.651
GATAD2B	0.157	2.794	0.006	0.651
JAM2	-0.430	-2.790	0.006	0.651
FOXQ1	-0.114	-2.789	0.006	0.651
SLC13A3	0.125	2.788	0.006	0.651
C11orf97	0.112	2.788	0.006	0.651
NCEH1	0.128	2.786	0.006	0.651
USP40	0.150	2.785	0.006	0.651
GDF2	0.121	2.785	0.006	0.651
ZDHHC4	-0.176	-2.778	0.006	0.651
ACADL	0.129	2.776	0.006	0.651
ACTG2	-0.281	-2.776	0.006	0.651
CTIF	-0.141	-2.772	0.006	0.651
COL12A1	-0.411	-2.772	0.006	0.651
LOC115110	0.117	2.770	0.006	0.651
UBA2	-0.261	-2.769	0.006	0.651

MED1	-0.191	-2.768	0.006	0.651
COBL	0.246	2.768	0.006	0.651
PELP1	-0.154	-2.766	0.007	0.651
MS4A14	-0.156	-2.766	0.007	0.651
ANKRD36C	0.360	2.763	0.007	0.651
LOC102723701	0.122	2.755	0.007	0.651
MCM10	0.109	2.750	0.007	0.651
FAR2	0.182	2.750	0.007	0.651
RIMBP3	-0.146	-2.746	0.007	0.651
TPCN1	0.242	2.745	0.007	0.651
NTAN1	0.183	2.744	0.007	0.651
CTSZ	-0.156	-2.743	0.007	0.651
NFATC3	0.151	2.743	0.007	0.651
YME1L1	-0.155	-2.741	0.007	0.651
NAGPA	-0.097	-2.740	0.007	0.651
VIMP	-0.153	-2.736	0.007	0.651
BSN	0.110	2.735	0.007	0.651
DAND5	0.097	2.733	0.007	0.651
PPIL2	0.205	2.732	0.007	0.651
HIST1H4A	-0.360	-2.731	0.007	0.651
ADRM1	-0.121	-2.730	0.007	0.651
SPINT1	0.174	2.729	0.007	0.651
GANAB	-0.181	-2.729	0.007	0.651
HSFX1	0.156	2.726	0.007	0.651
INHA	0.092	2.725	0.007	0.651
SPIDR	0.166	2.723	0.007	0.651
ZMAT2	-0.198	-2.722	0.007	0.651
TTC25	0.133	2.721	0.007	0.651
CTTNBP2	0.150	2.721	0.007	0.651
RP11-466A19.5	0.159	2.721	0.007	0.651
ARHGEF9	0.314	2.720	0.007	0.651
ATXN7L1	0.171	2.720	0.007	0.651
SRRM3	0.131	2.719	0.007	0.651
CNKSR1	0.181	2.718	0.007	0.651
SEMA3D	-0.099	-2.717	0.008	0.651
DUX5	0.095	2.715	0.008	0.651
APOBEC3B	0.109	2.714	0.008	0.651
ZNF782	0.129	2.713	0.008	0.651
MAP4K1	0.119	2.709	0.008	0.651
PPFIA2	0.212	2.706	0.008	0.651
PEX14	0.112	2.705	0.008	0.651
MANEA	-0.130	-2.704	0.008	0.651
FAM49B	0.138	2.703	0.008	0.651
C14orf159	0.088	2.703	0.008	0.651
AURKC	0.120	2.703	0.008	0.651
GAREM1	-0.115	-2.702	0.008	0.651
SYNM	-0.161	-2.702	0.008	0.651

LMNTD2	0.076	2.698	0.008	0.651
SMARCB1	0.154	2.698	0.008	0.651
SULT1A4	0.089	2.695	0.008	0.651
CSF2RA	-0.084	-2.694	0.008	0.651
ENPP4	-0.134	-2.693	0.008	0.651
PDGFRA	-0.429	-2.687	0.008	0.651
AGO1	0.156	2.686	0.008	0.651
SULF1	-0.432	-2.685	0.008	0.651
TSPAN19	-0.097	-2.683	0.008	0.651
NPIPB6	0.609	2.682	0.008	0.651
C9orf72	0.121	2.678	0.008	0.651
ZNF417	0.170	2.678	0.008	0.651
PTPN3	0.161	2.676	0.008	0.651
ENTPD3	0.129	2.674	0.008	0.651
WWC2-AS2	0.137	2.673	0.008	0.651
GSTM1	0.160	2.673	0.008	0.651
TREML2	0.120	2.673	0.008	0.651
EGLN1	-0.198	-2.672	0.009	0.651
KMT2A	0.163	2.671	0.009	0.651
RPL36A-HNRNPH2	-0.188	-2.671	0.009	0.651
MED13L	-0.122	-2.666	0.009	0.651
RPS27A	-0.206	-2.664	0.009	0.651
FAM71E1	-0.093	-2.663	0.009	0.651
RPL6	-0.315	-2.662	0.009	0.651
CCDC127	-0.218	-2.661	0.009	0.651
USP24	-0.127	-2.661	0.009	0.651
SNRK	-0.208	-2.661	0.009	0.651
TGFB1I1	-0.115	-2.660	0.009	0.651
GCN1	0.103	2.660	0.009	0.651
COL6A2	-0.143	-2.660	0.009	0.651
COL6A3	-0.292	-2.658	0.009	0.651
RBM7	0.149	2.655	0.009	0.653
NUTM1	0.089	2.654	0.009	0.653
C6orf132	-0.112	-2.651	0.009	0.655
SAP30L	0.120	2.649	0.009	0.655
HINT1	-0.167	-2.646	0.009	0.655
FAM157A	0.145	2.645	0.009	0.655
HADHA	0.143	2.644	0.009	0.655
SAMD8	-0.147	-2.643	0.009	0.655
SLC12A2	-0.314	-2.642	0.009	0.655
TMEM138	0.195	2.642	0.009	0.655
POC1B	-0.089	-2.642	0.009	0.655
WDR35	0.161	2.639	0.009	0.656
MYDGF	-0.156	-2.637	0.009	0.658
EFCAB2	0.182	2.635	0.009	0.660
FAIM	-0.145	-2.632	0.010	0.662
DCN	-0.409	-2.631	0.010	0.662

BICC1	-0.190	-2.628	0.010	0.664
MED14OS	-0.096	-2.626	0.010	0.664
ANAPC15	0.234	2.625	0.010	0.664
POMGNT1	0.112	2.625	0.010	0.664
INPP5K	0.169	2.623	0.010	0.664
STK32B	0.098	2.621	0.010	0.664
SIGLEC6	-0.100	-2.621	0.010	0.664
EFR3B	-0.129	-2.620	0.010	0.664
AHI1	0.275	2.619	0.010	0.664
UQCRFS1	-0.129	-2.618	0.010	0.664
TNPO3	-0.112	-2.616	0.010	0.665
MTMR8	0.106	2.612	0.010	0.668
GOLGA8F	0.150	2.610	0.010	0.668
FAM3C	-0.213	-2.610	0.010	0.668
MBD2	0.349	2.607	0.010	0.668
FAM9B	0.105	2.607	0.010	0.668
KIAA1161	-0.092	-2.606	0.010	0.668
NAP1L4	-0.237	-2.605	0.010	0.668
COL3A1	-0.239	-2.604	0.010	0.668
GPSM1	-0.096	-2.603	0.010	0.668
ZNF142	0.165	2.600	0.010	0.668
APOBEC3A	0.117	2.600	0.010	0.668
SPARC	-0.453	-2.598	0.010	0.668
TRIM13	0.297	2.596	0.011	0.668
IGF2BP2	-0.194	-2.595	0.011	0.668
PPP3R2	-0.093	-2.593	0.011	0.668
CUBN	-0.292	-2.593	0.011	0.668
IFIH1	0.149	2.590	0.011	0.668
DECR1	0.306	2.589	0.011	0.668
CHURC1-FNTB	-0.206	-2.588	0.011	0.668
KRT81	0.100	2.587	0.011	0.668
MLLT4	0.185	2.587	0.011	0.668
FAM228B	0.134	2.585	0.011	0.668
NANOS3	0.104	2.584	0.011	0.668
RNMT	-0.102	-2.584	0.011	0.668
LUC7L3	0.292	2.583	0.011	0.668
MAGEC1	0.112	2.582	0.011	0.668
CA1	0.380	2.582	0.011	0.668
ATG7	0.374	2.580	0.011	0.668
ARCN1	-0.182	-2.579	0.011	0.668
RFWD3	0.102	2.578	0.011	0.668
EVL	0.165	2.576	0.011	0.668
KRTAP3-3	0.133	2.574	0.011	0.668
MAP7	0.147	2.573	0.011	0.668
TADA1	0.126	2.572	0.011	0.668
CARHSP1	0.123	2.571	0.011	0.668
RAD21	-0.123	-2.571	0.011	0.668

SEPT11	-0.299	-2.570	0.011	0.668
ADCYAP1R1	-0.115	-2.568	0.011	0.668
THBS2	-0.228	-2.567	0.011	0.668
RGPD5	0.165	2.567	0.011	0.668
SPATA31A6	0.133	2.566	0.011	0.668
FBXO25	0.132	2.563	0.012	0.668
PRNP	-0.168	-2.562	0.012	0.668
UBXN2A	-0.122	-2.562	0.012	0.668
ICE2	0.176	2.562	0.012	0.668
TAS1R2	-0.117	-2.560	0.012	0.670
TIMP1	-0.423	-2.557	0.012	0.671
PUDP	-0.137	-2.556	0.012	0.671
ATIC	0.157	2.556	0.012	0.671
KCND2	-0.166	-2.554	0.012	0.671
FNTA	-0.201	-2.554	0.012	0.671
OSBPL8	-0.207	-2.544	0.012	0.689
SLC17A5	-0.116	-2.540	0.012	0.691
PDIA6	-0.180	-2.536	0.012	0.691
MRPL17	-0.135	-2.536	0.012	0.691
NAA50	0.181	2.536	0.012	0.691
LMOD1	-0.157	-2.535	0.012	0.691
NLRP5	0.109	2.535	0.012	0.691
SMC1B	0.131	2.534	0.012	0.691
MSI2	0.143	2.534	0.012	0.691
FGFR2	-0.186	-2.533	0.013	0.691
C4orf3	-0.122	-2.529	0.013	0.692
FBXO2	0.109	2.528	0.013	0.692
MVB12B	0.221	2.527	0.013	0.692
CATSPERB	0.141	2.526	0.013	0.692
KCNA2	0.119	2.526	0.013	0.692
PCDH10	-0.252	-2.525	0.013	0.692
C4orf36	-0.105	-2.525	0.013	0.692
MBD3L2	0.165	2.523	0.013	0.694
CEP295NL	-0.282	-2.522	0.013	0.694
UBE2B	-0.157	-2.518	0.013	0.699
ASPH	-0.311	-2.516	0.013	0.699
MIR7162	0.106	2.515	0.013	0.699
MFAP3	-0.147	-2.515	0.013	0.699
CT45A10	0.118	2.514	0.013	0.699
C11orf44	0.091	2.513	0.013	0.699
SERPINB10	0.116	2.512	0.013	0.699
PAPPA	0.102	2.511	0.013	0.700
PMP22	-0.248	-2.507	0.013	0.700
HMBOX1	0.114	2.505	0.013	0.700
ICOSLG	0.090	2.505	0.014	0.700
IRF2BP1	0.115	2.504	0.014	0.700
ZNF664	-0.171	-2.504	0.014	0.700

ATMIN	0.172	2.503	0.014	0.700
VIP	-0.176	-2.502	0.014	0.700
ZNF638	0.092	2.502	0.014	0.700
UFM1	-0.170	-2.501	0.014	0.700
KIAA0922	0.182	2.501	0.014	0.700
TPM4	-0.178	-2.500	0.014	0.700
MELK	0.087	2.498	0.014	0.701
PABPN1	0.218	2.495	0.014	0.705
RAB3B	0.238	2.493	0.014	0.706
RPAP3	0.100	2.492	0.014	0.706
ANKRD36	0.145	2.490	0.014	0.706
PPIB	-0.170	-2.489	0.014	0.706
RWDD2A	-0.112	-2.489	0.014	0.706
ACTR2	-0.225	-2.488	0.014	0.706
PLA2R1	-0.101	-2.485	0.014	0.706
STAC	0.090	2.485	0.014	0.706
STX4	0.107	2.483	0.014	0.706
FAM96A	-0.158	-2.483	0.014	0.706
LOXHD1	0.144	2.483	0.014	0.706
JMJD1C	0.246	2.483	0.014	0.706
SOX13	0.143	2.481	0.014	0.706
RALBP1	-0.157	-2.480	0.014	0.706
ATP5A1	-0.165	-2.480	0.014	0.706
PARD3B	0.160	2.479	0.014	0.706
GPR42	-0.097	-2.478	0.015	0.707
MGC27345	0.130	2.477	0.015	0.707
NUP85	-0.143	-2.473	0.015	0.711
DPEP3	0.081	2.473	0.015	0.711
SPG21	-0.168	-2.471	0.015	0.711
LRP1	-0.222	-2.471	0.015	0.711
GADD45GIP1	0.103	2.465	0.015	0.720
CALU	-0.121	-2.458	0.015	0.721
TMEM251	-0.128	-2.458	0.015	0.721
H1F0	-0.159	-2.458	0.015	0.721
RHPN2	0.176	2.457	0.015	0.721
SH3GLB1	-0.189	-2.457	0.015	0.721
SACM1L	0.160	2.456	0.015	0.721
ECE1	-0.150	-2.451	0.016	0.721
CANX	-0.277	-2.450	0.016	0.721
PAFAH1B2	-0.226	-2.450	0.016	0.721
FKBP10	-0.104	-2.449	0.016	0.721
CHN1	-0.157	-2.447	0.016	0.721
TXNL1	-0.224	-2.447	0.016	0.721
FAM206A	-0.103	-2.445	0.016	0.721
CLCA1	-0.323	-2.445	0.016	0.721
ITGA2	-0.158	-2.445	0.016	0.721
OR9G4	0.103	2.444	0.016	0.721

TFEC	0.083	2.444	0.016	0.721
FAM227B	0.144	2.443	0.016	0.721
HOXD4	-0.127	-2.443	0.016	0.721
POTEC	0.246	2.443	0.016	0.721
TM4SF20	-0.272	-2.439	0.016	0.721
HIST1H3B	-0.213	-2.438	0.016	0.721
HSPA5	-0.138	-2.437	0.016	0.721
MAGEB3	0.118	2.437	0.016	0.721
REG3A	-0.278	-2.437	0.016	0.721
ZNF618	0.117	2.437	0.016	0.721
PPM1B	0.138	2.436	0.016	0.721
YPEL2	0.213	2.436	0.016	0.721
MRPS33	-0.209	-2.435	0.016	0.721
OR10A2	0.100	2.434	0.016	0.721
SPEM1	-0.102	-2.434	0.016	0.721
PELO	-0.094	-2.434	0.016	0.721
EVA1C	0.158	2.434	0.016	0.721
C3orf52	0.085	2.432	0.016	0.721
C14orf28	-0.103	-2.431	0.016	0.721
LDHB	-0.231	-2.431	0.016	0.721
ACTA2	-0.325	-2.429	0.017	0.721
BRD8	0.242	2.429	0.017	0.721
VCL	-0.279	-2.429	0.017	0.721
SAR1A	-0.183	-2.429	0.017	0.721
LYPLAL1	0.136	2.427	0.017	0.721
PNISR	0.179	2.427	0.017	0.721
FNBP4	0.148	2.427	0.017	0.721
FER1L5	0.119	2.426	0.017	0.721
N6AMT2	0.102	2.423	0.017	0.724
PDE6A	-0.110	-2.419	0.017	0.724
DEFB115	0.107	2.418	0.017	0.724
DDX28	0.119	2.418	0.017	0.724
NBPF26	0.114	2.417	0.017	0.724
BTNL2	0.094	2.417	0.017	0.724
APOPT1	-0.127	-2.417	0.017	0.724
ST6GALNAC5	0.123	2.416	0.017	0.724
BTBD19	0.101	2.416	0.017	0.724
NUMB	0.208	2.415	0.017	0.724
PPP1R16A	0.096	2.415	0.017	0.724
SUMF2	-0.127	-2.414	0.017	0.724
DENND2C	0.102	2.414	0.017	0.724
OR1B1	0.136	2.413	0.017	0.724
TVP23C	-0.168	-2.411	0.017	0.725
POSTN	-0.218	-2.409	0.017	0.728
HCG9	0.120	2.408	0.017	0.728
CKAP4	-0.137	-2.407	0.017	0.728
MYO5A	0.126	2.405	0.018	0.731

KCP	0.097	2.404	0.018	0.731
SLC16A7	-0.138	-2.403	0.018	0.731
COL5A1	-0.180	-2.402	0.018	0.731
PIBF1	0.195	2.402	0.018	0.731
GDI2	-0.146	-2.400	0.018	0.731
SLITRK6	-0.186	-2.399	0.018	0.731
TMLHE	-0.107	-2.399	0.018	0.731
CIPC	-0.093	-2.397	0.018	0.732
PHPT1	0.168	2.396	0.018	0.732
RAPGEF2	0.100	2.396	0.018	0.732
S100B	-0.188	-2.395	0.018	0.732
C8orf46	0.091	2.394	0.018	0.732
ALMS1	0.189	2.393	0.018	0.732
PCSK5	-0.181	-2.393	0.018	0.732
REXO1L10P	0.153	2.392	0.018	0.732
FOXF2	-0.107	-2.391	0.018	0.733
C6orf201	0.092	2.389	0.018	0.733
PRRX1	-0.161	-2.388	0.018	0.733
NOVA1	0.363	2.387	0.018	0.733
SUPT3H	0.140	2.387	0.018	0.733
C8orf88	-0.251	-2.387	0.018	0.733
GJB3	0.084	2.386	0.019	0.733
DSCAM	0.141	2.385	0.019	0.733
CPO	-0.124	-2.385	0.019	0.733
MYO7B	0.166	2.384	0.019	0.733
PPP4C	-0.123	-2.381	0.019	0.735
KRT40	0.160	2.380	0.019	0.735
RNF157	-0.090	-2.380	0.019	0.735
IDH2	-0.162	-2.380	0.019	0.735
RPL27	-0.161	-2.379	0.019	0.735
RPL23	-0.315	-2.377	0.019	0.737
NDST4	-0.155	-2.376	0.019	0.737
C9orf152	0.122	2.376	0.019	0.737
CCDC112	0.091	2.375	0.019	0.737
C1orf111	0.120	2.373	0.019	0.740
GDPD3	0.188	2.371	0.019	0.742
CDC73	-0.101	-2.370	0.019	0.742
TKTL2	0.106	2.370	0.019	0.742
MAGED4	-0.165	-2.368	0.019	0.742
ZFAND1	-0.199	-2.367	0.019	0.743
ATP2C2	0.136	2.365	0.020	0.745
SFRP2	-0.308	-2.364	0.020	0.745
MMD	-0.120	-2.363	0.020	0.745
EEF2	-0.175	-2.363	0.020	0.745
ERVW-1	0.129	2.361	0.020	0.746
HEATR9	0.082	2.361	0.020	0.746
CPE	-0.343	-2.361	0.020	0.746

ATXN3L	-0.073	-2.359	0.020	0.746
ANKRD42	-0.093	-2.359	0.020	0.746
CHD7	0.111	2.356	0.020	0.750
LRRC4B	-0.111	-2.355	0.020	0.750
MT1B	0.136	2.354	0.020	0.750
SPATA13	0.107	2.354	0.020	0.750
FBXO40	0.075	2.353	0.020	0.751
IFT52	-0.258	-2.346	0.021	0.751
KRTAP10-5	0.090	2.345	0.021	0.751
MORC1	-0.082	-2.344	0.021	0.751
PVRL3	-0.104	-2.343	0.021	0.751
IDI2	0.105	2.343	0.021	0.751
TMX4	0.125	2.343	0.021	0.751
MAP3K4	0.229	2.343	0.021	0.751
IMPDH2	-0.132	-2.343	0.021	0.751
GOLGA6L3	0.186	2.342	0.021	0.751
TRUB2	-0.127	-2.342	0.021	0.751
ZDHHC9	-0.099	-2.341	0.021	0.751
ZNF512	-0.175	-2.341	0.021	0.751
PCDHB16	0.183	2.340	0.021	0.751
ANKRD33B	0.082	2.340	0.021	0.751
CNTN3	0.307	2.340	0.021	0.751
ALOX12	0.095	2.338	0.021	0.751
ZFP1	0.089	2.337	0.021	0.751
SLC43A3	-0.144	-2.337	0.021	0.751
CNN1	-0.448	-2.337	0.021	0.751
FBXL18	0.073	2.337	0.021	0.751
TTC28	0.114	2.335	0.021	0.751
KLHL13	-0.099	-2.335	0.021	0.751
NME1	-0.121	-2.334	0.021	0.751
ASB2	-0.120	-2.334	0.021	0.751
ADPRM	-0.140	-2.333	0.021	0.751
ATP6V1E1	-0.286	-2.331	0.021	0.751
HIST1H2AI	-0.128	-2.331	0.021	0.751
CLASP2	0.097	2.330	0.021	0.751
RFPL4AL1	0.115	2.330	0.021	0.751
RWDD1	-0.158	-2.329	0.021	0.751
CNN3	-0.318	-2.328	0.021	0.751
DSC3	0.089	2.328	0.021	0.751
PTRF	-0.176	-2.327	0.022	0.751
TNFRSF9	0.115	2.326	0.022	0.751
PRM1	0.091	2.326	0.022	0.751
LCORL	0.192	2.325	0.022	0.751
STK26	0.132	2.324	0.022	0.751
RNF6	-0.207	-2.324	0.022	0.751
SETDB1	0.128	2.323	0.022	0.751
NOTCH4	0.083	2.323	0.022	0.751

GSK3B	0.177	2.323	0.022	0.751
KDM7A	0.134	2.322	0.022	0.751
YLPM1	-0.090	-2.318	0.022	0.753
VAMP4	-0.105	-2.316	0.022	0.753
HTN1	0.096	2.315	0.022	0.753
RNASE6	-0.187	-2.315	0.022	0.753
ETNK1	0.114	2.314	0.022	0.753
OR7G2	0.102	2.314	0.022	0.753
LINC01588	0.101	2.313	0.022	0.753
C5orf22	-0.128	-2.312	0.022	0.753
AFF3	0.187	2.312	0.022	0.753
KCNIP3	0.098	2.312	0.022	0.753
PARVB	-0.207	-2.309	0.023	0.753
C16orf45	-0.140	-2.307	0.023	0.753
ZNHIT1	-0.143	-2.306	0.023	0.753
TXNRD3NB	0.085	2.306	0.023	0.753
KRT8	0.125	2.306	0.023	0.753
CFL2	-0.179	-2.306	0.023	0.753
C1QL3	-0.093	-2.305	0.023	0.753
CYCS	-0.241	-2.304	0.023	0.753
ZNF658B	0.100	2.303	0.023	0.753
PICALM	-0.226	-2.302	0.023	0.753
B3GNT3	-0.090	-2.302	0.023	0.753
AGA	-0.124	-2.301	0.023	0.753
ARRDC4	-0.144	-2.301	0.023	0.753
ZCWPW1	0.101	2.301	0.023	0.753
ZNF714	0.131	2.301	0.023	0.753
EXOC7	0.096	2.301	0.023	0.753
ZNF891	0.095	2.300	0.023	0.753
SLC14A1	-0.099	-2.300	0.023	0.753
FCF1	-0.142	-2.300	0.023	0.753
SH3TC1	0.069	2.299	0.023	0.753
UNC119B	0.127	2.299	0.023	0.753
PPT1	-0.151	-2.297	0.023	0.753
GOLGA6L5P	0.165	2.297	0.023	0.753
SND1	-0.101	-2.296	0.023	0.753
CYP51A1	-0.224	-2.295	0.023	0.753
C17orf64	0.099	2.292	0.024	0.753
CCDC33	0.092	2.291	0.024	0.753
PPME1	-0.118	-2.291	0.024	0.753
IL3	0.084	2.291	0.024	0.753
KIF11	0.099	2.290	0.024	0.753
INTS8	0.156	2.289	0.024	0.753
TMCC3	-0.176	-2.288	0.024	0.753
ZNF436-AS1	0.072	2.286	0.024	0.753
PHF19	-0.087	-2.286	0.024	0.753
SLC41A2	-0.111	-2.286	0.024	0.753

NFASC	0.175	2.285	0.024	0.753
ZNF254	0.221	2.284	0.024	0.753
AHR	-0.318	-2.283	0.024	0.753
SLAIN2	0.145	2.283	0.024	0.753
PNLIPRP1	0.092	2.283	0.024	0.753
SPCS3	-0.130	-2.282	0.024	0.753
DHX37	0.103	2.282	0.024	0.753
SGMS1	-0.109	-2.282	0.024	0.753
JOSD1	0.128	2.281	0.024	0.753
AKAP9	0.188	2.278	0.024	0.753
OPCML	-0.118	-2.278	0.024	0.753
KCTD4	0.114	2.278	0.024	0.753
WHSC1	0.148	2.276	0.024	0.753
CD99	-0.155	-2.276	0.025	0.753
ZNF562	0.177	2.275	0.025	0.753
MTX2	-0.083	-2.275	0.025	0.753
APBA1	-0.092	-2.275	0.025	0.753
C1QBP	-0.117	-2.275	0.025	0.753
LRRN4	0.110	2.274	0.025	0.753
MYSM1	0.137	2.274	0.025	0.753
TMEM206	0.101	2.274	0.025	0.753
KIAA1211L	0.129	2.273	0.025	0.753
PTN	0.211	2.272	0.025	0.753
CHM	0.082	2.272	0.025	0.753
ORC5	-0.184	-2.271	0.025	0.753
MFSD2B	0.098	2.271	0.025	0.753
KLHL8	0.112	2.269	0.025	0.753
TTC9	-0.150	-2.269	0.025	0.753
DNAH12	0.118	2.269	0.025	0.753
UBE3A	0.291	2.269	0.025	0.753
AP3S2	-0.200	-2.268	0.025	0.753
HAP1	0.100	2.267	0.025	0.753
SPATA4	-0.080	-2.266	0.025	0.753
SMARCC2	0.142	2.265	0.025	0.753
ETF1	-0.174	-2.265	0.025	0.753
ITGAL	0.098	2.264	0.025	0.753
DCTN5	0.115	2.264	0.025	0.753
TUBB	-0.135	-2.264	0.025	0.753
TRNAU1AP	-0.122	-2.263	0.025	0.753
TGFB2	-0.160	-2.262	0.025	0.753
NAA16	0.176	2.262	0.025	0.753
MLC1	0.121	2.261	0.025	0.753
CSH2	0.084	2.261	0.025	0.753
GJD2	0.146	2.260	0.025	0.753
BIVM-ERCC5	0.125	2.260	0.025	0.753
RBM10	0.105	2.260	0.026	0.753
PML	0.104	2.258	0.026	0.753

CIR1	0.133	2.258	0.026	0.753
ZNF219	0.146	2.258	0.026	0.753
CLCC1	-0.102	-2.256	0.026	0.753
CASD1	0.261	2.256	0.026	0.753
DIP2A	-0.107	-2.256	0.026	0.753
RPL19	-0.124	-2.255	0.026	0.753
SAE1	-0.119	-2.255	0.026	0.753
ZMIZ1	-0.100	-2.255	0.026	0.753
WNK3	-0.120	-2.255	0.026	0.753
UBE2N	-0.140	-2.253	0.026	0.753
ZC3H12B	-0.092	-2.253	0.026	0.753
CCDC22	0.068	2.253	0.026	0.753
KANSL2	0.113	2.252	0.026	0.753
SGOL2	0.066	2.252	0.026	0.753
CLN6	0.096	2.252	0.026	0.753
MRE11A	-0.088	-2.252	0.026	0.753
BCKDHA	-0.114	-2.252	0.026	0.753
HIST1H4D	-0.186	-2.251	0.026	0.753
TRIB2	-0.126	-2.250	0.026	0.753
SLX1A-SULT1A3	0.109	2.249	0.026	0.753
TMEM185B	0.139	2.249	0.026	0.753
DPM1	0.087	2.248	0.026	0.753
C9orf163	0.099	2.247	0.026	0.753
GPN2	0.096	2.246	0.026	0.753
KCNN1	0.091	2.244	0.027	0.753
GNG11	-0.202	-2.244	0.027	0.753
GMFG	0.151	2.244	0.027	0.753
KIF23	-0.097	-2.243	0.027	0.753
ZNF773	0.128	2.243	0.027	0.753
OR7D2	0.080	2.243	0.027	0.753
TCEAL4	-0.162	-2.243	0.027	0.753
AK3	-0.233	-2.243	0.027	0.753
CPT2	-0.110	-2.242	0.027	0.753
ARL17B	-0.167	-2.241	0.027	0.753
RMI2	-0.098	-2.240	0.027	0.755
VGF	-0.146	-2.240	0.027	0.755
E2F4	0.181	2.238	0.027	0.756
HP09025	-0.086	-2.237	0.027	0.756
PSMC6	-0.118	-2.237	0.027	0.756
MTR	0.103	2.236	0.027	0.757
PLA2G16	0.097	2.235	0.027	0.757
USP12	0.101	2.235	0.027	0.757
FAM26D	0.074	2.234	0.027	0.757
OR4K14	-0.098	-2.234	0.027	0.757
TUSC1	-0.098	-2.233	0.027	0.757
RPL26L1	-0.134	-2.233	0.027	0.757
BEST3	-0.118	-2.232	0.027	0.757

OR1N1	0.133	2.231	0.027	0.757
NOL6	0.106	2.231	0.027	0.757
SPATA31E1	-0.118	-2.229	0.028	0.758
WDR64	0.088	2.229	0.028	0.758
RPL15	-0.125	-2.227	0.028	0.758
NUPL2	-0.097	-2.227	0.028	0.758
TICRR	0.068	2.227	0.028	0.758
MIR659	0.105	2.227	0.028	0.758
OR4Q3	0.080	2.226	0.028	0.758
CCDC28B	0.117	2.225	0.028	0.758
DAPP1	0.080	2.225	0.028	0.758
FLNA	-0.147	-2.223	0.028	0.758
C1orf204	0.089	2.223	0.028	0.758
MPZL1	-0.215	-2.223	0.028	0.758
ACBD4	0.085	2.223	0.028	0.758
TMEM42	0.114	2.221	0.028	0.758
SI	-0.277	-2.220	0.028	0.758
MMP28	-0.095	-2.220	0.028	0.758
TRIM16	-0.136	-2.220	0.028	0.758
KLHL18	0.095	2.220	0.028	0.758
PNP	-0.192	-2.220	0.028	0.758
PLA2G12A	-0.120	-2.219	0.028	0.758
RPS24	-0.255	-2.218	0.028	0.758
GMEB2	-0.098	-2.218	0.028	0.758
AGGF1	-0.087	-2.216	0.028	0.759
SLC43A2	0.072	2.216	0.028	0.759
QARS	0.082	2.215	0.028	0.759
ATRIP	0.097	2.215	0.029	0.759
PARVA	-0.177	-2.214	0.029	0.760
BDKRB1	-0.107	-2.213	0.029	0.761
TMEM248	-0.164	-2.212	0.029	0.761
FBXW10	-0.098	-2.210	0.029	0.765
MSH5	0.256	2.208	0.029	0.767
CWC22	0.115	2.207	0.029	0.767
DEFA5	-0.259	-2.206	0.029	0.767
LCT	-0.092	-2.205	0.029	0.767
SERHL	0.156	2.205	0.029	0.767
COX7A2L	0.116	2.205	0.029	0.767
CCT3	-0.167	-2.204	0.029	0.767
PSMD1	0.106	2.203	0.029	0.767
PPA1	-0.192	-2.203	0.029	0.767
TRAPPC8	-0.133	-2.203	0.029	0.767
ITK	0.092	2.202	0.029	0.767
ALDH3A1	-0.089	-2.202	0.029	0.767
STIM2	0.207	2.200	0.030	0.770
ETV3L	0.066	2.199	0.030	0.771
TSPAN11	-0.108	-2.199	0.030	0.771

KCNT2	-0.323	-2.198	0.030	0.772
GOLM1	0.164	2.196	0.030	0.773
MAK	0.105	2.195	0.030	0.773
MTERF4	0.135	2.195	0.030	0.773
TYROBP	0.092	2.193	0.030	0.774
RUNDC3B	-0.108	-2.193	0.030	0.774
KSR2	0.184	2.190	0.030	0.779
HELZ	0.109	2.189	0.030	0.779
MAEL	0.082	2.189	0.030	0.779
PTPN12	-0.270	-2.189	0.030	0.779
AP5B1	0.082	2.188	0.031	0.780
NPHP3	-0.118	-2.187	0.031	0.780
HBS1L	0.197	2.187	0.031	0.780
NAT10	0.117	2.186	0.031	0.781
CES3	-0.319	-2.185	0.031	0.781
NFRKB	-0.129	-2.184	0.031	0.781
HSPE1	0.327	2.184	0.031	0.781
FAM117A	0.094	2.183	0.031	0.781
PCBP3	0.090	2.183	0.031	0.781
MUS81	0.091	2.182	0.031	0.781
ANPEP	-0.367	-2.180	0.031	0.783
C11orf24	-0.101	-2.179	0.031	0.783
KIAA1456	0.127	2.178	0.031	0.783
FBXW7	0.163	2.178	0.031	0.783
TSTD1	0.217	2.176	0.031	0.783
COL24A1	-0.112	-2.175	0.031	0.783
THADA	0.102	2.175	0.031	0.783
TLX2	-0.105	-2.175	0.031	0.783
GLTSCR1	-0.082	-2.174	0.032	0.783
B3GAT3	-0.089	-2.174	0.032	0.783
C6orf118	0.069	2.171	0.032	0.783
SP140	0.144	2.171	0.032	0.783
HOXA3	-0.083	-2.171	0.032	0.783
OR4K15	0.075	2.170	0.032	0.783
DNER	-0.174	-2.170	0.032	0.783
SLCO4A1	0.101	2.168	0.032	0.783
KRTAP10-11	0.107	2.168	0.032	0.783
GRAP	0.111	2.168	0.032	0.783
MFSD8	0.122	2.167	0.032	0.783
HYKK	-0.094	-2.167	0.032	0.783
C9orf69	0.092	2.166	0.032	0.783
BRICD5	0.066	2.166	0.032	0.783
PRDX1	-0.168	-2.166	0.032	0.783
DYNC2H1	-0.154	-2.166	0.032	0.783
NCOR2	0.085	2.165	0.032	0.783
BLOC1S5-TXNDC5	-0.129	-2.163	0.032	0.783
CYB5R4	-0.084	-2.163	0.032	0.783

NCAPH2	-0.084	-2.163	0.032	0.783
HPS4	0.123	2.162	0.032	0.783
BCKDHB	-0.224	-2.162	0.032	0.783
OR2H2	0.091	2.162	0.032	0.783
HLA-DQA2	0.087	2.162	0.032	0.783
ELL3	0.086	2.161	0.033	0.783
TXNDC5	-0.129	-2.159	0.033	0.783
BRE	0.185	2.159	0.033	0.783
CALD1	-0.304	-2.159	0.033	0.783
PLEC	-0.114	-2.159	0.033	0.783
NCBP2	0.147	2.159	0.033	0.783
BPNT1	-0.155	-2.158	0.033	0.783
FOXD2	0.101	2.157	0.033	0.783
PPIAP30	0.136	2.156	0.033	0.783
RINL	0.080	2.156	0.033	0.783
WWTR1	-0.114	-2.156	0.033	0.783
SGCD	0.109	2.155	0.033	0.783
AQP1	-0.189	-2.155	0.033	0.783
LRTM2	0.071	2.154	0.033	0.783
FXN	-0.133	-2.154	0.033	0.783
MOB1A	-0.092	-2.154	0.033	0.783
CAPN12	0.107	2.153	0.033	0.783
NRAP	0.117	2.153	0.033	0.783
BAIAP2	0.074	2.152	0.033	0.783
RNASE7	0.109	2.152	0.033	0.783
LPXN	0.096	2.151	0.033	0.783
DNAJC8	-0.085	-2.150	0.033	0.783
PLPP7	0.083	2.150	0.033	0.783
CSAG3	0.132	2.149	0.033	0.783
MYH4	0.087	2.149	0.034	0.783
PBOV1	0.191	2.149	0.034	0.783
AKR7A2	0.100	2.148	0.034	0.783
VEPH1	0.340	2.148	0.034	0.783
SLC39A4	0.096	2.148	0.034	0.783
ROR1-AS1	0.145	2.148	0.034	0.783
AP1S1	-0.080	-2.147	0.034	0.783
SMCO3	0.140	2.147	0.034	0.783
MASTL	-0.140	-2.146	0.034	0.783
SPSB2	0.077	2.146	0.034	0.783
ZPBP2	-0.106	-2.146	0.034	0.783
MESDC1	-0.075	-2.145	0.034	0.783
P4HB	-0.162	-2.144	0.034	0.783
ATP2C1	0.122	2.143	0.034	0.783
CHMP1B	-0.119	-2.142	0.034	0.783
UGT2B15	-0.433	-2.142	0.034	0.783
DOCK4	0.093	2.141	0.034	0.783
ETV4	-0.132	-2.141	0.034	0.783

TMEM159	-0.121	-2.140	0.034	0.783
C6orf136	0.183	2.140	0.034	0.783
FAM35A	0.206	2.140	0.034	0.783
CD14	-0.104	-2.139	0.034	0.783
PPDPF	-0.114	-2.139	0.034	0.783
DDB2	0.093	2.139	0.034	0.783
BMS1P20	0.151	2.139	0.034	0.783
ANO2	-0.094	-2.138	0.034	0.783
SERINC1	-0.157	-2.138	0.034	0.783
B3GLCT	0.100	2.136	0.035	0.783
ATP6V1B1	-0.102	-2.136	0.035	0.783
STAC3	0.113	2.136	0.035	0.783
PTPRB	-0.129	-2.135	0.035	0.783
ST5	0.090	2.135	0.035	0.783
PKIG	-0.082	-2.135	0.035	0.783
FAM166B	0.132	2.135	0.035	0.783
LINC01561	0.084	2.135	0.035	0.783
ACVR1	0.181	2.135	0.035	0.783
LINC01343	0.084	2.134	0.035	0.783
DEFB119	0.084	2.134	0.035	0.783
MEX3D	-0.079	-2.133	0.035	0.784
CLU	-0.361	-2.131	0.035	0.785
ZXDA	0.081	2.131	0.035	0.785
EP300	0.107	2.131	0.035	0.785
MSL1	-0.214	-2.129	0.035	0.785
PDGFB	0.086	2.129	0.035	0.785
MBNL2	0.151	2.128	0.035	0.785
ZNF317	0.083	2.128	0.035	0.785
LMAN2L	0.098	2.128	0.035	0.785
SCN2A	0.209	2.127	0.035	0.785
C5orf15	0.125	2.127	0.035	0.785
C9orf139	0.084	2.126	0.035	0.785
NKTR	0.207	2.124	0.036	0.785
BPTF	0.168	2.123	0.036	0.785
NLRP13	0.100	2.123	0.036	0.785
UFC1	-0.166	-2.123	0.036	0.785
GALNT13	0.113	2.123	0.036	0.785
NAB2	0.071	2.123	0.036	0.785
ZNF587	0.166	2.122	0.036	0.785
LINC01387	0.072	2.122	0.036	0.785
SLC15A2	0.212	2.122	0.036	0.785
GPSM3	0.075	2.122	0.036	0.785
PZP	-0.184	-2.122	0.036	0.785
LRRC37A2	0.185	2.121	0.036	0.785
LYG2	0.117	2.119	0.036	0.789
LRRC53	0.117	2.118	0.036	0.789
TRPM2	0.098	2.118	0.036	0.789

IMPA2	-0.086	-2.117	0.036	0.789
CPSF4L	0.083	2.117	0.036	0.789
PLD3	-0.122	-2.116	0.036	0.789
SPARCL1	-0.457	-2.116	0.036	0.789
PSMB2	-0.135	-2.114	0.036	0.790
SCX	0.110	2.113	0.037	0.790
UBE2E1	-0.127	-2.113	0.037	0.790
BRWD1	0.168	2.112	0.037	0.790
PPAP2B	0.294	2.112	0.037	0.790
SDC2	-0.179	-2.112	0.037	0.790
CAV2	-0.105	-2.111	0.037	0.790
USH1G	-0.097	-2.110	0.037	0.790
GOLT1B	-0.107	-2.110	0.037	0.790
GDPD5	0.090	2.109	0.037	0.790
TMEM37	-0.159	-2.109	0.037	0.790
ZNF655	-0.086	-2.109	0.037	0.790
SCNN1B	0.173	2.109	0.037	0.790
BCCIP	0.137	2.108	0.037	0.790
GPR132	0.089	2.108	0.037	0.790
EPHX1	-0.427	-2.108	0.037	0.790
APH1B	0.161	2.107	0.037	0.790
SRGAP3	0.123	2.107	0.037	0.790
PRG2	0.083	2.107	0.037	0.790
PHF20L1	0.166	2.104	0.037	0.794
MRPS30	-0.198	-2.102	0.037	0.795
TSPAN32	0.085	2.102	0.037	0.795
ZCCHC16	0.105	2.102	0.037	0.795
CENPU	-0.097	-2.100	0.038	0.796
TTF1	-0.089	-2.099	0.038	0.796
PSMA3	-0.190	-2.099	0.038	0.796
ARHGAP17	0.116	2.099	0.038	0.796
SENP3	0.194	2.098	0.038	0.796
C2orf50	0.077	2.098	0.038	0.796
NAV2	0.136	2.098	0.038	0.796
C1QTNF5	0.082	2.096	0.038	0.796
GLRB	-0.124	-2.096	0.038	0.796
XPNPEP3	0.237	2.096	0.038	0.796
UBR3	0.105	2.096	0.038	0.796
NECAB3	0.085	2.096	0.038	0.796
ATP13A5-AS1	0.102	2.095	0.038	0.796
BCAS2	0.149	2.093	0.038	0.797
SEC23A	-0.236	-2.093	0.038	0.797
CST1	-0.343	-2.093	0.038	0.797
EPHA2	0.089	2.092	0.038	0.797
UBR1	0.231	2.092	0.038	0.797
CDKL2	0.194	2.092	0.038	0.797
NPM3	-0.113	-2.091	0.038	0.797

HIVEP2	0.116	2.091	0.039	0.797
PIGA	0.116	2.091	0.039	0.797
EXOSC5	0.099	2.090	0.039	0.797
SCYL1	0.090	2.090	0.039	0.797
SGK1	-0.371	-2.090	0.039	0.797
PLXDC2	-0.172	-2.088	0.039	0.799
CEP126	0.263	2.087	0.039	0.799
LAMB4	-0.113	-2.086	0.039	0.799
MED13	0.281	2.086	0.039	0.799
MYH8	-0.078	-2.086	0.039	0.799
TTC39C	-0.276	-2.086	0.039	0.799
FEZF2	-0.078	-2.085	0.039	0.799
MRPL34	-0.094	-2.084	0.039	0.799
FCGR1A	-0.191	-2.083	0.039	0.799
MYO5C	0.114	2.083	0.039	0.799
ATG12	-0.108	-2.082	0.039	0.799
ROCK1	-0.160	-2.082	0.039	0.799
DGKB	0.098	2.082	0.039	0.799
TUBA4B	0.072	2.082	0.039	0.799
MICALCL	0.111	2.081	0.039	0.799
C1QTNF9B	0.105	2.081	0.039	0.799
LOC441155	0.113	2.080	0.039	0.799
PAPLN	0.104	2.080	0.040	0.799
NAALADL2	-0.104	-2.079	0.040	0.799
FAT2	-0.089	-2.079	0.040	0.799
ADAMDEC1	-0.232	-2.079	0.040	0.799
DMXL2	0.257	2.078	0.040	0.799
NEXN	-0.382	-2.078	0.040	0.799
AHNAK2	-0.127	-2.078	0.040	0.799
ACOT4	-0.097	-2.077	0.040	0.799
SMARCC1	0.146	2.077	0.040	0.799
NDUFA9	-0.152	-2.077	0.040	0.799
NT5C	-0.070	-2.075	0.040	0.799
MYL3	0.123	2.075	0.040	0.799
CRACR2A	0.108	2.074	0.040	0.799
CA13	0.069	2.074	0.040	0.799
PDE6H	0.088	2.073	0.040	0.799
ACAT1	-0.395	-2.072	0.040	0.799
C19orf44	0.106	2.071	0.040	0.799
CYP2U1	-0.078	-2.071	0.040	0.799
CALML4	0.193	2.071	0.040	0.799
OGG1	0.088	2.071	0.040	0.799
ZNF57	0.171	2.070	0.040	0.799
OR7E24	0.087	2.070	0.040	0.799
TRADD	-0.114	-2.070	0.040	0.799
FAM228A	-0.081	-2.070	0.040	0.799
FAR1	-0.112	-2.069	0.040	0.799

PINLYP	0.105	2.069	0.041	0.799
RFC3	0.095	2.069	0.041	0.799
SLC26A9	-0.069	-2.069	0.041	0.799
CNTN4	-0.143	-2.068	0.041	0.800
MST1R	0.085	2.067	0.041	0.802
TCF20	0.088	2.066	0.041	0.802
CHRAC1	0.104	2.066	0.041	0.802
SLC35F2	-0.111	-2.065	0.041	0.802
LIPE	-0.091	-2.065	0.041	0.802
ZBTB22	0.082	2.063	0.041	0.803
FOXA3	0.102	2.062	0.041	0.803
ZMYND8	0.190	2.062	0.041	0.803
USP34	0.134	2.061	0.041	0.803
ATP5G1	-0.141	-2.061	0.041	0.803
GHSR	0.177	2.060	0.041	0.803
LOX	-0.151	-2.059	0.041	0.803
ANO4	0.092	2.059	0.041	0.803
AKR1E2	-0.120	-2.059	0.042	0.803
ZADH2	-0.146	-2.059	0.042	0.803
PIK3R5	-0.090	-2.059	0.042	0.803
DAP	-0.253	-2.058	0.042	0.803
KCNN3	-0.115	-2.057	0.042	0.803
SMR3B	0.098	2.057	0.042	0.803
MYH3	0.095	2.057	0.042	0.803
FAM157B	0.094	2.057	0.042	0.803
ITGB3	-0.090	-2.056	0.042	0.803
TP53BP1	0.207	2.055	0.042	0.803
ELOVL6	-0.181	-2.054	0.042	0.803
CBWD1	0.235	2.054	0.042	0.803
UNG	-0.084	-2.053	0.042	0.803
XAGE5	0.098	2.052	0.042	0.803
PGM2	0.091	2.052	0.042	0.803
KDELR1	-0.152	-2.052	0.042	0.803
ND2	-0.293	-2.051	0.042	0.803
SRPK3	-0.085	-2.050	0.042	0.803
MRPL18	-0.082	-2.050	0.042	0.803
ZNF385B	0.355	2.049	0.042	0.803
MAP2K4	-0.198	-2.048	0.043	0.803
ELP6	-0.120	-2.047	0.043	0.803
C6orf106	-0.099	-2.047	0.043	0.803
SLC6A4	0.095	2.046	0.043	0.803
CLP1	-0.081	-2.046	0.043	0.803
PHGDH	0.119	2.046	0.043	0.803
CELF6	-0.084	-2.045	0.043	0.803
UBN1	0.177	2.045	0.043	0.803
TBC1D22A	-0.102	-2.045	0.043	0.803
KLHL11	0.096	2.044	0.043	0.803

SLC13A1	-0.105	-2.044	0.043	0.803
TK2	0.089	2.044	0.043	0.803
C21orf62	0.125	2.043	0.043	0.803
PCSK9	0.083	2.042	0.043	0.803
AKAP8L	0.259	2.042	0.043	0.803
PHC1	0.084	2.042	0.043	0.803
PCDHB1	0.111	2.041	0.043	0.803
WFDC13	0.087	2.041	0.043	0.803
DNAH10	-0.089	-2.041	0.043	0.803
CHURC1	-0.103	-2.040	0.043	0.803
EXO5	0.091	2.038	0.044	0.803
CXorf56	0.154	2.038	0.044	0.803
CTPS1	0.079	2.038	0.044	0.803
FAM3C2	-0.166	-2.037	0.044	0.803
GOLGA7B	0.091	2.036	0.044	0.803
USP17L23	0.152	2.036	0.044	0.803
CCNG2	0.057	2.036	0.044	0.803
AAGAB	0.072	2.036	0.044	0.803
KLK15	0.079	2.035	0.044	0.803
EP400	0.097	2.035	0.044	0.803
C18orf25	-0.117	-2.034	0.044	0.803
RPTN	0.081	2.033	0.044	0.803
STRN	0.116	2.033	0.044	0.803
KLHL33	-0.075	-2.032	0.044	0.803
C7orf73	-0.170	-2.031	0.044	0.803
IL6ST	-0.194	-2.031	0.044	0.803
C11orf91	0.082	2.031	0.044	0.803
CHPT1	-0.102	-2.031	0.044	0.803
C10orf76	0.108	2.030	0.044	0.803
SNX2	-0.265	-2.029	0.044	0.803
PPM1L	0.073	2.029	0.045	0.803
MPPED2	-0.126	-2.029	0.045	0.803
DPPA3	0.121	2.028	0.045	0.803
TFAP4	0.113	2.028	0.045	0.803
FAM229A	-0.073	-2.028	0.045	0.803
SPN	0.070	2.028	0.045	0.803
PBDC1	-0.108	-2.028	0.045	0.803
FOXN3	-0.286	-2.027	0.045	0.803
TBC1D9	-0.134	-2.027	0.045	0.803
TAGLN	-0.249	-2.027	0.045	0.803
WIZ	0.065	2.027	0.045	0.803
ADH7	-0.082	-2.027	0.045	0.803
EID1	-0.109	-2.026	0.045	0.803
CCDC191	0.136	2.026	0.045	0.803
NETO1	-0.135	-2.026	0.045	0.803
SAMHD1	0.208	2.026	0.045	0.803
FAM221B	0.070	2.026	0.045	0.803

RASSF7	0.098	2.025	0.045	0.803
PFN1	-0.176	-2.025	0.045	0.803
LINC00174	0.083	2.025	0.045	0.803
CCDC62	0.069	2.025	0.045	0.803
DCAF6	0.153	2.024	0.045	0.803
HIST1H2AK	-0.115	-2.023	0.045	0.803
DNAJC3	-0.078	-2.023	0.045	0.803
YBX1	0.142	2.023	0.045	0.803
GRM3	0.081	2.023	0.045	0.803
LINC00471	0.086	2.023	0.045	0.803
ANKFN1	-0.081	-2.023	0.045	0.803
NAT8L	0.082	2.022	0.045	0.803
MYLK	-0.254	-2.022	0.045	0.803
MPV17	-0.174	-2.021	0.045	0.803
PPARD	0.085	2.021	0.045	0.803
CALB2	-0.143	-2.021	0.045	0.803
TTLL6	0.187	2.020	0.045	0.803
HIST1H4H	-0.150	-2.020	0.045	0.803
MT3	0.070	2.019	0.046	0.803
LOC100131496	0.125	2.019	0.046	0.803
ZNF558	0.097	2.019	0.046	0.803
NBPF19	0.116	2.019	0.046	0.803
ARMC6	0.085	2.019	0.046	0.803
ITGA5	-0.211	-2.018	0.046	0.803
TMEM114	0.082	2.018	0.046	0.803
NEU1	0.084	2.017	0.046	0.803
MOS	0.097	2.017	0.046	0.803
SLC5A11	-0.070	-2.017	0.046	0.803
FKTN	-0.103	-2.017	0.046	0.803
OR52D1	0.101	2.016	0.046	0.803
MAGEE1	0.107	2.016	0.046	0.803
PPID	0.108	2.016	0.046	0.803
BPY2C	-0.080	-2.016	0.046	0.803
FAM13B	0.108	2.015	0.046	0.803
FABP2	-0.223	-2.014	0.046	0.803
OR10J1	0.087	2.014	0.046	0.803
TBC1D8	0.087	2.014	0.046	0.803
MEGF11	0.220	2.014	0.046	0.803
IFNL1	0.080	2.014	0.046	0.803
NFIA	0.124	2.014	0.046	0.803
TRIM17	0.089	2.013	0.046	0.803
SLC4A1AP	0.116	2.013	0.046	0.803
IL22RA1	0.167	2.012	0.046	0.803
GPR3	-0.094	-2.011	0.046	0.803
HIBCH	0.084	2.011	0.046	0.803
RSG1	0.073	2.011	0.046	0.803
NHSL1	0.137	2.010	0.046	0.803

SHTN1	0.225	2.010	0.047	0.803
TAAR9	0.098	2.009	0.047	0.803
TSC22D3	-0.192	-2.009	0.047	0.803
CRY1	0.093	2.009	0.047	0.803
NAV1	0.132	2.008	0.047	0.803
HIST1H4B	-0.089	-2.008	0.047	0.803
HEATR1	-0.151	-2.008	0.047	0.803
CDC42EP3	0.184	2.007	0.047	0.803
ZNF622	-0.088	-2.007	0.047	0.803
TPRX1	-0.073	-2.007	0.047	0.803
RBKS	-0.088	-2.006	0.047	0.803
SASS6	0.111	2.006	0.047	0.803
HDAC3	0.086	2.005	0.047	0.803
SYNCRIP	0.117	2.004	0.047	0.803
PCDHB4	0.104	2.004	0.047	0.803
CASZ1	0.092	2.003	0.047	0.803
HEXIM2	-0.106	-2.003	0.047	0.803
PRICKLE2	0.056	2.003	0.047	0.803
NGB	0.077	2.001	0.048	0.803
GOLGA8A	0.205	2.000	0.048	0.803
BRMS1L	-0.095	-2.000	0.048	0.803
DAAM2	-0.153	-2.000	0.048	0.803
CKAP2	0.120	1.999	0.048	0.803
CENPB	-0.094	-1.998	0.048	0.803
PFKFB2	-0.116	-1.997	0.048	0.803
ENDOG	-0.102	-1.997	0.048	0.803
FAM160A1	0.082	1.997	0.048	0.803
GRIK2	0.175	1.997	0.048	0.803
DUOX2	-0.115	-1.997	0.048	0.803
AMH	0.068	1.997	0.048	0.803
MID1	-0.085	-1.997	0.048	0.803
IL23R	0.118	1.996	0.048	0.803
AGAP4	0.187	1.996	0.048	0.803
HIST1H2AA	-0.120	-1.996	0.048	0.803
TBC1D14	-0.090	-1.995	0.048	0.803
SLC2A4RG	0.107	1.995	0.048	0.803
ALG1L2	0.135	1.994	0.048	0.803
CDK10	0.145	1.994	0.048	0.803
C1orf112	-0.084	-1.994	0.048	0.803
TLE6	0.077	1.993	0.048	0.803
ZC3H10	0.072	1.992	0.048	0.803
TBC1D29	0.077	1.991	0.049	0.803
PPFIA1	0.065	1.991	0.049	0.803
RNF34	0.141	1.991	0.049	0.803
GPRC5B	-0.071	-1.989	0.049	0.803
ATG14	-0.141	-1.989	0.049	0.803
PCDH18	-0.114	-1.989	0.049	0.803

ERVK13-1	0.159	1.988	0.049	0.803
SLC5A3	-0.114	-1.987	0.049	0.803
DEFB130	0.105	1.987	0.049	0.803
C10orf105	0.092	1.987	0.049	0.803
ALDOB	-0.512	-1.987	0.049	0.803
DLK2	-0.082	-1.987	0.049	0.803
KLHL24	-0.121	-1.987	0.049	0.803
SEH1L	-0.082	-1.986	0.049	0.803
EFNB2	-0.130	-1.986	0.049	0.803
ATP6V1G2-DDX39B	0.099	1.986	0.049	0.803
SLC30A9	-0.149	-1.985	0.049	0.803
OST4	-0.114	-1.985	0.049	0.803
HIST1H1E	-0.191	-1.984	0.049	0.803
OR5AU1	-0.117	-1.984	0.049	0.803
NARS	-0.165	-1.983	0.049	0.803
TMEM91	-0.099	-1.983	0.050	0.803
MIA2	0.105	1.983	0.050	0.803
E2F3	-0.133	-1.982	0.050	0.803
PTK2B	0.083	1.982	0.050	0.803
CTAGE15	0.085	1.982	0.050	0.803
OR4Q2	0.078	1.981	0.050	0.803
ARF4	-0.180	-1.980	0.050	0.803
IMPACT	-0.150	-1.980	0.050	0.803
MRGPRG-AS1	0.090	1.980	0.050	0.803
FAM168B	0.140	1.979	0.050	0.803
RBBP4	-0.173	-1.979	0.050	0.803
LMAN1L	-0.082	-1.979	0.050	0.803
POLR3E	0.137	1.979	0.050	0.803
PGBD1	0.092	1.979	0.050	0.803
GOLGA6L9	0.119	1.979	0.050	0.803

Supplementary Table 5. Genes differentially expressed between patients with high and low signature scores. Differential expression analysis was performed for all genes between patients with high and low signature scores. A total of 1204 genes were differentially expressed, although only *SPP1*, *REXO1L2P* and *ATXN7* remained significant after multiple testing correction. Only significant DEGs are shown. The *Log (fold change)*, the *t-statistic*, the *p-value* and *FDR* are shown for each gene. A *p-value* < 0.05 was considered statistically significant.

Gene set	Collection	*P-value*	*FDR*	*LOG_2 (ERR)*	*ES*	*NES*	Size
Epithelial mesenchymal transition	Hallmark	$1.02 \cdot 10^{-21}$	$2.43 \cdot 10^{-19}$	1.204	-0.548	-2.794	197
Oxidative phosphorylation	Hallmark	$2.59 \cdot 10^{-12}$	$3.09 \cdot 10^{-10}$	0.899	-0.448	-2.283	197
Ribosome	KEGG	$4.67 \cdot 10^{-10}$	$3.72 \cdot 10^{-8}$	0.801	-0.556	-2.520	86
Focal Adhesion	KEGG	$4.07 \cdot 10^{-9}$	$1.94 \cdot 10^{-7}$	0.761	-0.406	-2.076	198
Systemic lupus erythematosus	KEGG	$3.84 \cdot 10^{-9}$	$1.94 \cdot 10^{-7}$	0.761	-0.464	-2.233	129
Myc targets V1	Hallmark	$1.92 \cdot 10^{-8}$	$7.64 \cdot 10^{-7}$	0.734	-0.391	-2.003	199
Alzheimers disease	KEGG	$2.53 \cdot 10^{-7}$	$8.65 \cdot 10^{-6}$	0.675	-0.405	-1.996	158
Oxidative phosphorylation	KEGG	$5.95 \cdot 10^{-7}$	$1.78 \cdot 10^{-5}$	0.659	-0.435	-2.080	124
Coagulation	Hallmark	$1.05 \cdot 10^{-6}$	$2.80 \cdot 10^{-5}$	0.644	-0.409	-1.977	136
ECM receptor interaction	KEGG	$1.25 \cdot 10^{-6}$	$2.98 \cdot 10^{-5}$	0.644	-0.471	-2.106	83
Parkinsons disease	KEGG	$2.48 \cdot 10^{-6}$	$5.39 \cdot 10^{-5}$	0.627	-0.419	-1.996	120
Huntington disease	KEGG	$3.83 \cdot 10^{-6}$	$7.63 \cdot 10^{-5}$	0.611	-0.373	-1.871	173
Angiogenesis	Hallmark	$1.51 \cdot 10^{-5}$	$2.53 \cdot 10^{-4}$	0.593	-0.594	-2.253	36
Apical Junction	Hallmark	$1.59 \cdot 10^{-5}$	$2.53 \cdot 10^{-4}$	0.576	-0.343	-1.753	200
Metabolism of xenobiotics by cytochrome P450	KEGG	$1.40 \cdot 10^{-5}$	$2.53 \cdot 10^{-4}$	0.593	-0.500	-2.118	60
mTORC1 signaling	Hallmark	$2.05 \cdot 10^{-5}$	$3.07 \cdot 10^{-4}$	0.576	-0.339	-1.729	197
Protein Secretion	Hallmark	$3.15 \cdot 10^{-5}$	$4.43 \cdot 10^{-4}$	0.557	-0.418	-1.916	96
Apoptosis	Hallmark	$4.14 \cdot 10^{-5}$	0.001	0.557	-0.356	-1.755	158
Fatty acid metabolism	Hallmark	$5.08 \cdot 10^{-5}$	0.001	0.557	-0.349	-1.717	155
Drug metabolism cytochrome P450	KEGG	$6.37 \cdot 10^{-5}$	0.001	0.538	-0.471	-2.000	62
Complement and coagulation cascades	KEGG	$9.78 \cdot 10^{-5}$	0.001	0.538	-0.442	-1.910	68
Glycolysis	Hallmark	$1.04 \cdot 10^{-4}$	0.001	0.538	-0.326	-1.669	198
Glycolysis and gluconeogenesis	KEGG	$2.51 \cdot 10^{-4}$	0.003	0.498	-0.436	-1.841	61
Hypoxia	Hallmark	$3.04 \cdot 10^{-4}$	0.003	0.498	-0.315	-1.611	196
Valine, leucine and isoleucine degradation	KEGG	0.001	0.006	0.477	-0.487	-1.894	43
Notch signalign pathway	KEGG	0.001	0.008	0.477	0.479	1.847	47
Xenobiotic metabolism	Hallmark	0.002	0.017	0.432	-0.293	-1.500	199
Unfolded protein response	Hallmark	0.002	0.018	0.432	-0.341	-1.591	111
Glutathione metabolism	KEGG	0.002	0.018	0.432	-0.431	-1.726	49
Small cell lung cancer	KEGG	0.002	0.018	0.432	-0.370	-1.660	84
Cadherin binding	GO	0.003	0.020	0.432	-0.257	-1.398	329
Adipogenesis	Hallmark	0.003	0.022	0.432	-0.291	-1.480	194
Pentose and glucuronate interconversions	KEGG	0.003	0.022	0.432	-0.602	-1.879	18
Ascorbate and aldarate metabolism	KEGG	0.004	0.026	0.432	-0.612	-1.873	16
Retinol metabolism	KEGG	0.004	0.030	0.407	-0.400	-1.636	54
Regulation of actin cytoskeleton	KEGG	0.005	0.032	0.407	-0.270	-1.391	211
Arginine and proline metabolism	KEGG	0.005	0.034	0.407	-0.417	-1.701	52
Selenoamino acid metabolism	KEGG	0.006	0.040	0.407	-0.500	-1.777	26
Citrate cycle and TCA cycle	KEGG	0.008	0.046	0.407	-0.477	-1.735	30

Supplementary Table 6. Significantly enriched gene sets in patients with high and low signature scores. Gene set enrichment analysis was performed between patients with high and low signature scores using the differential expression analysis results and multiple gene set collections. A total of 38 gene sets were significantly enriched in low signature score patients, while only 1 was significantly enriched in high signature score patients. Only significantly enriched gene sets are shown. The collection, *p-value*, *FDR*, expected error *LOG_2 (ERR)*, and the raw and normalized enrichment score, as well as the size are shown for each gene set. An *FDR < 0.05* was considered statistically significant.

Population	*Log (FC)*	*t*	*P-value*	*FDR*
Dendritic cells	0.92	3.248	0.001	0.100
Stroma score	-0.23	-2.437	0.016	0.348
naïve B-cells	1.52	2.302	0.023	0.348
Chondrocytes	-1.08	-2.295	0.023	0.348
CD8+ Tcm cells	1.42	2.253	0.026	0.348
B-cells	0.60	2.107	0.037	0.413
Macrophages M1	-0.76	-2.010	0.047	0.413
T regulatory cells	0.43	1.985	0.049	0.413

Supplementary Table 7. Significantly enriched immune and stromal cell populations in high and low signature score patients. The score for 64 immune and stromal cell populations was calculated using gene expression data in xCell. Differential expression analysis of cell population scores was performed between patients with high and low signature scores. A total of 7 populations were differentially expressed between groups, 2 were enriched in low score patients and 5 in high score patients. Additionally, low score patients had significantly increased stromal score. Only cell populations with significantly different scores are shown. The *Log (fold change)*, *t-statistic*, *p-value* and *FDR* are shown for each gene. A *p-value* < 0.05 was considered statistically significant.

Gene symbol	*Log (FC)*	*t*	*P-value*	*FDR*
TMEM41B	0.645	4.297	$1.52 \cdot 10^{-4}$	0.875
TXNDC12	-0.400	-4.200	$2.00 \cdot 10^{-4}$	0.875
OPN3	-0.374	-4.088	$2.74 \cdot 10^{-4}$	0.875
CNNM1	-0.396	-4.087	$2.75 \cdot 10^{-4}$	0.875
JDP2	0.291	3.950	$4.04 \cdot 10^{-4}$	0.875
SLC6A8	-0.449	-3.857	0.001	0.875
HDHD2	-0.444	-3.855	0.001	0.875
RPL17	-0.377	-3.832	0.001	0.875
SULT6B1	0.288	3.829	0.001	0.875
DDX58	0.286	3.813	0.001	0.875
PGRMC2	0.827	3.752	0.001	0.875
FCHSD2	0.321	3.737	0.001	0.875
C4orf27	-0.329	-3.729	0.001	0.875
LAMP5	-0.526	-3.676	0.001	0.875
EPB41L1	0.343	3.659	0.001	0.875
GRM8	-0.344	-3.625	0.001	0.875
C5orf58	-0.279	-3.608	0.001	0.875
SPP1	-0.941	-3.605	0.001	0.875
CAMK2D	0.535	3.583	0.001	0.875
HOXA7	0.351	3.554	0.001	0.875
TBC1D1	0.500	3.546	0.001	0.875
CLDN11	-0.318	-3.532	0.001	0.875
ZNF713	-0.567	-3.517	0.001	0.875
ZNF610	-0.445	-3.517	0.001	0.875

SNN	-0.247	-3.509	0.001	0.875
NT5C2	-0.596	-3.494	0.001	0.875
EPS8L3	0.763	3.488	0.001	0.875
C8orf48	-0.268	-3.483	0.001	0.875
DGAT1	0.456	3.467	0.002	0.875
DLGAP2	-0.314	-3.463	0.002	0.875
HIVEP1	0.519	3.454	0.002	0.875
ZNF543	-0.393	-3.443	0.002	0.875
TPH1	2.197	3.425	0.002	0.875
SLC35A4	-0.310	-3.423	0.002	0.875
ARHGEF10L	0.338	3.409	0.002	0.875
KCNJ5	-0.271	-3.404	0.002	0.875
SLC25A53	-0.486	-3.400	0.002	0.875
EMC7	-0.357	-3.397	0.002	0.875
RPS28	-0.412	-3.392	0.002	0.875
LOC101927844	-0.371	-3.380	0.002	0.875
MGAT4A	0.775	3.372	0.002	0.875
QTRTD1	0.295	3.368	0.002	0.875
IL2RG	0.863	3.342	0.002	0.875
HACD3	-0.325	-3.339	0.002	0.875
ZDHHC4	-0.375	-3.319	0.002	0.875
LEMD1	-0.407	-3.310	0.002	0.875
BECN2	-0.265	-3.293	0.002	0.875
FAM126B	0.362	3.281	0.003	0.875
PPFIBP1	0.471	3.275	0.003	0.875
IQCK	-0.371	-3.272	0.003	0.875
ZNF433	0.340	3.258	0.003	0.875
PPP1R11	0.458	3.256	0.003	0.875
RCAN3	0.394	3.253	0.003	0.875
USP17L17	-0.814	-3.240	0.003	0.875
AP1S2	-0.471	-3.239	0.003	0.875
CHST10	-0.419	-3.230	0.003	0.875
RGS7BP	0.541	3.228	0.003	0.875
XPO4	-0.378	-3.216	0.003	0.875
USP11	-0.387	-3.216	0.003	0.875
NR3C1	0.651	3.215	0.003	0.875
IP6K3	-0.285	-3.213	0.003	0.875
CGB1	0.425	3.210	0.003	0.875
SYT1	-0.452	-3.204	0.003	0.875
LRRC47	0.376	3.202	0.003	0.875
INS	-0.483	-3.196	0.003	0.875
CLDN34	-0.307	-3.196	0.003	0.875
PCDH10	-0.318	-3.168	0.003	0.875
HACE1	-0.285	-3.166	0.003	0.875
RIC8B	-0.426	-3.163	0.003	0.875
AZU1	-0.312	-3.159	0.003	0.875
GPR6	-0.232	-3.158	0.003	0.875

PKIB	0.621	3.155	0.003	0.875
ATXN7	0.403	3.152	0.004	0.875
FAAP20	0.258	3.144	0.004	0.875
OSBPL9	0.302	3.143	0.004	0.875
FRMPD3-AS1	0.257	3.134	0.004	0.875
KPNB1	-0.385	-3.133	0.004	0.875
MOSPD2	0.388	3.125	0.004	0.875
SLC18A1	1.166	3.105	0.004	0.875
SPINK1	-1.498	-3.104	0.004	0.875
SLC7A11	-0.366	-3.103	0.004	0.875
TYMS	-0.282	-3.101	0.004	0.875
ZNF77	-0.290	-3.097	0.004	0.875
SEMG2	-0.304	-3.091	0.004	0.875
MEST	-0.629	-3.088	0.004	0.875
CCDC70	-0.224	-3.077	0.004	0.875
PPP6R3	0.287	3.075	0.004	0.875
SUSD6	0.337	3.062	0.004	0.875
TRIB1	0.371	3.060	0.004	0.875
NCK1	-0.274	-3.058	0.004	0.875
FADS2	-0.486	-3.057	0.004	0.875
TCAF2	-0.330	-3.040	0.005	0.875
F13A1	0.387	3.036	0.005	0.875
EIF4B	-0.429	-3.033	0.005	0.875
RBM4	0.279	3.029	0.005	0.875
ASRGL1	0.399	3.018	0.005	0.875
BAIAP3	-0.273	-3.012	0.005	0.875
HPS4	-0.572	-3.010	0.005	0.875
PDLIM1	0.404	3.007	0.005	0.875
STXBP5L	0.577	3.005	0.005	0.875
SOBP	0.493	2.998	0.005	0.875
TMEM135	0.292	2.995	0.005	0.875
TM2D2	-0.289	-2.993	0.005	0.875
GMDS	0.398	2.990	0.005	0.875
COX11	-0.323	-2.987	0.005	0.875
CPB1	-2.186	-2.983	0.005	0.875
GPR119	-0.487	-2.978	0.006	0.875
KCNE1	-0.277	-2.977	0.006	0.875
CPPED1	0.212	2.976	0.006	0.875
SLC38A11	1.283	2.973	0.006	0.875
PCP4	-1.057	-2.973	0.006	0.875
VN1R1	-0.336	-2.972	0.006	0.875
ZNF398	-0.189	-2.966	0.006	0.875
P3H4	0.220	2.964	0.006	0.875
ALG13	0.304	2.958	0.006	0.875
UBA7	0.476	2.956	0.006	0.875
ZNF331	0.378	2.955	0.006	0.875
GOLGA6D	-0.299	-2.954	0.006	0.875

WDR54	-0.268	-2.952	0.006	0.875
CPT1B	-0.402	-2.951	0.006	0.875
ELP2	0.206	2.948	0.006	0.875
GJA3	-0.338	-2.947	0.006	0.875
GPR137	0.335	2.944	0.006	0.875
CCDC66	0.303	2.939	0.006	0.875
RBMY1F	-0.221	-2.939	0.006	0.875
RGR	-0.310	-2.937	0.006	0.875
MYO3A	-0.404	-2.931	0.006	0.875
KANK1	-0.429	-2.926	0.006	0.875
SLC22A17	0.255	2.922	0.006	0.875
MTRNR2L13	0.243	2.919	0.006	0.875
TMEM74B	0.353	2.918	0.006	0.875
RAF1	0.252	2.917	0.006	0.875
ADRB2	0.243	2.917	0.006	0.875
GPR19	-0.486	-2.913	0.006	0.875
CAMK2N1	0.492	2.913	0.006	0.875
EDN2	-0.414	-2.910	0.007	0.875
GPR89B	-0.406	-2.905	0.007	0.875
DBI	0.553	2.901	0.007	0.875
HIST1H2AC	0.229	2.899	0.007	0.875
ZNF536	-0.371	-2.895	0.007	0.875
OS9	-0.308	-2.893	0.007	0.875
NUDT4	-0.396	-2.890	0.007	0.875
TBRG1	0.356	2.877	0.007	0.875
SLC38A1	0.914	2.867	0.007	0.875
FAHD1	-0.227	-2.860	0.007	0.875
SPRED3	-0.426	-2.860	0.007	0.875
LDB2	-0.301	-2.857	0.007	0.875
ATP2B3	-0.229	-2.857	0.007	0.875
BARX2	0.277	2.855	0.008	0.875
ZNF182	-0.251	-2.855	0.008	0.875
MLEC	-0.323	-2.851	0.008	0.875
PLA2G10	0.305	2.851	0.008	0.875
TMEM145	-0.311	-2.843	0.008	0.875
SNTG1	0.310	2.842	0.008	0.875
ASXL2	-0.278	-2.836	0.008	0.875
STON2	0.297	2.835	0.008	0.875
UFSP2	-0.402	-2.831	0.008	0.875
FAM153A	0.265	2.831	0.008	0.875
SCIMP	-0.328	-2.827	0.008	0.875
TMEM8B	0.293	2.825	0.008	0.875
CD82	0.374	2.824	0.008	0.875
DDX39B	-0.544	-2.820	0.008	0.875
URI1	-0.329	-2.819	0.008	0.875
FAM120AOS	0.471	2.817	0.008	0.875
SH3RF3	-0.230	-2.816	0.008	0.875

DPCD	-0.341	-2.815	0.008	0.875
HEATR3	-0.294	-2.803	0.009	0.875
APCDD1	-0.531	-2.802	0.009	0.875
F10	-0.259	-2.796	0.009	0.875
AMHR2	0.260	2.795	0.009	0.875
ANKRA2	-0.365	-2.795	0.009	0.875
COL27A1	-0.507	-2.794	0.009	0.875
AFAP1L1	-0.223	-2.791	0.009	0.875
AASDH	-0.305	-2.787	0.009	0.875
CFAP74	-0.266	-2.786	0.009	0.875
OR7G1	-0.226	-2.786	0.009	0.875
ZNF594	-0.302	-2.784	0.009	0.875
TXNDC2	-0.215	-2.782	0.009	0.875
SV2B	-0.302	-2.781	0.009	0.875
ADGRG4	0.788	2.780	0.009	0.875
HFM1	-0.243	-2.775	0.009	0.875
PIGM	-0.416	-2.773	0.009	0.875
DLL1	-0.344	-2.772	0.009	0.875
SLC35E1	-0.241	-2.771	0.009	0.875
NBPF15	-0.249	-2.771	0.009	0.875
SRD5A3	-0.192	-2.770	0.009	0.875
TMEM132C	-0.378	-2.765	0.009	0.875
FAM21A	-0.371	-2.760	0.009	0.875
CNOT6L	0.265	2.757	0.010	0.875
TNFRSF11B	0.519	2.756	0.010	0.875
HIGD1B	-0.572	-2.755	0.010	0.875
PCNXL4	0.229	2.754	0.010	0.875
PNN	0.351	2.752	0.010	0.875
CCDC68	0.411	2.748	0.010	0.875
C16orf59	-0.232	-2.741	0.010	0.875
FAM179B	-0.285	-2.733	0.010	0.875
CHGA	1.060	2.729	0.010	0.875
C16orf45	0.320	2.728	0.010	0.875
MANF	0.171	2.725	0.010	0.875
RASA2	0.311	2.724	0.010	0.875
TTLL9	-0.306	-2.723	0.010	0.875
CNTN4	0.359	2.723	0.010	0.875
VCX2	-0.343	-2.722	0.010	0.875
C6orf52	0.315	2.719	0.010	0.875
GBP3	0.410	2.717	0.011	0.875
PITPNB	0.368	2.717	0.011	0.875
RRP15	-0.429	-2.717	0.011	0.875
ADGRG1	-0.644	-2.716	0.011	0.875
ZHX1-C8orf76	0.258	2.708	0.011	0.875
SLC12A5	-0.334	-2.707	0.011	0.875
ABCB5	-0.215	-2.707	0.011	0.875
ACO2	0.309	2.700	0.011	0.875

SRI	-0.355	-2.700	0.011	0.875
GABRG2	-0.327	-2.700	0.011	0.875
NFATC2IP	0.514	2.697	0.011	0.875
FAM151B	-0.421	-2.697	0.011	0.875
PDRG1	-0.211	-2.691	0.011	0.875
CACNA1G	-0.340	-2.690	0.011	0.875
PRMT8	-0.250	-2.688	0.011	0.875
HRASLS	0.786	2.688	0.011	0.875
KLHL24	0.314	2.687	0.011	0.875
LOC441155	-0.305	-2.687	0.011	0.875
KIAA0391	-0.289	-2.683	0.011	0.875
C2CD2	-0.282	-2.683	0.011	0.875
OCA2	-0.206	-2.681	0.012	0.875
DCAF4	-0.347	-2.681	0.012	0.875
DNTT	-0.276	-2.680	0.012	0.875
CREB3L1	0.263	2.680	0.012	0.875
KLF5	0.652	2.679	0.012	0.875
WBP2NL	0.295	2.679	0.012	0.875
LRRC43	-0.381	-2.672	0.012	0.875
GSR	0.329	2.672	0.012	0.875
PCDHB5	-0.270	-2.669	0.012	0.875
C7orf62	-0.333	-2.667	0.012	0.875
DRD1	-0.296	-2.665	0.012	0.875
RPAP3	-0.224	-2.665	0.012	0.875
MUC22	0.357	2.663	0.012	0.875
KRT23	-0.412	-2.662	0.012	0.875
C4orf33	0.256	2.660	0.012	0.875
GALNT9	-0.216	-2.659	0.012	0.875
C19orf44	-0.263	-2.658	0.012	0.875
ARHGEF11	-0.229	-2.653	0.012	0.875
NUCB2	-0.357	-2.652	0.012	0.875
HMG20A	0.442	2.652	0.012	0.875
TWISTNB	-0.249	-2.651	0.012	0.875
NUDCD3	-0.269	-2.650	0.012	0.875
SENP5	0.314	2.646	0.013	0.875
NUTF2	-0.233	-2.646	0.013	0.875
DYNC2H1	-0.310	-2.645	0.013	0.875
BRWD3	-0.180	-2.644	0.013	0.875
OR2AG2	-0.183	-2.643	0.013	0.875
GP1BB	0.323	2.631	0.013	0.875
RAP1A	0.301	2.630	0.013	0.875
PLPPR4	-0.428	-2.629	0.013	0.875
KRTAP29-1	-0.260	-2.628	0.013	0.875
OFD1	-0.512	-2.627	0.013	0.875
ATAD3C	-0.308	-2.626	0.013	0.875
QPCT	-0.649	-2.621	0.013	0.875
DMBX1	-0.214	-2.619	0.013	0.875

TRMT1	-0.537	-2.616	0.013	0.875
CDC14B	-0.352	-2.614	0.014	0.875
CCDC93	-0.569	-2.613	0.014	0.875
KHDC1L	-0.235	-2.613	0.014	0.875
WIF1	-0.261	-2.612	0.014	0.875
SPDYE1	0.438	2.611	0.014	0.875
PGBD5	-0.299	-2.610	0.014	0.875
MOV10	0.262	2.609	0.014	0.875
EFHD2	0.242	2.607	0.014	0.875
ANKRD36C	0.689	2.607	0.014	0.875
FKBP5	-0.337	-2.606	0.014	0.875
TEX26	0.205	2.605	0.014	0.875
BEAN1-AS1	0.467	2.604	0.014	0.875
PDCD6IP	0.178	2.603	0.014	0.875
BBIP1	0.488	2.602	0.014	0.875
EML1	-0.333	-2.601	0.014	0.875
FANCA	-0.262	-2.599	0.014	0.875
KCNG3	0.232	2.597	0.014	0.875
C20orf196	-0.354	-2.595	0.014	0.875
ZNF292	0.199	2.592	0.014	0.875
LINC01205	0.315	2.592	0.014	0.875
CDCA7	-0.244	-2.590	0.014	0.875
PDCL2	0.187	2.588	0.014	0.875
PRUNE2	0.318	2.587	0.014	0.875
IGDCC3	-0.227	-2.587	0.014	0.875
OBP2A	-0.286	-2.584	0.015	0.875
GPR18	0.338	2.582	0.015	0.875
CBR1	0.635	2.581	0.015	0.875
RARRES3	0.318	2.580	0.015	0.875
SCAF1	0.203	2.580	0.015	0.875
DRAM2	0.226	2.577	0.015	0.875
CD8B	0.190	2.575	0.015	0.875
SBK3	-0.316	-2.573	0.015	0.875
MNX1	0.460	2.572	0.015	0.875
SPATS2L	0.404	2.571	0.015	0.875
C5orf28	-0.202	-2.570	0.015	0.875
ZNF404	-0.350	-2.569	0.015	0.875
C20orf195	-0.230	-2.567	0.015	0.875
TMEM237	-0.330	-2.566	0.015	0.875
FAM229B	-0.272	-2.565	0.015	0.875
THUMPD1	-0.241	-2.562	0.015	0.875
EFHC1	-0.200	-2.561	0.015	0.875
CDCA7L	-0.520	-2.558	0.015	0.875
STAP1	0.259	2.554	0.016	0.875
COG4	-0.374	-2.551	0.016	0.875
EGR1	0.604	2.550	0.016	0.875
KCNA5	-0.236	-2.550	0.016	0.875

ZNF217	0.292	2.549	0.016	0.875
PBDC1	-0.287	-2.549	0.016	0.875
ZNF850	-0.375	-2.548	0.016	0.875
C1orf185	-0.172	-2.546	0.016	0.875
RNF43	-0.232	-2.545	0.016	0.875
C1QTNF8	-0.217	-2.545	0.016	0.875
ASAP3	0.392	2.544	0.016	0.875
DLX6	-0.259	-2.544	0.016	0.875
MICU2	0.210	2.542	0.016	0.875
ARL8B	0.358	2.540	0.016	0.875
ESRRG	-0.508	-2.538	0.016	0.875
SDF2	0.220	2.534	0.016	0.875
CETN2	-0.467	-2.534	0.016	0.875
DUT	0.305	2.532	0.016	0.875
GPM6A	0.354	2.531	0.016	0.875
C11orf87	-0.339	-2.530	0.017	0.875
CCNB2	-0.322	-2.527	0.017	0.875
MED31	-0.339	-2.527	0.017	0.875
MUSTN1	0.218	2.524	0.017	0.875
NCR3LG1	-0.281	-2.523	0.017	0.875
STAMBP	0.267	2.522	0.017	0.875
TRIM4	-0.216	-2.521	0.017	0.875
MBOAT4	-0.316	-2.520	0.017	0.875
DYNLT3	-0.245	-2.520	0.017	0.875
IL3RA	-0.219	-2.518	0.017	0.875
YIPF6	-0.235	-2.518	0.017	0.875
ANKRD20A3	-0.436	-2.515	0.017	0.875
ANKRD2	0.215	2.514	0.017	0.875
DDT	0.310	2.514	0.017	0.875
C12orf77	-0.283	-2.512	0.017	0.875
PTPRB	-0.233	-2.511	0.017	0.875
APOBEC3B	-0.214	-2.509	0.017	0.875
PRR13	0.305	2.509	0.017	0.875
CMPK1	0.213	2.508	0.017	0.875
FARSB	-0.267	-2.506	0.018	0.875
SETD2	0.398	2.503	0.018	0.875
ABCA7	-0.318	-2.502	0.018	0.875
CCT4	-0.292	-2.499	0.018	0.875
ZC3HAV1	0.324	2.498	0.018	0.875
SLC19A1	-0.277	-2.498	0.018	0.875
WDR7	0.381	2.498	0.018	0.875
PNLIP	-1.385	-2.498	0.018	0.875
ZNRF4	0.298	2.497	0.018	0.875
PITX2	0.311	2.497	0.018	0.875
WWOX	0.430	2.497	0.018	0.875
CXCL6	-0.171	-2.497	0.018	0.875
ADSS	0.385	2.495	0.018	0.875

ZFAND1	0.323	2.494	0.018	0.875
MELK	0.188	2.493	0.018	0.875
CHRNA3	-0.286	-2.493	0.018	0.875
ZDHHC17	-0.417	-2.491	0.018	0.875
ZNF473	-0.300	-2.491	0.018	0.875
LCOR	-0.286	-2.488	0.018	0.875
FHIT	-0.199	-2.488	0.018	0.875
SRA1	0.232	2.487	0.018	0.875
UBP1	0.253	2.486	0.018	0.875
MRPS25	0.340	2.486	0.018	0.875
FAM210A	-0.368	-2.486	0.018	0.875
APOBEC1	0.264	2.485	0.018	0.875
TBC1D23	-0.172	-2.484	0.018	0.875
CLU	-0.640	-2.483	0.018	0.875
LDLRAD3	-0.251	-2.482	0.019	0.875
FASTK	0.264	2.480	0.019	0.875
CERS4	0.289	2.480	0.019	0.875
BBS7	-0.299	-2.479	0.019	0.875
ATP5L	0.352	2.478	0.019	0.875
TMEM178B	-0.225	-2.476	0.019	0.875
SLC7A1	-0.280	-2.476	0.019	0.875
DNPEP	0.206	2.475	0.019	0.875
ARAP2	0.230	2.475	0.019	0.875
NGLY1	0.322	2.473	0.019	0.875
VWA3A	-0.261	-2.473	0.019	0.875
FHAD1	-0.223	-2.473	0.019	0.875
MOB3B	0.348	2.472	0.019	0.875
CDH9	-0.312	-2.471	0.019	0.875
MBD3L1	0.260	2.470	0.019	0.875
ANOS1	-0.306	-2.469	0.019	0.875
HTN3	-0.216	-2.469	0.019	0.875
PRSS3	-0.937	-2.464	0.019	0.875
NR4A2	0.552	2.462	0.019	0.875
CACNA1I	-0.281	-2.462	0.019	0.875
MIS18BP1	-0.222	-2.462	0.019	0.875
SKAP2	0.311	2.459	0.020	0.875
ZCCHC8	-0.412	-2.458	0.020	0.875
SIAH2	0.191	2.458	0.020	0.875
PDZD11	-0.299	-2.454	0.020	0.875
TIRAP	-0.265	-2.454	0.020	0.875
PLVAP	-0.216	-2.454	0.020	0.875
CBX7	0.494	2.452	0.020	0.875
IKBKB	0.218	2.452	0.020	0.875
GABRB1	-0.310	-2.452	0.020	0.875
COCH	0.255	2.451	0.020	0.875
ZFY	-0.230	-2.449	0.020	0.875
CRY2	0.232	2.448	0.020	0.875

B3GALT5	-0.211	-2.448	0.020	0.875
RRH	-0.313	-2.446	0.020	0.875
GRIA4	0.719	2.446	0.020	0.875
MED1	-0.291	-2.444	0.020	0.875
MRLN	0.266	2.441	0.020	0.875
ARMC7	0.202	2.441	0.020	0.875
STX7	0.361	2.440	0.020	0.875
MICA	-0.212	-2.440	0.020	0.875
LCE3B	-0.269	-2.440	0.020	0.875
RIPPLY3	-0.267	-2.439	0.020	0.875
CCNH	0.432	2.438	0.021	0.875
POLR2K	0.338	2.436	0.021	0.875
MAPKAPK3	0.230	2.436	0.021	0.875
EDA2R	0.188	2.435	0.021	0.875
NMT2	0.284	2.435	0.021	0.875
OR5B21	-0.206	-2.431	0.021	0.875
LAMTOR1	0.236	2.429	0.021	0.875
MED30	0.152	2.426	0.021	0.875
STXBP6	-0.282	-2.426	0.021	0.875
CTNNBL1	-0.391	-2.425	0.021	0.875
TES	0.376	2.425	0.021	0.875
TM9SF4	-0.322	-2.423	0.021	0.875
ADAL	-0.179	-2.423	0.021	0.875
CDK5RAP1	-0.229	-2.423	0.021	0.875
TEAD4	-0.216	-2.422	0.021	0.875
ADORA2B	-0.215	-2.421	0.021	0.875
TSEN15	0.235	2.420	0.021	0.875
CES4A	-0.361	-2.418	0.021	0.875
LRRN1	-0.227	-2.416	0.022	0.875
MYBPC1	0.231	2.415	0.022	0.875
ADD1	0.290	2.414	0.022	0.875
CNTNAP5	0.507	2.414	0.022	0.875
SLC25A27	0.664	2.413	0.022	0.875
ATP8A1	-0.233	-2.411	0.022	0.875
RAB1A	-0.252	-2.410	0.022	0.875
RELA	0.348	2.410	0.022	0.875
CCDC187	0.208	2.409	0.022	0.875
ADGRG3	-0.288	-2.409	0.022	0.875
OR4F17	-0.298	-2.405	0.022	0.875
COLQ	-0.402	-2.405	0.022	0.875
TMEM45B	-0.400	-2.403	0.022	0.875
KSR1	-0.221	-2.402	0.022	0.875
POLI	-0.312	-2.401	0.022	0.875
RCC2	-0.169	-2.399	0.022	0.875
RAB5A	0.450	2.399	0.022	0.875
TMEM163	-0.350	-2.398	0.023	0.875
SLC30A5	0.645	2.397	0.023	0.875

ZNF883	-0.361	-2.397	0.023	0.875
CPA1	-1.179	-2.396	0.023	0.875
SORCS2	0.324	2.396	0.023	0.875
NIPAL2	-0.328	-2.395	0.023	0.875
TEX264	-0.193	-2.393	0.023	0.875
TXNDC16	-0.192	-2.393	0.023	0.875
CARD6	0.209	2.393	0.023	0.875
SEZ6	-0.199	-2.389	0.023	0.875
C11orf70	-0.382	-2.389	0.023	0.875
RBM7	0.244	2.388	0.023	0.875
OPTN	0.231	2.388	0.023	0.875
PAFAH1B1	-0.315	-2.387	0.023	0.875
XKR7	-0.250	-2.387	0.023	0.875
PNMT	-0.230	-2.386	0.023	0.875
CDCA5	-0.245	-2.386	0.023	0.875
GRIK4	-0.248	-2.385	0.023	0.875
MCTS1	0.244	2.384	0.023	0.875
SPACA5	-0.955	-2.384	0.023	0.875
ATP6V1B2	0.307	2.384	0.023	0.875
NDUFS4	0.224	2.383	0.023	0.875
KLK12	0.254	2.381	0.023	0.875
MSANTD4	-0.297	-2.380	0.023	0.875
NIPAL3	0.486	2.380	0.023	0.875
RAD23B	-0.334	-2.380	0.023	0.875
DHX16	0.248	2.379	0.024	0.875
USP30	-0.634	-2.378	0.024	0.875
CEACAM16	-0.237	-2.377	0.024	0.875
TMEM203	-0.212	-2.377	0.024	0.875
PSG6	-0.179	-2.377	0.024	0.875
HCAR3	0.207	2.376	0.024	0.875
TMEM63A	0.462	2.376	0.024	0.875
CLN8	-0.196	-2.375	0.024	0.875
ANKEF1	-0.240	-2.375	0.024	0.875
LMX1A	0.319	2.374	0.024	0.875
RUNX1T1	0.476	2.373	0.024	0.875
PRKD2	-0.275	-2.373	0.024	0.875
HPCA	0.186	2.373	0.024	0.875
SLC22A15	-0.179	-2.373	0.024	0.875
DTD2	-0.213	-2.373	0.024	0.875
ZNF99	-0.202	-2.372	0.024	0.875
SUPT4H1	-0.244	-2.371	0.024	0.875
TMEM165	-0.271	-2.369	0.024	0.875
GTF2E2	0.302	2.368	0.024	0.875
CYB5R1	-0.259	-2.367	0.024	0.875
TRIP11	-0.257	-2.367	0.024	0.875
SOX10	0.277	2.367	0.024	0.875
CCDC65	-0.248	-2.366	0.024	0.875

SCAMP2	0.163	2.365	0.024	0.875
C15orf38-AP3S2	-0.274	-2.365	0.024	0.875
TBR1	0.208	2.365	0.024	0.875
U2SURP	0.408	2.364	0.024	0.875
STK17B	0.380	2.363	0.024	0.875
FUT4	0.190	2.360	0.025	0.875
VEGFB	0.293	2.359	0.025	0.875
LANCL2	-0.288	-2.356	0.025	0.875
CLDN10	-0.750	-2.356	0.025	0.875
MRPL33	0.267	2.353	0.025	0.875
NSUN5	0.163	2.353	0.025	0.875
CDK7	-0.302	-2.353	0.025	0.875
PTCD1	0.342	2.352	0.025	0.875
BRI3	0.248	2.351	0.025	0.875
RAD18	0.485	2.351	0.025	0.875
METTL9	0.353	2.351	0.025	0.875
SCD5	-0.268	-2.350	0.025	0.875
TRPC4	-0.313	-2.350	0.025	0.875
PCSK1N	0.355	2.349	0.025	0.875
TMC3	-0.222	-2.347	0.025	0.875
FAM27L	-0.259	-2.347	0.025	0.875
GPAT3	0.255	2.347	0.025	0.875
LIPE	0.221	2.346	0.025	0.875
RAB17	-0.313	-2.346	0.025	0.875
DRC3	0.241	2.345	0.025	0.875
SLC39A6	-0.565	-2.345	0.025	0.875
SETMAR	0.170	2.344	0.025	0.875
TP53BP1	-0.278	-2.343	0.026	0.875
CSNK1D	-0.237	-2.343	0.026	0.875
IKZF1	0.377	2.342	0.026	0.875
XPOT	0.214	2.340	0.026	0.875
CCDC122	-0.224	-2.339	0.026	0.875
FBXO15	-0.253	-2.339	0.026	0.875
RNF41	-0.171	-2.335	0.026	0.875
FOXA1	0.433	2.334	0.026	0.875
WTIP	0.187	2.333	0.026	0.875
UBE2F	0.337	2.333	0.026	0.875
ETV7	-0.178	-2.332	0.026	0.875
GOLGA1	-0.217	-2.330	0.026	0.875
AXDND1	-0.246	-2.330	0.026	0.875
PPIP5K2	-0.367	-2.328	0.026	0.875
CAAP1	-0.227	-2.327	0.026	0.875
FBXW8	-0.233	-2.327	0.026	0.875
LUZP1	0.300	2.327	0.026	0.875
RP11-998D10.7	0.195	2.325	0.027	0.875
OR2A25	-0.271	-2.325	0.027	0.875
FRG1	-0.425	-2.324	0.027	0.875

IL13RA2	-0.583	-2.324	0.027	0.875
VSIG4	0.299	2.323	0.027	0.875
BBS5	-0.209	-2.323	0.027	0.875
RGS17	0.306	2.319	0.027	0.875
YIPF7	0.164	2.319	0.027	0.875
RHOD	-0.299	-2.318	0.027	0.875
PYM1	0.340	2.318	0.027	0.875
POLR3C	-0.256	-2.318	0.027	0.875
NACAD	-0.339	-2.317	0.027	0.875
ARL5B	0.405	2.316	0.027	0.875
RNF4	-0.229	-2.316	0.027	0.875
CLEC5A	0.164	2.316	0.027	0.875
GPR160	0.667	2.316	0.027	0.875
MPC1L	0.186	2.315	0.027	0.875
FAM65B	-0.416	-2.314	0.027	0.875
FAM83F	-0.289	-2.313	0.027	0.875
GZF1	0.275	2.313	0.027	0.875
PFKFB4	-0.528	-2.313	0.027	0.875
COX4I1	0.305	2.313	0.027	0.875
CHCHD7	-0.332	-2.313	0.027	0.875
TRNAU1AP	0.266	2.312	0.027	0.875
TRAK1	0.209	2.311	0.027	0.875
PTBP1	-0.250	-2.311	0.027	0.875
TPI1	-0.266	-2.310	0.028	0.875
ARF6	0.309	2.309	0.028	0.875
USF3	0.258	2.308	0.028	0.875
PLEKHG4	-0.232	-2.307	0.028	0.875
KL	-0.514	-2.307	0.028	0.875
ZMAT4	0.365	2.306	0.028	0.875
FNDC9	0.176	2.306	0.028	0.875
SOS2	0.179	2.306	0.028	0.875
MUC4	-0.240	-2.304	0.028	0.875
TIGD1	0.172	2.303	0.028	0.875
IDNK	0.253	2.302	0.028	0.875
PROSER2	-0.163	-2.302	0.028	0.875
MSI1	-0.303	-2.301	0.028	0.875
NPIPB5	0.376	2.300	0.028	0.875
RCHY1	0.148	2.300	0.028	0.875
MSANTD3	-0.320	-2.299	0.028	0.875
RPS20	0.540	2.298	0.028	0.875
EGLN3	-0.308	-2.298	0.028	0.875
RCAN2	0.356	2.297	0.028	0.875
SH3GL1	-0.270	-2.297	0.028	0.875
CLCA1	0.557	2.296	0.028	0.875
C2orf72	0.259	2.296	0.028	0.875
TXNRD3	-0.271	-2.295	0.028	0.875
ERV3-1	0.415	2.295	0.028	0.875

PTH1R	-0.327	-2.293	0.029	0.875
SCGB1C1	-0.250	-2.292	0.029	0.875
NPHP4	-0.270	-2.292	0.029	0.875
QDPR	0.493	2.292	0.029	0.875
ARFGEF3	-0.406	-2.292	0.029	0.875
BHLHB9	-0.251	-2.291	0.029	0.875
RAP2C	-0.272	-2.291	0.029	0.875
RENBP	-0.234	-2.290	0.029	0.875
RNASE2	-0.234	-2.290	0.029	0.875
RND3	0.209	2.288	0.029	0.875
KARS	0.304	2.287	0.029	0.875
YWHAZ	-0.350	-2.287	0.029	0.875
KRT6A	-0.234	-2.286	0.029	0.875
FREM3	-0.263	-2.286	0.029	0.875
FAM73B	0.230	2.285	0.029	0.875
NUP214	-0.303	-2.284	0.029	0.875
AMTN	-0.225	-2.283	0.029	0.875
MCTP1	0.370	2.280	0.029	0.875
PCM1	0.282	2.280	0.029	0.875
FLT3	-0.202	-2.280	0.029	0.875
FAM220A	-0.234	-2.280	0.029	0.875
OR5F1	-0.260	-2.279	0.029	0.875
PIK3CB	0.187	2.278	0.030	0.875
SSR4	-0.357	-2.277	0.030	0.875
DMRT2	-0.210	-2.276	0.030	0.875
GALNT10	0.338	2.275	0.030	0.875
EZH2	0.178	2.274	0.030	0.875
TBX2	-0.241	-2.274	0.030	0.875
TFCP2L1	-0.323	-2.273	0.030	0.875
ALOX5	0.207	2.273	0.030	0.875
EDDM3B	-0.203	-2.273	0.030	0.875
C7orf60	-0.379	-2.272	0.030	0.875
LRIG2	-0.253	-2.272	0.030	0.875
BRD9	-0.185	-2.270	0.030	0.875
PHACTR4	0.189	2.268	0.030	0.875
BOK	0.182	2.268	0.030	0.875
ILDR1	-0.218	-2.268	0.030	0.875
CHCHD10	0.263	2.268	0.030	0.875
LINC00934	-0.204	-2.268	0.030	0.875
ATP6V1B1	0.186	2.267	0.030	0.875
NABP1	0.185	2.267	0.030	0.875
ALDH1B1	-0.194	-2.266	0.030	0.875
ZBTB24	-0.207	-2.266	0.030	0.875
IL26	-0.141	-2.264	0.030	0.875
CRHR2	-0.199	-2.264	0.031	0.875
CKAP4	-0.352	-2.263	0.031	0.875
PRKCSH	-0.333	-2.263	0.031	0.875

CTPS2	0.204	2.263	0.031	0.875
UBE2E2	0.376	2.262	0.031	0.875
PRSS1	-0.933	-2.262	0.031	0.875
C9orf114	-0.201	-2.261	0.031	0.875
OR8S1	0.156	2.261	0.031	0.875
ZSWIM3	-0.236	-2.260	0.031	0.875
SLC45A1	-0.219	-2.259	0.031	0.875
CUX1	0.406	2.259	0.031	0.875
PDE8B	-0.360	-2.258	0.031	0.875
CECR5	-0.169	-2.258	0.031	0.875
MCOLN3	-0.204	-2.257	0.031	0.875
DKK4	-0.730	-2.256	0.031	0.875
NCOR1	0.387	2.255	0.031	0.875
FCF1	0.503	2.255	0.031	0.875
COMMD10	-0.300	-2.255	0.031	0.875
COL8A1	0.217	2.254	0.031	0.875
RAPSN	0.216	2.254	0.031	0.875
DHX38	-0.308	-2.254	0.031	0.875
NUFIP1	-0.269	-2.252	0.031	0.875
OR52K2	-0.356	-2.252	0.031	0.875
ARID2	-0.258	-2.252	0.031	0.875
MEX3C	0.284	2.251	0.031	0.875
BLOC1S2	-0.253	-2.250	0.031	0.875
FAAP100	-0.190	-2.249	0.032	0.875
RPL27A	0.242	2.249	0.032	0.875
ZNF221	-0.226	-2.249	0.032	0.875
PARD6A	-0.239	-2.249	0.032	0.875
RPL8	0.335	2.248	0.032	0.875
SPAST	-0.220	-2.247	0.032	0.875
CSF3	0.165	2.247	0.032	0.875
MYCBP	-0.437	-2.246	0.032	0.875
STK32A	0.196	2.245	0.032	0.875
ATF6	-0.334	-2.245	0.032	0.875
MYADM	0.242	2.244	0.032	0.875
EIF2B1	-0.186	-2.244	0.032	0.875
ANKRD44	0.285	2.244	0.032	0.875
PEBP1	0.507	2.244	0.032	0.875
OCM	-0.266	-2.242	0.032	0.875
IK	0.358	2.241	0.032	0.875
ABTB1	0.248	2.240	0.032	0.875
ESPN	0.184	2.240	0.032	0.875
SNX11	0.277	2.239	0.032	0.875
SYNJ2	-0.287	-2.238	0.032	0.875
ARGLU1	0.672	2.237	0.032	0.875
PDXDC2P	0.604	2.237	0.032	0.875
ZNF707	-0.247	-2.237	0.032	0.875
CNOT7	0.241	2.236	0.033	0.875

BRK1	0.213	2.235	0.033	0.875
TACC2	0.217	2.234	0.033	0.875
ZFP42	0.146	2.234	0.033	0.875
EXD1	-0.178	-2.233	0.033	0.875
IL15	0.225	2.231	0.033	0.875
ZNF227	-0.456	-2.231	0.033	0.875
PTOV1	-0.268	-2.231	0.033	0.875
YBX3	0.312	2.230	0.033	0.875
GRAMD1A	0.245	2.230	0.033	0.875
CA2	0.283	2.229	0.033	0.875
GCLC	-0.280	-2.229	0.033	0.875
BIRC8	-0.181	-2.228	0.033	0.875
GLYATL2	0.165	2.227	0.033	0.875
ZBTB34	-0.201	-2.226	0.033	0.875
OR4E1	0.168	2.226	0.033	0.875
RHBG	-0.309	-2.224	0.033	0.875
TRAPPC11	-0.280	-2.223	0.033	0.875
PCK2	0.202	2.222	0.033	0.875
TCEB3	0.254	2.222	0.033	0.875
EZR	0.460	2.222	0.034	0.875
FOSB	0.439	2.219	0.034	0.875
CUL1	-0.231	-2.219	0.034	0.875
MPP6	-0.281	-2.219	0.034	0.875
PCDHB15	-0.218	-2.218	0.034	0.875
CFAP47	-0.162	-2.218	0.034	0.875
AGT	-0.893	-2.216	0.034	0.875
RPL13	0.227	2.215	0.034	0.875
NSD1	-0.210	-2.213	0.034	0.875
CYB5B	0.353	2.213	0.034	0.875
TUBB6	0.224	2.213	0.034	0.875
TRPM5	-0.232	-2.213	0.034	0.875
OR4F3	0.225	2.212	0.034	0.875
PSMD12	0.206	2.212	0.034	0.875
ZNF772	-0.248	-2.211	0.034	0.875
KRTCAP3	0.270	2.209	0.034	0.875
CACNA1A	-0.536	-2.208	0.035	0.875
OR10J5	-0.178	-2.207	0.035	0.875
ZNF175	-0.177	-2.207	0.035	0.875
ARL15	0.236	2.206	0.035	0.875
NDUFB4	0.325	2.205	0.035	0.875
MMEL1	-0.191	-2.204	0.035	0.875
U2AF1	0.229	2.204	0.035	0.875
MAN2A1	0.415	2.203	0.035	0.875
BCL3	0.261	2.203	0.035	0.875
KIF13B	0.297	2.203	0.035	0.875
ZNF277	0.153	2.202	0.035	0.875
TLK1	0.252	2.201	0.035	0.875

SRSF7	0.287	2.201	0.035	0.875
IKBKE	-0.258	-2.201	0.035	0.875
PPAT	-0.305	-2.200	0.035	0.875
TRMT112	0.249	2.200	0.035	0.875
SLC25A11	-0.211	-2.200	0.035	0.875
POU4F2	0.178	2.200	0.035	0.875
CD300E	-0.243	-2.200	0.035	0.875
RALB	-0.316	-2.199	0.035	0.875
OSTC	-0.283	-2.198	0.035	0.875
PNPLA1	-0.229	-2.198	0.035	0.875
KLF4	0.282	2.196	0.035	0.875
CPXCR1	-0.147	-2.196	0.035	0.875
PRSS16	-0.257	-2.196	0.035	0.875
ADAMTSL4	0.307	2.194	0.036	0.875
RIMKLA	-0.182	-2.194	0.036	0.875
RBMX2	-0.250	-2.193	0.036	0.875
SSBP3	0.301	2.192	0.036	0.875
TRIM27	0.323	2.192	0.036	0.875
SPOP	0.285	2.192	0.036	0.875
FLCN	0.238	2.192	0.036	0.875
SNX2	0.518	2.190	0.036	0.875
AGTPBP1	0.208	2.190	0.036	0.875
C16orf74	-0.243	-2.190	0.036	0.875
CDC42BPB	0.280	2.190	0.036	0.875
FFAR2	-0.261	-2.189	0.036	0.875
KDM5D	-0.294	-2.189	0.036	0.875
NAPA	0.335	2.188	0.036	0.875
ACHE	-0.192	-2.188	0.036	0.875
GABPA	0.157	2.187	0.036	0.875
COX20	0.449	2.187	0.036	0.875
SYAP1	0.217	2.187	0.036	0.875
SUN3	-0.239	-2.187	0.036	0.875
PLEKHG5	-0.292	-2.185	0.036	0.875
AMPD1	0.163	2.185	0.036	0.875
DAB1	0.210	2.185	0.036	0.875
CORO6	0.340	2.185	0.036	0.875
ANKRD54	-0.167	-2.184	0.036	0.875
PHKB	-0.255	-2.183	0.036	0.875
RAB41	-0.281	-2.183	0.037	0.875
FBXO46	-0.147	-2.181	0.037	0.875
COL4A2	0.183	2.181	0.037	0.875
KIAA1522	0.237	2.179	0.037	0.875
TACO1	-0.253	-2.178	0.037	0.875
ZFPL1	0.217	2.178	0.037	0.875
RAB3B	0.380	2.177	0.037	0.875
SBK2	0.163	2.177	0.037	0.875
SEMA4A	0.201	2.175	0.037	0.875

IGSF3	-0.218	-2.174	0.037	0.875
MYL6	0.350	2.174	0.037	0.875
RPS4Y1	-0.596	-2.173	0.037	0.875
TMEM141	0.305	2.173	0.037	0.875
NTPCR	0.234	2.172	0.037	0.875
ZC3HAV1L	-0.236	-2.171	0.037	0.875
LGALS13	-0.232	-2.171	0.037	0.875
CYP4F3	-0.470	-2.168	0.038	0.875
RICTOR	0.163	2.168	0.038	0.875
VRK3	-0.453	-2.166	0.038	0.875
TMEM65	0.342	2.166	0.038	0.875
FAM89A	-0.191	-2.164	0.038	0.875
FAM83E	0.176	2.162	0.038	0.875
CEP19	-0.221	-2.162	0.038	0.875
PSMD13	0.279	2.161	0.038	0.875
GPR148	0.392	2.161	0.038	0.875
IAH1	0.292	2.161	0.038	0.875
REG1B	-0.570	-2.160	0.038	0.875
ZNF138	-0.268	-2.159	0.038	0.875
HOXC6	0.225	2.158	0.039	0.875
RPL14	0.194	2.158	0.039	0.875
PLXNA3	-0.218	-2.157	0.039	0.875
KCNC4	-0.386	-2.156	0.039	0.875
RPL15	0.250	2.156	0.039	0.875
WDR20	0.285	2.155	0.039	0.875
F11-AS1	-0.216	-2.155	0.039	0.875
KCNJ15	-0.246	-2.154	0.039	0.875
ELF3	0.217	2.154	0.039	0.875
ZNF256	-0.255	-2.153	0.039	0.875
DIP2A	0.202	2.153	0.039	0.875
CEP350	0.255	2.151	0.039	0.875
DXO	0.193	2.151	0.039	0.875
KCNJ12	-0.214	-2.150	0.039	0.875
APOBEC2	-0.149	-2.149	0.039	0.875
KLK14	-0.206	-2.149	0.039	0.875
FAM159B	-0.699	-2.149	0.039	0.875
DCUN1D1	0.171	2.149	0.039	0.875
TCEB3CL	0.217	2.149	0.039	0.875
TEX13A	-0.229	-2.148	0.039	0.875
PAG1	-0.354	-2.147	0.039	0.875
CTSF	0.168	2.147	0.039	0.875
IL17RC	-0.258	-2.147	0.040	0.875
WWC2-AS2	0.234	2.146	0.040	0.875
PLA2G12A	-0.270	-2.146	0.040	0.875
RXFP2	0.178	2.146	0.040	0.875
LCA5L	0.392	2.146	0.040	0.875
ASB14	0.175	2.146	0.040	0.875

GRIA3	0.545	2.145	0.040	0.875
CNKSR2	-0.254	-2.145	0.040	0.875
PLA2G1B	-0.917	-2.145	0.040	0.875
MVP	0.497	2.145	0.040	0.875
TRIM16	-0.248	-2.144	0.040	0.875
FOXN3	0.548	2.144	0.040	0.875
CCDC174	0.252	2.143	0.040	0.875
CSDE1	0.436	2.141	0.040	0.875
SLC13A4	-0.197	-2.140	0.040	0.875
CNIH3	-0.202	-2.139	0.040	0.875
TMEM260	-0.268	-2.139	0.040	0.875
BCL2	0.229	2.138	0.040	0.875
SFRP5	-0.190	-2.137	0.040	0.875
LRP1B	0.232	2.137	0.040	0.875
GAS6-AS1	-0.327	-2.137	0.040	0.875
ESM1	-0.317	-2.137	0.040	0.875
DDC	0.689	2.136	0.040	0.875
PTGER2	0.200	2.136	0.040	0.875
ETV1	-0.657	-2.134	0.041	0.875
ZNF345	-0.225	-2.134	0.041	0.875
JMJD1C	0.332	2.134	0.041	0.875
DIRC3	-0.326	-2.133	0.041	0.875
NAB1	0.307	2.133	0.041	0.875
CCDC18	0.189	2.133	0.041	0.875
OTUD6B	0.244	2.133	0.041	0.875
DMKN	-0.647	-2.133	0.041	0.875
ERICH2	-0.254	-2.131	0.041	0.875
IER3	0.237	2.130	0.041	0.875
DKKL1	-0.213	-2.128	0.041	0.875
NAT9	-0.179	-2.126	0.041	0.875
GABARAPL2	0.293	2.125	0.041	0.875
RAB3IP	-0.267	-2.123	0.042	0.875
CXorf36	0.149	2.123	0.042	0.875
THAP8	-0.255	-2.123	0.042	0.875
DPP10	0.484	2.123	0.042	0.875
LCE5A	0.183	2.122	0.042	0.875
ANKMY2	-0.340	-2.121	0.042	0.875
TPX2	-0.230	-2.120	0.042	0.875
CEP152	-0.361	-2.120	0.042	0.875
LPGAT1	-0.359	-2.120	0.042	0.875
ERVW-1	-0.282	-2.120	0.042	0.875
DHRS4L2	0.209	2.119	0.042	0.875
ZNF714	0.237	2.119	0.042	0.875
TFAM	-0.162	-2.119	0.042	0.875
MRPL27	-0.245	-2.119	0.042	0.875
CCDC87	0.281	2.118	0.042	0.875
PMEPA1	-0.270	-2.118	0.042	0.875

CACNA1B	-0.248	-2.118	0.042	0.875
KNOP1	-0.208	-2.117	0.042	0.875
C19orf70	0.210	2.116	0.042	0.875
STRAP	-0.205	-2.116	0.042	0.875
TCTA	0.353	2.115	0.042	0.875
PPTC7	0.240	2.115	0.042	0.875
CSPG5	-0.280	-2.114	0.042	0.875
FOXN4	0.167	2.113	0.043	0.875
WNT16	-0.229	-2.113	0.043	0.875
DLG2	0.529	2.112	0.043	0.875
MPP5	0.227	2.111	0.043	0.875
VTCN1	-0.238	-2.111	0.043	0.875
MT1L	-0.337	-2.111	0.043	0.875
ECE2	-0.209	-2.110	0.043	0.875
KLHL22	-0.185	-2.109	0.043	0.875
ARHGAP26	-0.328	-2.108	0.043	0.875
ESYT2	0.217	2.107	0.043	0.875
URGCP	0.187	2.107	0.043	0.875
FAXDC2	-0.396	-2.107	0.043	0.875
IFNA6	-0.174	-2.106	0.043	0.875
IFT172	-0.344	-2.105	0.043	0.875
KBTBD6	-0.149	-2.105	0.043	0.875
CTRB2	-1.059	-2.105	0.043	0.875
FNTA	0.222	2.105	0.043	0.875
SLC30A6	-0.227	-2.105	0.043	0.875
ASCL3	0.369	2.104	0.043	0.875
CCDC7	-0.176	-2.103	0.043	0.875
SPCS3	-0.206	-2.103	0.043	0.875
OTOR	0.153	2.102	0.044	0.875
SPAG8	-0.350	-2.101	0.044	0.875
RFT1	-0.185	-2.100	0.044	0.875
OR2W3	-0.438	-2.100	0.044	0.875
HIST1H4C	0.465	2.100	0.044	0.875
TMEM233	-0.209	-2.099	0.044	0.875
SOWAHD	-0.239	-2.099	0.044	0.875
USP5	-0.190	-2.099	0.044	0.875
C5orf56	0.412	2.098	0.044	0.875
GNL1	0.295	2.098	0.044	0.875
ANKRD20A1	-0.238	-2.097	0.044	0.875
HSPB7	0.241	2.097	0.044	0.875
TCEAL5	-0.406	-2.097	0.044	0.875
POLR2E	-0.247	-2.096	0.044	0.875
VPS41	-0.275	-2.096	0.044	0.875
GLRA4	-0.171	-2.095	0.044	0.875
CATSPER4	-0.197	-2.095	0.044	0.875
UPB1	-0.234	-2.094	0.044	0.875
CLMP	0.445	2.094	0.044	0.875

HLA-DQA1	-0.264	-2.093	0.044	0.875
CNTNAP3P2	-0.576	-2.093	0.044	0.875
MYOM3	0.389	2.093	0.044	0.875
PSMA1	-0.176	-2.092	0.044	0.875
PLOD1	-0.235	-2.091	0.045	0.875
ZNF230	-0.204	-2.091	0.045	0.875
BLOC1S5-TXNDC5	0.302	2.090	0.045	0.875
KCNS3	0.271	2.089	0.045	0.875
RBP2	0.349	2.088	0.045	0.875
GPR158-AS1	-0.271	-2.088	0.045	0.875
C1QTNF7	-0.222	-2.088	0.045	0.875
HAUS8	0.178	2.088	0.045	0.875
C6orf183	-0.243	-2.086	0.045	0.875
REPS2	0.250	2.086	0.045	0.875
GABPB1	-0.222	-2.085	0.045	0.875
C1QTNF3-AMACR	-0.256	-2.085	0.045	0.875
TSPAN9	-0.355	-2.083	0.045	0.875
MUM1	-0.283	-2.083	0.045	0.875
FAM184A	0.287	2.082	0.045	0.875
ITGAD	-0.165	-2.082	0.045	0.875
YWHAG	0.231	2.081	0.046	0.875
IQGAP3	0.188	2.081	0.046	0.875
SRSF6	-0.237	-2.080	0.046	0.875
CNOT4	0.411	2.079	0.046	0.875
DPYD	0.421	2.079	0.046	0.875
TSPAN2	-0.232	-2.078	0.046	0.875
CDH24	-0.201	-2.078	0.046	0.875
SLC35A3	0.333	2.077	0.046	0.875
TTC21A	-0.275	-2.077	0.046	0.875
RWDD4	-0.303	-2.077	0.046	0.875
FAM35A	-0.325	-2.077	0.046	0.875
CSGALNACT1	-0.376	-2.076	0.046	0.875
CA4	-0.311	-2.076	0.046	0.875
POLQ	0.147	2.076	0.046	0.875
TTLL5	-0.380	-2.075	0.046	0.875
CXCL13	0.232	2.074	0.046	0.875
BIRC3	0.171	2.074	0.046	0.875
SPERT	-0.209	-2.074	0.046	0.875
GLE1	-0.302	-2.074	0.046	0.875
LOC100421561	0.248	2.074	0.046	0.875
GPM6B	-0.311	-2.074	0.046	0.875
TLDC2	0.170	2.073	0.046	0.875
GSTO1	0.201	2.072	0.046	0.875
PRPSAP1	-0.255	-2.072	0.046	0.875
OR14I1	0.219	2.072	0.046	0.875
OR9K2	0.141	2.071	0.047	0.875

ARNTL	0.266	2.068	0.047	0.875
BRD2	0.363	2.068	0.047	0.875
MCTP2	0.160	2.067	0.047	0.875
SPINK13	-0.182	-2.067	0.047	0.875
CBWD2	-0.431	-2.066	0.047	0.875
ASAH1	0.247	2.066	0.047	0.875
CBWD5	-0.183	-2.066	0.047	0.875
TMCO2	-0.157	-2.065	0.047	0.875
THEMIS	-0.203	-2.065	0.047	0.875
RNASE3	-0.319	-2.064	0.047	0.875
ZMYM6NB	0.253	2.063	0.047	0.875
RBX1	0.212	2.063	0.047	0.875
ACR	-0.227	-2.063	0.047	0.875
PSG11	-0.292	-2.062	0.047	0.875
PDE5A	0.279	2.062	0.047	0.875
MAGEA4	-0.244	-2.062	0.047	0.875
ZCCHC14	0.176	2.062	0.047	0.875
MKLN1	0.425	2.061	0.047	0.875
LOC730668	-0.255	-2.061	0.048	0.875
CKLF-CMTM1	0.249	2.061	0.048	0.875
LCLAT1	-0.405	-2.061	0.048	0.875
SPPL2C	-0.241	-2.061	0.048	0.875
UGGT1	-0.258	-2.060	0.048	0.875
CALY	0.235	2.058	0.048	0.875
ASIC3	-0.199	-2.058	0.048	0.875
TEX30	-0.158	-2.058	0.048	0.875
GPER1	-0.448	-2.057	0.048	0.875
LRP8	-0.164	-2.057	0.048	0.875
TENM3	-0.210	-2.057	0.048	0.875
RBMS1	-0.244	-2.057	0.048	0.875
ZNF264	-0.227	-2.057	0.048	0.875
ZNF385B	0.655	2.056	0.048	0.875
GSKIP	0.323	2.054	0.048	0.875
SAFB	-0.260	-2.054	0.048	0.875
OPN4	0.156	2.054	0.048	0.875
CHRM1	-0.169	-2.053	0.048	0.875
DEFB121	-0.444	-2.053	0.048	0.875
CCL3	-0.204	-2.053	0.048	0.875
DOCK1	0.184	2.053	0.048	0.875
NREP	-0.294	-2.052	0.048	0.875
CFAP77	-0.270	-2.051	0.049	0.875
TWIST1	-0.188	-2.051	0.049	0.875
KCNA6	0.154	2.051	0.049	0.875
ASB9	-0.261	-2.051	0.049	0.875
MYO7A	-0.219	-2.051	0.049	0.875
PRC1	-0.346	-2.050	0.049	0.875
OR52L1	-0.168	-2.049	0.049	0.875

CCDC40	0.283	2.049	0.049	0.875
PUS1	0.174	2.049	0.049	0.875
DPY19L1	-0.262	-2.049	0.049	0.875
RGS20	0.179	2.048	0.049	0.875
STK4	0.285	2.047	0.049	0.875
YTHDC1	0.473	2.046	0.049	0.875
NHSL2	0.199	2.046	0.049	0.875
GTF2H3	0.138	2.046	0.049	0.875
NETO1	0.249	2.045	0.049	0.875
GFRA1	0.247	2.045	0.049	0.875
CCNY	0.344	2.045	0.049	0.875
INSRR	-0.164	-2.044	0.049	0.875
GNRHR	0.221	2.043	0.049	0.875
NEDD4L	0.476	2.041	0.050	0.875
MAZ	0.306	2.040	0.050	0.875
C11orf97	-0.119	-2.039	0.050	0.875
CSTF2T	-0.226	-2.039	0.050	0.875
IFITM5	0.216	2.039	0.050	0.875
TMEM151A	0.190	2.037	0.050	0.875

Supplementary Table 8. Genes differentially expressed between high and low signature score patients in the H12O validation cohort. Differential expression analysis was performed for all genes between patients with high and low signature scores. A total of 1029 genes were differentially expressed. However, no gene was significantly different after multiple testing correction. *SPP1* and *ATXN7* were differentially expressed between high- and low-score patients. Conversely, *REXO1L2P* did not show any difference. Only significant DEGs are shown. The *Log (fold change)*, *t-statistic*, *p-value* and *FDR* are shown for each gene. A *p-value < 0.05* was considered statistically significant.

Gene set	Collection	*P-value*	*FDR*	*LOG₂ (ERR)*	*ES*	*NES*	Size
TNFα signalign via NFκb	Hallmark	$2.39 \cdot 10^{-9}$	$5.71 \cdot 10^{-7}$	0.775	0.402	2.098	198
Cadherin binding	GO	$2.14 \cdot 10^{-4}$	0.017	0.519	0.271	1.505	329
Parkinsons disease	KEGG	$1.59 \cdot 10^{-4}$	0.017	0.519	0.354	1.701	120
Leishmania infection	KEGG	$3.82 \cdot 10^{-4}$	0.023	0.498	0.417	1.808	70
Inflammatory response	Hallmark	0.001	0.024	0.477	0.291	1.513	197
Endocytosis	KEGG	0.001	0.024	0.477	0.304	1.551	177
Acute myeloid leukemia	KEGG	0.001	0.027	0.477	0.428	1.774	57
Ribosome	KEGG	0.001	0.028	0.477	0.377	1.687	86
Interferon γ response	Hallmark	0.001	0.036	0.455	0.290	1.507	196
Oxidative phosphorylation	KEGG	0.002	0.036	0.455	0.320	1.542	124
Primary immunodeficiency	KEGG	0.002	0.036	0.455	0.477	1.766	35
Neuroactive ligand receptor interaction	KEGG	0.002	0.045	0.432	-0.286	-1.452	269
Interferon α response	Hallmark	0.002	0.045	0.432	0.346	1.580	93
Prostate cancer	KEGG	0.003	0.052	0.432	0.345	1.562	89
Apoptosis	Hallmark	0.003	0.052	0.432	0.352	1.575	86
Systemic lupus erythematosus	KEGG	0.004	0.055	0.432	0.309	1.499	129
Endocrine system development	Other	0.005	0.073	0.407	0.312	1.504	125
Calcium signaling pathway	KEGG	0.030	0.219	0.352	-0.281	-1.346	176
Wnt β-catenin signaling	Hallmark	0.038	0.254	0.322	-0.391	-1.442	42
Angiogenesis	Hallmark	0.043	0.255	0.288	-0.409	-1.457	36
Myc targets V2	Hallmark	0.046	0.260	0.322	-0.357	-1.410	57

Supplementary Table 9. Significantly enriched gene sets in patients with high and low signature scores in the H12O validation cohort. Gene set enrichment analysis was performed between high and low signature score patients from the H12O validation cohort using the differential expression analysis results and multiple gene set collections. A total of 12 gene sets were significantly enriched in high signature score patients. Only 1 gene set was significantly enriched in low signature score patients after multiple testing correction. However, 4 additional gene sets were significantly enriched in low-score patients when using the uncorrected *p-value*. Only significantly enriched gene sets are shown (*p-value*). The collection, *p-value*, *FDR*, expected error *LOG_2 (ERR)*, and raw and normalized enrichment score, as well as the size are shown for each gene set. An *FDR* < 0.05 was considered statistically significant.

PFS		*HR (95%CI)*		Multivariable (*P-value*)	
		Axitinib (N = 95)	Placebo (N = 98)	Axitinib (N = 95)	Placebo (N = 98)
OPN		1.013 (1.00– 1.022)	0.994 (0.098 – 1.004)	*0.0022*	*0.259*
Prior lines of treatment (N)	0 (Ref.)	*Ref.*	*Ref.*	*Ref.*	*Ref.*
	1	1.33 (0.65 – 2.71)	1.77 (1.00 – 3.12)	*0.429*	*0.047*
	2+	1.52 (0.69 – 3.31)	2.61 (1.17 – 5.84)	*0.291*	*0.018*
Location	Lung (Ref.)	*Ref.*	*Ref.*	*Ref.*	Ref.
	Other	2.91 (0.32 – 26.27)	3.88 (1.17 – 12.85)	*0.339*	0.026
	GI other	0.79 (0.35 – 1.79)	1.35 (0.47 – 3.86)	*0.583*	0.573
	Small intestine	0.61 (0.31 – 1.19)	1.22 (0.61 – 2.48)	*0.151*	0.573
	Unknown	1.03 (0.33 – 3.18)	3.71 (1.48 – 9.25)	*0.958*	0.005
Grade	G1 (Ref.)	*Ref.*	*Ref.*	*Ref.*	*Ref.*
	G2	2.39 (1.02 – 5.58)	1.69 (0.97 – 2.98)	*0.043*	*0.065*
	G3	4.60 (0.87 – 24.38)	5.55 (1.09 – 28.19)	*0.072*	*0.038*
Time since diagnosis	High	1.36 (0.76 – 2.44)	1.92 (1.07 – 3.27)	*0.288*	*0.027*
Carcinoid syndrome	Yes	0.81 (0.41 – 1.59)	1.004 (0.52 – 1.95)	*0.551*	*0.988*

Supplementary Table 10. Multivariable analysis of OPN plasma levels in axitinib- and placebo-treated patients. Cox multivariable proportional hazards models using PFS and OPN plasma levels, along with other possible confounding variables in axitinib (N = 95) and placebo-treated (N = 98) patients, are presented. *Hazard ratios* (*HR*) and *p-values* are shown. OPN plasma levels were independently associated with PFS in axitinib-treated patients, but not in placebo-treated patients. Grade is also an independent predictor of PFS in both arms of the trial. Time since diagnosis, primary tumor location and the number of prior lines of treatment were also independent predictors in placebo-treated patients. *95%CI, 95% confidence interval. Ref, reference.*

PhD related publications

Anna La Salvia, **Alberto Lens-Pardo**, Angel López-López, Carlos Carretero-Puche, Jaume Capdevila, Marta Benavent, Paula Jiménez-Fonseca, Daniel Castellano, Teresa Alonso, Alexandre Teule, Ana Custodio, Salvatore Tafuto, Adelaida La Casta, Francesca Spada, Angeles Lopez-Gonzalvez, Beatriz Gil-Calderon, Paula Espinosa-Olarte, Coral Barbas, Rocio Garcia-Carbonero, Beatriz Soldevilla. **Metabolomic profile of neuroendocrine tumors identifies methionine, porphyrin, and tryptophan metabolisms as key dysregulated pathways associated with patient survival**. **European Journal of Endocrinology**. 2023. 190-1, pp.62-74. https://doi.org/10.1093/ejendo/lvad160. **IF: 5.3 (Q1).**

Beatriz Soldevilla*, **Alberto Lens-Pardo***, Paula Espinosa-Olarte, Carlos Carretero-Puche, Sonia Molina-Pinelo, Carlos Robles, Marta Benavent, Lourdes Gomez-Izquierdo, Marta Fierro-Fernández, Patricia Morales-Burgo, Paula Jimenez-Fonseca, Beatriz Anton-Pascual, Yolanda Rodriguez-Gil, Ana Teijo-Quintans, Anna La Salvia, Beatriz Rubio-Cuesta, Maria C Riesco-Martínez, Rocio Garcia-Carbonero. **MicroRNA signature and integrative omics analyses to define prognostic clusters and key pathways driving prognosis in patients with neuroendocrine neoplasms**. **Molecular Oncology**. 2023. Apr; 17(4):582-597. https://doi.org/10.1002/1878-0261.13393. **IF: 5.0 (Q1).**

Beatriz Soldevilla, Angeles López-López, **Alberto Lens-Pardo**, Carlos Carretero-Puche, Angeles Lopez-Gonzalvez, Anna La Salvia, Beatriz Gil-Calderon, Maria C. Riesco-Martinez, Paula Espinosa-Olarte, Jacinto Sarmentero, Beatriz Rubio-Cuesta, Raúl Rincón, Coral Barbas and Rocio Garcia-Carbonero. **Comprehensive Plasma Metabolomic Profile of Patients with Advanced Neuroendocrine Tumors (NETs). Diagnostic and Biological Relevance**. **Cancers (Basel).** 2021. 13-11. 2634 https://doi.org/10.3390/cancers13112634. **IF: 4.5 (Q1)**

Ángeles López-López, Joanna Godzien, Beatriz Soldevilla, Ana Gradillas, Ángeles López-Gonzálvez, **Alberto Lens-Pardo**, Anna La Salvia, María Del Carmen Riesco-Martínez, Rocío García-Carbonero, Coral Barbas. **Oxidized lipids in the metabolic profiling of neuroendocrine tumors – Analytical challenges and biological implications. Journal of Chromatography A.** 2020. 1625. https://doi.org/10.1016/j.chroma.2020.461233. **IF: 3.80 (Q1)**

Rocio Garcia-Carbonero, Beatriz Anton-Pascual, Andrea Modrego, Maria del Carmen Riesco-Martinez, **Alberto Lens-Pardo**, Carlos Carretero-Puche, Beatriz Rubio-Cuesta, Beatriz Soldevilla. **Advances in the Treatment of Gastroenteropancreatic Neuroendocrine Carcinomas: are we moving forward? Endocrine Reviews**. 2023. 44: 4. 724–736. https://doi.org/10.1210/endrev/bnad006. **IF: 22.0 (D1)**

Beatriz Rubio-Cuesta, Carlos Carretero-Puche, Patricia Llamas, Jacinto Sarmentero, Beatriz Gil, **Alberto Lens-Pardo**, Beatriz Antón-Pascual, Eduardo Rubio-González, Maria Cámara, Javier Salamanca Santamaría, Daniel Rueda, Marco Delcuratolo, Rocio Garcia-Carbonero. **Co-targeting SRC overcomes resistance to BRAF inhibitors in colorectal cancer. British Journal of Cancer.** 2025. Under revision.